



**HAL**  
open science

# Influence of the extreme grain size reduction on plastic deformation instability in an AlMg and AlMgScZr alloys

D. A. Zhemchuzhnikova

► **To cite this version:**

D. A. Zhemchuzhnikova. Influence of the extreme grain size reduction on plastic deformation instability in an AlMg and AlMgScZr alloys. Materials. Université de Lorraine, 2018. English. NNT : 2018LORR0324 . tel-02141620

**HAL Id: tel-02141620**

**<https://hal.univ-lorraine.fr/tel-02141620>**

Submitted on 28 May 2019

**HAL** is a multi-disciplinary open access archive for the deposit and dissemination of scientific research documents, whether they are published or not. The documents may come from teaching and research institutions in France or abroad, or from public or private research centers.

L'archive ouverte pluridisciplinaire **HAL**, est destinée au dépôt et à la diffusion de documents scientifiques de niveau recherche, publiés ou non, émanant des établissements d'enseignement et de recherche français ou étrangers, des laboratoires publics ou privés.



## AVERTISSEMENT

Ce document est le fruit d'un long travail approuvé par le jury de soutenance et mis à disposition de l'ensemble de la communauté universitaire élargie.

Il est soumis à la propriété intellectuelle de l'auteur. Ceci implique une obligation de citation et de référencement lors de l'utilisation de ce document.

D'autre part, toute contrefaçon, plagiat, reproduction illicite encourt une poursuite pénale.

Contact : [ddoc-theses-contact@univ-lorraine.fr](mailto:ddoc-theses-contact@univ-lorraine.fr)

## LIENS

Code de la Propriété Intellectuelle. articles L 122. 4

Code de la Propriété Intellectuelle. articles L 335.2- L 335.10

[http://www.cfcopies.com/V2/leg/leg\\_droi.php](http://www.cfcopies.com/V2/leg/leg_droi.php)

<http://www.culture.gouv.fr/culture/infos-pratiques/droits/protection.htm>

# THÈSE

Pour l'obtention du titre :

DOCTEUR de L'UNIVERSITÉ DE LORRAINE

École doctorale : Chimie Mécanique Matériaux Physique (C2MP)

Domaine de Recherche : Physique, Sciences des Matériaux

Présentée par :

**Daria ZHEMCHUZHNIKOVA**

---

## **Influence of the extreme grain size reduction on plastic deformation instability in an AlMg and AlMgScZr alloys**

---

Soutenance publique prévue le 11 décembre 2018 à Metz

### Composition du jury

|                     |   |                     |
|---------------------|---|---------------------|
| Matthieu MAZIERE    | Professeur, MINES ParisTech<br>Paris, France                          | <i>Rapporteur</i>   |
| Kristián MATHIS     | Professeur associé, Charles University<br>Praha, République Tchèque   | <i>Rapporteur</i>   |
| Véronique<br>DOQUET | Directrice de recherche, Université Paris-<br>Saclay<br>Paris, France | <i>Examineur</i>    |
| Roxane MASSION      | Maitre de conférences, LEM3, Université de<br>Lorraine, Metz, France  | <i>Examineur</i>    |
| Mikhail LEBEDKIN    | Directeur de recherche, LEM3, Université de<br>Lorraine, Metz, France | <i>Directeur</i>    |
| Olivier BOUAZIZ     | Professeur, LEM3, Université de Lorraine<br>Metz, France              | <i>Co-directeur</i> |

Université de Lorraine, CNRS, Arts et Métiers ParisTech, LEM3  
7 rue Félix Savart, 57070, Metz, France

# Acknowledgments

*The present thesis has been carried out in the Laboratoire d'Etude des Microstructures et de Mécanique des Matériaux (LEM3) at the Université de Lorraine during the period from 2015 to 2018.*

*Foremost, I would like to express my gratitude to my advisor Dr. Mikhail Lebedkin for the patient guidance of my PhD study, constant feedback and for all the support he gave me to implement this research project. I am also grateful to Prof. Olivier Bouaziz for attention to my research.*

*I would like to thank Prof. Rustam Kaibyshev, who offered me internship opportunities in the framework of his collaboration with the LEM3 and promoted the development of my career.*

*My sincere thanks to the doctoral committee, especially to Prof. Matthieu Mazière and Prof. Kristián Máthi who accepted to review the dissertation, for their kind attention to my work and careful reading of the text.*

*Heartfelt thanks go to all my friends, who have always been a major source of support through the entire process of researching and writing this thesis. Thank you for your time devoted to me, your advices and for always telling me “You can do it!”.*

*My research would have been impossible without the aid and continuous encouragement of my favorite scientist and husband Pavel Kusakin.*

*Finally, I am grateful to the colleagues from LEM3 for their friendship and help they extended to me during my stay in the laboratory, and for always making me feel so welcome.*

# Contents

|  |           |
|--|-----------|
| <b>Introduction.....</b>   | <b>5</b>  |
| <br>   |           |
| <b>1 Background .....</b>  | <b>8</b>  |
| 1.1 Portevin-Le Chatelier effect.....  | 8         |
| 1.1.1. Phenomenology of jerky flow .....                                       | 8         |
| 1.1.2. Microscopic mechanism of the PLC effect: Dynamic strain ageing.....     | 15        |
| 1.1.3. PLC bands characteristics .....   | 18        |
| 1.1.4. Models of the PLC effect .....  | 21        |
| 1.2. Influence of the microstructure parameters on the PLC effect.....         | 22        |
| 1.2.1. Precipitates .....  | 22        |
| 1.2.2. Grain size.....   | 24        |
| 1.3. Al-Mg-Sc-Zr alloys.....   | 26        |
| 1.4. Effect of the PLC bands on the onset of necking.....                      | 28        |
| 1.5. Statistical approach to collective deformation processes.....             | 31        |
| <br>   |           |
| <b>2 Experiment and data analysis .....</b>                                    | <b>39</b> |
| 2.1 Materials and microstructure characterization.....                         | 39        |
| 2.1.1. Objects of investigation.....   | 39        |
| 2.1.2. Methods of microstructure characterization.....                         | 40        |
| 2.1.3. Pretreatments using SPD .....   | 41        |
| 2.1.4. Microstructure of the studied alloys before and after SPD .....         | 42        |
| 2.2. Experimental methods and data processing.....                             | 46        |
| 2.2.1. Tensile tests .....   | 46        |
| 2.2.2. Local strain measurement.....   | 48        |
| 2.2.3. Acoustic emission measurement .....                                     | 54        |
| 2.2.4. Statistical analysis .....  | 55        |
| <br>   |           |
| <b>3 Effect of microstructure on spatiotemporal behavior of the PLC effect</b> | <b>56</b> |
| 3.1. Coarse-grained binary alloy and alloy with coarse particles .....         | 56        |
| 3.1.1. Deformation curves and types of serrations .....                        | 56        |
| 3.1.2. Type A behavior.....  | 57        |

|   |            |
|---|------------|
| 3.1.3. Type B behavior .....  | 62         |
| 3.1.4. Low strain-rate behavior .....   | 66         |
| 3.1.5. Lüders bands.....  | 70         |
| 3.1.6. Concluding remarks .....   | 72         |
| 3.2. Effect of severe plastic deformation .....   | 73         |
| 3.2.1. FG state.....  | 73         |
| 3.2.2. FGH state.....   | 80         |
| 3.2.3. Concluding remarks .....   | 82         |
| 3.3. Comparison with alloys containing fine precipitates.....                                       | 83         |
| 3.3.1. CG state .....   | 84         |
| 3.3.2 FG state.....   | 88         |
| 3.3.3. Concluding remarks .....   | 91         |
| 3.4. Possible mechanism of the slow propagation regime .....  | 91         |
| <br>  |            |
| <b>4 Interrelation between the Portevin Le-Chatelier effect and necking in<br/>AlMg alloys.....</b> | <b>95</b>  |
| 4.1. Deformation curves.....  | 96         |
| 4.2. Analysis of the Considère strain .....   | 98         |
| 4.3. PLC bands behavior .....   | 99         |
| 4.3.1. CG state .....   | 99         |
| 4.3.2. FG state.....  | 103        |
| 4.3.3. FGH state.....   | 104        |
| 4.4. Discussion .....   | 106        |
| 4.4.1. Fulfillment of the Considère criterion in the presence of jerky flow .....                   | 106        |
| 4.4.2. Interrelation between the PLC bands and necking.....   | 108        |
| 4.5. Concluding remarks .....   | 109        |
| <br>  |            |
| <b>5 Effect of microstructure on the statistics of instabilities .....</b>                          | <b>110</b> |
| 5. 1. Stress serrations .....   | 110        |
| 5.2. Acoustic emission .....  | 114        |
| 5.3. Discussion and concluding remarks.....   | 119        |
| <br>  |            |
| <b>General conclusions and perspectives for future research.....</b>                                | <b>121</b> |
| <b>Bibliography.....</b>  | <b>125</b> |

# Introduction

The present thesis study brings together two areas of research. The first one concerns the Portevin-Le Chatelier (PLC) effect [Portevin and Le Chatelier, 1923] – the phenomenon of plastic instability in alloys, caused by the interaction of dislocations with solute atoms, or dynamic strain ageing (DSA). It is related to complex spatiotemporal patterns of strain localization in moving or immobile deformation bands and the concomitant variations in the applied stress. Besides the obvious detrimental effect of the deformation bands on the surface quality of the fabricated pieces, the instability also affects various mechanical properties of the material, including work-hardening behavior, tensile strength, ductility, and type of failure [Estrin and Kubin, 1995]. The elaboration of new alloys reveals a high diversity of behaviors of materials with various composition and/or microstructure and sustains constant interest to the PLC instability since its discovery more than a century ago. Moreover, plastic instability attracts a growing interest since mid-1990th as a striking example of self-organization of dislocations [Kubin et al., 2002]. Such a fundamental aspect unifies this field of research with a general problem of behavior of complex systems in physics, chemistry, biology, and other fields of research [Nicolis and Prigogone, 1977]. At the same time, it makes the elaboration task even more complicated because the prediction of real behaviors requires understanding of self-organization of dislocations.

The second topic concerns a quickly developing field of nanostructured materials produced by severe plastic deformation (SPD), with grain size reduced to one micron and less, which demonstrate outstanding mechanical properties [Valiev et al., 2014]. Invented about 30 years ago, the SPD method has proved its effectiveness for the development of metallic materials with remarkable mechanical and physical properties. These materials do not only have a fine grain structure but also specific properties such as metastable grain boundaries, twinning and nanoscale particles, segregation at grain boundaries, and so on. These features result in improved functional properties (mechanical, electrical, corrosion, etc.), especially in terms of a high mechanical strength.

It is not surprising that the influence of plastic instability on mechanical behavior of such materials attracts strong attention. However, recent studies have revealed a wide range of behaviors that are often contradictory. The possible reason of these ambiguities may be a complex influence of microstructure on the unstable plastic flow that is inherently multiscale because of the self-organization of dislocations. The present thesis was thus aimed at a multiscale study combining several experimental techniques, namely, mechanical testing,

acoustic emission, and digital image correlation, on several AlMg-based alloys with different controlled microstructures.

The choice of Al-based systems was dictated by two factors. First, due to their low weight and high mechanical strength, Al alloys are important technological materials for diverse applications. Second, binary Al-based alloys, especially 5000 series with Mg as the main impurity, were used for a long time as model materials for investigation of the PLC instability. The effects of various parameters (impurity concentration, grain size, dislocation density, specimen and testing geometry...), as well as external factors, e.g., application of electric current, were intensively investigated with regard to the instability conditions and overall behavior, such as frequency and amplitude of stress serrations [Yilmaz, 2011]. It was found that patterns of stress serrations and deformation bands manifest some specific features allowing for a phenomenological classification of several types of behaviors [Rodriguez, 1984]. Furthermore, it was proven both experimentally [Lebedkina and Lebyodkin, 2008 ; Chihab et al., 1987 ; Bharathi et al., 2001; Louche et al., 2005; Zhang et al., 2005] and theoretically [Kok et al., 2003; Rizzi and Hähner, 2004; Kumar and Ananthakrishna, 2011; Böhlke et al., 2009] that the statistical analysis of serrations, local strain-rate bursts, and acoustic emission, on the one hand, and kinematics of the PLC bands, on the other hand, can provide important information on the dynamical mechanisms responsible for the specific behavior.

At the same time, the practical use of AlMg alloys is limited because of their low strength and also a high susceptibility to stress-corrosion cracking [Polmear, 2006]. Numerous efforts to improve usage properties of these alloys through precipitation hardening and/or extreme grain refinement showed that the specific microstructure can strongly affect the jerky flow [Aboulfadl et al., 2015; Halim et al., 2007; Mogucheva et al., 2016; Zhao et al., 2014; Sarkar et al., 2013; Lebedkina et al., 2014; Wagenhofer et al., 1999; Bazarnik et al., 2012]. The influence of various precipitates on the PLC instability was studied for a long time. However, these investigations mainly aimed at characterizing overall mechanical properties, whereas the peculiarities of spatiotemporal behavior remained mostly neglected. The investigations of the grain refinement effect started recently and led to contradictory conclusions. In particular, it was established that the SPD increases the critical strain for the onset of serrated flow and diminishes the serration amplitude and frequency, or even completely suppresses the PLC effect in dilute Al-Mg alloys [Sarkar et al., 2013; Lebedkina et al., 2014; Wagenhofer et al., 1999; Bazarnik et al., 2012]. Therewith, the work hardening and, consequently, the ductility are considerably reduced. In contrast, the grain refinement was found to intensify the PLC instability without significant ductility reduction in Al-Mg alloys containing non-shearable nanoscale particles [Mogucheva et al., 2016; Zhao

et al., 2014]. Furthermore, the grain boundaries and precipitates may produce a synergistic effect on the spatial coupling between local strains and the conditions of self-organization of dislocations. However, there exist little literature on the relationship between the occurrence of different serration patterns and the PLC band characteristics in such materials. Moreover, even investigations of PLC bands in conventional coarse-grained binary alloys rendered contradictory results. For example, both an increase [Ait-Amokhtar et al., 2006] and a decrease [Chihab et al., 1987] in the band width were observed when the strain rate was increased.

These examples prove the need of systematic and comprehensive investigations of the effect of the initial microstructure on complex spatiotemporal behavior of the PLC instability. The objective of the PhD thesis was to realize such investigations in a wide strain-rate range covering different instability types and compare behaviors of a binary Al-3%Mg alloy and several alloys with Zr and/or Sc additives. These additives have a high application potential due to a substantial improvement of strength through formation of Al<sub>3</sub>(Sc, Zr) nanoscale precipitates, without losing the corrosion resistance and weldability [Filatov et al., 2000]. The samples were prepared in various microstructure conditions similar for all investigated materials. Besides the conventional coarse-grained state, the alloys were subjected to Equal Channel Angular Pressing (ECAP) resulting in strong reduction of the grain size and increase in the dislocation density. Two alloys were also subjected to an additional cold rolling following ECAP, which led to an extreme increase in the dislocation density approaching critical values corresponding to failure of AlMg alloys.

The thesis contains five chapters. The first chapter shortly describes various aspects concerning the PLC effect, the microstructure and mechanical properties of the AlMg alloys strengthened by Zr and Sc additives, the ECAP technique of severe plastic deformation, the basics of the statistical approach to the analysis of complexity of jerky flow, including the acoustic emission (AE) accompanying the plastic deformation. Chapter 2 presents experimental details on the materials, mechanical testing, the AE technique, and two methods of local extensometry, concurrently applied in the work. The results of investigations are presented in Chapters 3 to 5. Chapter 3 summarizes data on mechanical behavior of the investigated alloys, with an accent put on the relationship between the serration and deformation band patterns. Chapter 4 raises a question of a relationship between the PLC instability and such a general kind of (geometric) instability as necking. Chapter 5 is devoted to the statistical analysis of stress serrations and acoustic emission for one of the precipitation strengthened alloys and its comparison to the known data for binary alloys. Finally, a general summary of results and a discussion of perspectives for future investigations complete the thesis.

# Chapter 1

## Background

### 1.1 Portevin-Le Chatelier effect

#### 1.1.1. Phenomenology of jerky flow

##### 1.1.1.1. Macroscopic manifestations

The Portevin–Le Chatelier (PLC) effect is one of the most known kinds of unstable plastic flow in solids [Portevin and Le Chatelier, 1923, 1924] (see also [Le Chatelier, 1909]). It was found in various alloys, both substitutional and interstitial, having different crystal lattices including *fcc*, *bcc* and *hcp* structures, and in various deformation conditions including uniaxial and biaxial tension, compression and torsion (see reviews [Rodriguez, 1984; Robinson and Shaw, 1994; Robinson, 1994; Yilmaz, 2011]). Aluminum base alloys, and among them Al-Mg, represent one of the mostly studied cases [Aboufadi et al., 2015; Lebyodkin et al., 2000; Bharathi, et al., 2002; Robinson, 1994; Bal k and Lukáč, 1993; Chihab et al., 1987; Horvath et al., 2007; Halim et al., 2007; Louche et al., 2005; Jiang et al., 2007]. They are often considered as a model object for the investigation of plastic instability. In what follows, the literature data will mostly illustrate behavior of such alloys in the mostly studied tension conditions.

The PLC effect manifests itself by abrupt localizations of plastic strain in transient deformation bands visible on the specimen surface with a naked eye (Fig. 1.1). When the sample is loaded with a constant speed, the occurrence of a PLC band gives rise to a stress drop followed by reloading. This means that the plastic strain rate of the sample shortly exceeds the imposed strain rate  $\dot{\varepsilon}_a$ . The resulting serration deformation is often called jerky flow (Fig. 1.2). The notion of the PLC effect is also often applied to stepwise strain-stress curves in the conditions of the constant loading rate. The microscopic mechanism of instability is indeed the same in both cases, namely, the interaction of dislocations with solute atoms. However, many authors distinguish between the Portevin-Le Chatelier and the Savart-Masson effect found even earlier [Savart, 1837; Masson, 1841]. The constant loading rate conditions will not be considered in the thesis.

The occurrence of deformation bands is one of the reasons of the great attention received by the PLC effect, because their traces left on the surface have an obvious detrimental impact on the quality of industrial pieces. Moreover, the plastic instability modifies overall characteristics of the material plasticity, including work-hardening behavior, ultimate tensile strength (UTS), ductility, and type of failure [Estrin and Kubin, 1995]. Since the 1980<sup>th</sup>, the studies of the PLC effect have been given a new impulse as a rich example of self-organization of dislocations [Kubin et al., 2002] (see § 1.4). This interest is especially strong because self-organization phenomena are widely spread in nature [Haken, 1982].

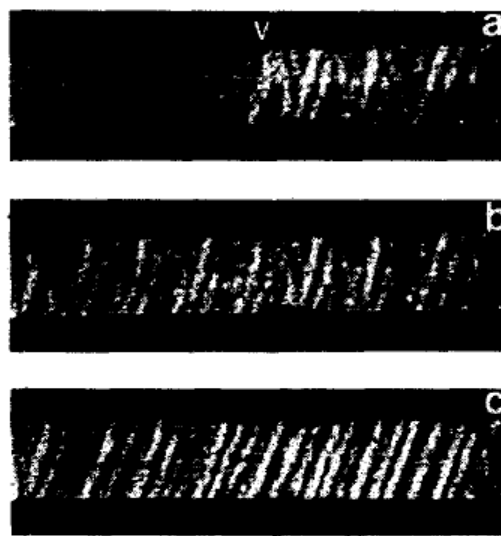


Figure 1.1: Traces of PLC bands on the surface of an Al-5at.%Mg alloy [Chihab et al., 1987].

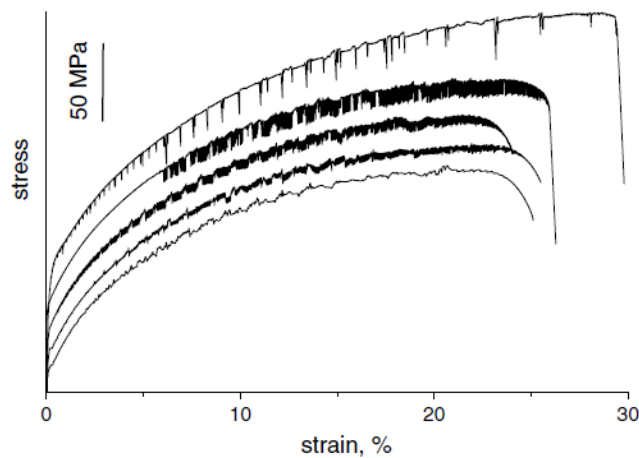


Figure 1.2: Examples of deformation curves for an Al-3%Mg alloy. The curves are deliberately shifted along the ordinate axis for clarity. The strain rate is varied from the upper curve downwards from  $4 \times 10^{-6} \text{ s}^{-1}$  to  $6 \times 10^{-3} \text{ s}^{-1}$  [Lebyodkin and Estrin, 2005].

### 1.1.1.2. Domains of observation

The instability occurs in bounded ranges of the imposed strain rate and temperature as illustrated in Fig. 1.3. Outside this domain, the plastic flow is stable. The boundaries of the domain depend on the material composition and microstructure and may vary by orders of magnitude of  $\dot{\epsilon}_a$  between different alloys.

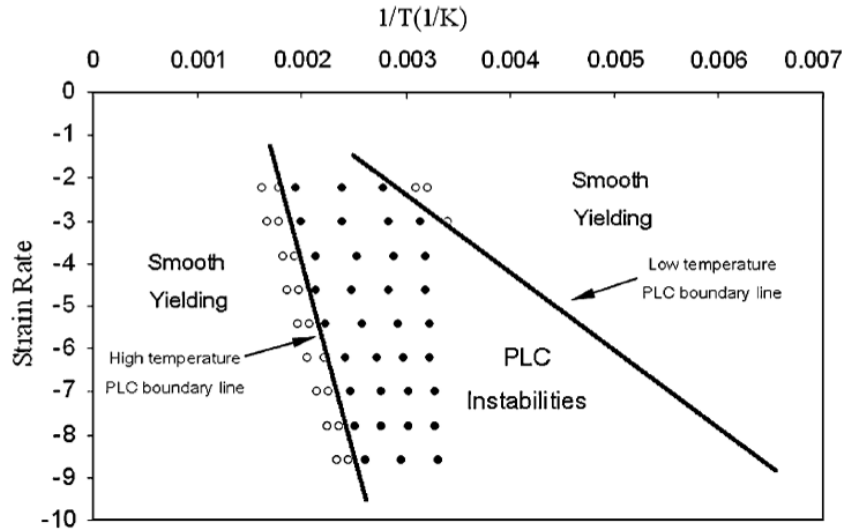


Figure 1.3: Example of boundaries of the PLC instability in AlMg alloy [Sheikh, 2010].

For given values of strain rate and temperature, the PLC effect often requires some incubation strain called critical strain,  $\epsilon_{cr}$  (Fig. 1.4). Depending on the experimental conditions, the dependence of  $\epsilon_{cr}$  on  $\dot{\epsilon}_a$  and  $T$  may have different signs [Bal k et al., 2000; Brechet and Estrin, 1995; Kubin and Estrin, 1990]. The most frequent “normal” behavior describes the case when  $\epsilon_{cr}$  increases with an increase in  $\dot{\epsilon}_a$  / decrease in  $T$ . The opposite dependences are referred to as “inverse” or “abnormal” behavior. Many alloys display normal behavior in a range of high strain rates (low temperatures) and a transition to inverse behavior in the opposite limit, as shown in Fig. 1.5. The nature of inverse behavior remains a matter of debate up to now [Bal k et al., 2000; Kobelev et al., 2017] (see § 1.1.4). It is noteworthy that the instability can also disappear after some deformation, thus implying a definition of a critical strain for cessation of the instability. In some cases, several critical strains are defined to describe an alternation between smooth and unstable plastic flow [Kubin and Estrin, 1990].

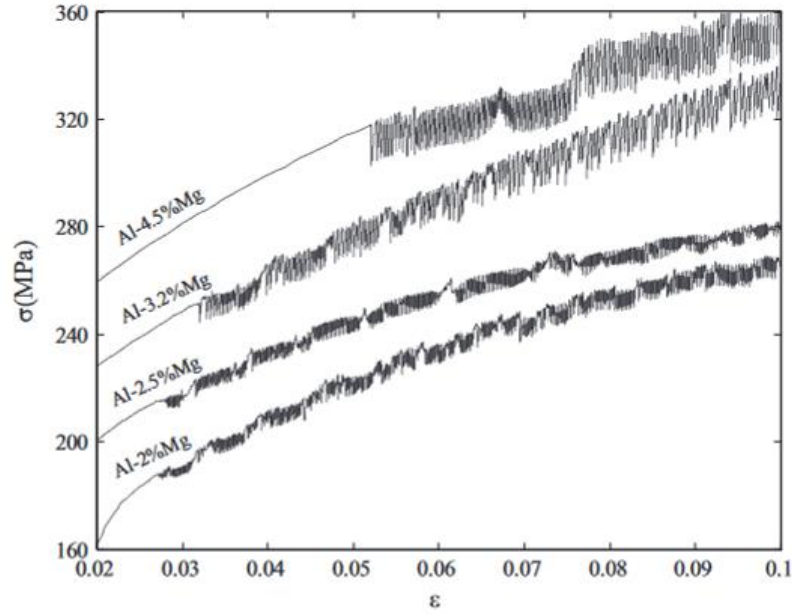


Figure 1.4: Deformation curves displaying the PLC effect at  $2.38 \times 10^{-4} \text{ s}^{-1}$  and room temperature for various Al-Mg alloys [Ait-Amokhtar et al., 2015].

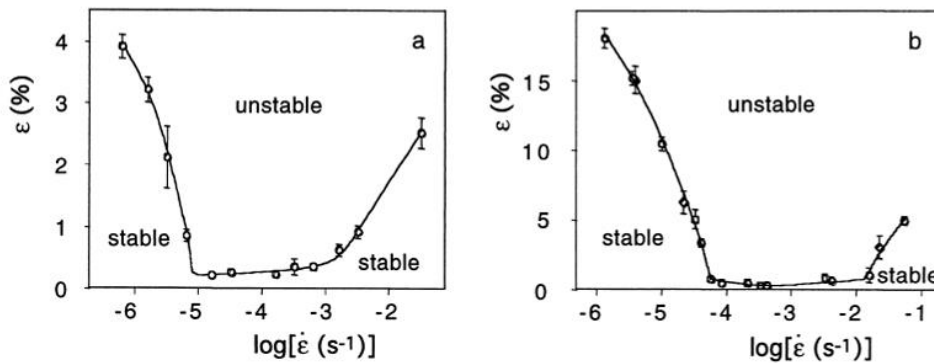


Figure 1.5: Dependences of the critical strain on the imposed strain rate for (a) an Al-2.6Mg alloy and (b) an Al-4.8Mg alloy [Bal k et al., 2000].

### 1.1.1.3. Types of spatiotemporal behavior

Macroscopic behavior of the PLC effect is associated with complex patterns of stress serrations related to nucleation and motion of deformation bands in the deforming material. Despite a great variety of specific shapes of serrated deformation curves observed for various materials, several generic types of behavior were distinguished on the basis of serration patterns and the concomitant band kinematics. Figure 1.6 represents the most general classification [Rodriguez, 1984, Robinson, 1994]. Based on the investigations of binary alloys, three major types (*A*, *B*, and *C*) are most often considered in the literature (e.g., [Jiang et al., 2007; Shashkov et al., 2012; Mogucheva et al., 2016]). They will be described

in some detail below. Additional types, *D* and *E*, are sometimes distinguished in order to take into account some specific patterns observed in commercial alloys [Rodriguez, 1984].

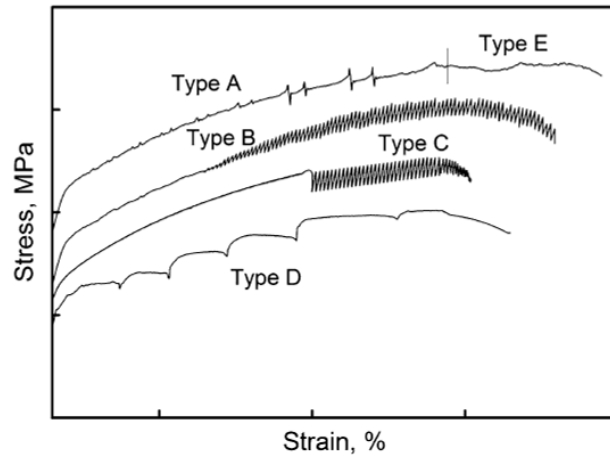


Figure 1.6: Types of stress serrations [Robinson and Shaw, 1994].

*Type A behavior.* Type *A* serrations, recognized as flow stress raises followed by a drop to or below the general stress level, are usually observed at high strain rates or low temperatures. They are associated with repetitive continuous propagation of deformation bands (Fig. 1.7). The raise in the stress is required to nucleate a new band, while its subsequent propagation proceeds at a lower stress level. The band is usually formed near one specimen edge and propagates quasi-continuously along the tensile axis with a high velocity reaching 10 cm/s at high enough  $\dot{\epsilon}_a$  [Chihab, et al., 1987; Ait-Amokhtar et al., 2006-1]. Figure 1.7a illustrates a gradual decrease in the band velocity with the material work hardening and an incipient transition to type *B* behavior at the latest stage of the test.

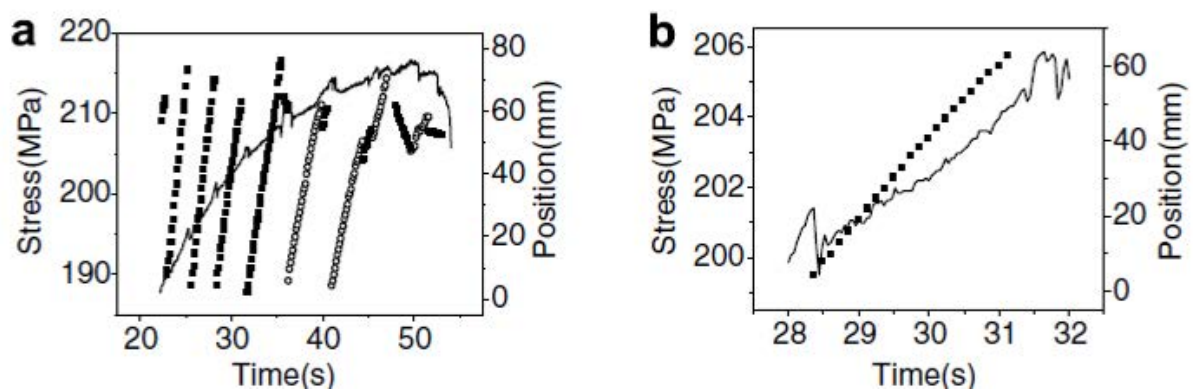


Figure 1.7: Example of type *A* bands [Jiang et al., 2007]. (a) Stress-time curve and the band positions at subsequent instants. Solid and open symbols correspond to two symmetric orientations of the bands with respect to the tensile axis (see § 1.1.3). (b) Zoom of (a) showing one propagation cycle.

*Type B.* Type *B* patterns occur at medium strain rates or temperatures. They are characterized by relatively regular abrupt stress oscillations about the general level of the stress-strain curve (Fig. 1.8). Such stress drops are caused by a brief occurrence of immobile bands in an ordered manner, so that this behavior is referred to as a relay-race, or hopping propagation. Figure 1.8 demonstrates an additional signature of type *B* serrations. Namely, the passage of a series of bands through the sample corresponds to a packet of regular stress serrations, followed by an interval of less regular fluctuations and an increase in the stress required to start a new relay-race in the work-hardened material. Like Figure 1.7 showed an incipient transition from type *A* to type *B* at large strains, Figs. 1.8a and Fig. 1.9 display a trend to a *B*  $\rightarrow$  *C* transition with increasing strain. More specifically, type *B* bands become less correlated and the respective serrations less regular.

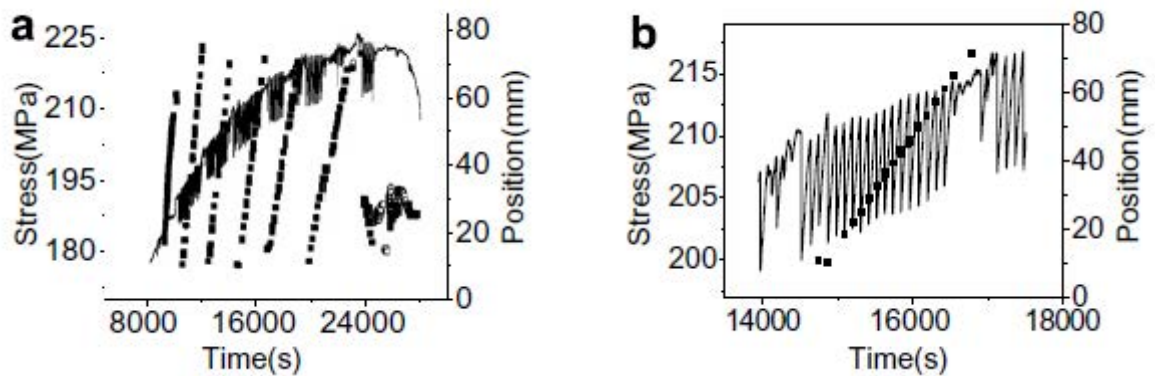


Figure 1.8: Example of type *B* bands [Jiang et al., 2007]. (a) See legend of Fig. 1.7a; (b) Zoom of (a) showing one series of bands propagation along the specimen.

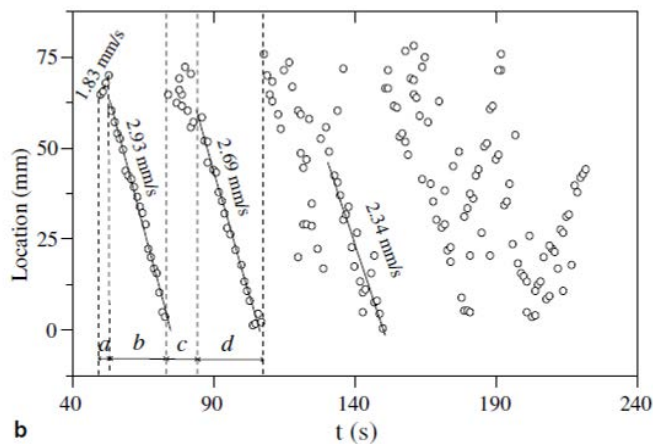


Figure 1.9: Space-time diagrams of type *B* bands hopping along a specimen of Al-4.5%Mg alloy at the strain rate of  $6 \times 10^{-4} \text{ s}^{-1}$  [Ait-Amokhtar et al., 2006-2].

*Type C.* Close to the lower boundary of the strain-rate domain of instability, this pattern is replaced by deep stress drops below the deformation curve, referred to as type *C* behavior. The corresponding spatial behavior is characterized by almost uncorrelated localized bands [Lebyodkin and Lebedkina, 2008]. The lack of correlation is schematically illustrated in Fig. 1.10. Since at room temperature, the occurrence of this regime often requires very low strain rates, type *C* patterns are much less common in the literature than types *A* or *B* regimes.

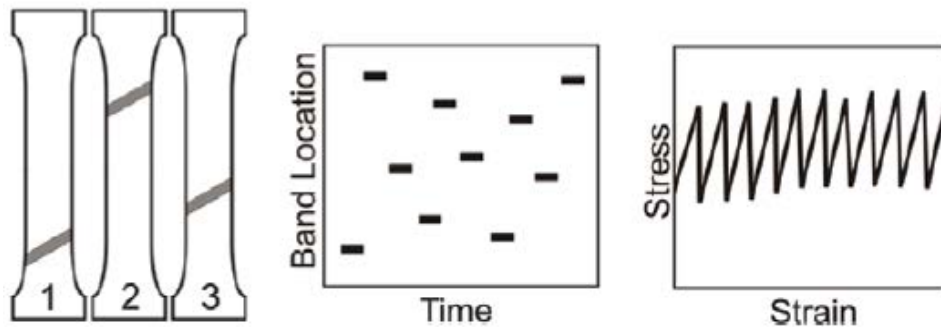


Figure 1.10: Schematic illustrations of the motion, orientation and spatio-temporal appearances of type *C* PLC bands [Yilmaz, 2011].

Finally, type *D* designates stepwise deformation curves corresponding to the propagation of each band at a constant stress level, i.e., without strain hardening. Type *E* also corresponds to a propagation regime. It sometimes follows type *A* mode at large enough strains [Rodriguez, 1984].

To summarize this conventional classification of the instability regimes, the appearance of serrations changes from type *A* to type *B* and finally to type *C* when either the strain rate is decreased or temperature is increased. As an example, the scheme of Fig. 1.11 displays domains corresponding to different regimes for a typical Al-3%Mg alloy. As underlined above, real behaviors may be much more complex. Not only additional types *D* and *E* are sometimes defined, but also combination of types may occur, especially in practically used alloys with complex compositions and initial structures [Robinson, 1994; Lebedkina et al., 2014, 2018; Andreau et al., 2014; Mogucheva et al., 2016; Valdes-Tabernerero et al., 2017]. Mixed *A+B* or *C+B* instabilities are often observed in some ranges of temperature and strain rate (see examples in Fig. 1.2 and the scheme in Fig. 1.11). Furthermore,  $A \rightarrow B$  and  $B \rightarrow C$  transitions may take place gradually in a single test (see Figs. 1.7–1.9), thus leading to complex transient behaviors [Ait-Amokhtar and Fressengeas, 2010; Mogucheva et al., 2016]. Besides the strain rate or temperature, these patterns depend on various microstructural parameters, such as grain size, dislocation density, and dispersion

of secondary phase particles. Their influence on the PLC types and the transitions between different types will be discussed in § 1.2.

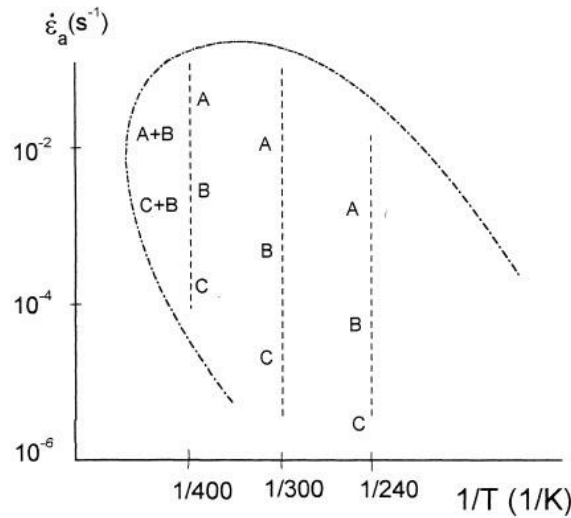


Figure 1.11: Schematic illustration of domains corresponding to different types of PLC behavior on the strain rate–temperature map for an Al-3at.% Mg alloy [Lebyodkin et al., 2000].

In spite of the complexity of real deformation curves, the phenomenological types have a profound physical sense as indicators of different regimes of collective dynamics of dislocations associated with the macroscopic plastic instability. The existence of persistent types of behavior of the PLC effect is itself an evidence of the collective nature of dislocation dynamics. During last two decades, the series of serrations were analyzed using various methods borrowed from the theory of nonlinear dissipative systems, such as the statistical and multifractal analysis [Lebyodkin et al., 1995; Bharathi et al., 2002], phase-space reconstruction [Bharathi et al., 2002; Noronha et al., 1997], wavelet analysis [Konstantinidis and Aifantis, 2002], recurrence analysis [Sarkar et al., 2008], Cohen decomposition [Darowicki et al., 2007], methods based on the random walk [Kugiumtzis et al., 2004] and Tsallis non-extensive statistics [Iliopoulos et al., 2015], and so on. In particular, the results of the statistical and multifractal analysis showed that the transitions from type *A* to type *B* to type *C* behaviors may be associated with the transition from the so-called self-organized criticality to deterministic chaos to synchronization phenomenon [Kubin et al., 2002]. These aspects will be presented in § 1.4.

### 1.1.2. Microscopic mechanism of the PLC effect: Dynamic strain ageing

Several reviews of the micromechanics and numerical models of the PLC effect have been published since the 1980<sup>th</sup> (e.g., [Estrin and Kubin, 1990; Estrin and Kubin, 1995;

Tamimi et al., 2015]). The first model of the effect was proposed in [Cottrell and Bilby, 1949]. It suggested that dislocations move quasi-viscously and drag solute clouds (“Cottrell atmosphere”). If the dislocation velocity reaches the critical value corresponding to the drift velocity of solutes, it is unpinned from the solute atmosphere and the resistance to its motion is decreased, i.e., deformation with a higher strain rate takes place at a lower stress. Therefore, the repeated pinning and unpinning of dislocations should give rise to stress serrations. However, theoretical estimates following from this model required unrealistic values for the dislocation densities and solute mobility.

The problem was resolved by taking into account the thermally activated nature of the dislocation motion through obstacles [Sleeswijk, 1958; McCormic, 1972; Van den Beukel, 1975]. It was suggested that solutes diffuse to dislocations during the waiting time  $t_w$  for thermal activation from the obstacles. Forest dislocations are considered as the main obstacles to the motion of dislocations in dilute single-phase alloys [Estrin and Kubin, 1990; Kubin and Estrin, 1991]. This concept, called dynamic strain aging (DSA), is now generally accepted as the microscopic mechanism of the PLC effect. Its key issue is the existence of a strain-rate range where the strain-rate sensitivity (SRS) of the deforming stress  $\sigma$ ,  $S = (\partial\sigma / \partial \ln \dot{\epsilon})_{\epsilon, T}$ , is negative [Estrin and Kubin, 1991]. It can be qualitatively explained considering the interplay between the  $t_w$  and the characteristic diffusion time of solute atoms,  $t_d$ . The solute atoms diffuse to the dislocation during  $t_w$  and additionally pin it. The deformation is stable in two limiting cases. First, when the plastic strain rate  $\dot{\epsilon}$  is high enough ( $t_w \ll t_d$ ), the dislocations are unaffected by solutes. Second, when it is low ( $t_w \gg t_d$ ), the solute atoms form a saturated cloud dragged by the dislocation. In both cases, the  $\sigma(\dot{\epsilon})$ -dependence has a positive slope (positive SRS) according to the thermally activated character of the dislocations motion, but the low strain-rate portion is shifted upwards because of the pinning force caused by solutes, as illustrated in Fig. 1.12a. The  $\sigma(\dot{\epsilon})$ -dependence changes the sign when  $t_w$  and  $t_d$  are comparable. Indeed, the higher  $\dot{\epsilon}$ , the smaller  $t_w$  and, therefore, the smaller the number of solutes in the cloud and the resulting additional pinning force. The dependence thus acquires an *N*-shape (Fig. 1.12a), with a range of a negative SRS. When  $\dot{\epsilon}_a$  is taken within this range, the plastic strain rate cannot reach  $\dot{\epsilon}_a$  but performs cyclic jumps between two branches of the *N*-shaped curve [Penning, 1972], i.e., the motion of dislocations proceeds via pinning–unpinning events. Suggesting identical conditions for all mobile dislocations, this mechanism gives rise to a periodic instability of relaxation-oscillation type (Fig. 1.12b), well known for dynamical systems of various nature [Ginoux and Letellier, 2012]. It should be noted that besides stress serrations, the DSA leads

to such anomalies of mechanical properties as peaks in the variation of the flow stress and work hardening rate with temperature, minima in the variation of the ductility and SRS with temperature, and others [Rodriguez, 1984; Kubin and Estrin, 1985; Robinson and Shaw, 1994].

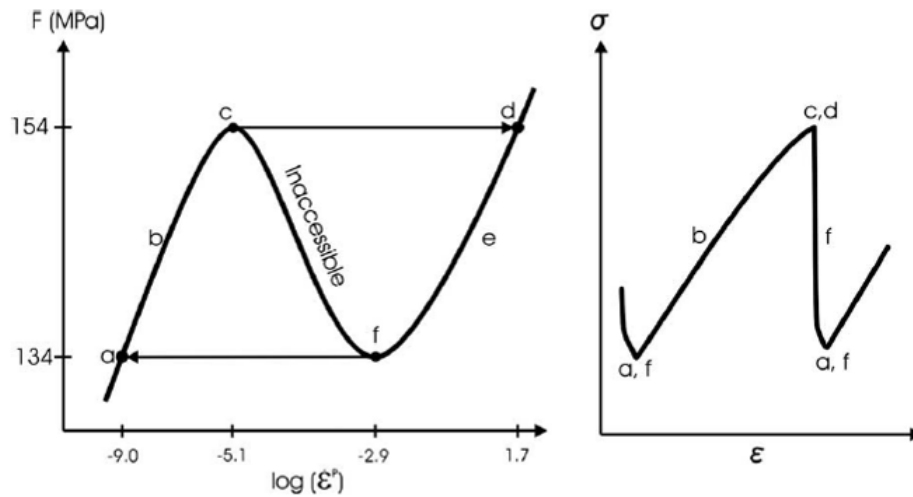


Figure 1.12: (a) Schematic representation of *N*-shaped curve describing the flow stress as a function of plastic strain rate; (b) The corresponding stress drop and reloading produced by strain rate jumps between two branches of the *N*-shaped curve [Kok et al., 2002].

The DSA concept continues being elaborated nowadays. Essentially for all further models of the PLC effect (see § 1.1.4), it was supposed that the effective ageing time of dislocations,  $t_a$ , is not equal to  $t_w$  but obeys a Boltzmann type relaxation equation (“retardation effect”),  $dt_a/dt = -(t_a - t_w)/\tau$ , where  $\tau \sim t_w$  is a relaxation time [McCormic, 1988]. Furthermore, the initially considered bulk diffusion of solutes occurred to be insufficient to give rise to DSA. Although it was expected that strain-induced vacancies could sufficiently enhance the diffusion coefficient, experiments showed that it was not the case [Cuddy and Leslie, 1972]. Consequently, it was suggested that a pipe diffusion along the core of dislocation is responsible for the DSA [Picu and Zhang, 2004]. Recently, cross-core diffusion from the compression side to the tension side of the dislocation slip plane was also suggested [Curtin et al., 2006; Aboufadel et al., 2015]. Finally, an important question was raised in [Hähner, 1996-1, Hähner, 1996-2]. It was shown that when a statistical distribution of ageing time is considered, the DSA theory is not sufficient to explain the negative SRS, unless collective effects due to dislocation interactions are also taken into account.

### 1.1.3. PLC bands characteristics

Diverse high-resolution real-time techniques were applied to study the above-described spatiotemporal patterns of series of PLC bands, but also various characteristics of individual bands: its geometry, the propagation velocity  $V_b$  and width  $w$ , the local strain rate  $\dot{\epsilon}_{loc}$  and the cumulated strain  $\Delta\epsilon_b$  in the band. A non-exhaustive list includes video-recording of the specimen surface [Chihab et al., 1987], digital image correlation (DIC) [Ait-Amokhtar et al., 2006-1], infrared thermography (IR) [Louche et al., 2005], digital speckle patterns interferometry (DSPI) [Jiang et al., 2007], laser scanning extensometry [Casarotto et al., 2005].

Despite these efforts, the literature data are quite contradictory and make one suggest that the band characteristics must essentially depend on the material. As a result, it is difficult to compare data reported by different authors. For example, the band width was observed both to decrease [Chihab et al., 1987] and increase [Ait-Amokhtar et al., 2006-1; McCormick et al., 1993] with increasing  $\dot{\epsilon}_a$ . Most authors find that  $V_b$  increases with  $\dot{\epsilon}_a$  according to a power-law dependence  $V_b \propto \dot{\epsilon}_a^\mu$  [Chihab et al., 1987; Ait-Amokhtar et al., 2006-1; Klose et al., 2004]. Nevertheless, a complex non-monotonous dependence was also observed [Bakir, 1995]. A qualitative consensus concerns the observation that  $V_b$  is reduced during the test. However, it is not the case for the quantitative description. Different authors reported an inverse proportionality to time [Louche et al., 2005] or stress [Ranc and Wagner, 2005], an exponential decrease with strain [Junying Min et al., 2014], or highly scattered dependences [Casarotto et al., 2003; Shabadi et al., 2004]. Another agreement concerns the band orientation. Consideration of the PLC bands as localized necks in thin sheets deformed under plane stress conditions allows to predict a close to  $55^\circ$  angle of inclination of the band with respect to the tensile axis [Hill, 1952]. Experiments show that this angle may depend on the microstructure and texture and varies in a large enough range, most typically, from  $52^\circ$  to  $60^\circ$  (e.g., [Ait-Amokhtar et al., 2006-1]). As was seen in Figs. 1.7 and 1.8, bifurcation between two symmetrical orientations may take place many times during the test.

Finally, it is agreed that the local strain rate within the band is non-uniform [Ait-Amokhtar et al., 2006-2; Zdunek et al., 2008]. It is often considered that it has a maximum at the center of the band as illustrated in Fig. 1.13 [Tong et al., 2005; Ait-Amokhtar et al., 2006-1]. Precise measurements in [Ait-Amokhtar et al., 2006-2] allowed to demonstrate that the maximum  $\dot{\epsilon}_{loc}$  may exceed  $\dot{\epsilon}_a$  by many orders of magnitude. The authors report the ratio of 7250 for type *C* bands observed at  $\dot{\epsilon}_a = 1.6 \times 10^{-4} \text{ s}^{-1}$ , 1106 for type *B* bands

( $\dot{\epsilon}_a = 6 \times 10^{-4} \text{ s}^{-1}$ ), and 54 for type *A* bands ( $\dot{\epsilon}_a = 5 \times 10^{-3} \text{ s}^{-1}$ ). The fact that the degree of strain localization strongly increases from propagating to static bands is confirmed by various authors. It should, however, be specified that most of papers provide significantly underestimated data (by an order of magnitude) because of the insufficient time resolution.

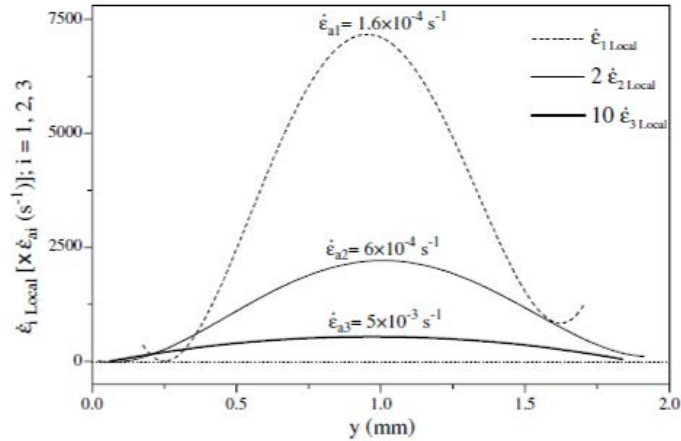


Figure 1.13: Local strain rate within a PLC band in Al-4.5%Mg as a function of applied strain rate [Ait-Amokhtar et al., 2006-2].

The constant improvement of the time resolution of the above-mentioned methods allowed for a recent progress in the investigation of the long-standing problem of the PLC band nucleation and relationship between the stress drops and the band development. The usually discussed scenarios of band nucleation were formulated in [Kocks, 1981; Chihab et al., 1987]. Two extreme cases consider the occurrence of either a relatively large embryo on a side surface of the specimen, followed by its transversal growth, or a thin (several atomic planes) transversal band that grows in the lateral direction. Besides, a combination of such scenarios can be envisaged, such that a band arises on a side surface and is thickened laterally during the transverse propagation, thus acquiring a wedge shape.

An example of such investigations is presented in Fig. 1.14. It shows a sequence of records of the accumulated strain in two subsequent type *B* bands in an Al-4.5Mg-0.7Mn alloy [Zdunek et al., 2008]. The images were taken with a frequency of 25 fps (frames per second). The arrows indicate that the nucleation of a band is immediately followed by an abrupt stress drop. The instant of the band nucleation was not captured. Nevertheless, the images allow to suggest that it corresponds to the stress maximum after which occurs the stress drop. The frames 3 and 7 bear evidence to a quasi-instantaneous nucleation of deformation bands across the whole specimen width. Although the accuracy (typical of such measurements) is yet insufficient for a definite conclusion, this hypothesis was confirmed in

two recent works where the acquisition frequency was as high as 1000–5000 fps [Tong et al., 2005] and 400–2500 [Casarotto et al., 2009]. At the same time, the latter work reported the observation of both quasi-simultaneous shear in various grains over the entire cross-section and a gradual growth of a wedge-shaped PLC band starting from one specimen side. The latter case, corresponding to the “mixed” nucleation scenario, is illustrated in Fig. 1.15. This diversity of observations corroborates other examples indicating that even qualitative patterns of behavior of the PLC effect may vary between materials with different microstructure.

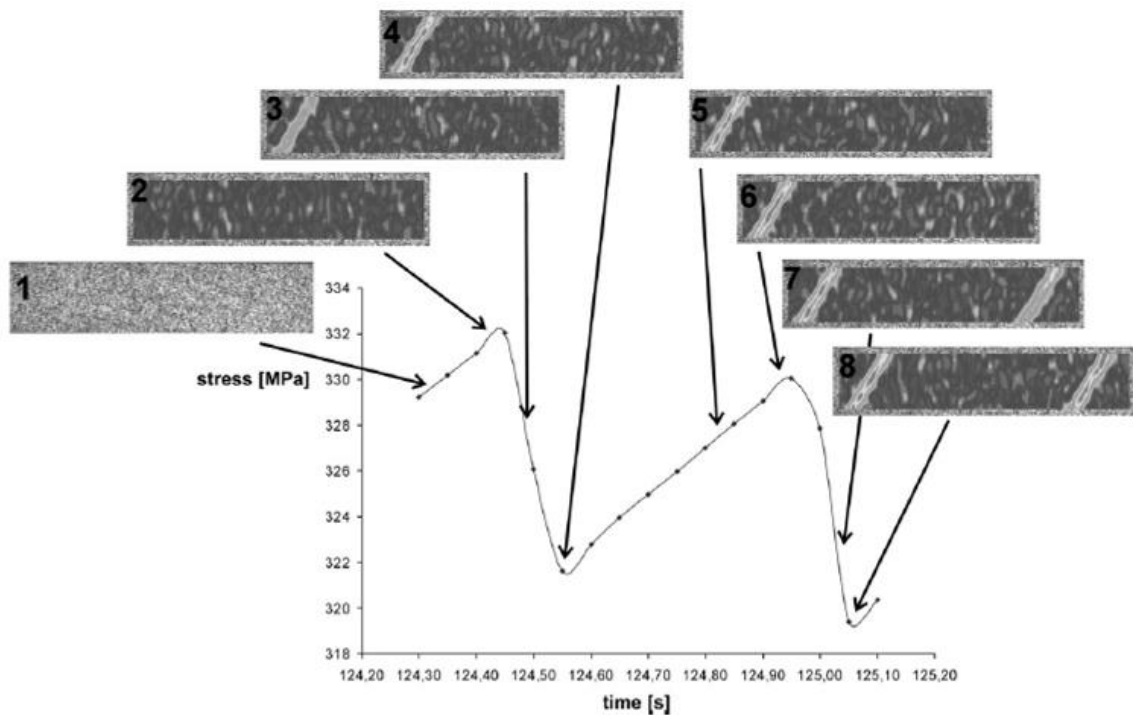


Figure 1.14: Correlation between two stress drops of type *B* and the corresponding deformation bands [Zdunek et al., 2008].

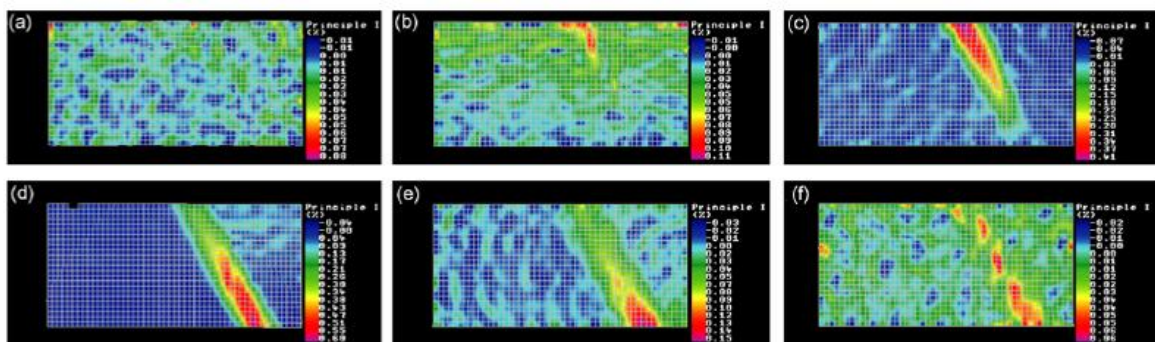


Figure 1.15: Example of a type *B* PLC band nucleation and growth through the width of an Al-3Mg specimen (image acquisition rate 900 fps) [Casarotto et al., 2009].

#### 1.1.4. Models of the PLC effect

As specified above, the microscopic models of DSA, which consider the  $N$ -shaped SRS but do not take into account collective dynamics of dislocations, represent the PLC instability as regular relaxation oscillations and cannot predict complex spatiotemporal patterns. However, the microscopic consideration allows to determine the conditions of plastic instability, in particular, the critical strain  $\varepsilon_{cr}$ . Early models, considering the occurrence of a negative SRS as the instability criterion, predicted normal behavior qualitatively, but were unable to reproduce the inverse trend (e.g., [Kubin and Estrin, 1990]). Various approaches were further explored. In particular, it was shown that inverse behavior may be caused by the modification of the DSA in the presence of shearable precipitates, e.g., in AlLi alloys [Brechet and Estrin, 1995] (cf. § 1.2.1). On the other hand, numerous experiments showed both dependences (descending at low strain rates and ascending in the opposite limit) in AlMg alloys [Bal k et al., 2000; Král and Lukáč, 1997] (see Fig. 1.5). It was found that modifying the law of evolution of mobile and forest dislocations suggested in [Kubin and Estrin, 1990], it is possible to reproduce behaviors illustrated in Fig. 1.5 [Bal k and Lukáč, 1993]. Recently, a unique phenomenological framework based on the consideration of strain dependences of the DSA parameters was proposed [Böhlke et al., 2009; Mazière and Dierke, 2012]. Moreover, the finite element (FEM) approach provided evidence that the condition of negative SRS is not sufficient, but the realistic instability criterion should consider an exponential growth of the initial perturbation [Mazière and Dierke, 2012]. This conclusion agrees with that following from recent experiments testifying that the phenomenological criterion describing low strain-rate behavior should reflect the abrupt character of the strain localization caused by the phenomenon of dislocation synchronization [Kobeleev et al., 2017] (see § 1.5).

Another challenge to modelling concerns the prediction of complex spatiotemporal behaviors described in the previous sections, which are caused by the collective dislocation dynamics. Early models introduced strain heterogeneity and spatial coupling between local strains by dividing the tensile specimen into a chain of slices coupled by elastic forces [Lebyodkin et al., 1995; McCormick and Ling, 1993]. Such elastic forces may have various causes. Without going into details, it is worth noting a general framework considering elastic stresses due to different straining of neighboring cross-sections, mathematically described by second gradients of strain [Zbib and Aifantis, 1988]. This physical origin of such stresses is easy to understand. Indeed, the plastic strain incompatibilities generated by the heterogeneous plastic flow, e.g., by the strain localization, must be compensated by elastic

strains giving rise to long-range internal stresses. Despite the simplicity of this approach, such models successfully reproduced the transitions between the main types of behavior, including static and propagating PLC bands, as well the concomitant transitions between types of statistics of stress serrations (see § 1.5) [Lebyodkin et al., 2000]. In comparison with this phenomenological models, FEM simulation of polycrystal plasticity allowed for a more physical consideration of spatial coupling stemming from plastic strain incompatibilities between various grains (e.g., [Kok et al., 2002; Kok et al., 2003; Mazière et al., 2010]).

An alternative approach borrowed from the theory of nonlinear dynamical systems and based on the so-called “reaction-diffusion scheme” was proposed at the same period as the block-and-spring models [Ananthakrishna and Valsakumar, 1982]. These models do not integrate explicitly the DSA theory but consider the evolution of three dislocation families: mobile, forest, and mobile dislocations dragging solute clouds. Coupled to the block-and-spring scheme, they also successfully reproduced various types of spatiotemporal dynamics and statistical properties [Ananthakrishna, 2007]. Recently, this kind of modeling was applied to explain properties of the acoustic emission accompanying the PLC instability [Kumar and Ananthakrishna, 2018].

## **1.2. Influence of the microstructure parameters on the PLC effect**

### *1.2.1. Precipitates*

Complex precipitation-strengthened alloys are widely used for modern technical applications and have been objects of numerous investigations. However, most of efforts were concentrated on the characterization of specific alloys, without studying the effect of precipitation on jerky flow. The investigations of the latter mainly concerned the influence of various kinds of precipitates on the critical strain for the onset of the PLC instability, the average size of stress serrations (e.g., [Robinson, 1994; Brechet and Estrin, 1995; Estrin and Lebyodkin, 2004; Wen et al., 2005; Pink and Krol, 1995; Thevenet et al., 1999; Kumar and Pink, 1995; Mulford, 1979; Qi Hu et al., 2011; Dierke et al., 2007; Pink, 1989]) and, in some cases, the duration, frequency, and statistics of stress drops [e.g., Pink et al., 2000]. Their main goal was to answer whether precipitation suppresses or favors the instability and detect the possible difference in the effects of small precipitates ( $< 10\text{-}15$  nm), which can be sheared by the mobile dislocations, and coarse non-shearable particles bypassed by Orowan bowing [general ref. from Chap. 3]. Various works dealt with different commercial alloys, were realized in different experimental conditions, often in a limited range (e.g., for one or

two values of the loading rate), and did not provide a unique opinion. For both kinds of precipitates, their supposed effect varied from assisting the instability, to “no effect”, to preventing from the instability (earlier references revealing the same contradictions can be found in [Pink et al., 2000]).

The following mechanisms of the effect of precipitation on the PLC instability are often discussed in the literature:

- The depletion of the solute concentration in the solid solution because the formation of precipitates would reduce the average amplitude of stress serrations. This mechanism is most often discussed in relation with the formation of coarse incoherent precipitates [Pink, 1989].
- The trapping of vacancies by precipitates would prevent from the PLC instability by reducing the solutes diffusion in the bulk of the material. This effect is attributed to fine shearable precipitates [Pink, 1989; Pink and Krol, 1995]. However, since it has been established that the DSA requires the solute diffusion in the dislocation core, while the bulk diffusion does not suffice for most materials, this mechanism is hardly likely.
- A straightforward influence consists in the increase in the number of obstacles to the dislocation motion and, therefore, the waiting time available for solutes diffusion towards dislocations. More specifically, it was predicted theoretically that shearing of small coherent precipitates in the bulk of the material may effect on the SRS and be responsible for the inverse behavior of the critical strain [Brechet and Estrin, 1995]. However, it is worth noting experimental observations testifying that precipitation does not considerably affect the DSA, in the sense that the change from a positive to negative SRS “occurs at the same temperature for a given material regardless of whether precipitates are present or not” [Mulford, 1979].
- Precipitates influence on the work-hardening processes, such as piling up and multiplication of dislocations. In particular, the density of mobile and forest dislocations is a central point of a well-known model of the critical strain for the PLC effect [Kubin and Estrin, 1990].
- It was also suggested that shearing and reversal (re-precipitation following the dissolution of the sheared particle) of coherent precipitates can provide an alternative mechanism of jerky flow, called “pseudo-PLC effect” because such a mechanism would also give rise to a negative SRS [Brechet and Estrin, 1994]. However, reliable

experimental proofs of such instability are missing. In particular, the analysis of the acoustic emission accompanying jerky flow, which helps to distinguish the dislocation motion in the crystal lattice from the particles shearing, did not support this hypothesis [Chmelik et al., 1998].

Finally, many authors arrived at a conclusion that the main role of the precipitates consists in changing the structural conditions, e.g., dislocation distributions and local stress concentrations, which would change the conditions of the deformation band nucleation and development [Pink et al., 2000, Dierke et al., 2007]. This suggestion motivates investigation of the effect of precipitates on the transitions between types of serrations and PLC band kinematics. To our knowledge, while some fragmentary data on types of serrations are present in the above literature, no systematic investigation of the effect of precipitates on the band kinematics has been performed so far.

### *1.2.2. Grain size*

The question of the effects of grain size on the PLC instability is similar to that of the precipitates, in the sense that grain boundaries also influence on the work-hardening processes, i.e., the density of mobile and forest dislocations, and therefore, can change both the conditions of the occurrence of the DSA (the critical strain, the strain rate and temperature boundaries of the domain of instability) and the collective dislocation dynamics (the magnitude and frequency of stress serrations, the types of behavior, the properties of the PLC bands). Moreover, it was suggested that the DSA may preferentially occur at grain boundaries [Rodriguez, 1984]. However, before the beginning of extensive investigations of fine-grained (FG) materials with submicronic grain size, little literature was available on the influence of grain size on the PLC effect. In particular, it was generally observed that a decrease in the grain size reduces the critical strain  $\epsilon_{cr}$  and enhances the magnitude of serrations [Brindley and Worthington, 1969; Wagenhofer et al., 1999]. As will be seen below, similar effects may characterize FG materials, but opposite trends are also often observed.

Extensive grain refinement by severe plastic deformation (SPD) is one of the key technique to produce high-strength alloys [Sabirov et al., 2013; Estrin and Vinogradov, 2013]. The high mechanical properties of these alloys, such as the enhanced yield stress and ultimate tensile stress are mainly attributed to the grain size strengthening according to Hall-Petch relationship [Sabirov et al., 2013; Malopheyev and Kaibyshev, 2015]. More specifically, the hardening results from the limitation of the dislocations free path due to the

decreasing grain size and increasing density of high angle grain boundaries. Such boundaries are effective obstacles to the dislocation motion because of the strongly different orientation of slip planes between neighboring grains. In addition, the SPD gives rise to a high density of other defects, such as forest dislocations and vacancies.

In view of these factors, investigations of jerky flow in FG alloys inevitably had to attract researchers' interest. However, first works only appeared at the beginning of the 2000<sup>th</sup>. This field of research is developing nowadays. The results obtained so far do not allow for a unique conclusion; perhaps, because the SPD process of different kinds generate very different microstructures. Moreover, even the same process may produce different microstructures depending on the applied total strain and the subsequent heat treatment. Many observations indicate that the strain interval where the PLC effect occurs is reduced in FG materials. A detailed study of the effect of subsequent passes of confined channel die pressing (CCDP) on the PLC instability in Al-Mg alloys with different Mg content was recently reported in [Zhao et al., 2014]. The final grain size depended on the Mg content and varied from 250 nm in Al-1Mg to 100 nm in Al-5Mg. The measurements demonstrated a considerable increase in  $\epsilon_{cr}$  with the CCDP strain (the number of passes). At the same time, the measurement of the DSA revealed non-monotonous behavior of the negative SRS with strain, decreasing after several first passes and increasing afterwards. These changes were discussed in the framework of the above-described DSA models (§ 1.1.2), taking into account the progressive changes in the microstructure with the SPD, particularly, the evolution of the densities of mobile and forest dislocations and various obstacles to the mobile dislocations. Grain refinement was reported to completely suppress the PLC effect in a dilute Al-3%Mg alloy with grain size about 500–700 nm, obtained by equal channel angular pressing (ECAP) [Lebedkina and Lebyodkin, 2008]. On the basis of the multifractal analysis of stress serrations, the authors suggested that the disappearance of the macroscopic instability may be due to hindering the synchronization of the dislocations dynamics in the FG state. The suppression of the instability was also reported in [Markushev and Murashkin, 2013]. In this study, the PLC effect was weakened in a submicrocrystalline (SMC) Al-6%Mg-0.6%Mn alloy but enhanced in the microcrystalline (MC) state, with grain sizes of 0.4  $\mu\text{m}$  and 5  $\mu\text{m}$ , respectively. Moreover, whereas the SMC alloy displayed a critical strain of 5%, jerky flow occurred immediately after the onset of plastic deformation in the MC state.

In contrast to these works, a considerable reinforcement of instability was reported after ECAP of Al-Mg-Sc alloys containing non-shearable nanoscale precipitates [Malopheyev and Kaibyshev, 2015; Mogucheva et al., 2016; Komarasamy and Mishra,

2014]. More exactly, jerky flow started immediately upon the elastoplastic transition, i.e., without visible critical strain, the instability domain was extended towards lower strain rates, and stress serrations were characterized by significantly higher amplitudes than in the initial coarse-grained state. An additional surface topography of tensile samples [Mogucheva et al., 2016; Komarasamy and Mishra, 2014] showed that grain refinement highly increased the local uniformity of the dislocation glide, decreased the surface roughness, and eliminated the difference in the sample roughness between the neck region and the regions far from the fracture site, as compared with the coarse-grained material. The enhancement of the PLC effect (a decrease in the critical strain and an increase in the amplitude of *B* type stress drops) with grain refinement was also observed in an AA5182 Al alloy containing Mg(Mg<sub>2</sub>Al<sub>3</sub>) precipitates [Wei Wen and Morris, 2004] and an Al-5356 alloy with Al<sub>3</sub>Mg<sub>2</sub> particles [Saad et al., 2010].

It is also of interest to mention a new research direction related to gradient surface structures. In a recent work [Meng et al., 2018], samples of a 5182 Al alloy with two grain sizes were subjected to surface mechanical attrition treatment (SMAT) to produce a gradient in the grain size from 80–200 nm in a 50 μm thick surface layer to 7 μm or 13 μm in the matrix. In both cases, it was found that such gradient structure may considerably postpone the PLC effect. It also led to an increase in the average stress drop amplitude. According to the authors, these effects may be ascribed to a significant increase in the dislocations density and formation on nanosize precipitates in the surface layer.

### 1.3. Al-Mg-Sc-Zr alloys

Non-heat-treatable Al alloys with Mg as the primary alloying element (5XXX series) are important commercial materials with a wide range of application, thanks to their good specific strength, corrosion resistance, weldability, superplasticity [Davis, 1993; Polmear, 2006]. In general, due to the solid solution strengthening, an increase in the Mg content leads to a higher strength, albeit a lower ductility of these alloys. At the same time, the low strength in annealed conditions and strong susceptibility to stress-corrosion cracking in work-hardened conditions, for Mg ≥ 3wt% [Taleff et al., 2001], limits their practical use. It was found that a substantial improvement of strength without loss of the corrosion resistance and weldability can be reached by addition of Sc and/or Zr forming nanoscale Al<sub>3</sub>(Sc,Zr) precipitates [Filatov et al., 2000].

Table 1.1. Mechanical properties of as-hot-rolled alloys:  $\sigma_B$  is the ultimate tensile strength (UTS),  $\sigma_{0.2}$  the yield strength, and  $\delta$  is the elongation [Zhimin Yin et al., 2000]

| Alloy (wt.%)       | $\sigma_B$ , MPa | $\sigma_{0.2}$ , MPa | $\delta$ , % |
|--------------------|------------------|----------------------|--------------|
| Al-5Mg             | 260              | 115                  | 31           |
| Al-5Mg-0.1Zr       | 272              | 129                  | 26           |
| Al-5Mg-0.2Sc       | 296              | 182                  | 18           |
| Al-5Mg-0.6Sc       | 360              | 228                  | 19           |
| Al-5Mg-0.2Sc-0.1Zr | 398              | 266                  | 18           |

Early experimental investigations of the influence of Sc addition on the properties and microstructure of aluminum alloys started in Russia at the end of the 1960s [Dritz et al., 1982; Filatov et al., 2000; Røyset and Ryum, 2005]. The strengthening effect of Sc is attributed to two main factors. First, it is caused by the formation of a high density of coherent intermetallic  $Al_3Sc$  particles that are thermodynamically stable and have an  $L1_2$ -type ordered *fcc* structure [Røyset and Ryum, 2005; Marquis and Seidman, 2005; Filatov et al., 2000; Davydov et al., 2000]. In particular, modelling of shearing of 1.5% volume fraction of 7–10 nm particles by mobile dislocations predicted an approximately 150 MPa increase in the strength of the material [Kendig and Miracle, 2002]. Due to a small lattice mismatch between the  $Al_3Sc$  phase and Al matrix ( $\sim 1\%$ , [Kharakterova et al., 1994]), the precipitates remain coherent up to diameters of about 40 nm and temperatures about 450–500°C [Marquis and Seidman, 2005; Marsha E. van Dalen et al., 2005; Jones and Humphreys, 2003]. Therewith, the driving rate for particle coarsening is small due to the similarity between the lattices of the inclusion and the matrix. Moreover, Mg increases the lattice parameter of the Al matrix and makes the match with  $Al_3Sc$  even more precise, thus leading to fine precipitation and a strong strengthening effect.

Second, the high density of  $Al_3Sc$  and the good match of the crystal lattices make these particles very effective for melt inoculation leading to stabilization of the non-recrystallized structure during the solidification process [Davydov et al., 2000; Norman et al., 1998]. The resulting grain refinement provides an additional strengthening effect.

The addition of zirconium allows to further improve the technology and the properties of these materials. According to [Toropova et al., 1998], Zr substitutes up to one third of Sc atoms in the  $Al_3Sc$  lattice. As zirconium is believed to diffuse slowly in the aluminum matrix, it additionally stabilizes the  $Al_3(Sc,Zr)$  precipitates through formation of a Zr-rich shell around the AlSc core [Gen Li et al., 2014]. Another advantage of adding Zr is related to the fact that scandium shows the modifying effect on the cast structure when it is present

with hypereutectic concentrations ( $> 0.6$  wt. % Sc) [Filatov et al., 2000]. Such a high concentration may lead to decomposition of the solid solution and coagulation of the second phase particles [Davydov et al., 2000]. To avoid it, scandium concentration should not exceed 0.35 wt.%. It occurs that if scandium is added together with zirconium, the modifying effect of scandium manifests itself at low enough concentrations [Filatov et al., 2000]. Finally, Zr has a lower cost than Sc. Therefore, the same volume fraction of the precipitates could be retained employing a smaller amount of Sc.

To summarize, this unique combination of properties makes Al-Mg-Sc-Zr alloys attractive for various applications that cover not only ambient and elevated temperatures, e.g., in the aerospace and ships industry, but also low temperatures used in cryogenic industry [Polmear, 2006; Filatov et al., 2000].

#### **1.4. Effect of the PLC bands on the onset of necking**

The necking represents a general kind of tensile instability occurring when the plastic deformation has hardened the material so that the remaining work hardening capacity is insufficient to compensate a random reduction in the cross-section area and sustain the macroscopically uniform plastic flow. The necking condition is expressed by the well-known Considère criterion,  $\Theta = \sigma$ , where the work hardening rate  $\Theta = d\sigma/d\varepsilon$ , and  $\sigma$  and  $\varepsilon$  respectively denote total values of true stress and strain [Considère, 1885; Havner, 2004]. When it is attained, a local increase in stress in some cross-section leads to progressive strain localization. The end of uniform elongation thus corresponds to the maximum load, or the UTS.

This geometrical approach was recently revisited in a microstructure-based framework for modeling of plastic deformation [Yasnikov et al., 2014; Vinogradov et al., 2016]. It was shown that the Considère criterion can be deduced from the evolution of the total dislocation density and is governed by the rate of dynamic recovery. More precisely, it naturally follows from the intrinsic instability of the dynamics of the dislocation ensemble in the limit of a strain-rate insensitive material. This conclusion makes one suggest that the Considère criterion should be fulfilled in the DSA conditions because the negative SRS of ageing materials is known to be small [Estrin, Kubin, 1995].

On the other hand, the PLC effect is related to the strain localization in deformation bands. Numerous investigations showed that the failure mechanism in AlMg-based alloys is controlled by plastic flow localization into shear bands [Korbel et al., 1986; Bird et al., 1987;

Spencer et al., 2002; Girard et al., 2004; Pineau et al., 2016; Hadianfard et al., 2008]. Thus, although the physical mechanism of the PLC instability stems from strain-rate softening (§ 1.1.2) and is therefore different from the shear banding, the question of a possible contribution of the PLC bands to the onset of necking appeared naturally and was studied in several works. However, the literature data on the influence of the PLC effect on the necking and, more largely, failure are contradictory.

Many authors conclude on the lack of correlation between the necking onset and the PLC bands. For example, such a conclusion followed from DIC visualization of PLC bands and necking in room-temperature tests on the samples of an AA5754 Al-Mg automotive alloy pre-strained at a low temperature below the domain of the PLC instability [Halim et al., 2007]. The shear banding leading to fracture did not correlate with the last PLC band in these tests. The authors conclude that the development of shear localization and nucleation of PLC bands (type *B* bands in the studied strain-rate range) occurred independently, so that PLC bands cannot be considered as nuclei for localized shear bands. This conclusion was later supported in [Jobba et al., 2015]. In this work, deformation of several Al-Mg alloys with different Mg content was studied at 4 K and 298 K in the conditions of thermomechanical and PLC instability, respectively. A complex analysis of the work-hardening behavior, Considère criterion and TEM images of the dislocation microstructure allowed for a conjecture that failure is governed by intrinsic properties of the work-hardened state and the dynamics of shear deformation, while the PLC instability does not contribute to the failure of the samples. More specifically, the failure takes place when a critical dislocation density corresponding to the average dislocation spacing about 8 nm is attained. A modelling approach to this problem, based on the 3D FEM simulations, was proposed in [Zhang et al., 2012; Hopperstad et al., 2007]. The simulations showed that although the negative SRS gives rise to both jerky flow and a reduced ductility, the suppression of jerky flow by varying the model parameters has a negligible effect on the localization strain. It follows that the reduction in ductility is not a direct consequence of jerky flow. The authors of [Zhang et al., 2012] mention, however, that the PLC bands may initiate necking if the geometric defect is small enough. In specimens with large defects, the model always displayed necking at the specimen center.

In contrast to these works, an early onset of necking in a AA5754 alloy deformed in type *B* conditions was interpreted in [Kang et al., 2005, 2006] from the viewpoint of the Considère strain reached locally due to strain localization within the PLC band. Premature failure was also reported in [Chung et al., 1977] for a 7075 Al alloy. It should be noted however that using DIC patterns, the authors of [Kang et al., 2006] observed the

development of the final shear when the PLC band met an already existing diffuse necking band.

Finally, although the question of fracture itself was not addressed in the present thesis, it is noteworthy that in [Cai et al., 2016], the occurrence of PLC bands in the region of fracture was observed just before the end of failure of a 5456 Al-based alloy, using two orthogonal digital image correlation systems. The authors observed a deviation of the inclination angle of shear localization in the necking region in comparison with other literature data and suggested that it is related to the intrinsic material characteristics associated with the PLC effect. Two fracture modes proposed in this paper are illustrated in Fig. 1.16. If the orientation of the captured PLC band bifurcates in the necking area, the failure occurs by shearing-to-opening mode and microcracks are initialized horizontally in the vicinity of the intersection of the PLC bands with antisymmetric orientations (Fig. 1.16a-b). If the PLC band remains the same, a pure shearing mode is observed (Fig. 1.16a'-c'). It should be stressed, however, that these models describe the interaction of the PLC bands with the already formed neck, without observations preceding necking.

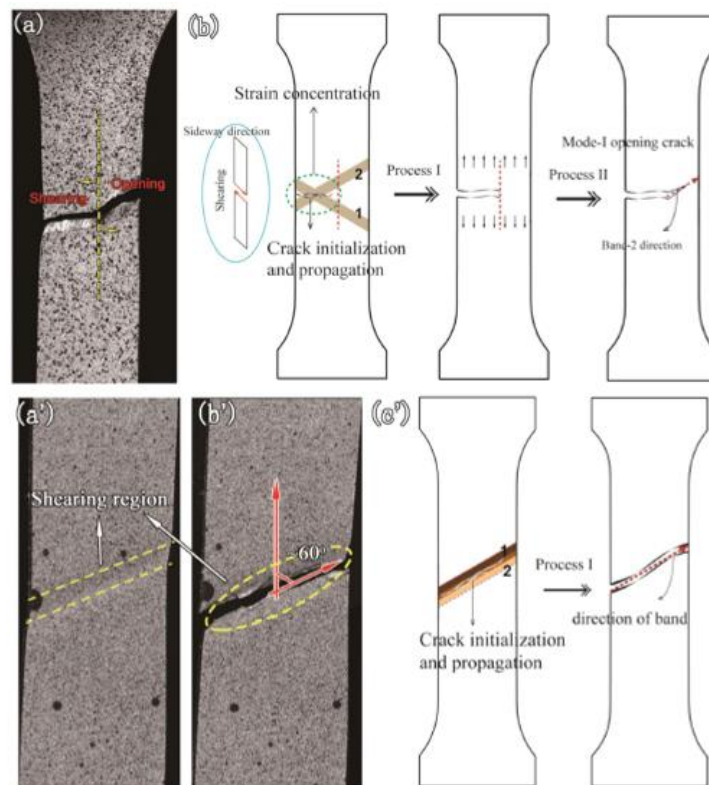


Figure 1.16: Fracture modes proposed in [Cai et al., 2016]: (a)–(b) shearing-to-opening mode, i.e., the opening-crack fracture induced by shearing; (a')–(c') pure shearing fracture.

## 1.5. Statistical approach to collective deformation processes

The complex collective nature of plastic deformation processes is now generally recognized for crystalline [Kubin, 1993; Zaiser, 2007; Ananthakrishna, 2007; Pustovalov, 2008; Greer and Hosson, 2011] and even amorphous [Qiao et al., 2016] solids. A direct manifestation of self-organized motions of dislocations stems from observations of jerkiness of deformation curves of microscopic size samples (Fig. 1.17a) [Greer and Hosson, 2011]. Such a discontinuity is smoothed out in the case of bulk samples which usually display even deformation curves. However, application of sensitive experimental techniques, e.g., based on the acoustic emission (AE) [Kumar and Ananthakrishna, 2018] or local extensometry [Fressengeas et al., 2009], allowed for a conclusion that in bulk specimens, too, intermittency manifests itself on a mesoscopic scale (Figs. 1.18a and 1.19a). The statistical analysis of series of various jump-like “events” (strain or strain-rate jumps, AE hits) revealed power-law distributions,  $P(x) \sim x^{-\alpha}$ , in all cases (plots (b) in Figs. 1.17–1.19). Such scale-free statistics, indicating the presence of events of “all sizes”, are inherent to avalanche behavior [Turcotte, 1999; Dorogovtsev et al., 2008; Kawamura et al., 2012]. More specifically, these observations were interpreted in terms of self-organized criticality (SOC) [Bak et al., 1988], one of the main concepts used to explain scale-free statistics of avalanche phenomena.

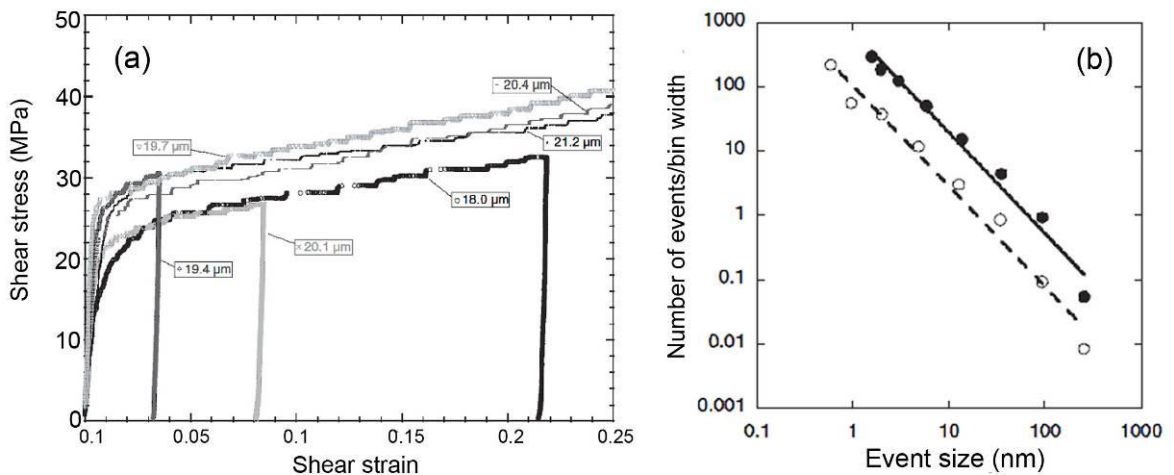


Figure 1.17: (a) Step-wise deformation curves of several Ni micropillars  $\sim 20 \mu\text{m}$  in diameter. (b) Frequency distribution of the detected displacements. Open symbols – data for a single sample; solid symbols – aggregate data for several samples [Dimiduk et al., 2006].

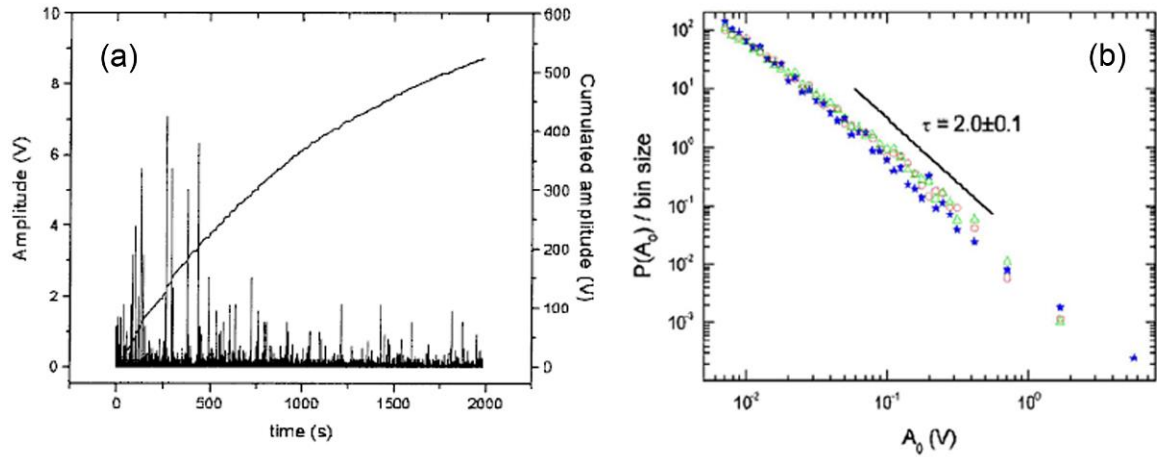


Figure 1.18: (a) Acoustic emission recorded during a compression creep test on an ice single crystal [Weiss et al., 2001]. (b) Probability density function for AE amplitudes recorded during compression creep of ice (stars) and tension test on Cd single crystals [Weiss et al., 2007]. Circles and triangles correspond to stage I and stage II of work hardening.

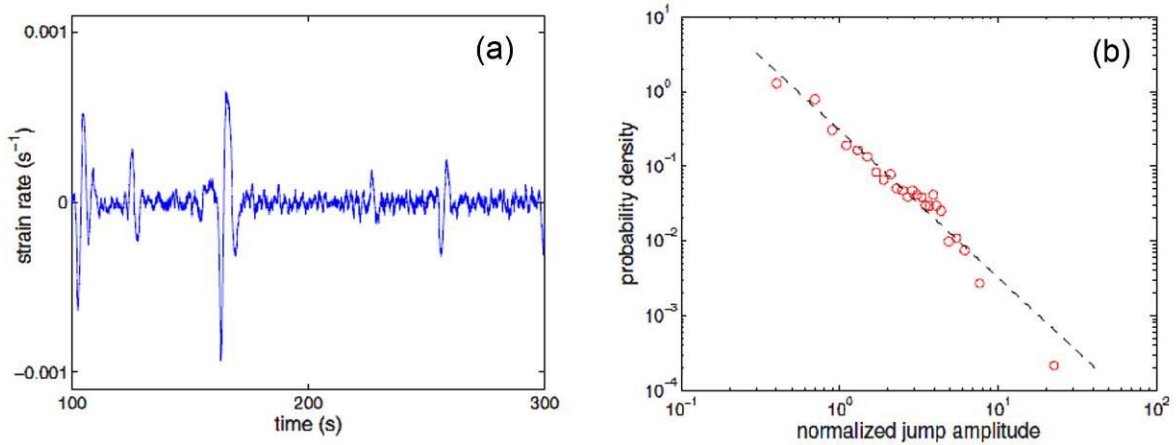


Figure 1.19: (a) Variations in the axial strain rate about the driving strain rate, recorded by an optical method over a 1-mm base length [Fressengeas et al., 2009]. (b) The corresponding probability density (normalized to bin size) of “burst” amplitudes.

The phenomenon of plastic instability occupies a specific place in this field of investigation because in this case, the collective character of deformation processes concerns a much wider scale range, including the macroscopic scale of deformation curves. Among various mechanisms of plastic instability (see, e.g., the reviews in Refs. [Ananthakrishna, 2007; Pustovalov, 2008]), the PLC effect displays the richest behavior unifying many kinds of collective dynamics observed in complex systems of various natures [Van den Beukel, 1975]. Moreover, as its occurrence often requires reaching a critical strain, the study of the PLC effect provides an opportunity to compare collective behavior during smooth (before  $\varepsilon_{cr}$ ) and unstable (after  $\varepsilon_{cr}$ ) plastic flow.

In contrast to the ubiquitous power-law character of statistics relevant to the mesoscopic scale, the analysis of series of stress serrations showed that different types of

PLC instabilities are characterized by different statistics. More exactly, type *A* serrations are also described by scale-invariant distributions (see examples of a histogram in Fig. 1.20a and a PDF in Fig. 1.21a). This avalanche-like behavior on the macroscopic scale was also interpreted in terms of SOC [Lebyodkin et al., 1995; Lebyodkin et al., 2000; Lebedkina and Lebyodkin, 2008]. An alternative mechanism akin to a turbulent flow at high Reynolds numbers was suggested in [Bharathi and Ananthakrishna, 2002; Ananthakrishna and Bharathi, 2004]. At the same time, the distributions of stress drops occurred to be sensitive to the transitions between the types of behavior [Bharathi, et al., 2001; Pink and Weinhandl, 1998; Lebedkina and Lebyodkin, 2008; Lebyodkin et al., 2012; Shashkov et al., 2012]. Namely, when  $\dot{\epsilon}_a$  is decreased, the statistics change from scale-free dependences to histograms with a characteristic scale. Therewith, rather complex histograms were observed for type *B* behavior and attributed to deterministic chaos (Fig. 1.20b) [Bharathi, et al., 2001]; close-to-Gaussian distributions were found for type *C* serrations (Fig. 1.20c) [Lebedkina and Lebyodkin, 2008]. The conclusion on the nonuniqueness of statistical properties of serrations series was also confirmed by other methods of analysis of complexity, indispensable when the observed behavior cannot be described by a unique statistical law [Lebyodkin et al, 1995; Bharathi et al., 2002; Noronha et al., 1997; Konstantinidis and Aifantis, 2002; Sarkar et al., 2008; Darowicki et al., 2007; Kugiumtzis et al., 2004; Iliopoulos et al., 2015] (see § 1.1.2).

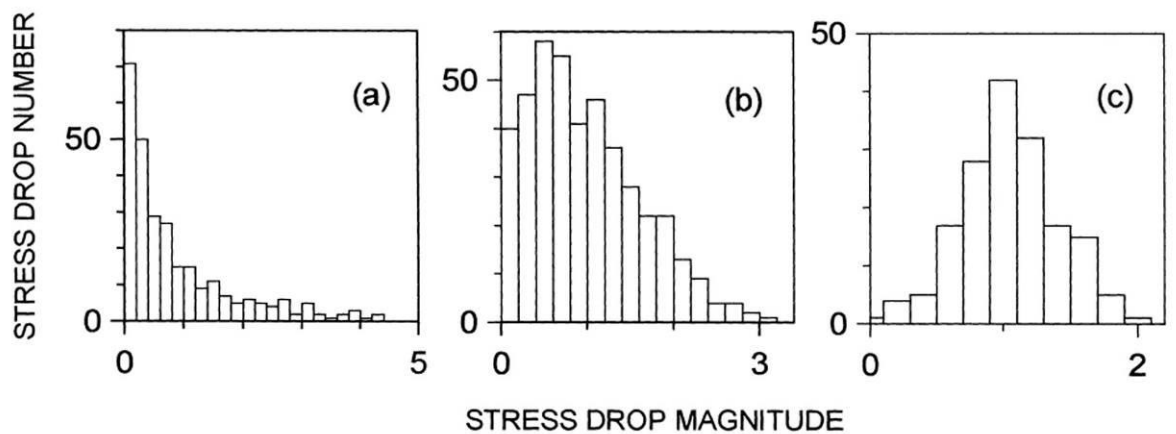


Figure 1.20: Examples of histogram shapes for different types of behavior of the PLC effect: (a) type *A*; (b) type *B*; (c) type *C*. [Lebyodkin et al., 2000].

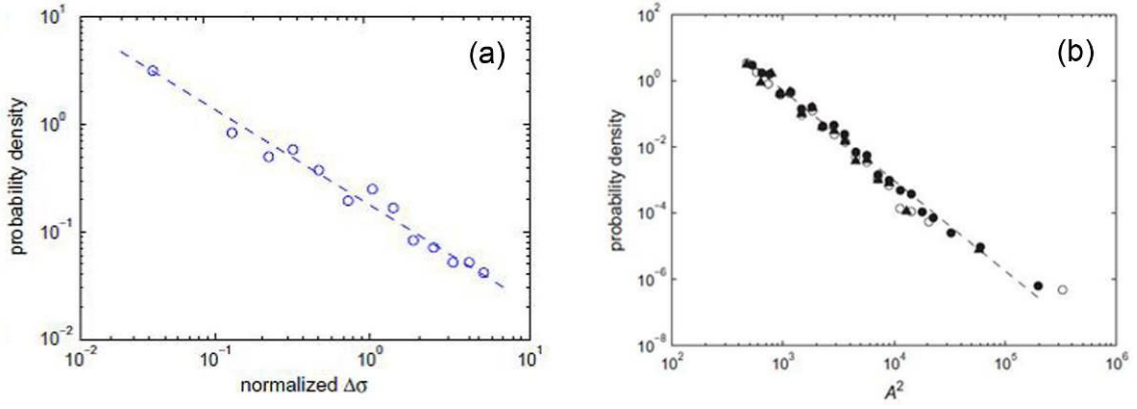


Figure 1.21: (a) Example of a PDF for amplitudes of stress drops in the case of type *A* PLC behavior in AlMg alloy ( $\dot{\epsilon}_a = 2 \times 10^{-3} \text{ s}^{-1}$ ). (b) Examples of PDF for squared amplitude of AE events collected for three samples of the same alloy deformed in the conditions of type *C* behavior ( $\dot{\epsilon}_a = 2 \times 10^{-5} \text{ s}^{-1}$ ).

Different symbols correspond to different choices of HDT and HLT [Lebyodkin et al., 2012]. According to [Weiss et al., 2007], the squared amplitude of the AE event,  $A^2$ , reflects the energy dissipated during the respective deformation process.

Surprisingly, the statistical analysis of the AE accompanying the PLC instability in a binary AlMg alloy showed persistent power-law behavior at all strain rates, i.e., for all three types of behavior (Fig. 1.21b). This result seemingly contradicts the existence of characteristic scales of type *C* and type *B* serrations. This transition between the mesoscopic scale of the AE and the macroscopic scale of deformation curves was interpreted in [Lebyodkin et al., 2012; Shashkov et al., 2012] as stemming from a competition between SOC and the phenomenon of synchronization also well-known for complex dynamical systems [Pérez et al., 1996]. The phenomenon of synchronization, detected at low enough strain rates in the conditions of the PLC effect, is illustrated in Fig. 1.22. This figure traces series of logarithmic amplitude,  $M$ , and duration,  $\tau$ , for the AE events recorded, respectively, before and after the onset of type *C* serrations. It can be seen that AE events occur within the same amplitude range during both the stress serrations and the intervals of smooth loading between them. More exactly, small stress drops sporadically occurring before  $\epsilon_{cr}$  correlate with higher-amplitude AE hits, but hits with similar and even higher amplitudes are also present on smooth parts. As far as the instants of type *C* serrations are concerned, they are indistinguishable in the  $M$ -series. Furthermore, examination of both  $M$ - and  $\tau$ -series testifies to clustering of AE hits at the instants of serrations, which becomes stronger with deformation. Indeed, small drops are accompanied by groups of AE hits; Type *C* serrations are accompanied by an AE event with a duration orders of magnitude higher than the common values, which can be explained by the incapacity of the acoustic system to resolve individual hits. These results allow for the following suggestions: (i) The elementary deformation processes are the same during smooth and jerky flow; (ii) Like in the case of

macroscopically stable deformation, the power-law statistics of the AE bears evidence to their avalanche nature; (iii) Deep stress serrations do not correspond to single dislocation avalanches but are caused by chaining of many avalanches similar to those observed during smooth intervals between serrations.

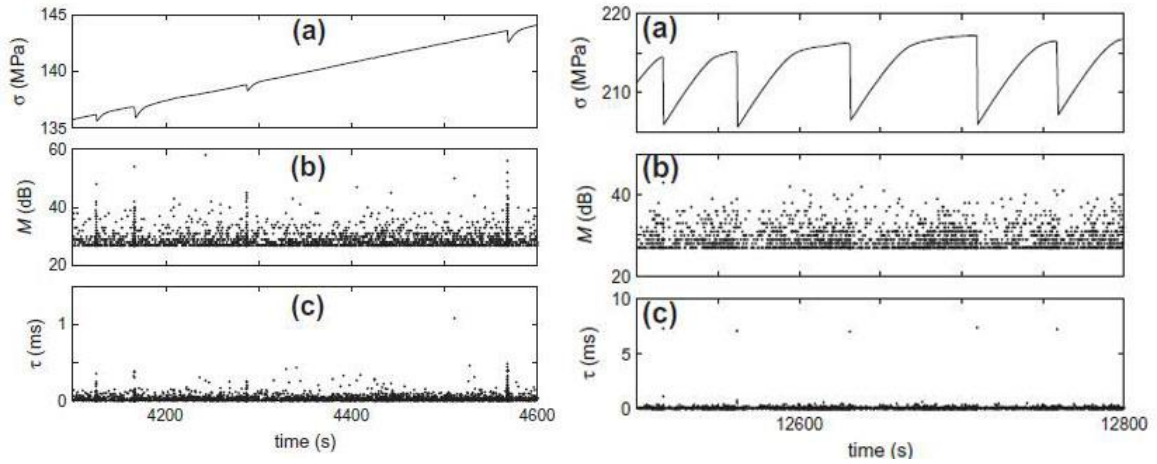


Figure 1.22: Deformation curve and the concomitant AE before (left) and after (right)  $\epsilon_{cr}$  for the onset of type C serrations at  $\dot{\epsilon}_a = 2 \times 10^{-5} \text{ s}^{-1}$ . (a)  $\sigma(t)$  curve; (b) Logarithmic amplitude  $M$  of the accompanying AE events; (c) Duration  $\tau$  of the accompanying AE events [Lebyodkin et al., 2012].

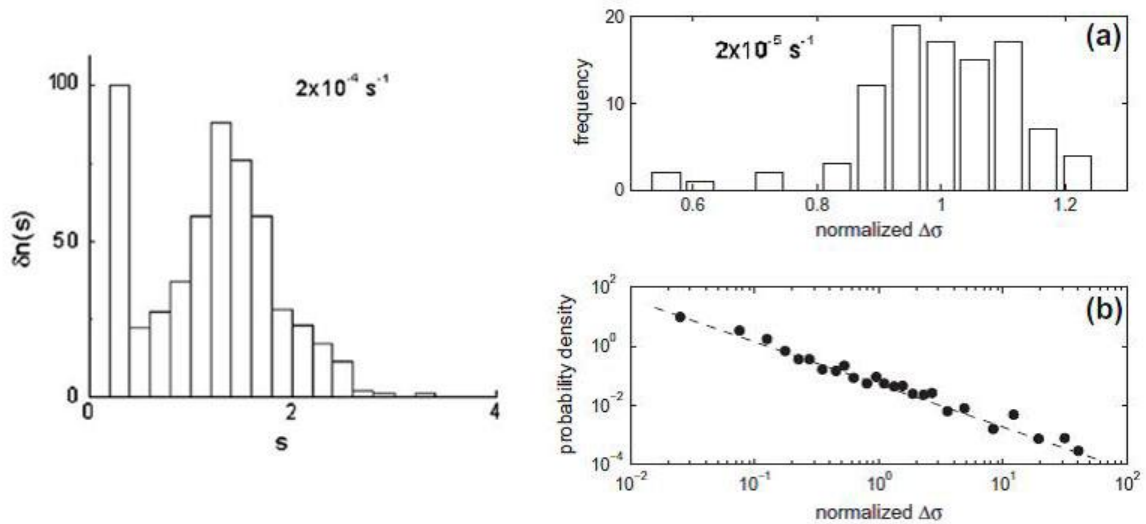


Figure 1.23: Left column: Example of a bimodal histogram of normalized stress drop amplitudes (here denoted as  $s$ ) for type B behavior. [Lebedkina and Lebyodkin, 2008]. Right column: (a) Bell-shaped histogram obtained for type C serrations; (b) Power-law PDF obtained for the low-amplitude stress drops in the same strain interval [Lebyodkin et al., 2012].

An additional experimental confirmation of these suggestions follows from the statistical analysis of small serrations. Such serrations are not only observed before  $\epsilon_{cr}$  but also accompany deep stress drops, leading to bimodal distributions of amplitudes of type B and type C serrations (Fig. 1.23, left column). In the case of type C behavior, the entire

ensemble of serrations decays into two amplitude ranges, so that their statistics can be processed separately. Such an analysis renders histograms with a characteristic scale for deep stress drops (Fig. 1.23a, right column) and scale-invariant statistics for small serrations (Fig. 1.23b, right column).

When  $\dot{\varepsilon}_a$  is increased, the AE activity is overall increased and the clustering of AE events is globally enhanced, leading to some increase in the average  $\tau$  value [Lebyodkin et al., 2012; Lebedkina et al., 2018-2]. However, the correlation between stress serrations and  $\tau$  bursts degrades progressively and is virtually absent in type *A* conditions. This limit corresponds to scale-free statistics of amplitudes and durations of AE events and stress serrations, usually ascribed to SOC.

These findings attest that the statistical analysis of the AE may provide information on the influence of the microstructure on the mesoscopic-scale deformation processes in the conditions of the macroscopic plastic instability. Let us first summarize the suggestions stemming from the above data. The observation of a persistent power-law character of the AE statistics testifies to an inherently scale-free avalanche-like dynamics of dislocations, which applies to both unstable plastic deformation and macroscopically stable flow. The general validity of this conjecture is confined from above by a mesoscopic scale pertaining to the AE and, perhaps, low-amplitude stress serrations in the case of the PLC effect.<sup>1</sup> In [Weiss et al., 2007], it was discussed that the smoothness of the macroscopic deformation curves of most materials means that there exist inherent factors limiting the size of the dislocation avalanches, in particular, intrinsic lengths related to the microstructure and the crystallography of the dislocation glide. Although it is tentative to attribute the PLC serrations to formation of extremely powerful dislocation avalanches in the presence of the dynamic strain aging, such a suggestion would contradict the observation of a similar AE intensity range at the instants of deep serrations and during intervals of smooth plastic flow (Fig. 1.22). Thus, similar limitations must apply to the macroscopically unstable deformation. The occurrence of macroscopic plastic instabilities can thus be attributed to clustering of dislocation avalanches, which would depend on the spatial coupling between dislocations and, therefore, on the internal stress field, in its turn depending on the microstructure. This logic is corroborated by some generic models considering the

---

<sup>1</sup> It should be noted that the critical exponent found for either type *A* serrations or the small stress serrations accompanying type *C* behavior is usually considerably lower than that obtained for the AE (Table 1). This is likely to be due to a lower amplitude resolution and a low frequency band (< 500 Hz) of the load cell [Lebedkina et al., 2018-1].

competition between SOC and synchronization phenomena in complex dynamical systems, which highlight an important role of spatial coupling [Pérez et al., 1996].

It should be noted that the first analyses of the AE accompanying the plastic flow, which were mostly performed on single crystals with an anisotropic *hcp* structure (ice, Cd, Zn, etc.) led to an opposite conclusion on universal power-law behavior corresponding to a critical exponent  $\alpha_{AE} \sim 1.5$  for the energy associated with the AE events or, equivalently, 2 for their amplitudes [Zaiser, 2007] (see Table 1.1). Considering that the mechanical work associated with a strain jump performed at a constant stress is proportional to its size, this assumption was also confirmed by a similar exponent value for statistics of strain jumps during deformation of monocrystalline micropillars [Greer and Hosson, 2011] (Table 1.1).

Table 1.1. Range of power-law exponents detected in various experimental conditions.

| Characteristic         | Conditions  | Exponent   |
|------------------------|---|--|
| AE                     | Bulk anisotropic materials [Zaiser, 2007, Weiss et al., 2015]                                       | $\sim 1.5$ (single crystals);<br>$\sim 1.2$ (ice polycrystals)*  |
|                        | Bulk isotropic materials [Weiss et al., 2015]   | $1.5 \div 2$   |
|                        | Binary AlMg alloys [Lebyodkin et al., 2012; Shashkov et al., 2012]                                  | $1.8 \div 2.2$ during microplastic flow.<br>Increases up to $2.5 \div 3.1$ at larger strains.  |
| Strain or stress jumps | Micropillars [Greer and Hosson, 2011]   | $\sim 1.5$   |
|                        | Binary AlMg alloys [Bharathi, et al, 2001; Pink and Weinhandl, 1998; Lebedkina and Lebyodkin, 2008] | High $\dot{\epsilon}_a$ : $1.0 \div 1.5$ .<br>Intermediate and low $\dot{\epsilon}_a$ : bell-shaped histograms.<br>Lowest $\dot{\epsilon}_a$ : $1.0 \div 1.5$ for the subset of low-amplitude stress fluctuations. |

\* The estimate of  $\alpha_{AE}$  for  $A^2$  was obtained from the exponent  $\alpha_A \approx 1.35$  determined for amplitude distributions [Zaiser, 2007]:  $\alpha_{AE} = (\alpha_A + 1)/2$ .

However, plastic deformation is mostly constrained to one slip system in these tests. The data obtained for bulk polycrystalline ice samples [Zaiser, 2007] and materials with an isotropic cubic structure (Al, Cu, etc.) [Weiss et al., 2015] testified that the power law can be sensitive to the glide crystallography and the microstructure. The variation of  $\alpha_{AE}$  between 1.5 and 2 observed in [Weiss et al., 2015] was attributed to a stochastic factor caused by the multiple slip leading to forest hardening, formation of dislocation structures, etc., therefore,

reducing the probability of large avalanches. It is natural to expect that the stochastic factor might acquire more importance in alloyed materials because of the additional solute hardening. This conjecture was used to explain high  $\alpha_{AE}$  values (up to 3) attained after certain work hardening of binary AlMg alloys [Lebyodkin et al., 2012; Shashkov et al., 2012] (Table 1.1).

In summary, the entirety of data described above motivates the application of the statistical analysis of both stress serrations and AE to evaluation of the PLC effect in materials with complex microstructures. Such a study was realized in the present thesis using the A2 alloy.

# Chapter 2

## Experiment and data analysis

### 2.1 Materials and microstructure characterization

#### 2.1.1. Objects of investigation

As specified in the introduction, one of the aims of the present study was to compare mechanical behaviors of alloys with different phase composition. For this purpose, we performed investigations on a binary Al-Mg alloy and several AlMg-based alloys with various additions. Table 2.1 represents the chemical composition of the materials provided for this study by the Belgorod National University in the framework of a France-Russia joint research program. The quantitative characterization was performed using an optical emission spectrometer Foundry-Master with a tungsten electrode. As there is no exact correspondence with the international nomenclature of aluminum alloys, the materials are denoted hereinafter as A1 (binary alloy), A2, A3, and A4. Designations according to the Russian nomenclature of precipitation-strengthened materials are given in parentheses.

Table 2.1. Chemical compositions of investigated alloys (in wt.%).

| Alloy   | Mg   | Mn   | Zr   | Sc  | Si   | Fe    | Al.  |
|---|------|------|------|-----|------|-------|------|
| A1<br>(Al-Mg)                                   | 3.0  | -    | -    | -   | 0.04 | 0.06  | Rest |
| A2<br>(1561 Al [Nikulín et al.,2012])           | 5.43 | 0.52 | 0.1  | -   | 0.12 | 0.014 | Rest |
| A3<br>(1575C Al [Zhemchuzhnikova et al., 2013]) | 6.0  | 0.35 | 0.08 | 0.2 | 0.02 | 0.02  | Rest |
| A4<br>(5024 Al [Mogucheva et al.,2013])         | 4.57 | 0.35 | 0.09 | 0.2 | -    | -     | Rest |

The as-received or coarse-grained (CG) state of A1 and A2 alloys was produced by semi-continuous casting followed by homogenization annealing at 500°C for 4 h and 360°C

for 6 h, respectively, and rolling at ambient temperature with a total reduction of 70%. The rolled sheets were annealed for 2 h at 400°C. The CG A3 alloy was manufactured by direct chill casting and homogenized at 360°C for 12 h. The A4 alloy was fabricated by continuous casting. Ingots 620 mm in diameter were subjected to homogenization annealing at 370°C for 12 h, followed by extrusion at 380°C into a billet with a rectangular cross section and dimensions of 155 mm × 255 mm.

### *2.1.2. Methods of microstructure characterization*

The specimens for microstructure examination were cut from the central part of the billets and rods. Optical metallography was carried out using an Olympus GX71 optical microscope after polishing and etching of the specimens by the standard Keller's reagent (0,5 HF-1,8 HCl-2,7 HNO<sub>3</sub>-95 H<sub>2</sub>O, in wt.%). To visualize the grain structure and characterize misorientations of grain and subgrain boundaries, electron back scattering diffraction (EBSD) analysis was performed in a FEI Quanta 600FEG scanning electron microscope (SEM) with OIM (orientation imaging microscopy) analysis software. In the present study, high-angle boundaries (HAB) were defined for grain misorientations  $\geq 15^\circ$ ; Low-angle boundaries (LAB) corresponded to misorientation within the range of 2-15°. Boundaries with misorientation less than 2° were disregarded. The average grain size was measured by the mean linear intercept method using at least 300 grains for each state [Saltykov, 1970]. EBSD analysis was also applied to evaluate the SPD effect on the initial texture of the investigated materials.

The specimens for transmission electron microscopy (TEM) were mechanically thinned down to 0.15-0.2 mm and electropolished using the standard 25% HNO<sub>3</sub>+ 75% CH<sub>3</sub>OH solution at -32°C and 19.5 V and a Tenupol-5 twinjet polishing unit. The foils were examined using a JEM-2100EX TEM operating at 200 kV and equipped with an EDAX energy dispersive X-ray analyzer for identification of constituent phases.

The dislocation density was estimated by counting individual dislocations crossing the thin foil surface. For each sample, a minimum of 5 foils from different regions were analyzed. However, as this method is based on the analysis of small areas, the dislocation density was additionally evaluated by X-ray diffraction (XRD) profile analysis. This verification was applied to A1 alloy using an ARL-Xtra diffractometer operated at 45 kV and 35mA with CuK $\alpha$  radiation [Saltykov, 1970]. The value of the dislocation density  $\rho$  was calculated using the Williamson-Hall method from the average value of the crystallite size

D, and microstrain  $\varepsilon$ , which are determined from XRD true peak broadening. The following relationship was used for calculations [Yuzbekova et al., 2017]:

$$\rho = \frac{3\sqrt{2\pi\varepsilon^{1/2}}}{Db}, \quad (2.1)$$

where  $b$  is the Burgers vector ( $b= 2.86\times 10^{-10}$  m). It was found that the discrepancy between dislocation densities obtained by two methods in the CG and FG conditions of A1 alloy was negligible. The dislocation densities calculated by the first method are given below.

### 2.1.3. Pretreatments using SPD

In order to investigate the influence of microstructure on plastic instability, the alloys were prepared in three different conditions referenced to as follows: coarse-grained state, fine-grained state, and severely deformed state. The latter two conditions were obtained, respectively, by Equal Channel Angular Pressing (ECAP) and ECAP followed by additional cold rolling (CR), as described below.

*ECAP.* To produce a fine-grained (FG) microstructure, rods with dimensions of 20 mm  $\times$  20 mm  $\times$  100 mm were cut from ingots of each alloy and deformed using an isothermal die in a L-shaped channel configuration with a 90° angle of intersection and a 20 $\times$ 20 mm<sup>2</sup> cross-section (Fig. 2.1). The pressing consisted of 12 passes via route Bc [Valiev and Langdon, 2006], where the rod was rotated between passes by 90° around its long axis. In the case of the Al-Mg alloy, the rods were initially pressed 8 times at 300°C and then 4 times at 200°C. For A2 and A4 alloys all ECAP passes were performed at 300°C, for A3 alloy at 320°C. To let the samples attain the temperature of the die before each new pass, pressing was started 2 minutes after mounting the billet in the die. The temperature was controlled by thermocouples with the measurement error  $\pm 5^\circ\text{C}$ . The pressing speed was  $\sim 3$  mm/s. Finally, the billets were quenched into water after the last deformation pass.

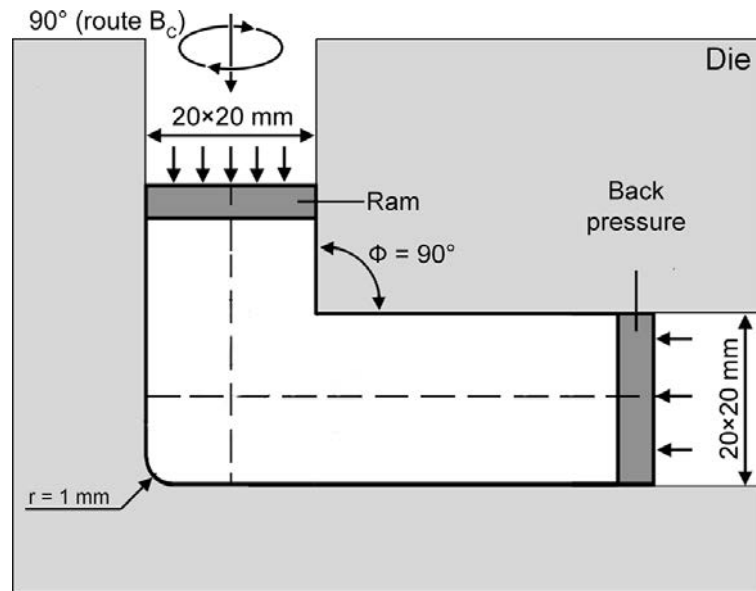


Figure 2.1: Schematic illustration of ECAP.

*ECAP+CR*. After ECAP, half of billets of A1 and A2 alloys were additionally cold rolled at room temperature with a total reduction of 80% using a two-roller mill. The rolling speed was  $\sim 1$  m/min with the reduction rate  $\sim 10\%$  per pass. The rolling direction coincided with the previous ECAP direction. To underline the associated strain hardening effect, this material state is designated as FGH.

#### 2.1.4. Microstructure of the studied alloys before and after SPD

The microstructure of the A1 and A3 alloys was studied in the present thesis. The A2 and A4 alloys were characterized using the same methods, respectively, in [Nikulin et al., 2012] and [Mogucheva et al., 2013; 2016]. Below, details relevant to the thesis work will be presented altogether.

Figure 2.2 presents examples of TEM micrographs of the investigated materials in the CG state. Transmission electron microscopy did not reveal second phase particles in the binary A1 alloy (Fig. 2.2a). The A2 alloy was found to contain incoherent  $\text{Al}_6(\text{Mn,Fe})$  dispersoids with an average size about 25-30 nm uniformly distributed within the grain interiors (Fig. 2.2b). Two kinds of secondary phases were found within the grains of A3 alloy: the major secondary phase consisting of uniformly distributed coherent  $\text{Al}_3(\text{Sc,Zr})$  dispersoids with an average size about 10–15 nm, and sparse plate-like or round-shaped incoherent  $\text{Al}_6(\text{Mn,Fe})$  dispersoids with an average thickness of 25 nm. In addition, some incoherent  $\text{Al}_3(\text{Sc,Zr})$  particles 40 nm in size were detected on the grain boundaries (Fig. 2.2c). In the A4 alloy (Fig. 2.2d), the main secondary phase was represented by coherent

dispersoids of an  $\text{Al}_3(\text{Sc,Zr})$ -phase with average size about 10–15 nm; Incoherent dispersoids were identified as an  $\text{Al}_6(\text{Mn,Fe})$  phase with an average diameter of 30 nm and were primarily observed within the grain interiors.

The parameters of the grain structure in the investigated alloys in various conditions are synthesized in Table 2.2. In the CG state, the polycrystalline structure of the A1, A2, and A3 alloys consisted of equiaxed grains (see examples for the A1 and A3 alloys in Fig. 2.3a and Fig. 2.4a, respectively). The A4 alloy in CG state was characterized by a bimodal distribution of grain size. The dominant structural component was represented by coarse grains with a mean size of 200  $\mu\text{m}$  and 20  $\mu\text{m}$  in the direction of the extrusion axis and the transverse direction, respectively. Besides, chains of fine equiaxed grains with an average size of 2  $\mu\text{m}$  and volume fraction of 2% were located along these coarse grains [Mogucheva et al.,2016]. The density of lattice dislocations in this condition did not exceed  $10^{13} \text{ m}^{-2}$  in all alloys (Figs. 2.2, 2.3a').

ECAP resulted in the formation of almost uniform fine-grained microstructures (Table 2.2), with the fraction of recrystallized regions exceeding 90% and the lattice dislocation density close to  $10^{14} \text{ m}^{-2}$  for all alloys (see example for the A1 alloy in Fig. 2.3b'). The recrystallization was less complete in the A1 alloy (Fig. 2.3b, b'), as evident from the comparison of the fractions of HABs in Table 2.2. This material showed elongated grains subdivided into equiaxed micron-size crystallites by low-angle boundaries (LABs), as well as some remnants of coarser grains.

The subsequent rolling produced no visible effect on the grain size in A1 alloy (Fig. 2.3c). In the A2 material, it resulted in a threefold decrease compared with the FG state. Such SPD treatment resulted in the highest dislocation density of  $10^{15} \text{ m}^{-2}$  in both alloys (Fig. 2.3c').

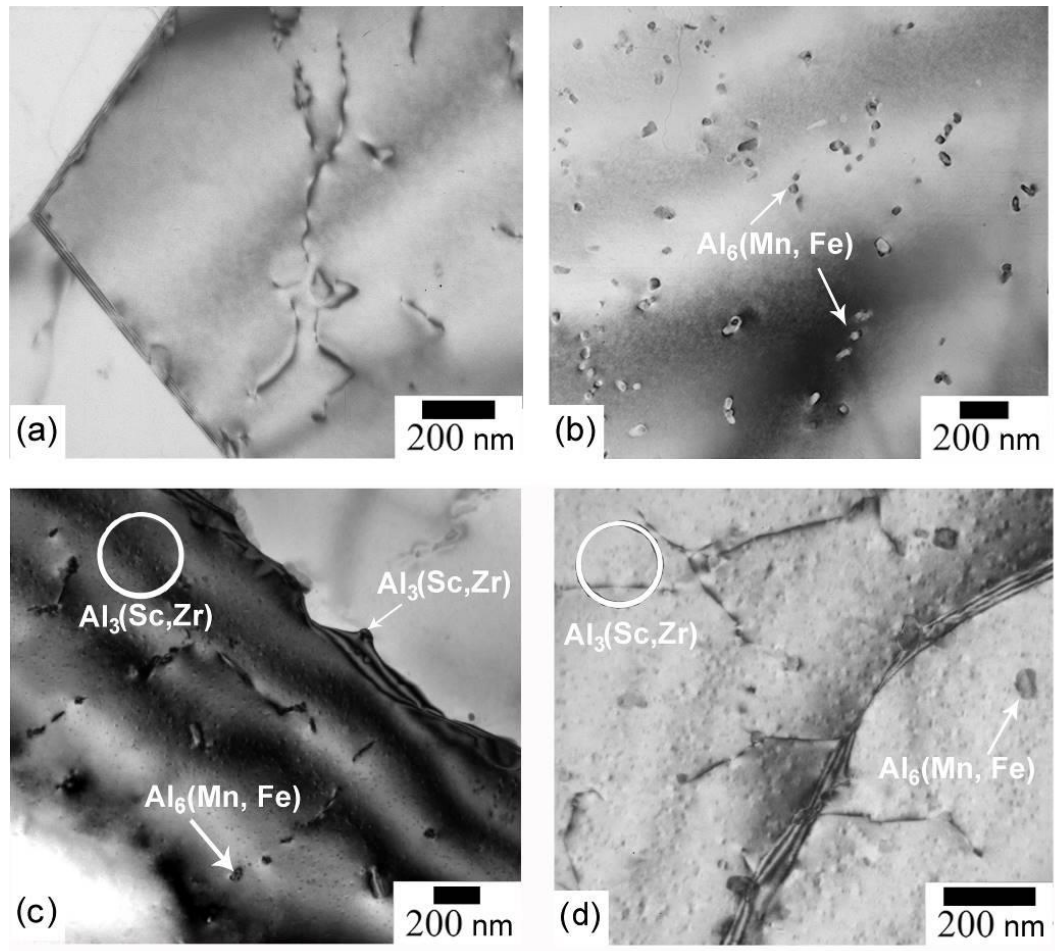


Figure 2.2: TEM micrographs of the studied alloys in the coarse-grained state: (a) A1, (b) A2, (c) A3 and (d) A4 (Table 2.1).

Table 2.2. Polycrystalline structure of the investigated alloys in different conditions: grain size,  $d$ , and fraction of high-angle boundaries (HAB).

| Alloy | Material condition  |         |                     |         |                     |         |
|-------|---------------------|---------|---------------------|---------|---------------------|---------|
|       | CG                  |         | FG                  |         | FGH                 |         |
|       | $d$ , $\mu\text{m}$ | HABs, % | $d$ , $\mu\text{m}$ | HABs, % | $d$ , $\mu\text{m}$ | HABs, % |
| A1    | 40                  | 47      | 2                   | 37      | 2                   | 40      |
| A2    | 15.4                | 93      | 1                   | 70      | 0.33                | 54      |
| A3    | 22                  | 87      | 0.8                 | 84      | -                   | -       |
| A4    | 200/20              | 36      | 1.01/0.88           | 70.4    | -                   | -       |

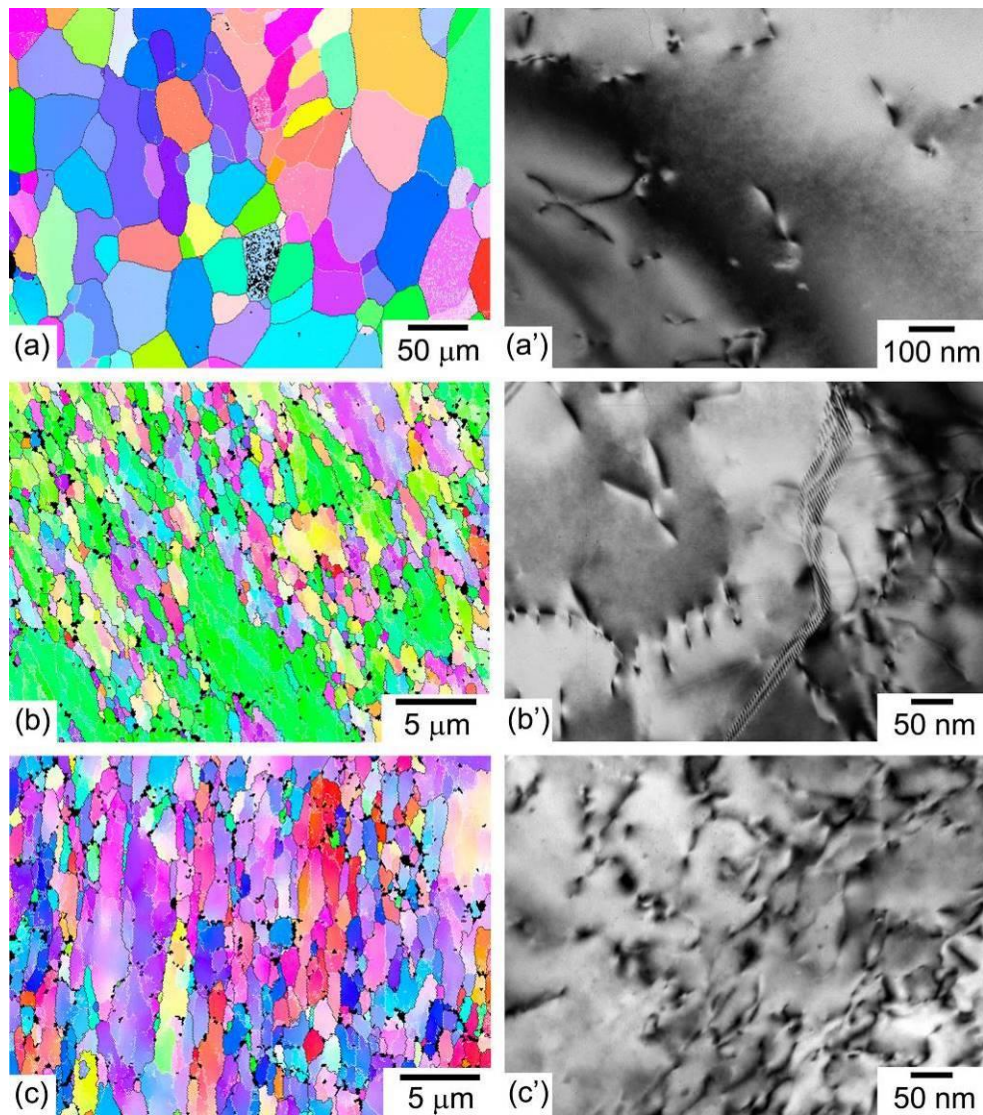


Figure 2.3: Microstructure of the Al alloy in CG (a,a'), FG (b,b') and FGH (c,c') conditions. EBSD- misorientation maps (a-c) and TEM micrographs (a' - c').

In all alloys, severe plastic deformation did not produce any visible effect on the size and distribution of second phase particles. This is illustrated, e.g., in Fig. 2.4 that compares TEM micrographs of the A3 alloy in CG and FG states.

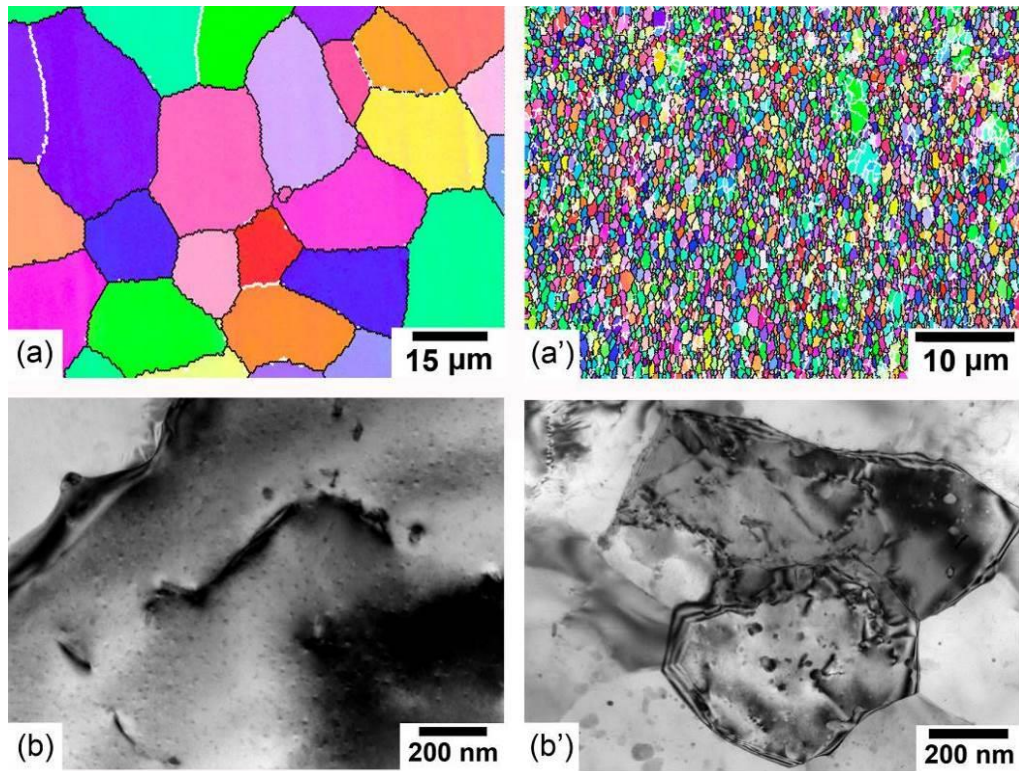


Figure 2.4: Microstructure of A3 alloy: (a,b) CG state; (a',b') FG state after ECAP.

## 2.2. Experimental methods and data processing

The entire experimental setup allowed for simultaneous recording of the tensile curve, the evolution of the local strain field on the specimen surface and the acoustic emission accompanying plastic deformation. The scheme of the setup is illustrated in Fig. 2.5. Details of the experimental techniques are given in the following paragraphs.

### 2.2.1. Tensile tests

Tensile tests were performed using a screw-driven machine Zwick/Roell 1476. Specimens with a dog-bone shape and the gage section of  $35 \times 7 \times 3 \text{ mm}^3$  were cut parallel to the last extrusion or/and rolling axis of the billets, mechanically polished with SiC papers up to 2400 grid, and tested at room temperature with a constant grip velocity corresponding to the nominal applied strain rate,  $\dot{\varepsilon}_a$ , ranging from  $2.86 \times 10^{-5} \text{ s}^{-1}$  to  $1.43 \times 10^{-2} \text{ s}^{-1}$  (Fig. 2.5). Two to four specimens were tested for each strain rate. To avoid an overflow of the machine storage, the sampling time for recording stress-time curves was selected from 500 ms in the slowest tests to 2 ms in the fastest tests.

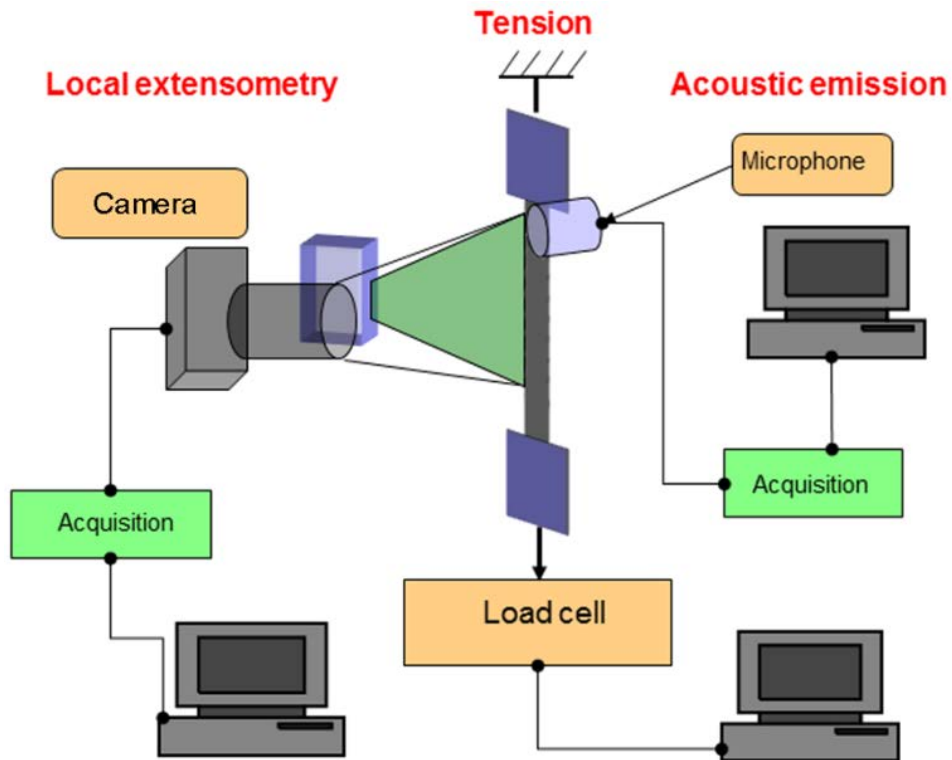


Figure 2.5: Scheme of experimental setup used in the present study [Bougherira, 2011].

To trace the stress-strain curves and calculate the work-hardening index, the total strain values were obtained from the data of digital image correlation (see below). Besides, to verify the conclusions on the necking criterion, control tests were performed on several samples using a high-precision laserXtens Zwick/Roell extensometer (it could not be used simultaneously with the local extensometry setups).

The evaluation of the work hardening rate in the case of unstable plastic flow needs explanation because the instantaneous rate of change of stress is virtually discontinuous at the instants of stress drops. The approach adopted in this work makes use of the fact that the Considère analysis examines the conditions of stability of the uniform plastic flow and is based on the total values of stress and strain. For this reason, the true stress-true strain curves were first smoothed and then derived to obtain an average work-hardening rate. Various kinds of smoothing were tested, including running average and polynomial fits, and rendered similar results, provided that the applied method efficiently removed the serrations. The present results are obtained by 9th order polynomial fitting of the deformation curves.

### 2.2.2. Local strain measurement

Two complementary techniques were used to examine behavior of the PLC bands.

First, a one-dimensional (1D) extensometry technique was applied to visualize the evolution of the local strain field along the tensile axis of the specimen. This method is based on the recording of longitudinal displacements of a sequence of transversal surface markers (Fig. 2.6a), with the aid of a CCD (charge-coupled device) camera. The markers were formed by painting 1 mm wide black stripes on the large specimen surface preliminarily painted white. The CCD camera captured and followed the positions of the transitions between black and white colors. In order to avoid possible effects of the markers bending or inclination in the course of deformation, the camera was accurately focused on the axis of symmetry of the specimen. The distance between black stripes, i.e., the width of the white stripes, was also 1 mm. Accordingly, the camera with a 20 mm field of vision allowed for simultaneous recording of the positions of twenty 1 mm distant markers, with a spatial resolution of 1.3  $\mu\text{m}$  and a sampling frequency of  $10^3$  Hz.

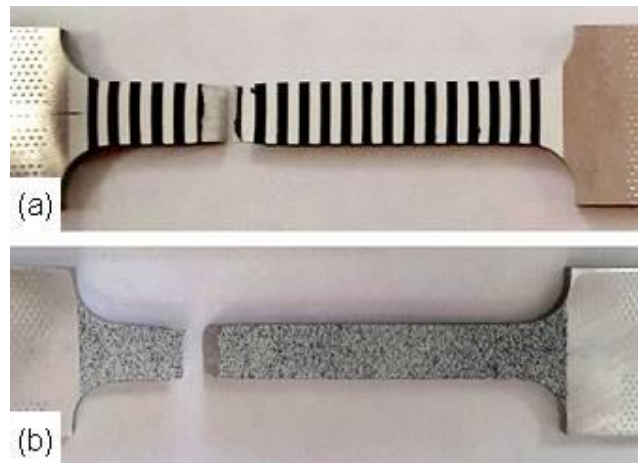


Figure 2.6: Photographs of specimens used for (a) 1D local extensometry and (b) 2D DIC.

The markers displacements were then processed using Matlab to calculate values of the local strain along the specimen axis. Although the calculation of strain for a local extensometer formed by two markers is direct, one precaution is noteworthy here. The local strain  $\varepsilon_i$ , also designated as  $\varepsilon_{loc}$  when it does not create confusion, was calculated using second neighbors to avoid biasing of the results by possibly unequal sensitivity of the camera to black-white and white-black transitions [Lebedkina et al., 2009; McDonald, 2009]:

$$\varepsilon_i(t) = \ln \frac{x_{i+2}(t) - x_i(t)}{x_{i+2}(0) - x_i(0)}, \quad (2.2)$$

where  $x_i$  is the coordinate of the  $i$ th transition. The strain data could then be numerically differentiated with respect to time to obtain the corresponding local strain-rate values.

Figure 2.7a represents an example of experimental records of markers positions as functions of the testing time. Figures 2.7b and c respectively display the results of calculation of the local strain and strain rate values. Each curve in these charts corresponds to one local extensometer. It should be clarified that during the tensile test, some bottom markers leave the field of vision of the CCD camera and some top markers enter it, so that only a part of them are constantly surveyed during a given time interval. So, only a 14 mm long part of the gage length remaining in the field of vision during the entire test is represented in Figure 2.7a.

These data allow for a conventional representation of the PLC band kinematics by constructing a local strain-rate map as a function of time and coordinates of the extensometers, as illustrated in Fig. 2.7d. The  $\dot{\varepsilon}_{loc}$  scale is represented by a color bar. Although the 1D method does not allow for observing the deformation band shape across the sample, such maps have an advantage of high-frequency visualization of the time evolution of the band position for the entire test. For example, they facilitate the detection of transitions between different band patterns upon the material strain hardening, as well as estimation of the band width and velocity.

An example of synchronization of a part of stress-strain curve with the respective strain-rate map is shown in Figure 2.8 illustrating type *A* band behavior. The bottom plot displays a successive propagation of four PLC bands through the specimen gage length. The stress jumps corresponding to deformation band nucleation occur earlier than the bands appear in the field of vision of the camera. Indeed, as type *A* bands usually nucleate at a specimen end that is located outside the surveyed length in Fig. 2.8, the nucleation process is not seen here. The instants of band nucleation can be guessed, though, due to dark spots which indicate local compressions caused by the elastic reaction (“spring-back”) of the material outside the deformation band. The further band propagation corresponds to a relatively smooth deformation. It can be seen that each band passes the field of vision and continues propagating until the nucleation of a new deformation band at the same specimen end. The slopes of the colored traces provide an accurate estimation of the velocity of the PLC bands,  $V_b$ . The vertical cross-sections of the traces allow for estimating the band width (Fig. 2.8). However, the coarse discreteness of the system of markers makes the former

estimate quite rough. The DIC technique described below provides a more reliable estimate of the band width.

Finally, a current drawback of the 1D technique used in the thesis is that the recording equipment limits the record duration by an interval of ten minutes, making it impractical for low strain rates when only portions of tests could be surveyed.

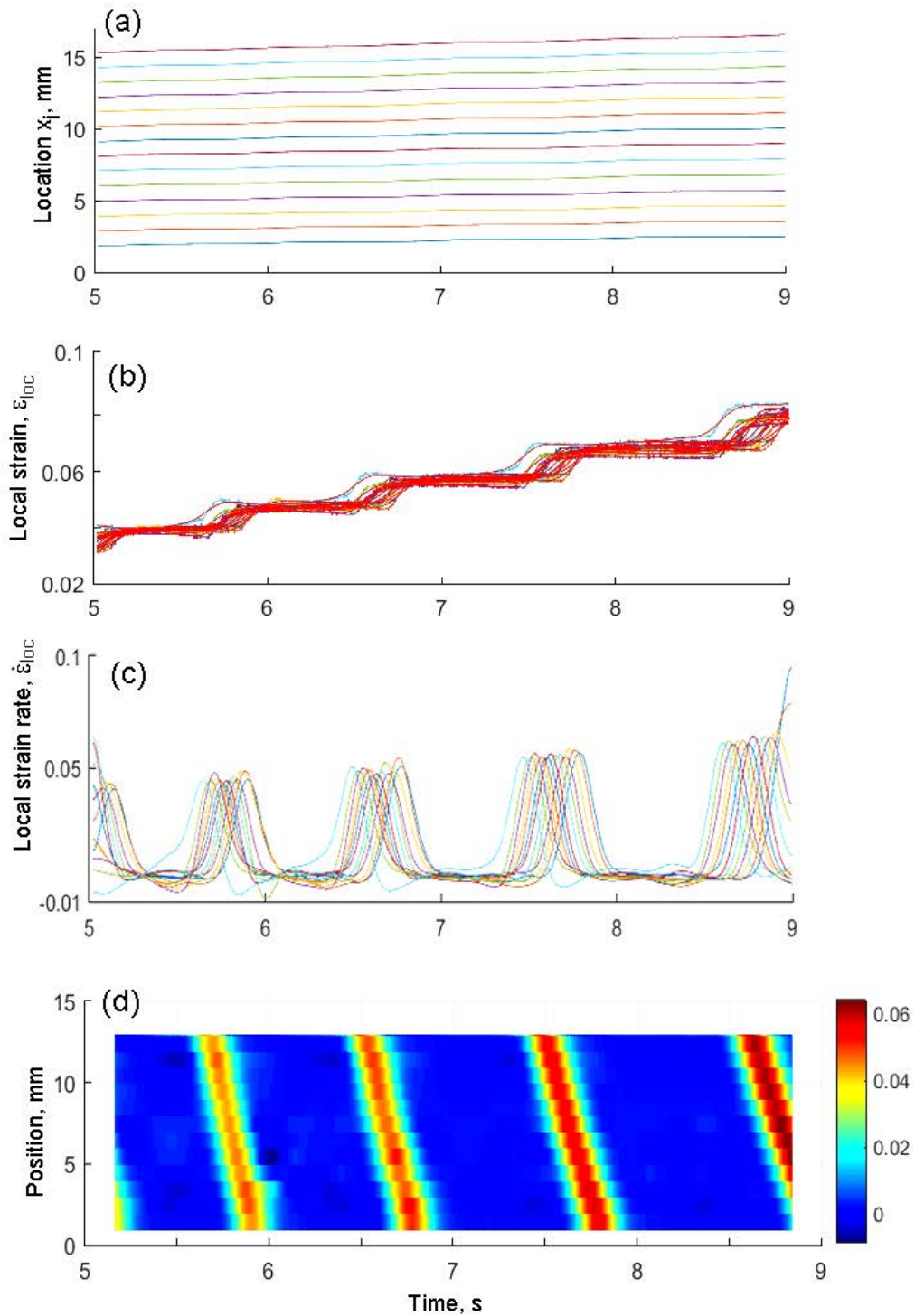


Figure 2.7: Example of experimental records as a function of testing time in coarse-grained A3 alloy at  $1.42 \times 10^{-2} s^{-1}$ : (a) positions of markers, (b) local strain, (c) local strain rate, used to construct a strain-rate map (d). The color bars quantify the strain-rate scale ( $s^{-1}$ ).

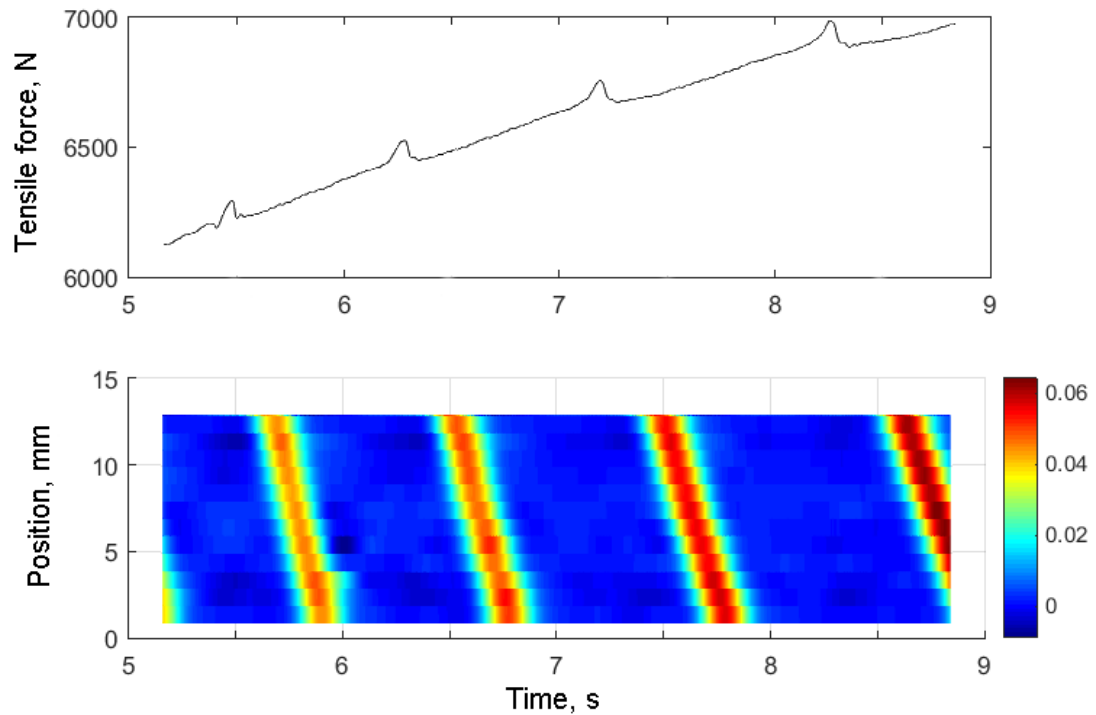


Figure 2.8: Spatiotemporal pattern showing the time evolution of the local strain rate along the tensile axis of a sample of the coarse-grained A3 alloy at  $1.42 \times 10^{-2} s^{-1}$ . Color bar quantifies the local strain-rate scale in  $s^{-1}$ .

*The second technique*, based on the 2D digital image correlation (DIC), did not have such limitation of the test duration, which was particularly important in the low strain-rate tests. To create markers for 2D measurements, one specimen surface was painted white and then a speckle pattern was deposited onto it using a spray of black paint (Fig. 2.6b). A 2D digital camera recorded consecutive images of the entire gage part of the specimen with a rate of 1 frame per 65 ms and the spatial resolution about 25 pixels per mm. The local strain-rate field was calculated with the aid of a standard image correlation software, Vic-2D [Vic-2D system]. Although the temporal and spatial resolutions of this method are worse than in the above-described case, it has advantages of visualization of the shape of the deformation band and a smaller discreteness corresponding to a mesh-size about 0.1 mm. An example of 2D images of a PLC band is presented in Fig. 2.9. Successive series of such images were also used to construct local strain-rate maps (see Inset in Fig. 2.10). For this, the data were collected from the DIC images along the vertical centerline of the specimen as a function of time.

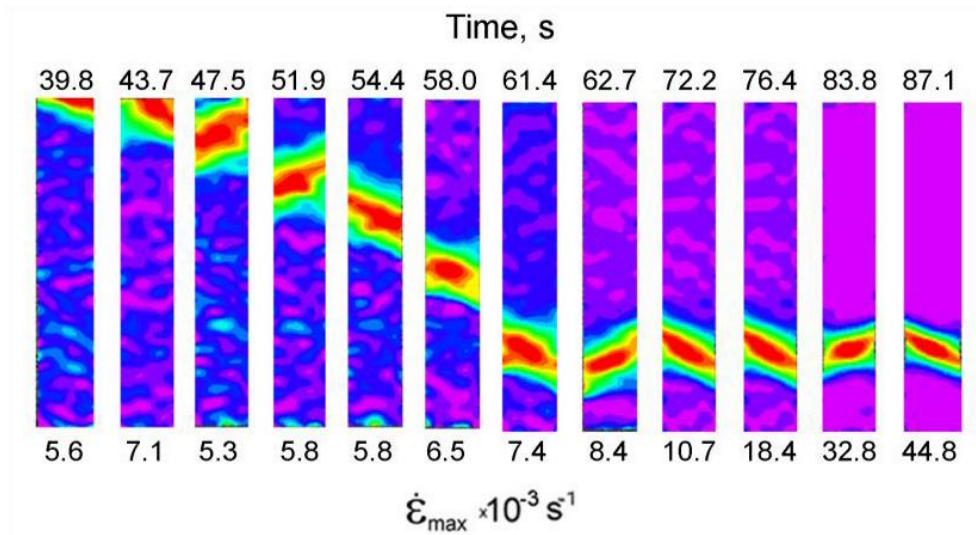


Figure 2.9: An example of successive series of 2D images showing the propagation and immobilization of a PLC band. The corresponding maximum local strain rate values and time instants are indicated underneath and over each frame, respectively.

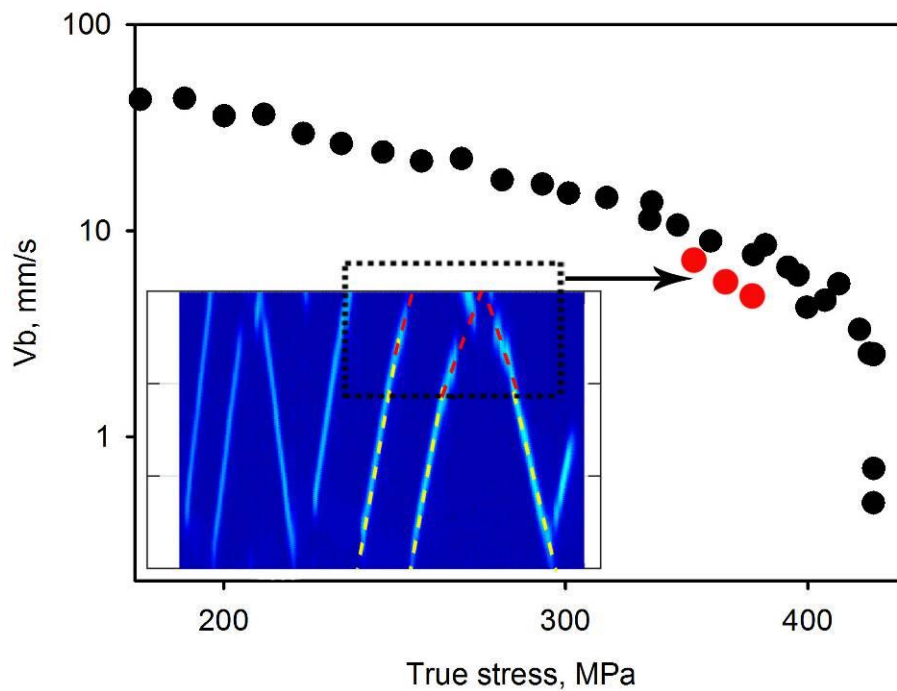


Figure 2.10: Scheme explaining the evaluation of the band velocity  $V_b$ . Red dashed lines and the corresponding red circles indicate deviations of  $V_b$  from the general trend.

Figure 2.10 also clarifies the approach to estimating the deformation band velocity from these maps. Namely, some deviation from the general slope was sometimes observed near the edge of the sample. In Fig. 2.10, such deviations are shown by red dashed lines and the corresponding  $V_b$  values by red dots on the  $V_b(\sigma_{\text{true}})$ -plot. As can be seen, these red spots drop out of the regular curve. Consequently, they were not taken into account in further calculations.

The DIC system also provided a channel for recording the output signal of the testing machine simultaneously with the CCD camera taking images. The accuracy of these measurements was relatively low but they served to synchronize the series of images with the deformation curve recorded by the load cell. The synchronization of two force-time curves took use of some well-defined events, such as the abrupt stress fall at the specimen failure and deep stress drops. The matching quality is illustrated in Fig. 2.11 presenting a series of type *B* serrations. It is seen that the instants corresponding to the onset and end of each serration coincide for two curves within the accuracy determined by the imaging rate. The three charts of Fig. 2.11 also qualify the image acquisition frequency regarding the details of stress fluctuations at different  $\dot{\epsilon}_a$ . To catch rapid processes of plastic instability, the maximum imaging rate was used in all tests. The example of Fig. 2.11 demonstrates that in not very fast tests corresponding to type B and type C (not shown) behaviors, all features of serrated deformation curves are captured by the corresponding images. Moreover, even at high strain rates (the middle and bottom charts), the acquisition frequency allows for visualizing each significant event.

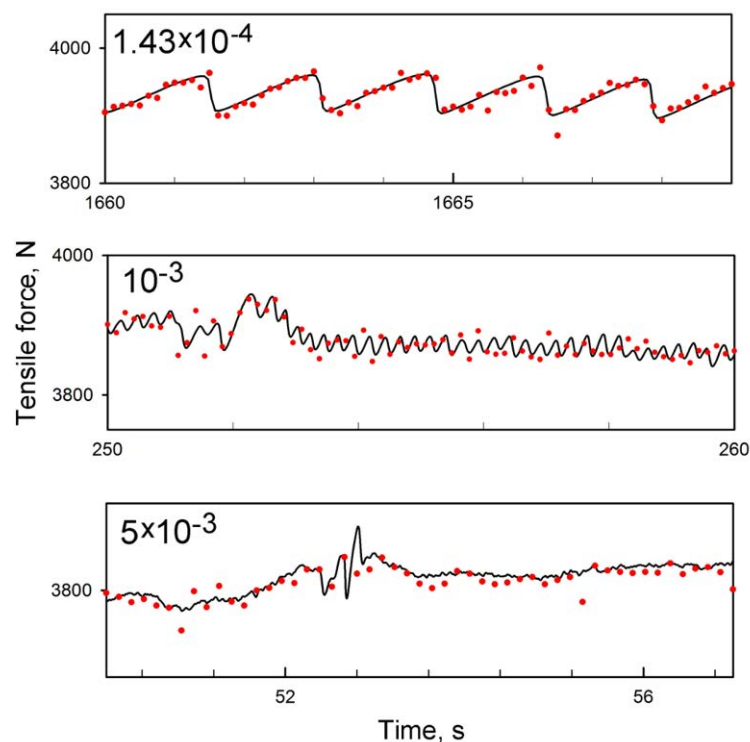


Figure 2.11: The correlation of deformation curves of coarse-grained A1 alloy at different strain rates (in  $\text{s}^{-1}$ ) with digital images taken at successive time intervals. Each red circle on the curve represents moment of image recording.

### 2.2.3. Acoustic emission measurement

The AE was recorded during tensile tests using a piezoelectric transducer with a frequency band of 200–900 kHz, clamped to the greased surface of the specimen near the upper grip. The transducer was pre-amplified by 40 dB in a 10–900 kHz frequency band and registered using a Euro Physical Acoustic system [Lebedkina et al., 2018-1; Lebyodkin et al., 2012]. Figure 2.12 defines the parameters used by the build-in software to extract meaningful acoustic events (hits) in the real time. The event starting time,  $t_o$ , is defined as the instant when the acoustic signal exceeds a threshold voltage  $U_o$ . The threshold was set to 25 dB in the present study, which corresponded to the noise level of the acoustic signal measured in the free-running deformation machine.

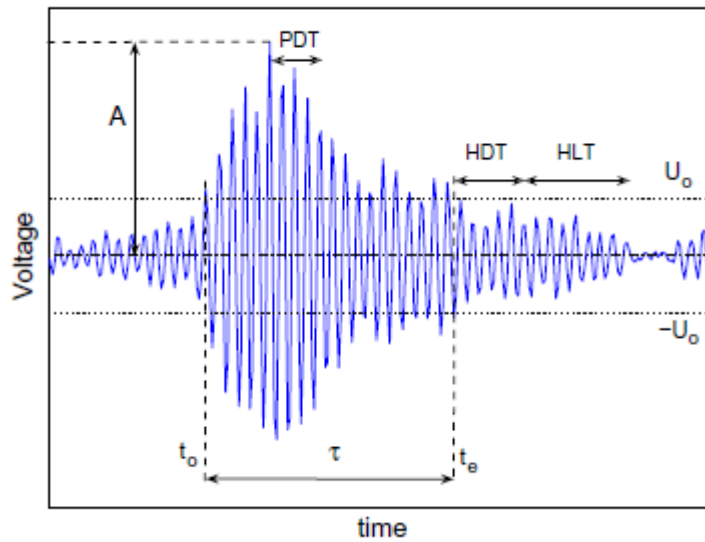


Figure 2.12: Definition of the parameters used to extract individual AE events [Lebyodkin et al., 2012].

If the signal remains below  $U_o$  longer than for a hit definition time (HDT), the event is considered to have come to an end ( $t_e$ ). The local maximum of the signal is recorded as the event's peak amplitude if it has not been exceeded during the peak definition time (PDT). To filter out sound reflections after the end of the event, the system does not record hits during the “dead time” interval, or a hit lockout time (HLT). Like in [Lebyodkin et al., 2012], the PDT was taken equal to half HDT. In the present work, two values of HDT were utilized to check the robustness of the statistics, 100 and 300  $\mu\text{s}$ . The results of the statistical analysis were similar in both cases. HLT was taken equal to 40  $\mu\text{s}$ , and the PDT was taken equal to half HDT (cf. [Lebyodkin et al., 2012]). It should be specified that the device stores logarithmic amplitudes of the events. To avoid confusion, the notation  $A$  is used for the peak

amplitude after conversion from the logarithmic to linear units. The described parameters and its values were used to measure characteristics of acoustic events during deformation process and were used for the statistical analysis given in the last chapter of the study.

#### 2.2.4. Statistical analysis

To compare the statistics of stress serration and acoustic emission with the literature data for binary alloys, the same procedure as in [Bharathi et al., 2001; Lebyodkin et al., 2012] was applied in Chap. 5. The basic principles are as follows:

- In the case of AE, the analyzed variable was the squared amplitude  $I = A^2$ , reflecting the energy dissipated in the deformation process [Weiss et al., 2001].

- As the amplitudes of the AE and stress serrations may evolve during the test, the distributions were calculated over intervals of approximately constant range of variation of the studied variable.

- The above precaution is less constraint in the case of stress serrations, the evolution of which often consists in a simple growth of their average amplitude, without effect on the characteristic patterns. This increase can usually be taken into account through normalization of the stress-time curve  $\sigma(t)$  by a smooth function obtained through running-average or polynomial fitting [Bharathi et al., 2001]. To distinguish from the non-normalized data, the magnitudes of normalized serrations are designated  $\Delta s$  in what follows.

- To compare the probability density functions (PDF) obtained for different variables or for the same variable in different conditions, histograms were calculated using data rescaled by the average value of the studied quantity,  $X/\langle X \rangle$ , where  $X$  means either  $I$  or  $\Delta s$ .

- To calculate the PDF in statistically significant intervals, the equal-sized bins of the histograms were first grouped by adding the right-hand neighbors until gathering at least 5 events in each of the resulting bins. The PDF was then calculated as  $P(X) = \frac{1}{\delta X} \frac{\delta N(X)}{N}$ , where  $N$  is the total number of data in the statistical sample and  $\delta N(X)$  is the corresponding histogram with  $X$  taken in the middle of the bin  $\delta X$ .

# Chapter 3

## Effect of microstructure on spatiotemporal behavior of the PLC effect

As described in Chapter 1, binary Al-Mg alloys have been a model system for studying the PLC instability for a long time. At the same time, the practical use of such alloys is limited because of their low strength. A substantial improvement of mechanical properties of these alloys could be reached by precipitation strengthening and/or grain refinement. However, the observed effects of microstructure on serrated flow are diverse and sometimes opposite to each other. To provide a systematic basis for investigation of the effect of microstructure and phase composition on the plastic flow instability, this Chapter presents the results of experimental studies of the PLC effect in several AlMg-based alloys, namely, a “model” Al-Mg alloy and commercial alloys containing precipitates, in a wide strain-rate range covering different types of stress serration patterns. Besides the initial coarse-grained state, the investigated alloys were prepared with microstructures distinctly distinguished by the grain size and lattice dislocation density using various SPD processes.

The most detailed study of the polycrystalline structure, covering the CG conditions and two different fine-grained states obtained by ECAP and ECAP followed by cold-rolling, was realized for the binary A1 alloy and the A2 alloy containing coarse non-shearable precipitates. The results of these investigations are described in §§ 3.1 and 3.2. The last part of this Chapter compares these results with the data obtained for the alloy with fine precipitates (A3) and the alloy containing both kinds of precipitates (A4), in CG conditions and after ECAP.

### 3.1. Coarse-grained binary alloy and alloy with coarse particles

#### 3.1.1. Deformation curves and types of serrations

Overall tensile behavior of CG state of A1 and A2 alloys is illustrated in Fig 3.1. Although for a given strain rate, deformation curves obtained for different alloys do not resemble each other, the entire families of curves correspond in both cases to the common types of serration patterns described in Chap. 1. The curves exhibit a well-defined yield

plateau followed by the PLC effect, which manifests itself by repetitive stress drops on the deformation curves. The dispersion-hardened A2 alloy shows a significantly higher yield and tensile strength and a slightly lower ductility than the A1 alloy. An extensive initial strain hardening of the stress-strain curves was observed in the A1 alloy, while it was less pronounced in the case of A2 alloy. It can be seen that in both alloys, the curves display negative strain-rate sensitivity, in conformity with the observation of the PLC instability.

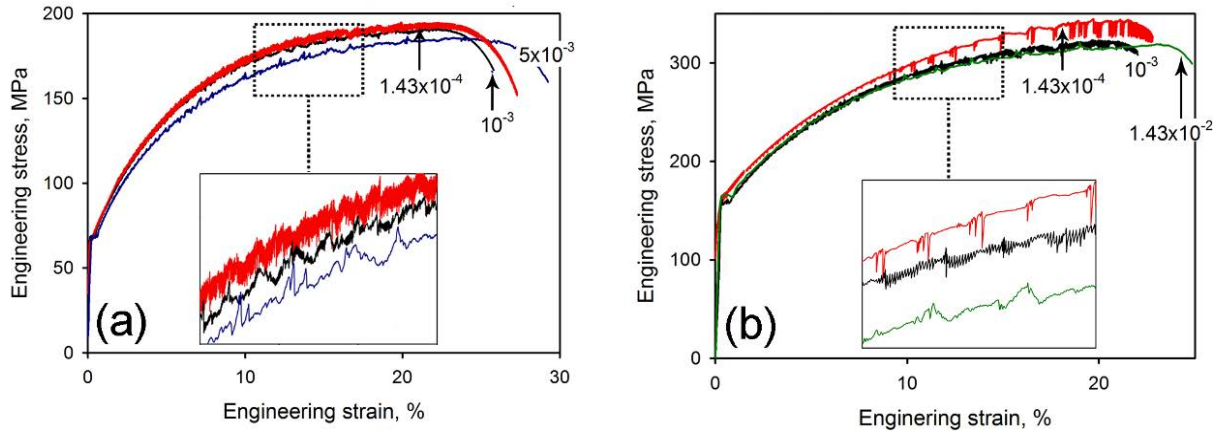


Figure 3.1: Examples of engineering deformation curves of A1 (a) and A2 (b) alloys in CG state for various strain rates (given in  $s^{-1}$ ). Some of the portions of the curves presented in the insets were shifted to avoid superposition and better clarify details of serrations.

The CG A1 samples show clear type *A* behavior at  $5 \times 10^{-3} s^{-1}$  (Fig. 3.1a) and  $1.43 \times 10^{-2} s^{-1}$  (not shown). Type *B* serrations can be recognized at large strains in the tests at  $10^{-3} s^{-1}$  and become dominant at  $1.43 \times 10^{-4} s^{-1}$ . Mixed *B+C* serrations are observed at  $2.86 \times 10^{-5} s^{-1}$ . The transition to pure type *C* serrations was not complete at the lowest strain rate. However, since the precipitation hardening should lead to an increase in the waiting time of dislocations on obstacles, the A3 alloy expectedly displayed a shift of the transitions between types of behavior towards higher  $\dot{\epsilon}_a$  values [cf. Mogucheva et al., 2016]. As a result, all three nominal types of serration patterns have been detected (Fig. 3.1b). Type *B* serrations are preponderant in the example for  $10^{-3} s^{-1}$ . For convenience, this strain rate is utilized hereinafter as a reference value. Types *C* and *A* serrations occur, respectively, for strain rates below and above this value.

### 3.1.2. Type *A* behavior

Figures 3.2 and 3.3 present examples of spatiotemporal maps observed in the CG state of the A1 alloy and A2 alloy at  $10^{-3} s^{-1}$  and  $5 \times 10^{-3} s^{-1}$ , respectively. The PLC bands nucleate

immediately after the propagation of one or two successive Lüders bands. The Lüders behavior will be specified in Sec. 3.1.5. The maps display several well-known features of the PLC effect at high strain rates.<sup>2</sup> On the early stage of deformation, the behavior corresponds to the proper type *A* behavior. Each deformation band is nucleated at one specimen end and continuously propagates toward the other end. A well-known tendency to a transition from type *A* to type *B* patterns can be recognized at larger strains, as breaks in the regular continuous propagation of the bands and alternation between the upward and downward propagation of successive bands (the latter is denoted as “band reflection” in [Ait-Amokhtar and Fressengeas, 2010]). This tendency is rather weak in the example for the A1 alloy (Fig. 3.2). In contrast, type *B* pattern becomes dominant close to the end of the test ( $t \approx 55$  s) on the A2 sample (Fig. 3.3). Figure 3.3 also illustrates that the final onset of necking corresponds to a progressive termination of the PLC band propagation. A detailed analysis of the interrelation between the immobilization of the PLC bands and the necking formation will be presented in Chap. 4.

Figure 3.4 presents an example of DIC data illustrating propagation of a type *A* deformation band along the gage length and nucleation of the next band in a CG A1 sample tested at the reference strain rate of  $10^{-3} \text{ s}^{-1}$ . Several typical features of type *A* bands can be remarked in the DIC images. The bands are well-contoured and inclined about  $60^\circ$  to the tensile axis, alternating between two symmetrical orientations. This swapping occurs after some strain and has a simple explanation in terms of the need to compensate the rotation of the specimen axis, produced by the shear band, and keep the specimen aligned in the direction of the applied force. When the swapping takes place during one propagation event, two conjugate bands can appear simultaneously, leading to cross-shaped strain localizations (e.g., the frame at  $t = 37.5$  s). In this case, the swapping proceeds through nucleation of a second band with a symmetrical orientation and exhaustion of the first band.

---

<sup>2</sup> A closer view uncovers plastic flow heterogeneities on smaller scales that can be discerned, e.g., in Fig. 3.2. The analysis of such small-scale patterns goes beyond the scope of the thesis and will be analyzed in future works. Nevertheless, the presence of such heterogeneities is related to the nature of the acoustic emission accompanying the plastic deformation. Accordingly, this aspect will be concerned in Chapter 5.

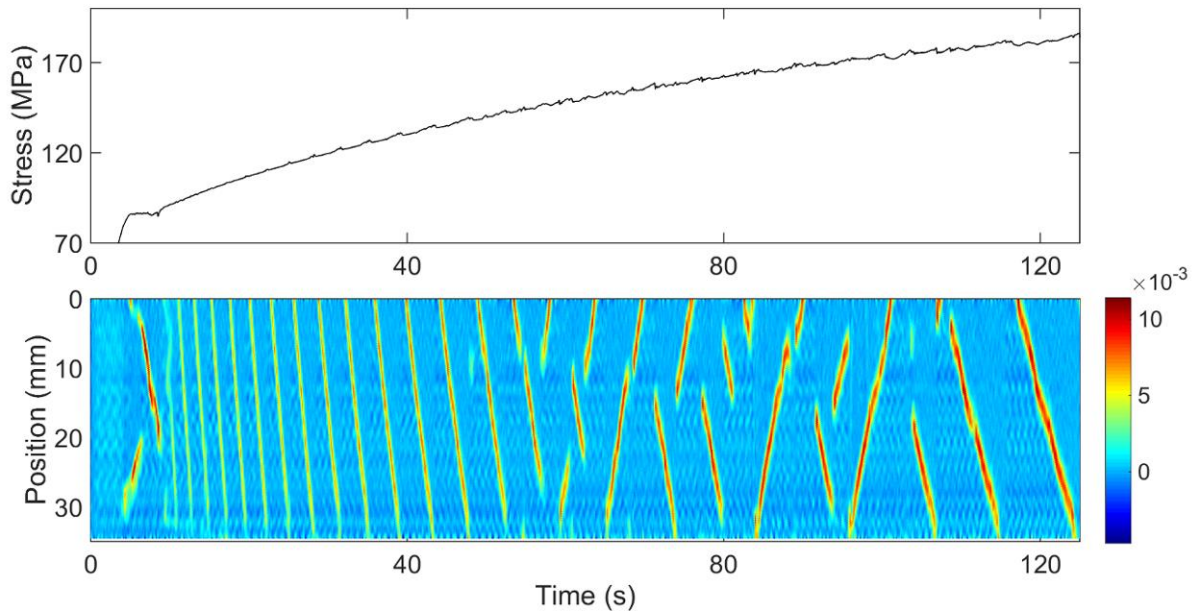


Figure 3.2: Example of stress-time curve displaying type *A* serrations in the CG A1 alloy at  $10^{-3} \text{ s}^{-1}$  and the corresponding local strain-rate map showing the propagation of deformation bands. The color bar represents the local strain-rate scale in  $\text{s}^{-1}$ .

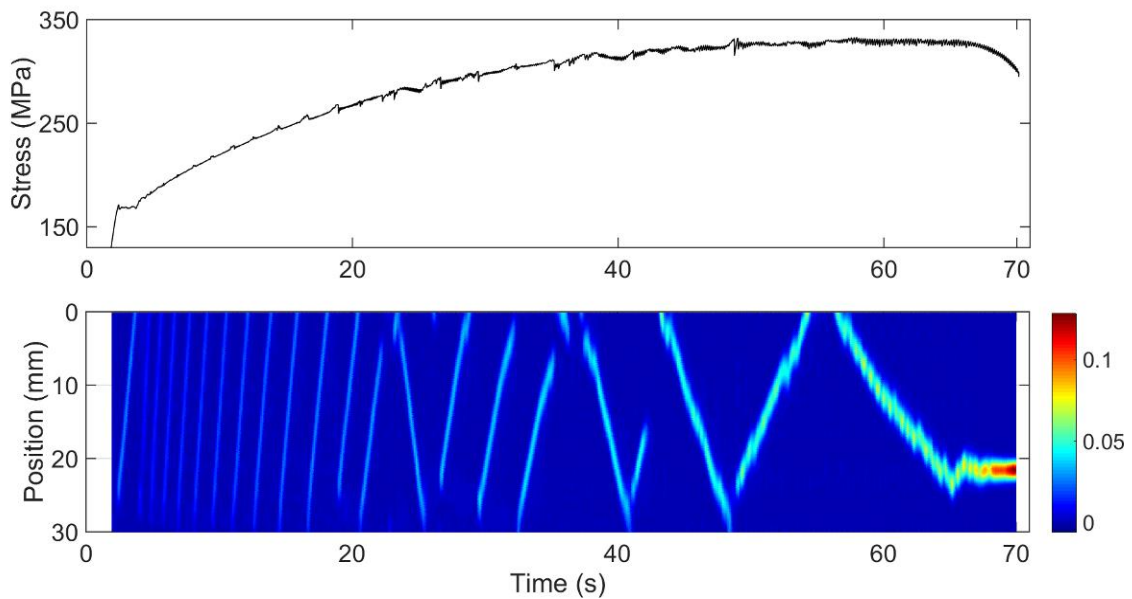


Figure 3.3: Example of stress-time curve displaying type *A* serrations in the CG A2 alloy at  $5 \times 10^{-3} \text{ s}^{-1}$  and the corresponding local strain-rate map showing the propagation of bands. The color bar represents the local strain-rate scale in  $\text{s}^{-1}$ .

The propagation velocity of deformation bands,  $V_b$ , decreases during the test (Fig. 3.5), while the local strain rate within the band is increased (Fig. 3.6), thus testifying to a stronger strain localization. As the local strain rate is not uniform within the deformation band, the evolution of the degree of strain localization will be further attested using the corresponding maximum value (for simplicity, it will be denoted as  $\dot{\epsilon}_{loc}$  if not stated otherwise), normalized

to  $\dot{\epsilon}_a$  in order to compare results for different conditions. As can be seen in Fig. 3.6, the ratio  $\kappa = \dot{\epsilon}_{loc} / \dot{\epsilon}_a$  increases from several to somewhat more than ten during high strain-rate tests corresponding to type *A* behavior.

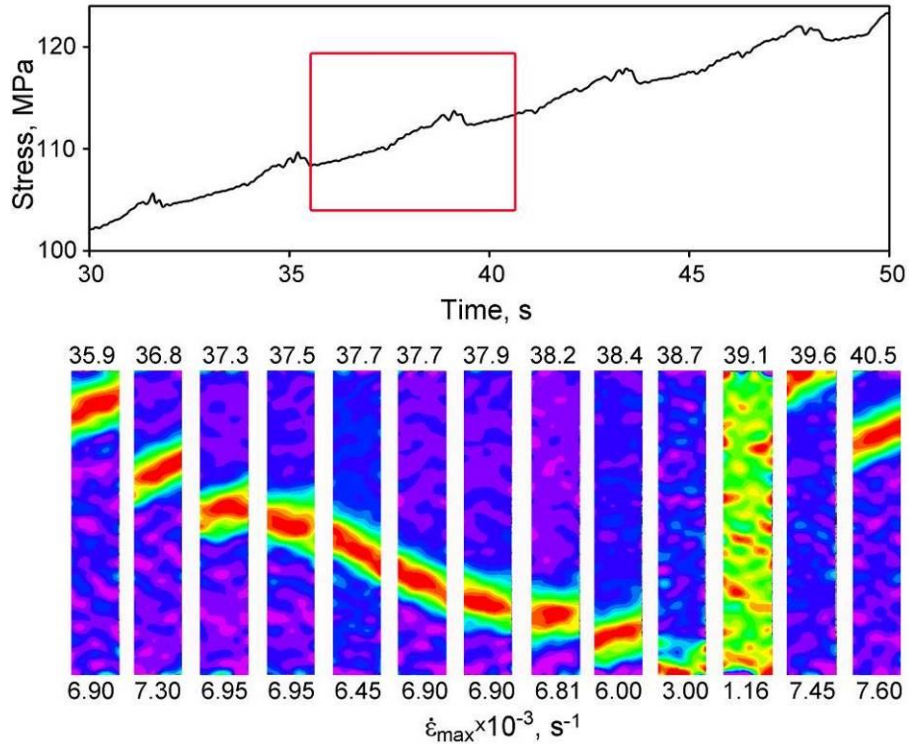


Figure 3.4: Portion of a stress-time curve of the sample of Fig. 3.2 displaying type *A* serrations and a series of DIC images of the specimen surface, taken within the interval indicated by the rectangle. Numbers above the images specify the corresponding time instants. The image height is approximately 34.5 mm and corresponds to almost the entire gage length at this strain.

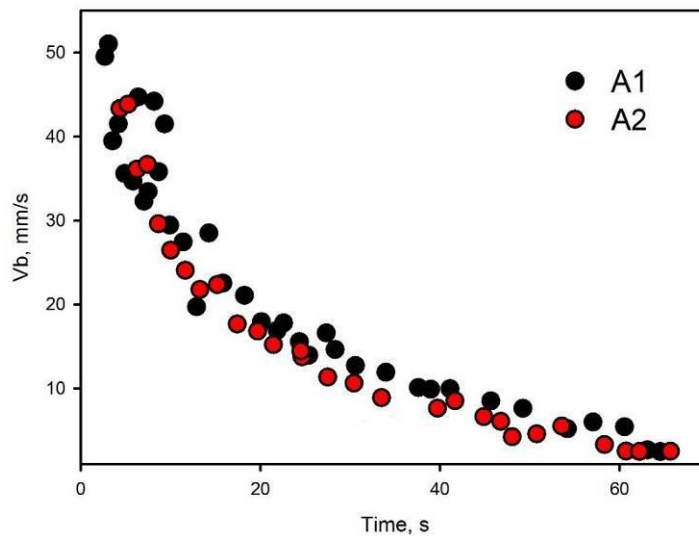


Figure 3.5: Examples of evolution of the deformation band velocity during deformation of CG A1 and A2 samples at  $5 \times 10^{-3} \text{ s}^{-1}$ .

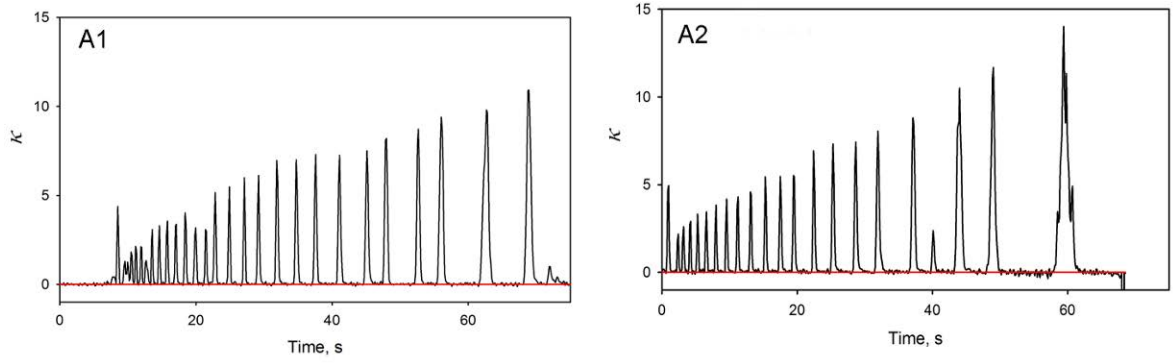


Figure 3.6: Evolution of the value of  $\kappa = \dot{\epsilon}_{loc} / \dot{\epsilon}_a$  at a point (pixel) on the centerline of the samples of CG (a) A1 and (b) A2 alloys tested at  $5 \times 10^{-3} \text{ s}^{-1}$ . The solid straight line presents the current value of the imposed strain rate corrected with respect to the actual specimen length. The first high peak corresponds to the Lüders band.

Figure 3.5 testifies that the evolution of  $V_b$  during the test follows a similar course for both alloys. Namely,  $V_b$  decreases with strain hardening, such slowing down being generally ascribed to the increasing number of obstacles to the dislocation motion [Ait-Amokhtar et al., 2006]. Furthermore, the beginning of the  $A/B$  transition in the A2 alloy close to 40 s does not qualitatively affect the dependence, but only amplifies the data scatter, partly because of the uncertainty in the determination of intervals of relatively stationary (with the same velocity) hopping propagation.

Although the decrease in  $V_b$  is reported in all available literature, the quantitative dependences obtained by different authors do not display unique behavior with strain or stress (see Chapter 1). Figure 3.7a plots the data from Fig. 3.5 as functions of the true stress. The arrows show the maximum load, or UTS, attained for each specimen. It can be seen that each curve can be approximately described by a power-law  $V_b(\sigma_{true}) \sim \sigma_{true}^m$  during a large part of the test, with a cutoff somewhat beyond the maximum load. The estimate of the power-law exponent renders  $m \approx 1.55 \pm 0.10$  and  $2.71 \pm 0.14$  for the A1 and A2 alloy, respectively (least square errors are indicated). The difference between these estimates for two alloys conforms to the diversity of such dependences reported in the literature for various materials. Nevertheless, the comparison of the dependences obtained at different strain rates for the same material are rather close, as illustrated in Fig. 3.7b for the A1 alloy. To our knowledge, such a similitude has not been reported earlier. Moreover, it should be noted that this figure combines data for type  $A$  and type  $B$ . Namely, the bottom curve corresponds to the proper type  $B$  case. As the existence of a unique dependence could provide grounds for further progress in the understanding of the PLC band kinematics, these results motivate more detailed investigations of this aspect in the future.

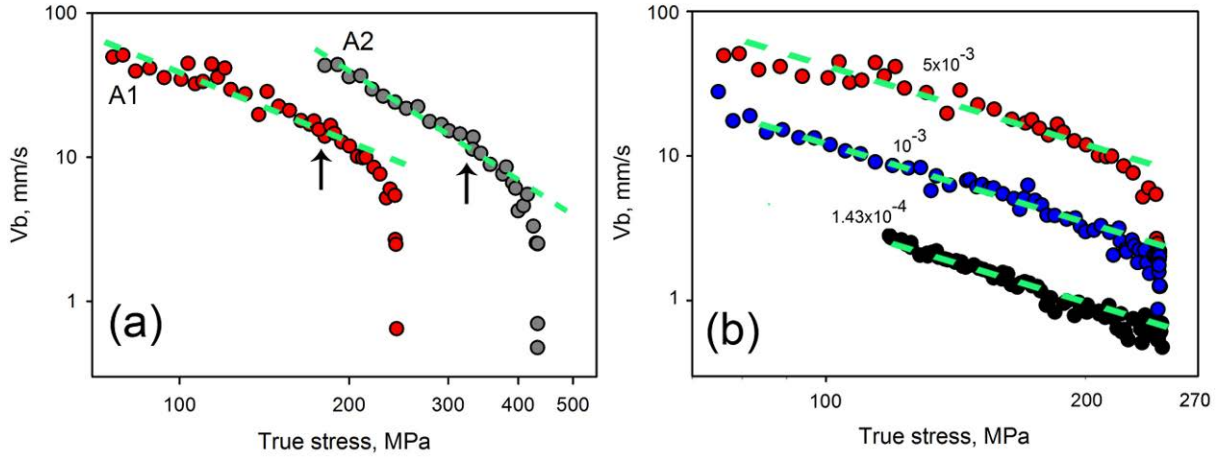


Figure 3.7: Dependence of the band velocity,  $V_b$ , on the true stress: (a) for CG A1 and A2 alloy tested at  $5 \times 10^{-3} \text{ s}^{-1}$  (data from Fig. 3.5), (b) for CG A1 alloy at different strain rate (in  $\text{s}^{-1}$ ). The arrows indicate the UTS.

It is noteworthy that for a plane-parallel band moving with a constant velocity, the following relationships stem from geometrical consideration provided that deformation of the rest of the specimen can be neglected (e.g., [Feng et al., 2012]):  $\varepsilon_b V_b = \dot{\varepsilon}_b w = V$ , where  $\varepsilon_b$  and  $\dot{\varepsilon}_b$  are the average strain and strain rate in the deformation band,  $w$  denotes its width, and  $V$  is the mobile grip velocity. Both  $w$  and  $\dot{\varepsilon}_b$  are not well-defined characteristics because of the varying shape of deformation bands and the local strain rate inhomogeneity within the band. Therefore, these relationships can only be verified approximately. The estimates showed that the product  $\dot{\varepsilon}_{loc} w$  using the maximum local strain rate values agrees well with the grip velocity in the case of the weak strain localization at the beginning of deformation, notably in the Lüders bands, but increases about twice at large strains, thus confirming the strain localization strengthening within the deformation band, stemming from Fig. 3.6.

It should also be underlined that although a cutoff in the dependences is observed in the interval corresponding to necking, the deformation bands preserve some mobility after having reached the maximum load. These results will be discussed in Chap. 4, in relation with the question of the neck development in the presence of the PLC instability.

### 3.1.3. Type B behavior

When the strain rate decreases, type B behavior gradually becomes dominant for the entire tests on CG alloys. An example of type B patterns is shown in Fig. 3.8 for the specimen of CG A2 alloy deformed at  $10^{-3} \text{ s}^{-1}$ . Each stress drop is produced by an individual

deformation band whereas the following reloading corresponds to a roughly uniform plastic flow. The subsequent bands form relay-race propagation series characteristic of type *B* dynamical regime (see details of such a relay race in Fig. 3.8b). An additional interest to this example is due to illustration of an often observed alternation of bands (or series of bands) propagating in the opposite direction over a part of the gage length. Such behavior is seen at  $t < 100$  s and is later substituted with series of bands propagating through the entire specimen length. Figure 3.9 provides a magnification of a short time interval illustrating the slowing down and termination of one series of deformation bands (frames at 75.6-78.9 s) and nucleation and motion of the next series of bands with the same orientation (frames at 78.7-80.2 s). On the other hand, like in Fig. 3.4, the change of the band orientation and short-time coexistence of two bands can be observed during three frames at 78.7-78.9 s. It can be concluded, similar to the case of type *A* behavior (Fig. 3.4), that the band orientation can change during one propagation sequence, such flip taking place through a competition of two conjugate bands (frames at 76.1 s and 76.5 s). Finally, Fig. 3.8a shows a change from the alternate band propagation to the propagation along the entire gage length. In any case, the discontinuous (“hopping”) propagation remains the primary mode (Fig. 3.8b). The intensity of strain localization within the bands presented in Figs. 3.8 and 3.9 is similar to that in type *A* bands. However, this result is atypical and is likely to be due to the closeness of  $\dot{\varepsilon}_a$  to the range of type *A* behavior. In most cases, the estimates rendered  $\kappa \sim 20-50$  for type *B* bands. Moreover, taking into account the abruptness of type *B* PLC bands, the exact  $\dot{\varepsilon}_{loc}$  may considerably exceed the measured values (according to some authors, this difference may reach orders of magnitude [Ait-Amokhtar et al., 2006; Renard et al., 2010]), so that the real ratio may be much more significant.

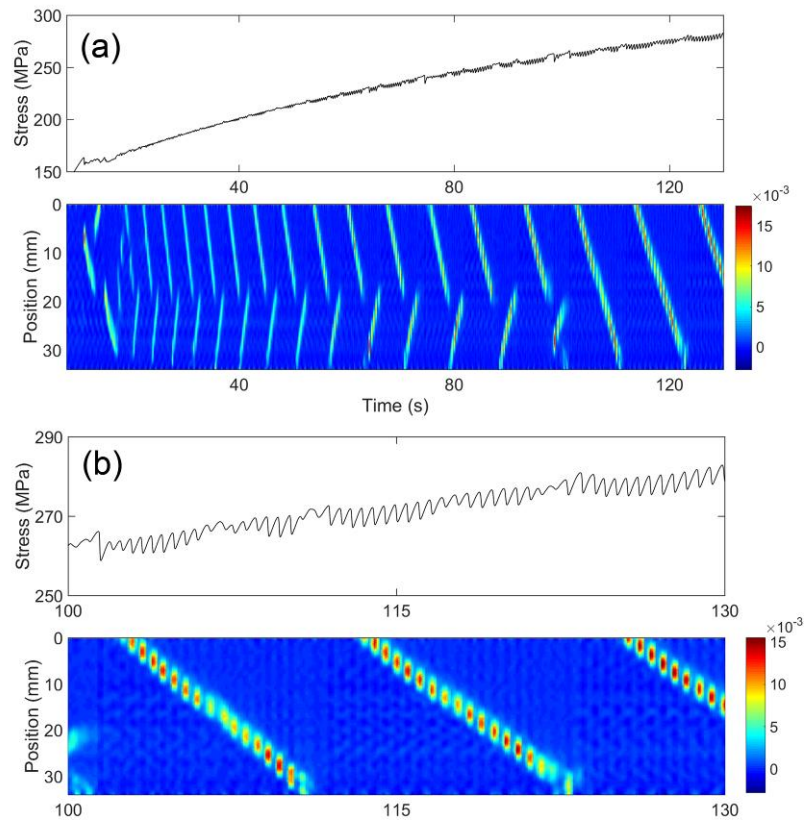


Figure 3.8: Portions of a stress-time curve displaying type *B* serrations in the CG A2 alloy at  $10^{-3} \text{ s}^{-1}$  and the corresponding local strain-rate map showing the propagation of deformation bands. The chart (b) shows details of the right-hand part on chart (a). The color bar represents the local strain-rate scale in  $\text{s}^{-1}$ .

Although the above pattern of relay-race propagation is well-known [Ait-Amokhtar and Fressengeas, 2010; H. Louche et al., 2005; Jiang et al., 2007] the DIC technique allowed for getting new information on the nucleation of static deformation bands and its correspondence to various phases of formation of deep stress drops. This process is illustrated in Fig. 3.10 using an example of CG A1 alloy tested at  $1.43 \times 10^{-4} \text{ s}^{-1}$ . Well-formed deformation bands with  $\kappa \sim 40\text{--}50$  are observed at the instants corresponding to the maximum load at the onset of deep serrations (frames 1 and 7). A relatively uniform local strain-rate field with small-size weak heterogeneities ( $\kappa \sim 3\text{--}5$ ) is observed during the fast quasi-elastic reloading between the subsequent stress drops (frames 3 and 4). The fifth frame demonstrates that a diffuse deformation band starts forming quite early in the region corresponding to the next sharp PLC band. Importantly, although the intensity of this heterogeneity is weak ( $\kappa \sim 6$ ), yet it crosses the entire width of the specimen.

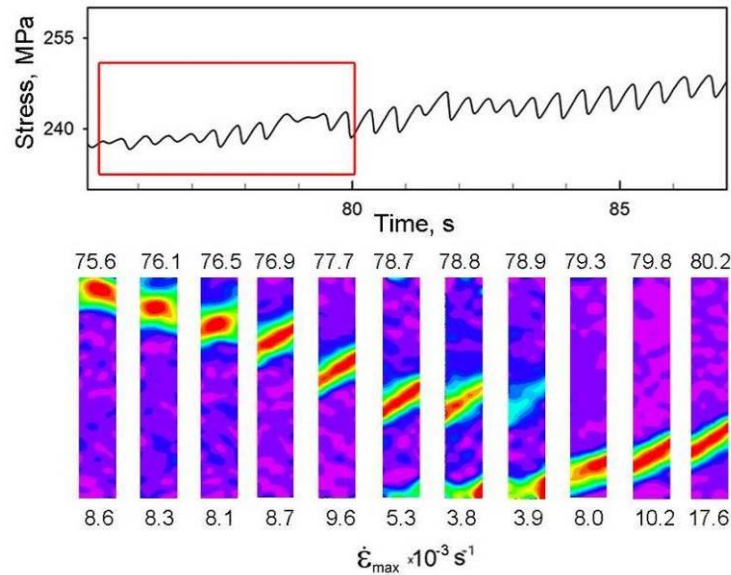


Figure 3.9: Portion of a stress-time curve of the sample of Fig. 3.8 displaying type *B* serrations and a series of DIC images of the specimen surface, taken within the interval indicated by the rectangle. Numbers above the images specify the corresponding time instants. The image height is approximately 34 mm and corresponds to almost the entire gage length at this strain.

These results allow for two conjectures. First, it can be suggested that the deformation band is nucleated progressively, i.e., the strain heterogeneity is gradually formed during reloading and prepares the catastrophic instability. Second, it testifies that this process did not imply the nucleation of an embryo (see § 1.1.3). The data of Fig. 3.10 suggest that the nucleating band has a size close to its final size from the very beginning. Such a conclusion agrees with [Tong et al., 2005; Zdunek et al., 2008]. However, these authors only surveyed the time interval corresponding to the fast stress drop, i.e., a well delineated PLC band, but did not observe the prior formation of a diffuse deformation band. Moreover, quite unexpectedly, Figure 3.10 also uncovers a diffuse band in the wake of the PLC band (frame 2). This observation bears evidence that the termination of the instability is neither immediate but also proceeds progressively.

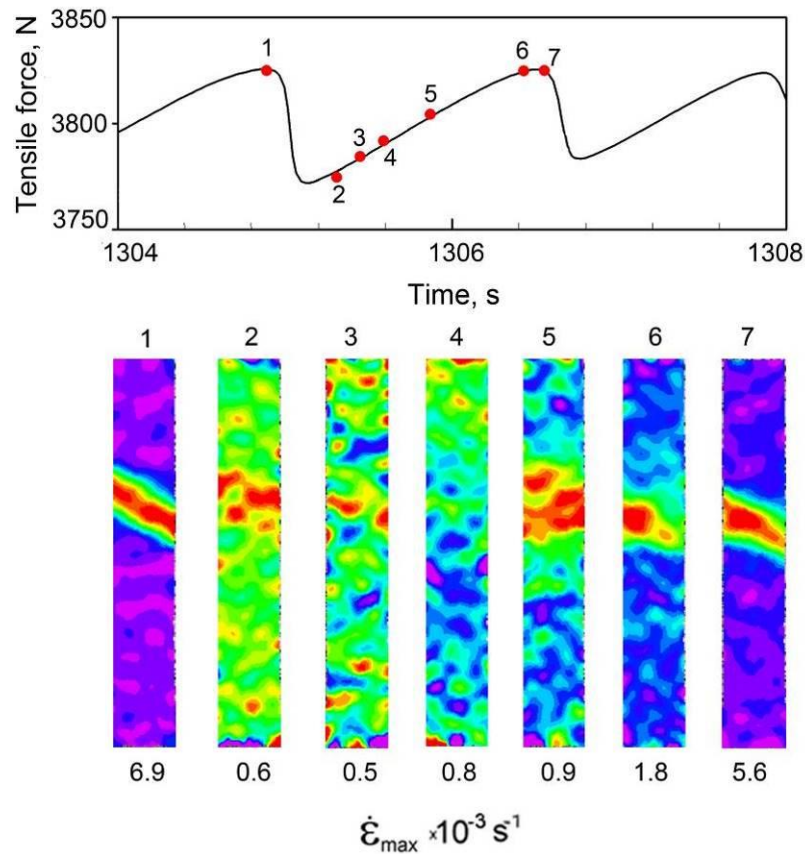


Figure 3.10: Portion of a stress-time curve displaying type *B* serrations in the CG A1 alloy at  $1.43 \times 10^{-4} \text{ s}^{-1}$  and a series of DIC images of the specimen surface, taken within this interval. Numbers above the images specify the corresponding time instants. The image height is approximately 34 mm.

### 3.1.4. Low strain-rate behavior

The above-described examples illustrated two of the basic types of PLC effect, corresponding to the ranges of high (type *A*) and middle (type *B*) strain rates, and the gradual *A/B* transition taking place when the applied strain rate is diminished. In general, the further decrease in  $\dot{\epsilon}_a$  leads to a transition from the type *B* to type *C* instability. Such a trend was observed for both materials studied in this Chapter although the transition occurred to be incomplete in the CG A1 alloy even at the lowest strain rate and large strains, as was remarked in § 3.1.1 regarding the respective serration patterns. It is noteworthy that in the case of mixed transitory behaviors, the deformation curves alone do not allow for a certain conclusion on the preponderant type of behavior. In such cases, the analysis of the local strain-rate field is indispensable. Overall, the deformation curves obtained at  $2.86 \times 10^{-5} \text{ s}^{-1}$  for the CG A1 alloy were similar to those recorded at  $1.43 \times 10^{-4} \text{ s}^{-1}$  (Fig. 3.1a) and corresponding to type *B* sequences of deformation bands. As can be seen from the example of DIC measurements in Fig. 3.11a, the spatiotemporal pattern demonstrates relay-race patterns at the beginning of deformation (see also § 3.1.5), even if they are relatively short

and less regular (cf. Fig. 3.8b). However, the relay race becomes less pronounced after some deformation, and an uncorrelated nucleation of deformation bands associated with type *C* behavior is detected in the work-hardened alloy (Fig. 3.11b). The trend to the type *C* also conforms to the progressive increase in the *k*-ratio during the test. It evolves from about 20 for type *B* to 180 for type *C* deformation bands in Fig. 3.11a and 3.11b, respectively. Such an increase agrees with the trends reported by other authors using methods with a similar resolution (see § 3.1.3).

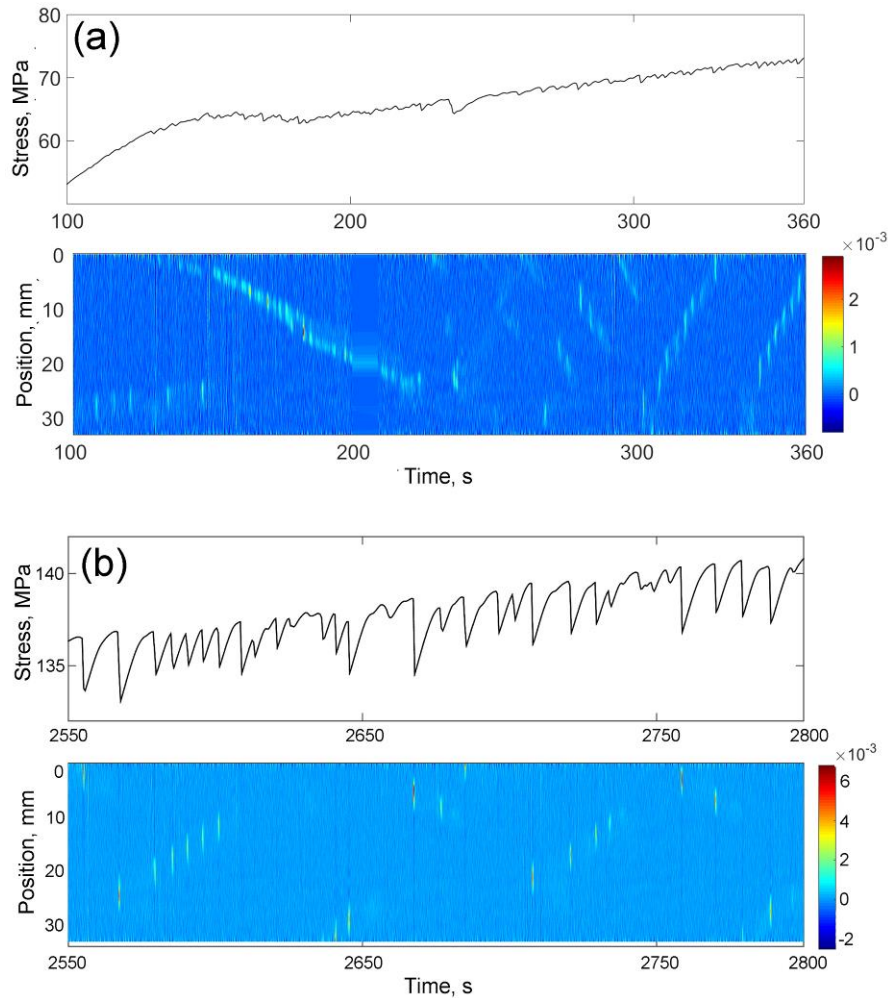


Figure 3.11: Details of a deformation curve of a CG Al sample tested at  $2.86 \times 10^{-5} \text{ s}^{-1}$ . (a) Onset of plastic deformation; (b) Work-hardening region.

In the case of the A2 alloy, a well-defined type *C* instability starts being observed on the deformation curve when the strain rate is decreased down to  $1.43 \times 10^{-4} \text{ s}^{-1}$  (Fig. 3.1b). Its behavior needs some clarification. Deep stress drops characteristic of type *C* behavior appear after a large critical strain  $\varepsilon_{\text{cr}}$ , about 10%, which is typical for type *C* deformation curves. At the same time, serrations with lower amplitude occur starting from the elastoplastic transition. The nature of such serrations has been a subject of discussion for a long time

[Abbadi et al., 2002; Lebedkina and Lebyodkin, 2008; Lebyodkin et al., 2012; Kobelev et al., 2017]. Recent studies, in particular, with the aid of the acoustic emission, led to a conclusion that small serrations are also caused by the DSA and have the same nature as the deep stress drops. This interpretation agrees with the DIC observations in the present work. Indeed, brief occurrence of static deformation bands is observed both at the instants of small serrations at the beginning of the test (Fig. 3.12) and during deep stress drop beyond  $\epsilon_{cr}$  (Fig. 3.13b).

Importantly, unusual strain localization patterns were found to accompany static deformation bands in the CG A2 alloy at low strain rate. In binary alloys, smooth deformation before  $\epsilon_{cr}$  and during reloading between stress serrations is known to be related to a largely uniform plastic flow. On the contrary, weak propagating bands were observed in the A2 alloy during these intervals (Figs. 3.12 and 3.13).

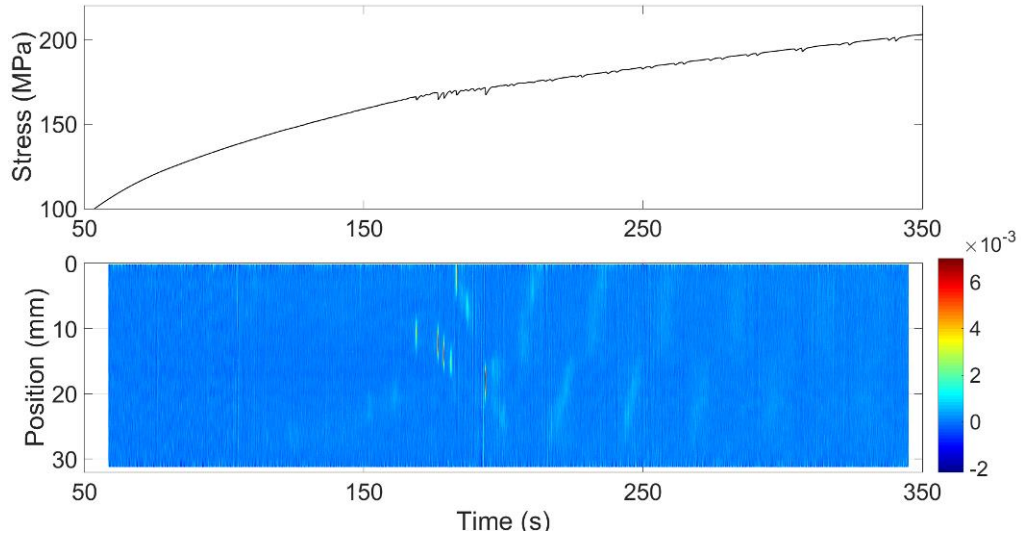


Figure 3.12: Initial portion of a deformation curve of the CG A2 alloy recorded at  $1.43 \times 10^{-4} \text{ s}^{-1}$  and the corresponding strain rate map showing the nucleation and propagation of deformation bands.

The properties of these bands are similar to type *A* bands. The corresponding  $\kappa$ -ratio fluctuates about 7 while it is expectedly higher for static *C* type bands ( $\kappa \sim 140$  in Fig. 3.13). Figure 3.14 plots estimates of  $V_b$  in a similar stress interval for the two high  $\dot{\epsilon}_a$ -values corresponding to type *A* bands and the low  $\dot{\epsilon}_a$  (see Fig. 3.13). Even if a quantitative conclusion on the  $V_b(\dot{\epsilon}_a)$ -dependence will require more experiments, it can be seen that the data points conform to a power law close to linear dependence,  $V_b \propto \dot{\epsilon}_a^\mu$  ( $\mu \approx 0.94$ ), in agreement with the literature data for quasi-continuous and hopping propagation of type *A* and type *B* bands [Ait-Amokhtar et al., 2006; Klose et al., 2004]. It can thus be suggested

that the dynamics of the mobile deformation bands is governed by the same general mechanism at all strain rates.

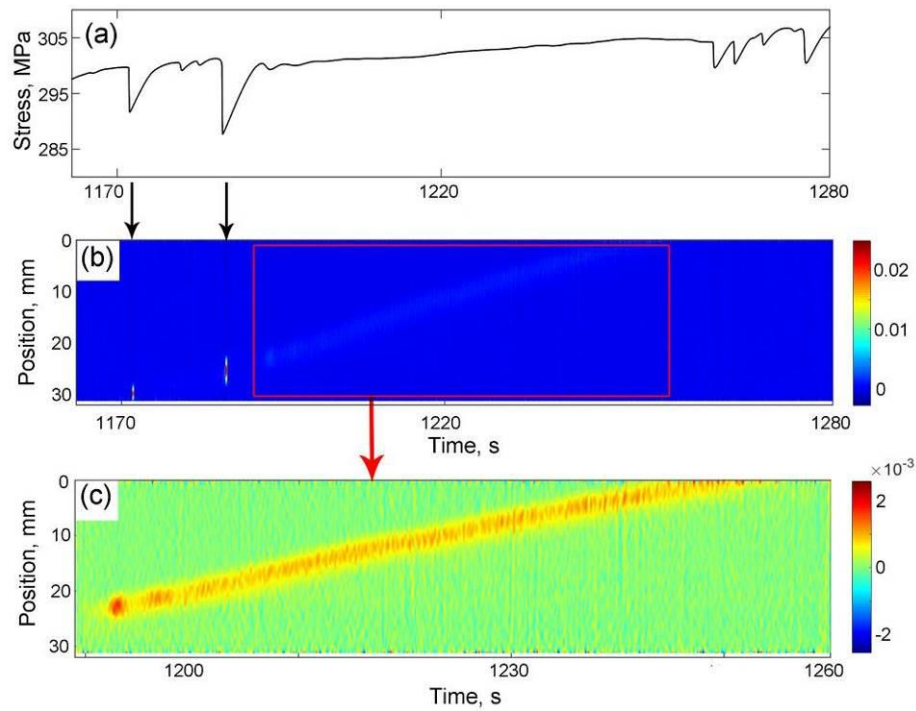


Figure 3.13: (a) Stress-time curve, (b) strain-rate map, and (c) its detail showing propagation of a deformation band for a CG A2 sample tested at  $1.43 \times 10^{-4} \text{ s}^{-1}$ .  $V_b \approx 0.4 \text{ mm/s}$ .

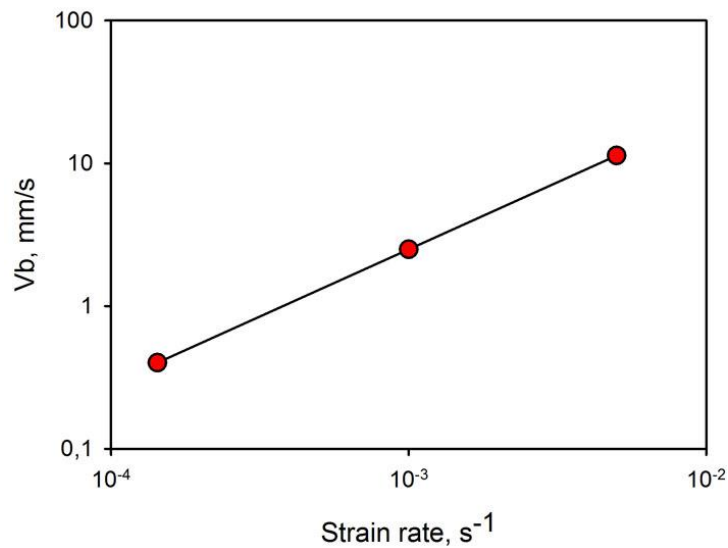


Figure 3.14: Dependences of the deformation band velocity on the imposed strain rate for  $\sigma_{\text{true}}$  around 330 MPa.

These results testify to strongly modified low strain-rate behavior of the PLC instability in the alloy containing precipitates, which manifests a mixture of type C and type

A features. As will be shown further, such unusual band propagation is a common feature of alloys with the microstructure strengthened by the precipitation and/or grain refinement. Its investigation will be one of the main goals in the further sections.

### 3.1.5. Lüders bands

The DIC method also allowed for getting detailed information on the onset of plastic flow in both alloys. As mentioned above, all deformation curves presented a yield plateau (Fig.3.1). This plateau is usually ascribed to the propagation of a Lüders band caused by a progressive unpinning of mobile dislocations from solute atmospheres in the statically aged material [Hallai and Kyriakides, 2013; Nogueira et al., 2011]. Although the investigation of the Lüders instability goes beyond the scope of the present thesis, some observations are noteworthy as they help to understand general features of strain localization and propagation in the studied alloys, common to both the Lüders and the PLC effects.

Figure 3.15 presents magnification of the initial portions of deformation curves of both alloys at high strain rate corresponding to the propagation of PLC bands. The corresponding examples for the low strain rates and static PLC bands were displayed in Fig. 3.11a and Fig. 3.12, respectively, for the A1 and A2 alloys. The concomitant spatiotemporal maps show that at high strain rates, the Lüders plateau is caused by the propagation of one or several successive deformation bands. The  $\dot{\epsilon}_{loc}$  within these bands is higher (see the first  $\dot{\epsilon}_{loc} / \dot{\epsilon}_a$  peak corresponding to the yield plateau in Fig. 6) and  $V_b$  is lower than the respective values for the subsequent PLC bands. At low strain rates, the yield plateau occurs to be accompanied with stress serrations which correspond to a series of relayed static deformation bands instead of a propagating band. Although the Lüders effect is usually thought of as a continuously propagating instability, such a discontinuous propagation was also observed by several authors [Shashkov et al., 2012, Nogueira et al., 2011]. These patterns confirm that there is no critical strain for the onset of the PLC effect in the studied alloys (cf. [Nogueira et al., 2011]).

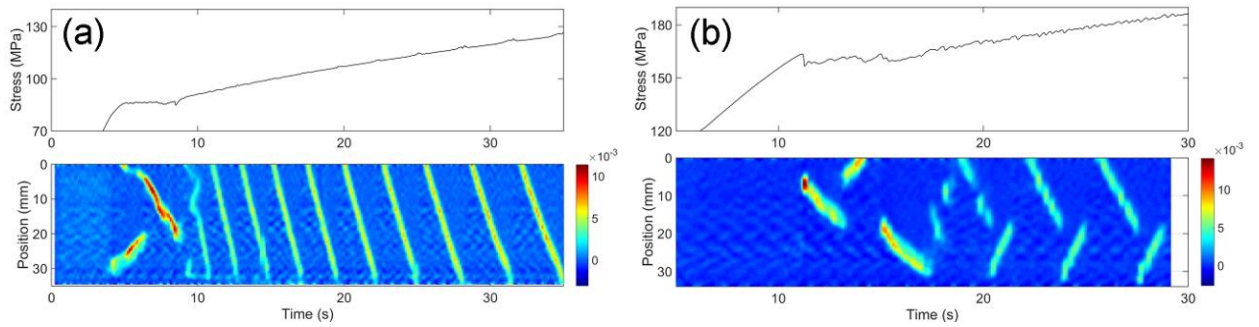


Figure 3.15: Propagation of deformation bands during the yield plateau in the CG (a) A1 and (b) A2 alloys tested at  $10^{-3} \text{ s}^{-1}$ .

Figure 3.16 presents successive DIC images taken during the onset of the yield plateau in both CG alloys. The comparison of these patterns, in particular, allows to understand the origin of the yield tooth which is frequently observed but does not show up in all materials [Hallai and Kyriakides, 2013; Nogueira et al., 2011]. As can be seen in the case of A1 alloy, the Lüders band nucleation occurs progressively at a relatively low stress level (Fig. 3.16a). Indeed, the first four frames show the process of band formation accompanied with a gradual increase in  $\dot{\epsilon}_{loc}$  within the band. The occurrence of a clear deformation band (frame at 3.62 s in Fig. 3.16a) corresponds to the onset of the stress plateau. On the contrary, the Lüders band appears abruptly in the A2 alloy and corresponds to a load drop, or a yield tooth (first two frames in the Fig. 3.16b). It can be suggested that the yield point and the abrupt formation of a Lüders band in the A2 alloy are due to a stronger resistance to the plastic yield because of the pinning of dislocations by the precipitates, in addition to the pinning of aged dislocations by the solute clouds. This suggestion is consistent with an almost twice higher yield stress in the A2 alloy than in the A1 alloy.

It is also noteworthy in this context that the area of localized deformation is oriented normal to the sample axis in Fig. 3.16a. Such orientation of the Lüders band was observed for all CG A1 samples. As can be seen in Figs. 3.4, 3.9 and in similar examples in the following sections, this band shape is indicative of a competition between two conjugate bands oriented symmetrically. In contrast, the Lüders band observed in the A2 alloy (Fig. 3.16b) represents a well-delineated shear band.

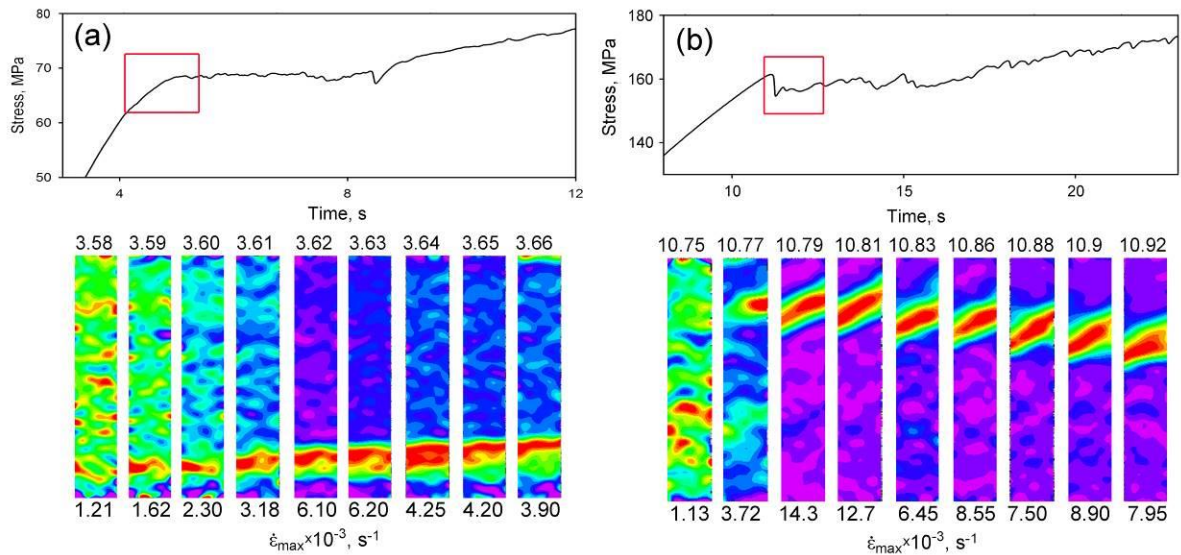


Figure 3.16: Onset of the yield plateau for the CG (a) A1 alloy and (b) A2 alloy at  $10^{-3}$  s $^{-1}$  and corresponding series of DIC images, taken within the interval indicated by the rectangle. Numbers above the images specify the corresponding time instants.

### 3.1.6. Concluding remarks

The overall tensile behavior and the features of the PLC effect in the CG state of both studied alloys correspond to the common notions described in Chap. 1. Namely, transitions between conventional types of stress serrations patterns and PLC band kinematics are found when the applied strain rate is increased. These observations justify the investigation into the effect of severe plastic deformation of the PLC instability in AlMg alloys, presented in the next sections. It is noteworthy that the transitions observed for the precipitation-strengthened alloy were shifted towards higher  $\dot{\epsilon}_a$  values in comparison with the binary alloy. Also, at all strain rates, deformation curves exhibited jerky flow upon the elastoplastic transition, so that no critical strain was required for the onset of the PLC effect in either alloy.

At the same time, the application of the DIC technique allowed to obtain new information on the kinematics of the deformation bands and revealed some unknown features of the PLC effect. The following observations should be recalled:

- The time-resolved mapping of static type *B* deformation bands showed that both the formation and the termination of the band take place progressively, through the phase of weak strain localization in a diffuse deformation band. Importantly, this band covers the entire cross-section of the specimen (Fig. 3.10). Therewith, the abrupt stress drop corresponds to the well-delineated PLC band characterized by a much higher intensity of strain-rate localization than that detected in the diffuse band.

- Similar observations during the Lüders band formation allowed to distinguish between an abrupt band nucleation leading to a yield tooth and a smoother band formation associated with smooth yielding.

- The general trend in the evolution of the propagation velocity of deformation bands during the test agrees with the literature data, i.e.,  $V_b$  decreases with strain hardening. For the investigated alloys, it can be described by a power-law dependence on the true stress, with a cutoff close to the maximum load, where the bands become progressively immobilized. Although the exponents differ for different alloys, the estimates of the power-law exponent render close values for different strain rates for the same alloy.

Finally, the most essential result in the context of this work is the observation of a persistent propagation of deformation bands over the entire strain-rate range in the case of precipitation-strengthened alloy. This behavior is related to an unusual mixture of type  $C+A$  patterns found at the lowest strain rate. It has not been observed nor predicted for the PLC effect so far and opens new prospective for a better understanding of plastic instability in complex alloys. It can be suggested that the mechanism of strain propagation in this alloy is due to over stresses originating from the precipitates. This hypothesis will be verified in the further sections.

## **3.2. Effect of severe plastic deformation**

### *3.2.1. FG state*

Figure 3.17 presents examples of deformation curves of A1 and A2 alloys subjected to ECAP. It can be seen that the formation of a fine-grained microstructure produces similar qualitative changes in mechanical behavior of both alloys. The ECAP enhances the yield stress and UTS as compared with CG state. Concurrently, the work-hardening rate and ductility are reduced. At the same time, although the qualitative trends are the same, the quantitative changes are considerably stronger in the binary alloy that is softer in CG conditions (cf. Fig. 3.1). Particularly, its yield stress becomes increased more than three times (the factor is close to two for A2 alloy). Furthermore, in contrast to CG state, both alloys have a similar ductility after ECAP. Overall, the mechanical characteristics of two alloys become more similar.

As far as the PLC effect is concerned, deformation curves of FG alloys exhibit stress serrations in the entire range of strain rates, like their CG counterparts. Accordingly, the FG alloys also display a negative SRS, although this conclusion can only be made on the overall because the scatter between samples is considerably enhanced after ECAP (e.g., curves

corresponding to the strain rates of  $10^{-3} \text{ s}^{-1}$  and  $5 \times 10^{-3} \text{ s}^{-1}$  in Fig. 3.17a display a seemingly inversed order).

Importantly, the stress serrations patterns change significantly and show a strong tendency to deep stress serrations with type *C* and type *B* features [cf. Mogucheva et al. 2016; Eddahbi et al., 2012], so that not only mechanical characteristics of two alloys but also their serration behavior become more similar after grain refinement. In both alloys, stress serrations start immediately after the onset of plastic flow. The deformation curves of A2 alloy exhibit a yield plateau, though, which is superimposed with serrations, but the yield plateau is fully suppressed in the A1 alloy. Type *A* or type *D* patterns can still be recognized at early stages of deformation at  $\dot{\epsilon}_a \geq 10^{-3} \text{ s}^{-1}$  in the FG A1 alloy (e.g., curve at  $5 \times 10^{-3} \text{ s}^{-1}$  in Fig. 3.17a) and  $1.4 \times 10^{-2} \text{ s}^{-1}$  in the FG A2 alloy (e.g.,  $1.43 \times 10^{-2} \text{ s}^{-1}$  in Fig. 3.17b). In any case, type *B* serrations are also present from the very beginning of plastic deformation and become prevailing at large strains.

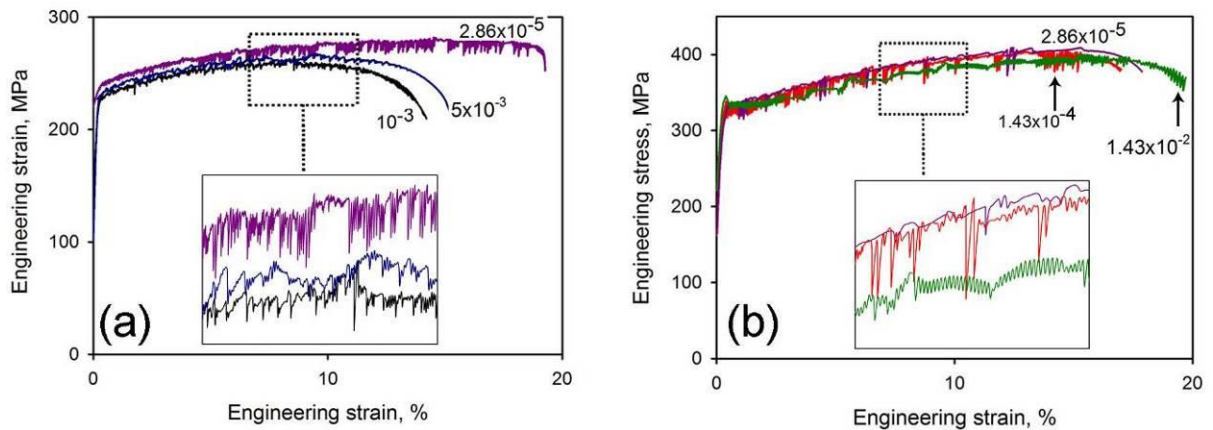


Figure 3.17: Example of deformation curves of (a) A1 and (b) A2 alloys in FG state for various strain-rates. The strain-rate values are given in  $\text{s}^{-1}$ .

Figure 3.18 displays an example of type *A* PLC band behavior observed at small strains in the FG state of the A1 alloy deformed at  $\dot{\epsilon}_a = 10^{-3} \text{ s}^{-1}$ . Similar maps are recognized in the maps obtained for A2 material at  $\dot{\epsilon}_a \geq 5 \times 10^{-3} \text{ s}^{-1}$ . In comparison with the typical type *A* map for CG state (§ 3.1.2), it can be seen that the spatial correlation of the bands is strongly reduced. The tendency to continuous propagation at the beginning of deformation alternates with the uncorrelated nucleation of bands. As expected for type *A* bands, the  $\kappa$ -ratio is relatively low and does not exceed 15-20. At large strains, type *A* patterns are replaced by type *B* ones, characterized by hopping, or relay-race, band propagation. Finally, Fig. 3.18

also demonstrates that like in CG samples, the onset of necking occurs through immobilization of deformation bands and is related to a repeated localization of plastic deformation in the same cross-section of the specimen.

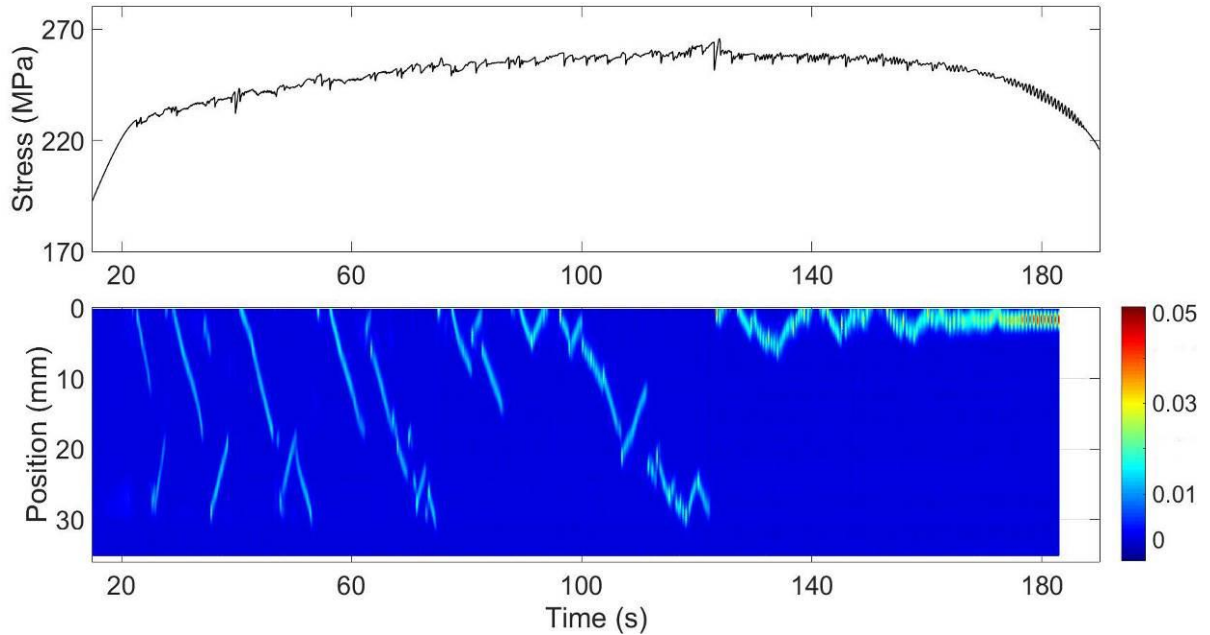


Figure 3.18: Example of a stress-time curve displaying type *A* serrations in the FG A1 alloy at  $10^{-3} \text{ s}^{-1}$  and the corresponding local strain-rate map showing the propagation of deformation bands. The color bar represents the local strain-rate scale in  $\text{s}^{-1}$ .

Figure 3.19 illustrates regular serrations accompanied by typical series of type *B* deformation bands for an FG A2 sample deformed at  $10^{-3} \text{ s}^{-1}$ . The spatiotemporal characteristics of such bands are similar to those described in the CG case (Sec. 3.1). Each series of stress serrations, separated by intervals of low-amplitude fluctuations terminating by a relatively deep stress drop, display a one-to-one correspondence with the series of deformation bands. For this sample, the early deformation stage is associated with the relay-race propagation of PLC bands along approximately a half of the specimen length. The propagation distance increases at later stages. Also, as was mentioned for CG state, the deformation band orientation may swap both between the series of stress serrations and within one series.

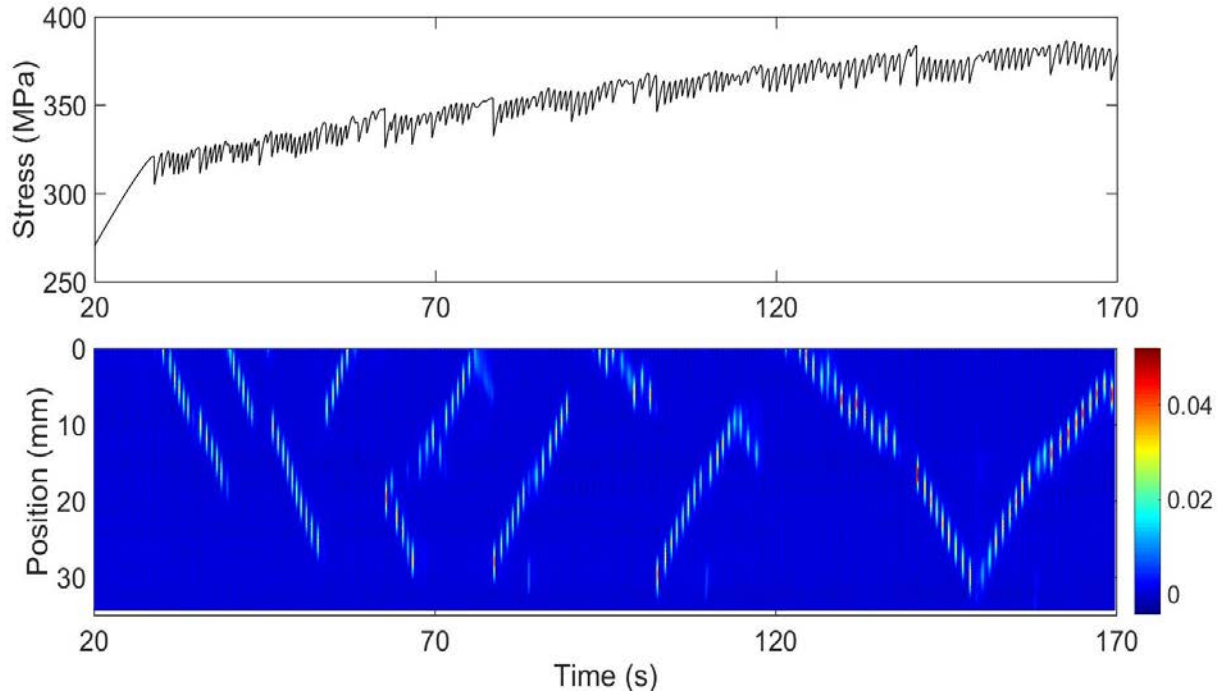


Figure 3.19: Example of a stress-time curve displaying type *B* serrations in the FG A2 alloy at  $10^{-3} \text{ s}^{-1}$  and the corresponding local strain-rate map showing the propagation of deformation bands. The color bar represents the local strain-rate scale in  $\text{s}^{-1}$ .

The evolution of  $V_b$  during the test is qualitatively similar to that described in § 3.1.2. Namely,  $V_b$  decreases with strain hardening (Fig. 3.20). The quantitative analysis is in this case less certain because of a higher data scatter, but also because of smaller ranges of stress variation between the yield point and the UTS. Although a thorough quantitative analysis will require more experiments, the data obtained in the present work allow for some observations. First, despite the scatter,  $V_b(\sigma_{\text{true}})$ -dependences can also be described by power-law functions. Like in the CG case, these functions are different for two alloys, but the curves obtained for the same alloy at different strain rates have similar slopes. The latter corroborates the hypothesis of the existence of a nominal dependence for the given material. At the same time, while the grain refinement did not noticeably change the power-law exponent for the precipitate-strengthened A2 alloy ( $m \approx 2.55 \pm 0.33$  for the data presented in Fig. 3.20), it strongly increased  $m$  in the case of the A1 alloy ( $m \approx 4.93 \pm 0.63$ ) that is much softer in the initial CG state. Moreover, the corresponding  $m$ -value for the FG A1 material is higher than that for A2 alloy in both conditions (FG and CG), so that the relationship between  $m$ -values of two alloys is inverted regarding the CG state.

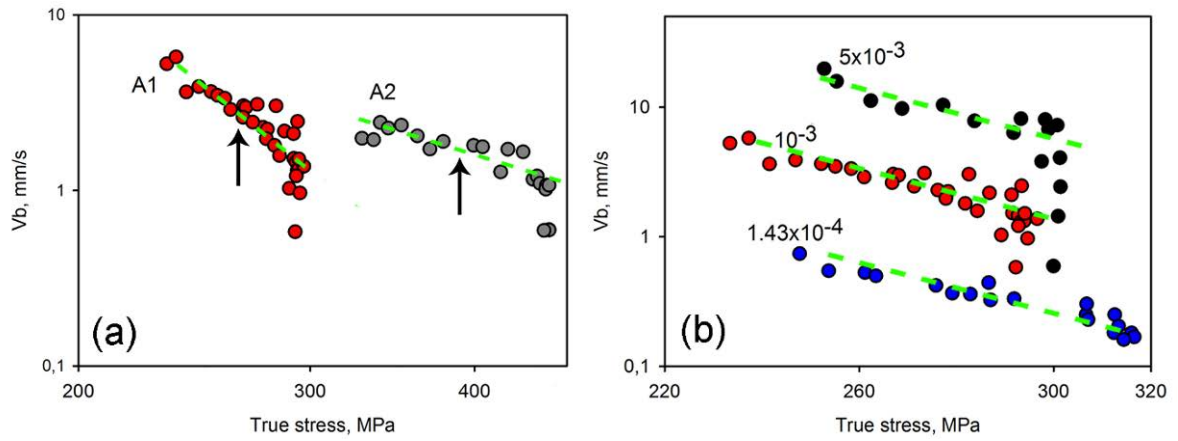


Figure 3.20: Dependence of the band velocity,  $V_b$ , on the true stress. (a) Data for FG A1 and A2 samples tested at  $10^{-3} \text{ s}^{-1}$ ; (b) For several FG A1 samples deformed at different strain rates ( $\text{s}^{-1}$ ).

The further decrease in  $\dot{\epsilon}_a$  leads to degrading correlations within the series of type *B* deformation bands and gives rise to a tendency to type *C* behavior. For example, Figure 3.21 illustrates such a trend for an A2 sample deformed at  $1.43 \times 10^{-4} \text{ s}^{-1}$ . It is seen that even if the proper type *B* behavior is observed at small strains (Fig. 3.21a), the transition to type *C* progressively takes place later (Fig. 3.21b).

Several specific observations should be remarked. First, the unusual propagation regime alternating with type *C* deformation bands at low strain rates (cf. Fig. 3.13) was found in FG state of both A1 and A2 alloys. It was much less pronounced in the former case, though, in agreement with the absence of such mode in the CG A1 samples. Such mobile bands were tracked at both  $1.4 \times 10^{-4} \text{ s}^{-1}$  (Fig. 3.21c) and  $2.9 \times 10^{-5} \text{ s}^{-1}$  (Fig. 3.22) in the A2 alloy, and for the lowest  $\dot{\epsilon}_a$  in the A1 alloy. Since grain boundaries can also serve as sites of stress concentration, this observation is consistent with the above hypothesis on the role of over stresses in the mechanism promoting propagation at slow deformation.

On the other hand, some of the propagation patterns in FG conditions indicate a competition with the opposite trend to static strain localization consistent with the overall type *C* character of stress serrations. Fig. 3.21c illustrates this feature for the FG A2 sample. Indeed, the relatively smooth portions between type *C* serrations display low-amplitude stress oscillations matching a beat in the band propagation pattern. From the quantitative viewpoint, the beat means that  $\dot{\epsilon}_{loc}$  never drops to the level of  $\dot{\epsilon}_a$ , contrarily to the case of localized deformation bands, nor sustains a constant level above  $\dot{\epsilon}_a$ , as it would be in the case of quasi-continuous propagation, but fluctuates between two values above  $\dot{\epsilon}_a$ . As will be described in Chap. 4, a similar beat was also observed during necking in some high strain-rate tests.

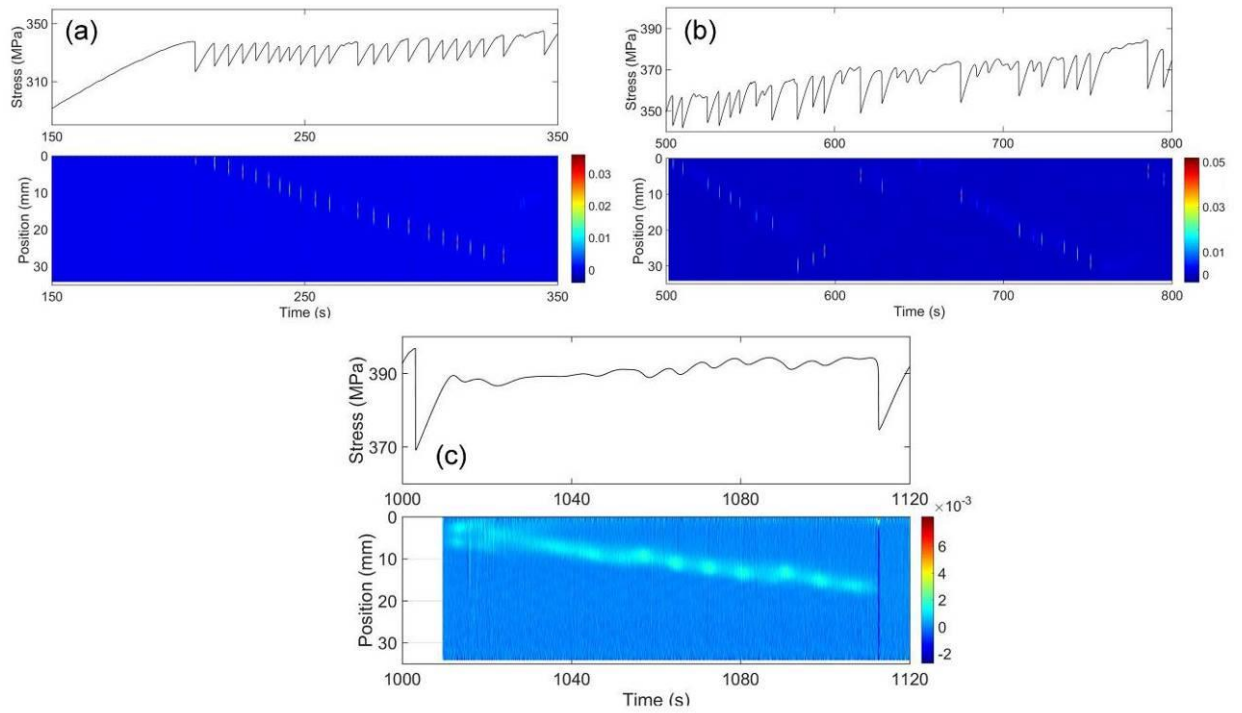


Figure 3.21: Portions of a stress-time curve of a FG A2 sample deformed at  $1.43 \times 10^{-4} \text{ s}^{-1}$  and the corresponding local strain-rate maps.  
 (a) Type *B* behavior on an early deformation stage;  
 (b) Transition to type *C* behavior after some strain;  
 (c) Magnification of the relatively smooth interval between two type *C* drops.  $V_b \approx 0.2 \text{ mm/s}$ .

Figure 3.22 illustrates a proper propagation mode without beat for the same alloy. Chart 3.22b uncovers two bands occurring upon reloading after a type *C* serration (Chart 3.22a) and moving in the opposite directions. The local strain rate within the propagating bands is several times higher than  $\dot{\epsilon}_a$ , i.e., corresponds to  $\kappa$ -values typical of type *A* bands, while  $\kappa$  reaches about 1400 in the static band related to the stress drop. Figure 3.23 presents  $V_b(\dot{\epsilon}_a)$ -dependences similar to Fig. 3.14 for the CG A2 alloy, which corroborate the conjecture of the same dynamical mechanism governing the dynamics of mobile deformation bands at various strain rates.

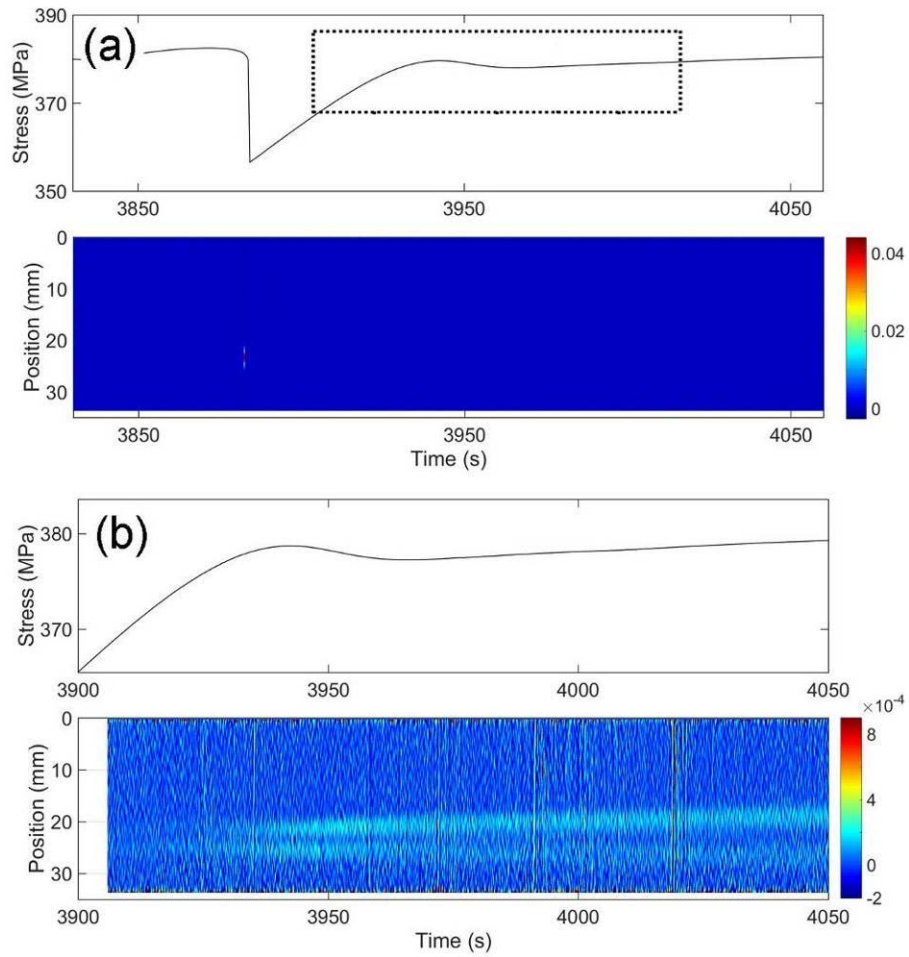


Figure 3.22: (a) Portion of a stress-time curve with a type C stress drop in the FG A2 alloy at  $2.86 \times 10^{-5} \text{ s}^{-1}$ . (b) Magnification within the rectangle in Chart (a).  $V_b \approx 0.023 \text{ mm/s}$ .

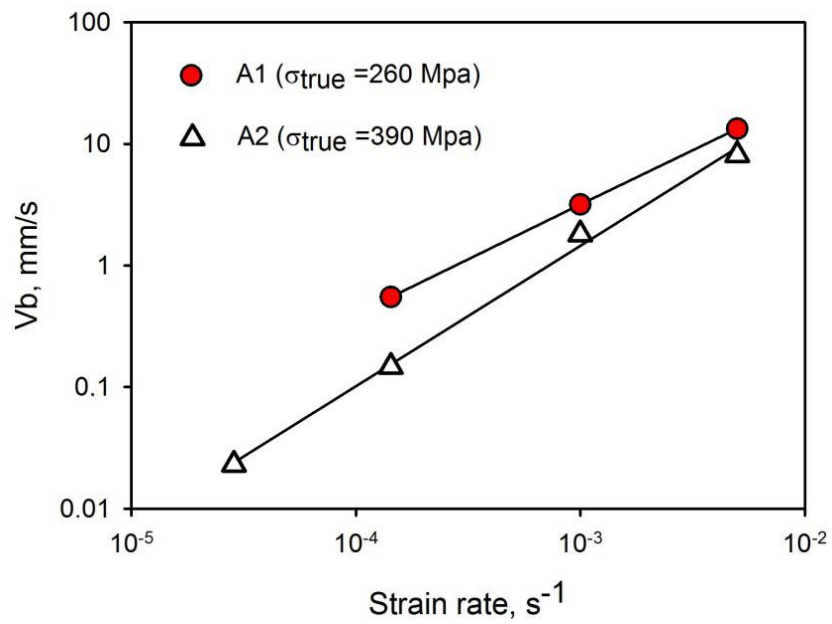


Figure 3.23:  $V_b(\dot{\epsilon}_a)$ -dependences for the A1 and A2 alloys in FG conditions. The estimates of the slope of the dependences render  $\mu \approx 0.89$  (A1) and 1.16 (A2).

### 3.2.2. FGH state

The additional cold rolling induced further changes in the average mechanical properties, which followed the same course as after ECAP. The FGH samples displayed the highest strength and the lowest values of work hardening and ductility (Fig. 3.24). Although the data scatter prevented from a quantitative comparison of the ductility, a qualitative trend to a lower ultimate elongation can be noticed for the A1 alloy. Furthermore, such extreme treatment effectively suppresses serrated behavior [cf. Lebedkina et al., 2014], in agreement with the vanishing SRS. Only sporadic serrations were observed before the onset of necking (e.g., Fig. 3.24b, curve for an A2 sample deformed at  $1.43 \times 10^{-4} \text{ s}^{-1}$ ). On the other hand, a transition to oscillatory behavior was detected during necking at medium and low strain rates, especially, in the A1 alloy. This transition is unusual regarding most of the literature data (see Chap. 1) testifying that the instability does not change qualitatively upon the onset of necking but retains a certain continuity with the previously developed type of behavior. For example, the data of Figs. 3.1 and 3.17 attest indeed such continuity. In contrast, data of Fig. 3.24a illustrate strong oscillations arising upon the onset of necking in A1 samples deformed at  $\leq 10^{-3} \text{ s}^{-1}$ . Weaker oscillations can also be discerned in the necking region of curves recorded at  $1.43 \times 10^{-4} \text{ s}^{-1}$  and  $10^{-3} \text{ s}^{-1}$  for A2 samples (Fig. 3.24b).

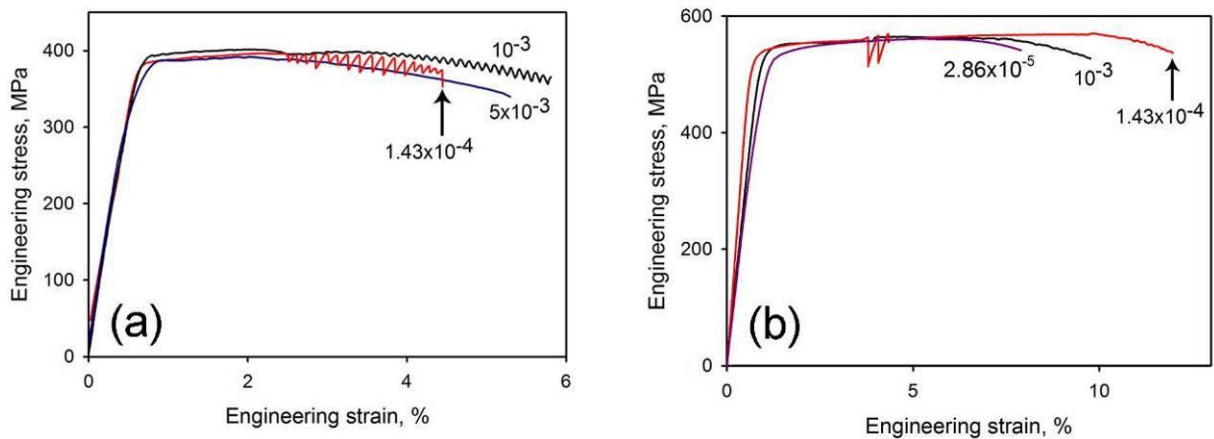


Figure 3.24: Examples of deformation curves of (a) A1 and (b) A2 alloys in FGH state for various strain rates ( $\text{s}^{-1}$ ).

Although the deformation curves of FGH materials are quite smooth in the work-hardening region, the DIC analysis shows that the smoothness is not due to a uniform plastic flow but to the propagation nature of the PLC instability at all strain rates. Unexpected regarding the known behaviors of the PLC effect, this result conforms to the above-described trends caused by the microstructure strengthening. The A2 alloy demonstrates virtually the

same behavior at all values, illustrated in Fig. 3.25 for the reference strain rate. The elastoplastic transition is associated with the nucleation of a PLC band that propagates along either a large portion or the entire gage length and is “reflected” in the opposite direction. The change in the propagation direction involves a stress rise which corresponds to the maximum load. The further propagation demonstrates the same scenario of approaching the final strain localization in the neck as the examples of type *A* bands presented above for CG and FG conditions. Despite the already decreasing applied stress, the band continues shifting over a long distance and is finally damped to give rise to the ultimate necking.

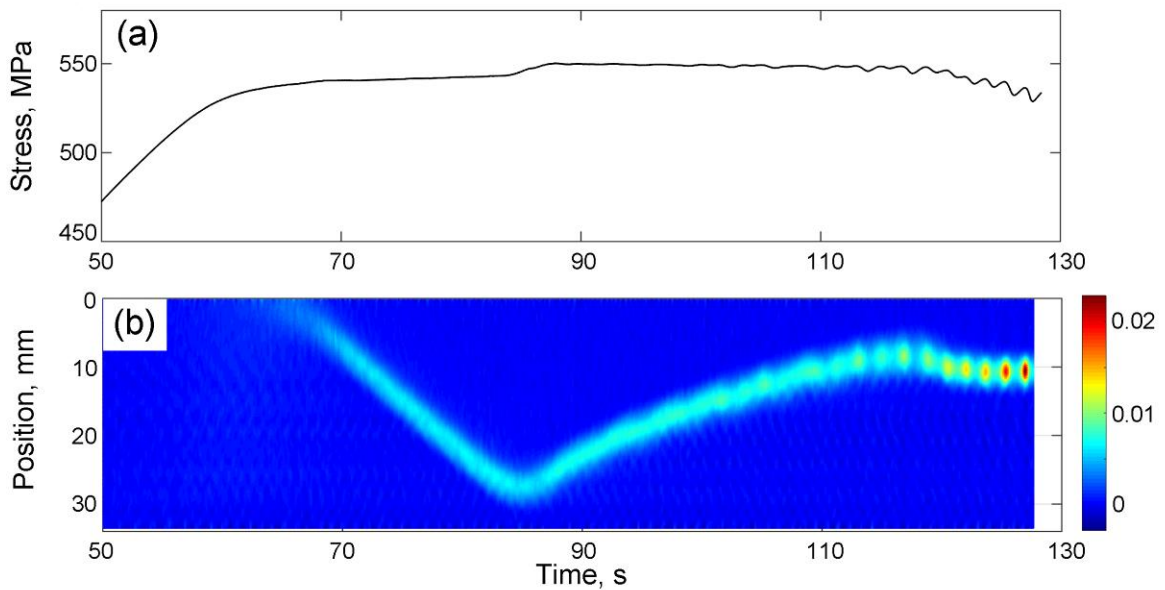


Figure 3.25: (a) Stress-time curve and (b) strain-rate map showing propagation of a deformation band for a FGH A2 sample tested at  $1 \times 10^{-3} \text{ s}^{-1}$ .

The FGH A1 alloy showed qualitatively similar behavior. However, a detailed comparison of data for all strain rates suggests a stronger tendency to the propagation mode in the FGH A2 material. Indeed, at the high strain rate, the PLC band propagation in the A1 alloy was usually bounded by a shorter length, from one fourth to half the gage length, and was less regular, in the sense that slow fluctuations in the band width and velocity led to a less monotonous (than in A2 samples) work-hardening stage of the deformation curve (Fig. 3.24a). Additional arguments for this comparison will be provided in Chap. 4 relative to the question of neck formation. It is worth noting here that the observation of large oscillations during neck development at medium and low strain rates (Fig. 3.24a) is related to a stronger trend to the occurrence of a series of distinct deformation bands instead of a beat.

### 3.2.3. Concluding remarks

In summary, Sect. 3.2 presents data of investigation of the influence of severe plastic deformation on the PLC effect in A1 and A2 alloys. Several conclusions can be drawn from the data obtained in FG and FGH conditions:

- On the overall, the material strengthening by ECAP, resulting in a substantial grain refinement and an increase in the dislocation density (see § 2.1.4), leads to a firm tendency to type *B* and type *C* serration patterns. These patterns are usually associated with localized deformation bands (to avoid any confusion, it should be reminded that type *B* represents immobile bands occurring in an ordered manner described as hopping propagation). Type *A* behavior, related to quasi-continuous propagating mode at high strain rates, is considerably suppressed. Nevertheless, the DIC analysis shows that the unusual propagation at low strain rates, which, in the CG state, is only detected for the particle-strengthened alloy, occurs in both materials after ECAP. Concerning serration patterns, this mode is associated with a mixture of types *C* and *A* (long intervals of relatively smooth deformation between deep serrations) ending by a transition from type *C* to type *A* patterns after some strain. As both precipitates and grain boundaries are effective obstacles to the dislocation motion, these observations corroborate the hypothesis that the unusual propagation is caused by the concentration of internal stresses. It is noteworthy that the deformation curves of both materials become very similar after ECAP, even if the transitions between types remain somewhat shifted in terms of the imposed strain rate. It can thus be suggested that grain boundaries play a more significant role in the dynamics of the PLC instabilities than the precipitates.

- Another unexpected feature found after ECAP is the beat in the band propagation at low strain rates. As unusual as it would seem, it is however consistent with the generally accepted role of the imposed strain rate, i.e., a tendency to static strain localization at slow loading. Apparently, such a beat reveals a competition between two opposite trends, the one to the band propagation and the other to the strain localization.

- The quantitative analysis of the velocity of deformation band propagation confirms the conclusions made for CG materials. Despite a higher data scatter, the  $V_b$  diminution during deformation can be described by a power-law dependence vs true stress with a cutoff beyond the UTS. The corresponding exponents  $m$  differ for different alloys but are close for the same alloy deformed at different strain rates. Interestingly, the ECAP did not change  $m_{A2}$  within the experimental error, whereas  $m_{A1}$  was increased three times, so that the initial relationship between these values,  $m_{A1} < m_{A2}$ , changed sign after ECAP. The change in  $m_{A1}$

also testifies to an important role of grain boundaries in the dynamics of the PLC instabilities. At same time, the fact that ECAP drastically changes serration patterns in both alloys but does not affect  $m_{A2}$ , means that the synergistic effect of both precipitates and grain boundaries is complex and would require quantitative modelling.

- Finally, the additional cold rolling, resulting in extremely high dislocation densities without additional reduction in the grain size, leads to an efficient suppression of stress serrations during the work hardening stage (before the onset of necking). Deformation curves become virtually smooth and globally similar at all strain rates. Nevertheless, the DIC analysis testifies that such smooth curves are not due to uniform straining of the tensile specimen, as it would be natural to suggest, but are associated with the propagation of one or two PLC bands. Therewith, the FGH A2 samples manifest a somewhat stronger tendency to the propagation mode. At the same time, they also display a higher ductility than the A1 samples. As the A2 material shows a stronger tendency to the band propagation and a less significant reduction of ductility after both kinds of SPD processing, these results put on a question on a possible relationship between the capacity of a strain localization to propagate and the effective ductility (see Discussion in Chap. 4).

### **3.3. Comparison with alloys containing fine precipitates**

In the previous parts of the present Chapter, unusual modes of propagation of the PLC bands were found in AlMg alloys strengthened by grain refinement and/or coarse (25-30 nm) incoherent  $Al_6(Mn,Fe)$  precipitates. It was supposed that the proneness to the deformation band propagation stems from overstresses caused by the grain boundaries and precipitates acting as obstacles to the dislocation motion. At the same time, it is known that the interaction of dislocations with precipitates depends on the particle size. Whereas coarse precipitates are bypassed by the mobile dislocations via Orowan bowing mechanism, small precipitates with size below 10-15 nm can be sheared by dislocations [Fazeli et al., 2008]. It can be suggested that their contribution to overstresses may be different. The objective of the last part was a comparative analysis of the PLC effect in the Al-Mg alloys with different kinds of precipitates. A detailed comparison in a wide strain-rate range in CG and FG conditions was realized using the A3 alloy with small (~10 nm) coherent  $Al_3(Sc,Zr)$  particles. Additional control tests were performed on the A4 alloy containing both kinds of particles. Moreover, since the A4 alloy had the initial grain structure distinctly different from other studied materials, but this difference disappeared after ECAP, these tests provided an additional piece of information on the grain-size effect.

### 3.3.1. CG state

For the reader's convenience, the pertinent microstructural parameters of all alloys are reproduced in Table 3.1. For more details, see § 2.1.4.

Table 3.1. Microstructural characteristics of the investigated alloys: grain size,  $d$ , fraction of high-angle boundaries, HABs.

| Alloy | Main Precipitates  | Material condition  |         |                     |         |
|-------|--|---------------------|---------|---------------------|---------|
|       |  | CG state            |         | FG state            |         |
|       |  | $d$ , $\mu\text{m}$ | HABs, % | $d$ , $\mu\text{m}$ | HABs, % |
| A2    | Incoherent $\text{Al}_6(\text{Mn,Fe})$ ,<br>25-30 nm in size   | 15.4                | 93      | 1                   | 70      |
| A3    | Coherent $\text{Al}_3(\text{Sc,Zr})$ ,<br>10-15 nm in size   | 22                  | 87      | 0.8                 | 84      |
| A4    | Coherent $\text{Al}_3(\text{Sc,Zr})$ , 10-15<br>nm in size + incoherent<br>$\text{Al}_6(\text{Mn,Fe})$ , 30 nm in size | 200/20              | 36      | 1.01/0.88           | 70.4    |

Families of typical deformation curves of A2 to A4 alloys in CG state are presented in Fig. 3.26. To avoid any confusion, it has to be clarified that both DIC and 1D high-frequency extensometry prevented from the simultaneous use of a standard extensometer to measure the total strain. This difficulty was easily overcome in the case of DIC technique that provided imaging of the entire sample during the entire test. In contrast, the high-frequency extensometry had a 10-minutes limitation of the record duration, so that records were only taken within the most interesting time intervals. The latter technique was used in many tests on A3 and A4 alloys. For this reason, contrarily to the Chart A2, where the strain data were taken from the DIC measurements, all curves in Charts A3 and A4 were recalculated from  $\sigma(t)$ -curves. Accordingly, the initial (relatively) linear loading does not correspond to the elastic modulus of the specimen but to the combined sample-machine stiffness. Such measurements overestimate the total strain by several percent. However, this difficulty does not have an impact on the questions raised in the thesis. It is noteworthy that the A2 alloy demonstrates a lower yield stress and a higher work hardening rate, in agreement with the usually observed differences between the effects of coarse and fine precipitates on the material strengthening [Smallman and Bishop, 1999].

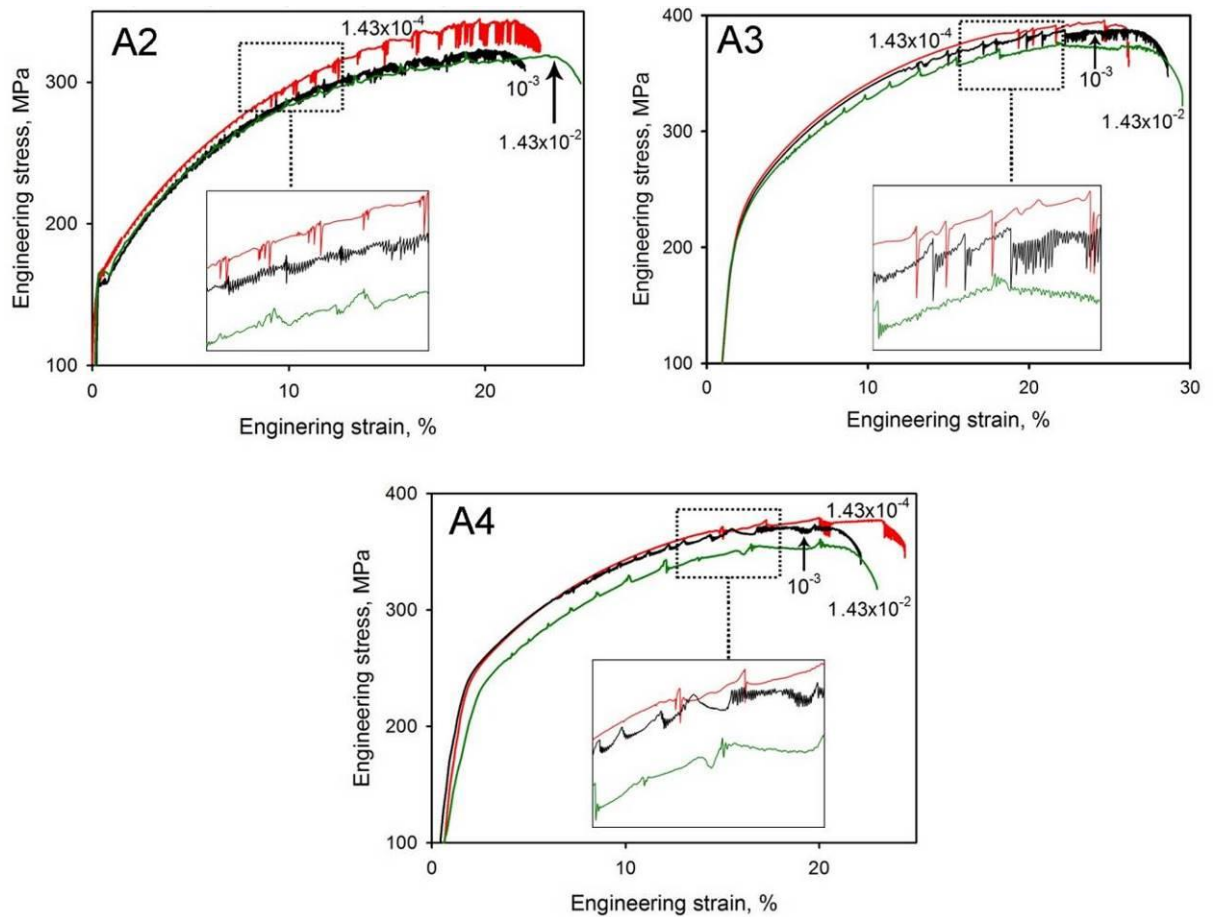


Figure 3.26: Examples of deformation curves for A2 (data of Fig. 3.1b), A3 and A4 alloys in CG state. The values of the imposed strain rate are given in s<sup>-1</sup>.

Figure 3.26 testifies that the type of precipitates has a certain influence on the conditions for plastic instability. In particular, in contrast to A2 material, A3 and A4 alloys display a smooth elastoplastic transition without Lüders plateau and require a critical strain for the onset of the instability. Therewith, in qualitative agreement with this modification,  $\epsilon_{cr}$  is significantly higher in the A3 (only fine precipitates) than in the A4 (mixed case) alloy (Fig. 3.27). Control tests at  $\dot{\epsilon}_a = 3 \times 10^{-5}$  s<sup>-1</sup> showed that the plastic flow of A3 is stable in this limit, which thus lies below the low strain-rate boundary of instability. Figure 3.27 also reveals that for both alloys,  $\epsilon_{cr}$  decreases with increasing  $\dot{\epsilon}_a$  in a large interval, in consistence with the predictions of “inverse” behavior (see Chap. 1) for alloys with shearable precipitates [McCormic, 1972; Brechet and Estrin, 1995; Chihab et al., 2002].

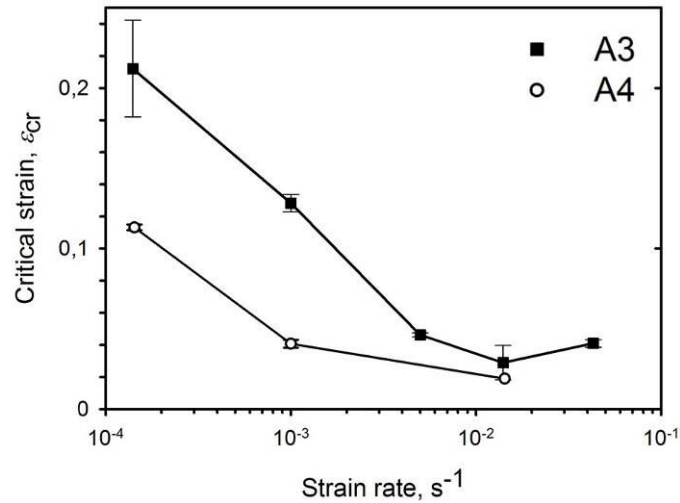


Figure 3.27: Dependences of the critical strain on the imposed strain rate in CG state of A3 and A4 alloys. The standard error bars for  $\epsilon_{cr}$  illustrate the data scatter between tests on different specimens.

The stress serrations patterns are rather similar in Charts A3 and A4, although at first glance, look different from those in Chart A2 (Fig. 3.26). Nevertheless, the closer view testifies to qualitatively similar trends in all cases, except that the A2 alloy displays more pronounced type *B* and type *C* serrations. Indeed, all alloys show repetitive stress humps at  $1.4 \times 10^{-2} \text{ s}^{-1}$ , indicative of type *A* behavior at high strain rates. Type *B* serrations occur when  $\dot{\epsilon}_a$  is decreased to  $10^{-3} \text{ s}^{-1}$ . The main difference with the A2 alloy is that pure type *B* was not found in the A3 and A4 case at the investigated strain rate values. At  $10^{-3} \text{ s}^{-1}$ , e.g., unstable type *A* serrations occur prior to type *B* behavior that is only observed at large strains. The further decrease in  $\dot{\epsilon}_a$  does not lead to a transition to type *B*, but to type *C* patterns. These low strain-rate serrations display long smooth intervals between deep stress drops, which make one suggest the presence of the propagation mode, similar to that found in the A2 alloy. This is indeed the case, as demonstrated hereinafter.

Figure 3.28 displays spatiotemporal maps for the CG A3 alloy. As can be seen in Plot (a), at high strain rate the regular propagation of deformation bands along the sample axis is expectedly dominant during the entire test. At the intermediate strain rate, the tendency to the hopping propagation becomes stronger, in the sense of shorter distances of quasi-continuous propagation (Figs. 3.28b, c). Nevertheless, magnification of these plots did not allow for distinguishing individual type *B* bands (cf. Fig. 3.8), except for the latest stages of deformation, so that type *A* behavior remained a primary mode even at intermediate strain rates. Regular propagation of deformation bands through the entire gage length sets on again at the lowest strain rate (Figs. 3.28d). On the overall, the proneness to the propagation mode

is manifested even stronger than in the CG A2 alloy, for which pure type *B* sequences were found over the entire deformation curve at intermediate strain rates (Fig. 3.8).

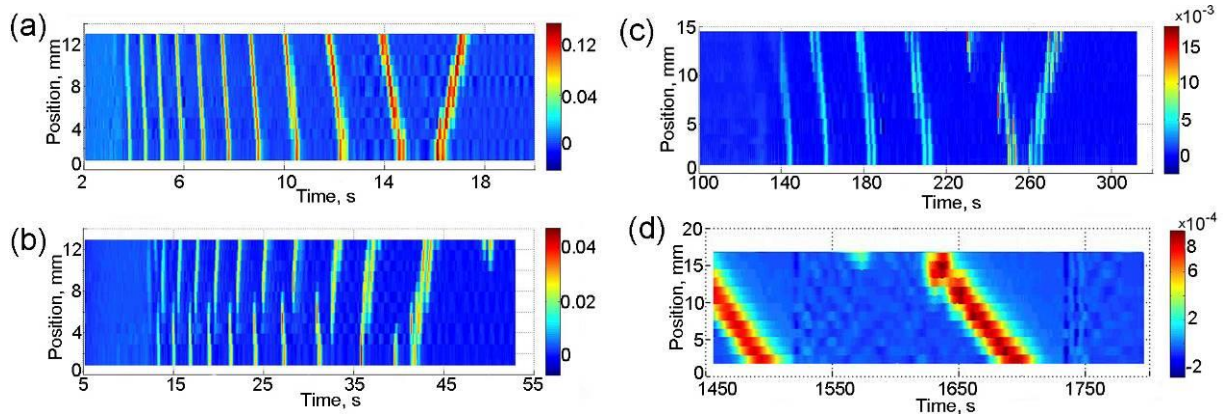


Figure 3.28: Maps showing the time evolution of the local strain rate along the tensile axis for CG A3 samples. (a) -  $\dot{\epsilon}_a = 1.4 \times 10^{-2} \text{ s}^{-1}$ ; (b) -  $\dot{\epsilon}_a = 5 \times 10^{-3} \text{ s}^{-1}$ ; (c) -  $\dot{\epsilon}_a = 10^{-3} \text{ s}^{-1}$ ; (d) -  $\dot{\epsilon}_a = 1.4 \times 10^{-4} \text{ s}^{-1}$ . The color bars quantify the strain-rate scale ( $\text{s}^{-1}$ ).

Figure 3.29 compares deformation bands propagating at the lowest strain rate in all three alloys. The characteristics of the bands are quite similar. The *k*-ratio is close to 7 in all cases. The band velocity is also similar. Obviously, the exact correspondence should not be expected even for the same stress range because the evolution of  $V_b$  during the test means that it depends on the microstructure and can vary between different materials. However, the entirety of data testifies to the same mechanism of band propagation in all studied alloys, although the quantitative properties of the propagating bands may depend on the specific type of precipitates. In particular, Fig. 3.30 presents  $V_b(\dot{\epsilon}_a)$ -dependences for several strain intervals for the CG A3 alloy, consistent with the curves of Figs. 3.14 and 3.23.

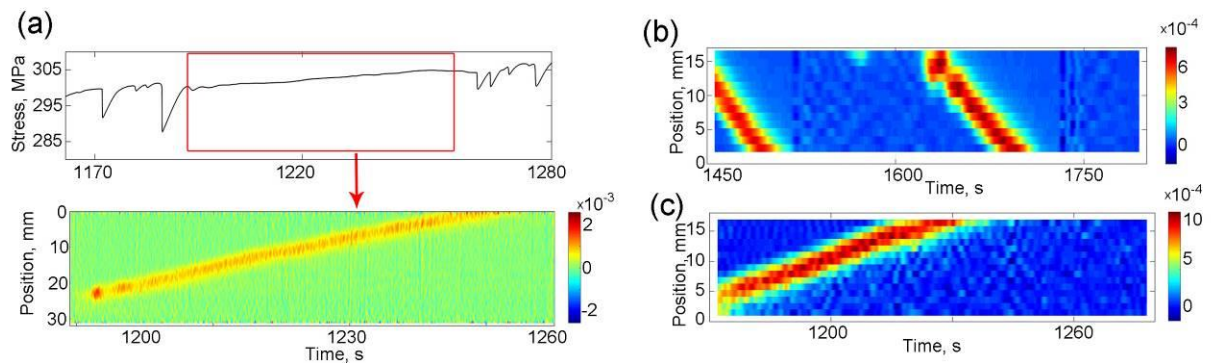


Figure 3.29: Strain rate maps showing moving deformation bands between type *C* stress drops at  $1.43 \times 10^{-4} \text{ s}^{-1}$  for the CG state of three materials. (a) A2 alloy; (b) A3 alloy; (c) A4 alloy.  $V_b$ , mm/s: (a) 0.40 ( $\sigma_{\text{true}}$  in the region of 300 MPa); (b) 0.25 (370 MPa); (c) 0.24 (370 MPa).

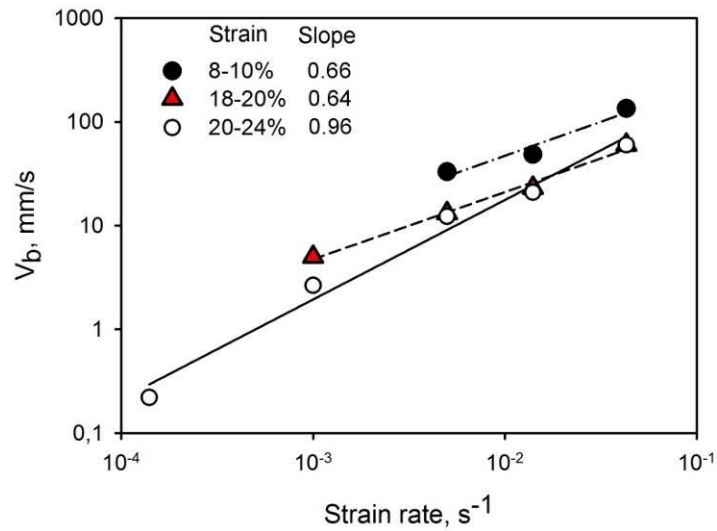


Figure 3.30: Dependences of the band velocity on the imposed strain rate for the A3 alloy.

### 3.3.2 FG state

In all investigated alloy, ECAP resulted in the formation of a fully recrystallized structure of equiaxed grains  $\sim 1 \mu\text{m}$  in size (see Table 3.1). Figure 3.31 illustrates that both the overall deformation behavior and serration patterns become similar after such treatment (see also §3.2.1, Fig. 3.17), thus indicating the preponderant role of grain boundaries in the plasticity of FG alloys. In particular, all FG samples demonstrate discontinuous yielding [Schwab and Ruff, 2013; Antolovich and Armstrong, 2014]. Serrations start immediately with the onset of the macroscopic plastic flow, which is typical for materials with a high initial dislocation density and is consistent with the DSA mechanism [Kubin and Estrin, 1990].

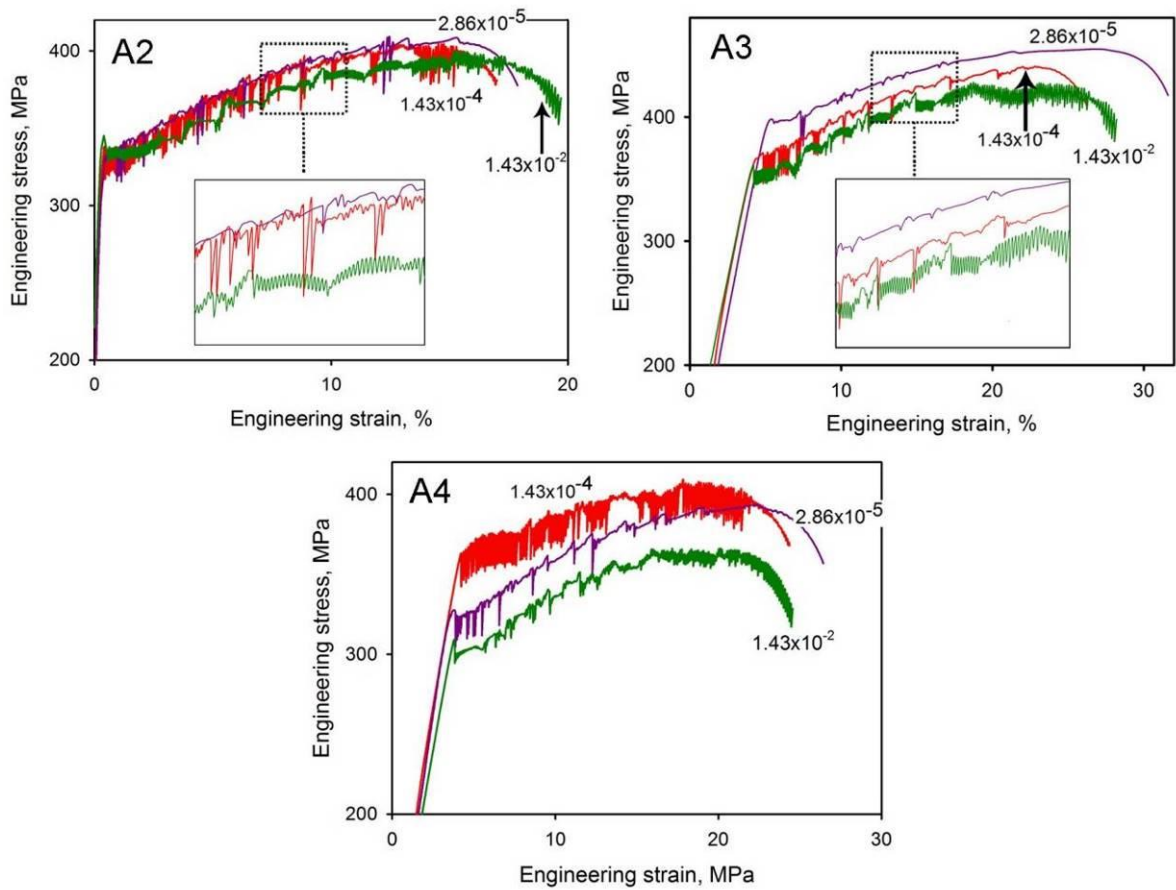


Figure 3.31: Typical deformation curves of A2, A3 and A4 alloys in FG state. The values of the imposed strain rate are given in  $s^{-1}$ .

As was described in § 3.2.1, grain refinement drastically modifies serration patterns and promotes deep type *B* and type *C* serrations. In contrast to the CG state, type *B* stress drops are dominant at high and intermediate  $\dot{\epsilon}_a$ -values, even if type *A* or type *D* features are observable at the highest  $\dot{\epsilon}_a$  (Fig. 3.31). Intervals of smoother flow between deep stress drops, indicating a transition to type *C* behavior, appear when  $\dot{\epsilon}_a$  is decreased to  $1.43 \times 10^{-4} s^{-1}$ . In the case of A2 and A4 alloys, this transition is completed at  $2.86 \times 10^{-5} s^{-1}$  characterized by clear type *C* serrations. In the case of FG A3 alloy, such patterns are already observed at  $1.43 \times 10^{-4} s^{-1}$ .

Figure 3.32 presents spatiotemporal maps for the FG A3 samples deformed at different strain rates (cf. Fig. 3.28 for the CG A3 alloy). It can be seen that the propagation mode is also important at high and intermediate rate in FG conditions (Charts (a)-(c)), although type *B* serrations dominate on the deformation curves shown in Fig. 3.31. The clear hopping propagation, characteristic of type *B*, can only be seen at large enough strain and intermediate strain rate (Fig. 3.32b and c). Figure 3.32d illustrates a transition from

immobile type *C* bands, observed at the beginning of the test at  $1.43 \times 10^{-4} \text{ s}^{-1}$ , to the propagation patterns after some deformation (cf. Fig. 3.21).

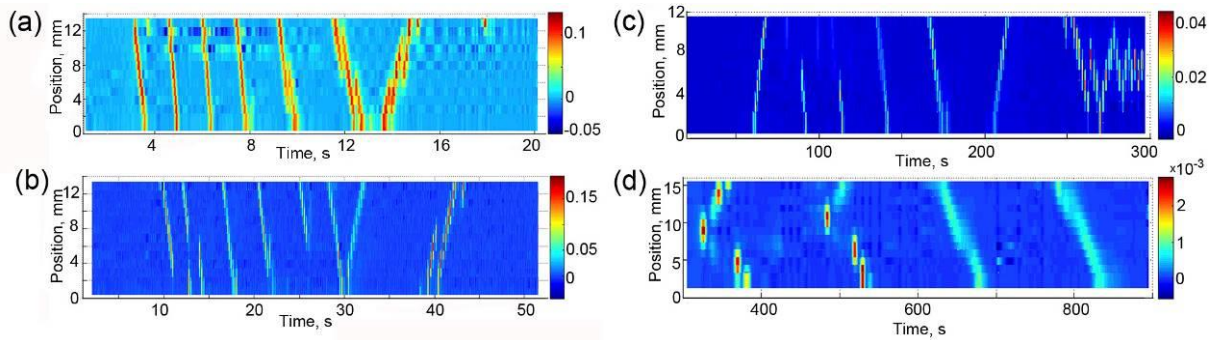


Figure 3.32: Maps for the FG A3 alloy for the same strain rates as in Fig. 3.28 for the CG conditions.

Finally, Figure 3.33 compares deformation bands propagating at low strain rates in FG conditions. It can be seen that the low strain-rate regime is similar in all cases, i.e., both between all FG alloys and with CG alloys containing precipitates. Figure 3.33b allows for an additional observation concerning the small-scale strain-rate heterogeneity evoked in footnote 1 (Fig. 3.2). Due to a high time resolution of the 1D extensometry technique, it can be seen in this map that the small-scale heterogeneity does not only exist outside the deformation band, i.e., in slowly deforming cross-sections, but also characterizes the band interior. As a matter of comparison, the small bright spots within the deformation band of Fig. 3.33b correspond to the maximum  $\kappa$ -value about 700.

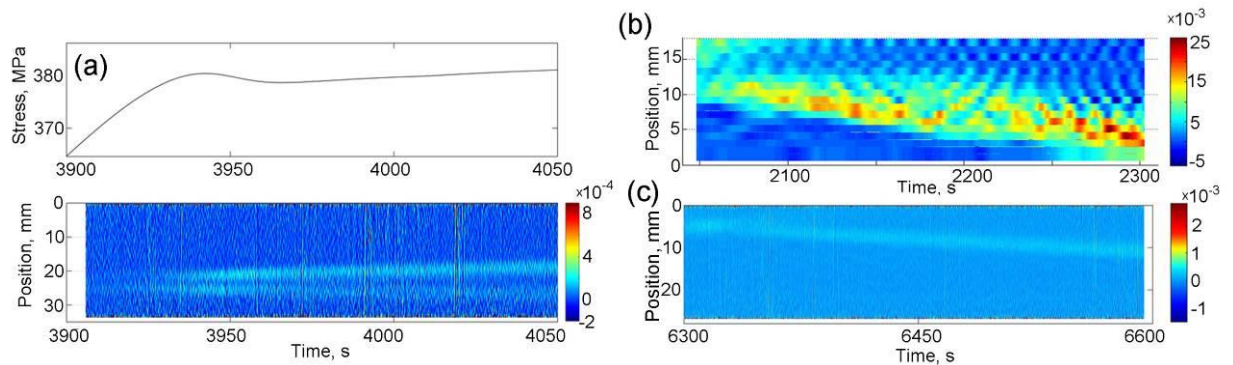


Figure 3.33: Strain rate maps showing moving deformation bands at  $2.86 \times 10^{-5} \text{ s}^{-1}$  in FG conditions. (a) A2 alloy; (b) A3 alloy; (c) A4 alloy.

$V_b$ , mm/s: (a) 0.023 (375 MPa); (b) 0.029 (380 MPa); (c) 0.021 (385 MPa).

### 3.3.3. Concluding remarks

The dislocation interaction with coarse and fine particles obeys qualitatively different mechanisms [Smallman and Bishop, 1999]. Therefore, it could not be suggested *a priori* that their effect on the PLC instability would be the same. A simple reasoning should take into account that the Orowan bowing of large non-coherent precipitates results in an increase in the mobile dislocation density through generation of dislocation loops and, therefore, changes the conditions of dislocation-dislocation interactions. Small coherent particles can be cut by dislocations and would not produce such an effect. In spite of it, small particles also efficiently strengthen the material. A straightforward reason for this is the smaller inter-particle distance, i.e., a larger density of obstacles to the dislocation motion. Besides, a realistic mechanism should consider many factors, such as precipitation in the material bulk or on the dislocations, influence on the elastic modulus, and so on. The present data show that despite physically different mechanisms associated with coarse and fine precipitates, the qualitative changes in the kinematics of the PLC bands are similar and may be rationalized in terms of an increase, in one or another way, of local stresses promoting the band propagation. This hypothesis is also corroborated by the observation of a similar persistence of the propagation mode after grain refinement, even in the absence of precipitates in the binary alloy. Moreover, the above examples bear evidence that the initial difference between serration patterns and PLC band kinematics in alloys with different precipitates is virtually levelled out after SPD. The suggested hypothesis will thus be discussed in more detail in the concluding part of this Chapter.

### 3.4. Possible mechanism of the slow propagation regime

One of the major results of this Chapter concerns the observation of the unusual mode of PLC band propagation at low strain rate. The occurrence of this mode is accompanied with long intervals of relatively smooth loading between deep type *C* serrations associated with short-term uncorrelated deformation bands. Although the behaviors observed in the present Chapter are quite diverse, they allow for distinguishing some pertinent features:

- The low strain-rate propagation was not found in the CG binary (A1) alloy, but was observed in all investigated alloys containing precipitates or/and high density of grain boundaries created by the SPD.
- The tendency to propagation was present at all strain rates in the materials with precipitates. More exactly, besides the well-known type *A* behavior at fast deformation and the low strain-rate propagation mode, the intermediate strain rates

were characterized by mixed *A/B* behavior, while the well-defined hopping propagation (type *B*) was not detected. It should be noted that the slow propagation regime occurred upon the onset of jerky flow, but evolved to usual type *C* behavior (series of deep serrations) at the late deformation stages.

- The effect of the grain refinement by ECAP was even more complex. In the FG Al alloy, the slow propagation was found at the smallest strain rate, only, and was much less pronounced than in other alloys. In all materials, ECAP resulted in a strong tendency to type *B* behavior at intermediate and even high strain rates. At the same time, it favored the propagation at low strain rates. Moreover, after ECAP, the deformation curves of three alloys containing precipitates acquired very similar shapes corresponding to similar PLC band kinematics. Therewith, the evolution of spatiotemporal behavior with strain was in some sense inverse to the above-described case of CG samples of these alloys. Namely, more pronounced type *C* serrations occurred at the beginning of deformation, but gradually disappeared, giving place to relatively smooth plastic flow resembling type *A*. Such a transition goes in the opposite direction regarding the known strain-hardening effect impeding the band propagation.
- In all cases, the dependence of the deformation band velocity on the imposed strain rate was unique over the entire range of strain rates where propagation was observed (quasi-continuous propagation at high/slow deformation or relay race at medium strain rate). It can thus be suggested that it is determined by the same dynamical mechanism.
- Finally, almost smooth deformation curves were found at all strain rates after additional cold rolling (FGH samples). Despite this smoothness, the local extensometry showed that the deformation was not controlled by a uniform plastic flow but by the propagation of one or two deformation bands.

The ubiquity of the slow propagation, in the sense that it was observed for distinct kinds of additional obstacles to the dislocation motion (coherent and non-coherent precipitates, grain boundaries), suggests the existence of an inherent mechanism common in all cases. Accordingly, it was presumably attributed to stress concentration on the obstacles that locally harden the material and may promote the plastic strain transfer to the neighboring sites, i.e., the propagation of a deformation band. An additional hint in favor of such a conjecture is that a similar peculiarity was observed in twinning induced plasticity

(TWIP) steels which plastic flow is governed by a combination of dislocation glide and twinning [Lebedkina et al., 2009, Bouaziz et al., 2011]. The unstable plastic flow in TWIP steels has also been attributed to the PLC effect. As the AlMg alloy are not prone to mechanical twinning, the similarity of the kinematics of deformation bands in two materials may be due to the presence of a high density of twin boundaries acting as obstacles to dislocation glide.

A general framework consistent with this mechanism was proposed recently [Bharathi et al., 2002; Lebyodkin et al., 2012]. It is based on the considerations of conditions for relaxation and homogenization of internal stresses generated by strain localizations in the deformation bands, as described in Chapter 1 in relation to the statistics of jerky flow. Similar arguments can be used to consider the transition between the static and propagation modes of kinematics of the PLC bands. Indeed, if the relaxation of the incompatibility stresses is insufficient, be it because of the fast reloading (high strain rate) or a high density of obstacles to the dislocation motion, the local stress state will constantly be heterogeneous and close to the instability threshold all over the sample. Consequently, an excess of the internal stress would result in the propagation of relatively weak strain localizations. In particular, this situation is likely to take place at all strain rates in the extremely hardened FGH material. In the opposite case, the efficient relaxation of the incompatibility stresses would provide strain uniformization in the specimen, leading to two consequences: The instability conditions will only be reached when the applied stress approaches the critical level; Breakthrough of dislocations in one site would result in a catastrophic process. The catastrophe could have involved the whole specimen but the elastic reaction of the deformation machine would lead to an abrupt decrease in the stress and stop the further development of the instability, giving rise to a deep stress drop.

As specified in Chap. 1, this scenario of collective dynamics of dislocations is analogous to the phenomenon of synchronization in extended dynamical systems. The data presented above testify that the transition between the synchronization and propagation modes is continuous and gives rise to diverse patterns including the relay-race propagation. This conjecture is confirmed, in particular, by the observation of progressive changes in the  $\kappa$ -value when the strain rate or microstructure is varied.

In spite of the general character of this scheme, it should not be forgotten that the specific features of the band propagation are not the same in the cases when either precipitates or grain boundaries are the main microstructure elements. To account for these differences, one would need to admit that grain boundaries may play a more complex role, assisting, on the one hand, the local stress concentration because of the dislocation pinning

and, on the other hand, stress relaxation because of the dislocation drainage and/or nucleation of new dislocations. For example, this aspect may be responsible for the persistence of type *B* behavior in the FG state, so that the transition to type *A* is not fully accomplished even at a very high strain rate.

In summary, although the overall behavior of alloys strengthened by precipitation or grain refinement differs from the well-known transitions between three conventional types, all these patterns can be integrated into a general scheme rationalized in terms of a competition between synchronization of dislocations, leading to strain localization when the local strain field is sufficiently uniform, and propagation of plastic activity in heterogeneous strain conditions. One of the factors controlling this subtle balance is the efficiency of relaxation of internal stresses which is affected by both precipitates and grain boundaries. Consequently, the precise manifestations of the PLC instability in alloys with complex compositions may be system specific and will require a systematic study of various alloys.

## Chapter 4

### **Interrelation between the Portevin Le-Chatelier effect and necking in AlMg alloys**

Since the PLC effect causes strain localization within deformation bands, it seems natural to suggest that it may lead to a premature onset of necking. However, as was demonstrated in Chap. 1, there exist little experimental data in the literature on the correlation between the PLC effect and onset of necking. Moreover, the existing viewpoints contradict each other. Such a difficulty may be due to the diversity of behaviors of the PLC effect, so that the authors studying the problem in different conditions arrive to contradictory conclusions. This Chapter presents an experimental investigation of the relationship between plastic flow instability and neck formation in the binary (A1) and precipitation-strengthened (A2) alloys in all three different initial microstructure conditions (see Chap. 2), and the strain-rate range covering three orders of magnitude. As described in Chap. 3 for these alloys, their overall deformation behavior depends on the microstructure and strain rate and includes virtually all common types (*A*, *B*, *C*, and *D*) of spatiotemporal patterns, thus assuring a systematic study of the formulated problem.

## 4.1. Deformation curves

Details of deformation behavior of A1 and A2 alloys in different microstructure conditions (CG, FG and FGH) at strain rates of  $10^{-5}$  to  $10^{-2} \text{ s}^{-1}$  were described in Chap. 3. Since our attention is now focused on the investigation of the effect of PLC bands on the neck formation, some pertinent details will be reminded here. Let us first summarize the types of the PLC instability observed in each microstructure condition of A1 and A2 alloys.

Figure 4.1 shows engineering tensile curves for the strain-rate values selected to represent characteristic serration patterns, or types of behavior, for each of three kinds of both alloys. In CG state, A1 alloy displays clear type *A* behavior at  $\dot{\epsilon}_a \geq 5 \times 10^{-3} \text{ s}^{-1}$  (Fig. 4.1a). Type *B* serrations can be recognized at large strains in the tests at  $10^{-3} \text{ s}^{-1}$  and become dominant at  $1.4 \times 10^{-4} \text{ s}^{-1}$ . Mixed *B+C* serrations are observed at lowest  $\dot{\epsilon}_a = 2.9 \times 10^{-5} \text{ s}^{-1}$ . In the case of the CG A2 alloy, type *B* serrations are preponderant in the example for  $10^{-3} \text{ s}^{-1}$  (it was denoted as a reference strain rate in § 3.1.1); and types *C+A* and *A* serrations occur, respectively, for strain rates below and above this value (Fig. 4.1a’).

After severe plastic deformation by ECAP, the stress serrations patterns changed significantly and showed a strong tendency to deep stress serrations with type *C* and type *B* features. Type *A* or type *D* behavior can be recognized at  $\dot{\epsilon}_a \geq 10^{-3} \text{ s}^{-1}$  in the FG A1 alloy (e.g., curve 4 in Fig. 4.1b) and  $1.4 \times 10^{-2} \text{ s}^{-1}$  in the FG A2 alloy (e.g., curve 5 in Fig. 4.1b’). In any case, type *B* serrations are also present from the very beginning of plastic deformation and become prevailing at large strains. Overall, ECAP led to a significant increase in strength and decreases in  $\Theta$  and ductility. It is noteworthy that the changes in the strength and work hardening are stronger in the initially softer A1 alloy. According to the Considère criterion, these observations agree with a more significant ductility reduction for this material. Overall, both alloys have a similar ductility in the FG state.

The FGH samples displayed the highest strength and the lowest values of work hardening and ductility, and almost smooth deformation curves, at least, during the work hardening stages. A transition to oscillatory behavior was detected during necking in FGH A1 samples deformed at  $\dot{\epsilon}_a \leq 10^{-3} \text{ s}^{-1}$  (Fig. 4.1c). Weaker oscillations can also be discerned in the necking region of curves 2 and 3 obtained in similar conditions for A2 samples (Fig. 4.1c’).

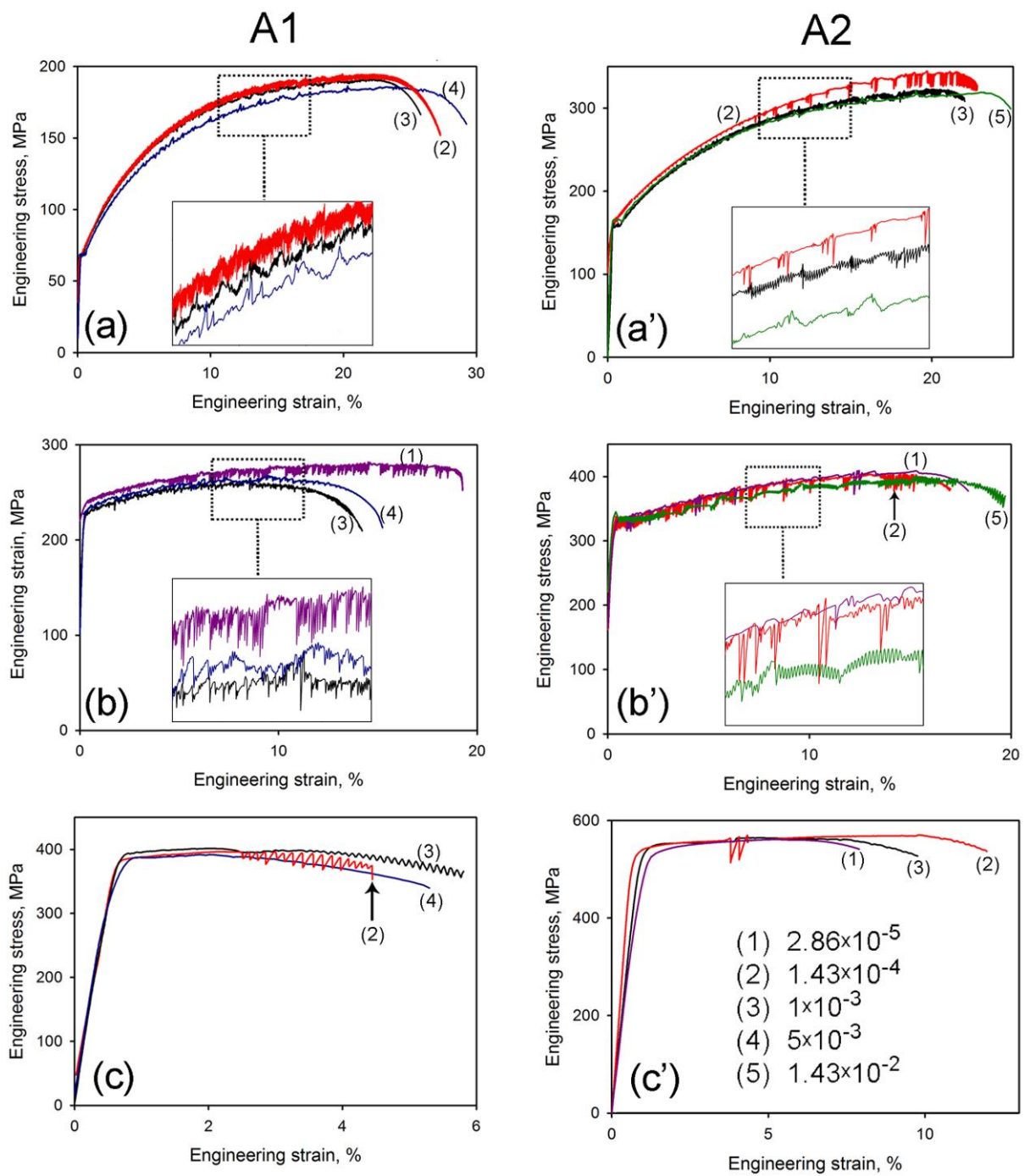


Figure 4.1: Engineering deformation curves for A1 (left column) and A2 (right column) alloys. (a,a') CG state; (b,b') FG state; (c,c') FGH state. The legend represents  $\dot{\epsilon}$  in  $s^{-1}$ . Some of the portions of the curves presented in the insets were shifted to avoid superposition and better clarify details of serrations.

## 4.2. Analysis of the Considère strain

To compare in the same chart the results obtained for different states of the same material, the Considère criterion is represented as  $n = \varepsilon$  in Fig. 4.2, where the work hardening index  $n = d(\ln \sigma) / d(\ln \varepsilon) = \varepsilon \times d\sigma / (\sigma \times d\varepsilon)$ . Accordingly, the Considère strain corresponds to the intersection between the straight line,  $n = \varepsilon$ , and the  $n(\varepsilon)$  dependence calculated from the deformation curve. The method of evaluation of  $n$  in the case of serrated flow was described in § 2.2.1.

Fig. 4.2 shows examples of verification of the Considère criterion at  $\dot{\varepsilon}_a = 10^{-3} \text{ s}^{-1}$ . As follows from the above description of serration patterns obtained at this reference value in different cases, this choice allows to illustrate the results of analysis for practically all types of behavior of the PLC effect. Since the FGH A2 alloy presents a step in the middle of the deformation curve (Fig. 4.1c'), the origin of which was described in § 3.2.2, the curve was subdivided into two parts and the calculation was performed for each part separately. The circles indicate the positions of the maximum load. They coincide very well with the intersections indicating the Considère strain. A similar correspondence was found for other values, as well. It can thus be concluded that despite the discontinuous nature of plastic flow, the onset of necking is well determined by the Considère criterion.

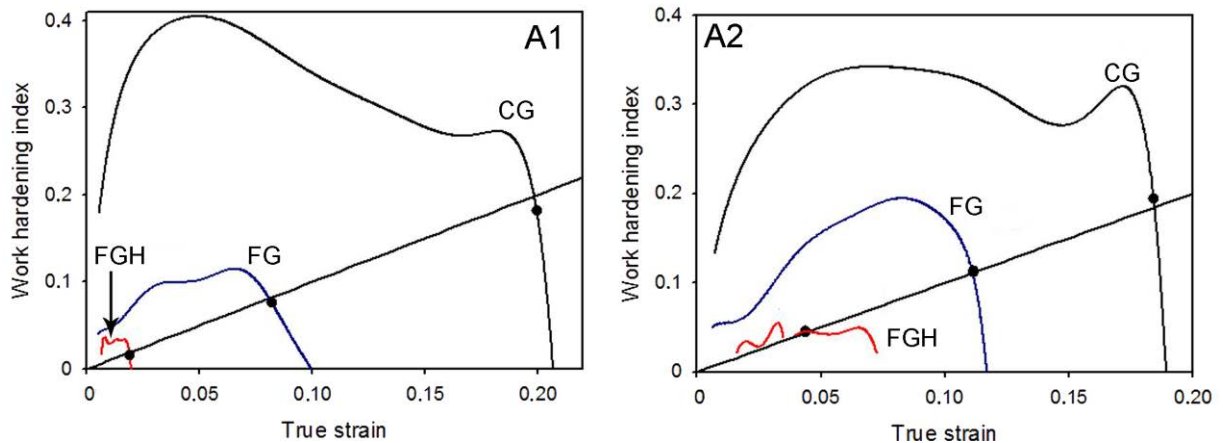


Figure 4.2: Work hardening index  $n$  as a function of true strain  $\varepsilon$  for A1 and A2 alloys with three different initial microstructures tested at the reference strain rate of  $10^{-3} \text{ s}^{-1}$ . Strain lines correspond to the Considère criterion,  $n = \varepsilon$ . Black dots indicate the position of the maximum load.

Some clarifications are needed to put this conclusion into a proper perspective. First, since the smoothed deformation curve passes between the local maxima and minima of stress serrations, some local maxima occurring close to the UTS may take on higher  $\sigma$  values than the vertex of the smooth fitting curve. That is, the absolute maximum might appear

earlier than that designated by the circles in Fig. 4.2. Second, since the strain hardening rate is very low in FGH samples and besides, their deformation curves fluctuate, the Considère criterion may be satisfied several times before the ultimate onset of necking (see the right-hand plot). Despite this ambiguity, the visualization of the PLC bands and the development of the ultimate shear band revealed the same basic relationship between these instabilities in all conditions, as presented in the next section.

### 4.3. PLC bands behavior

#### 4.3.1. CG state

Figure 4.3 displays the evolution of *A* type deformation bands during the entire test on a CG A1 sample at a relatively high strain rate. As can be seen, a series of bands propagate at  $\sim 1$  cm/s along the specimen at early stages of deformation. Their intensity (the maximum  $\dot{\epsilon}_{loc}$  value) increases and the velocity decreases with strain [see Chap. 3 for details]. Breaks in the regular continuous propagation of the bands and their reflections [Ait-Amokhtar and Fressengeas, 2010] reflect the transition from type *A* to type *B* behavior at larger strains.

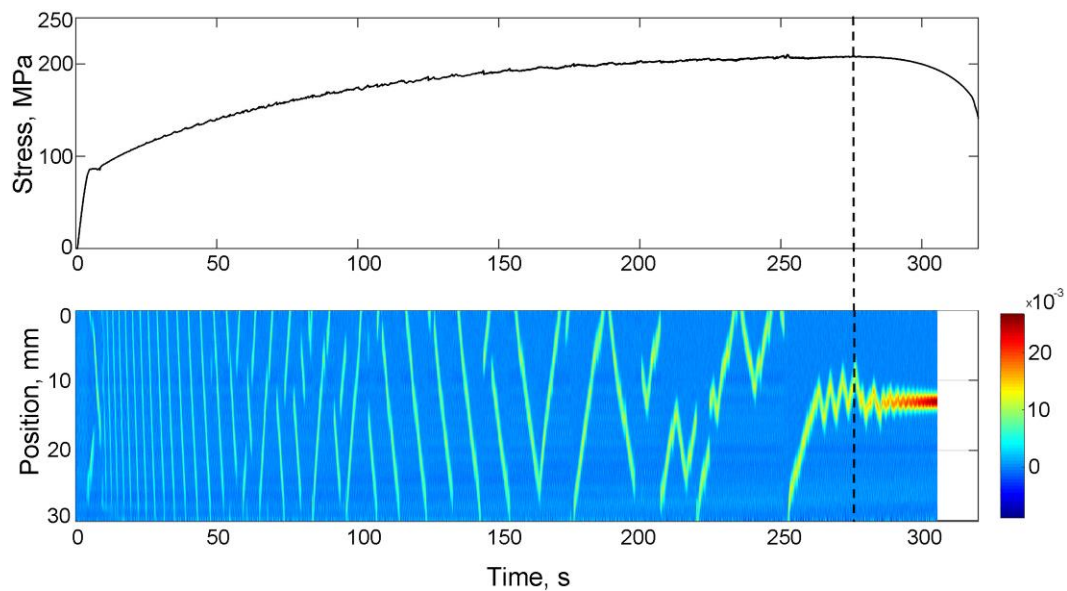


Figure 4.3: The entire stress-time curve for a CG A1 sample tested at  $10^{-3} \text{ s}^{-1}$  and the corresponding local strain-rate map showing the time evolution of the local strain rate along the vertical centerline (tensile axis) of the sample. The color bar represents the local strain-rate scale in  $s^{-1}$ . The vertical dashed line indicates the maximum load.

Two striking observations concern the strain interval about the onset of necking. On the one hand, the map reveals immobilization of the last deformation band via back-and-

forth movements started before the UTS. On the other hand, such movements last for some time after the onset of necking. The band is finally stabilized at the specimen cross-section where fracture will occur. The neck development manifests itself through the constantly increasing  $\dot{\epsilon}_{loc}$  in this cross-section. It can be suggested from this example that the necking is realized through progressive immobilization of a PLC band. This picture is qualitatively different from the common mechanism of formation of a diffuse deformation band in the uniformly deforming material, which condenses into the ultimate shear band.

The above conjecture holds for all cases studied in the present work, despite distinct types of spatiotemporal behavior in different experimental conditions. Figure 4.4 displays a similar strain-rate map for a higher  $\dot{\epsilon}_a$ , characterized by a quasi-continuous propagation of deformation bands during the entire tensile test. Again, the necking displays continuity with the last PLC band. Since the proneness to deformation band propagation is the stronger the higher  $\dot{\epsilon}_a$ , it is not surprising that instead of multiple back-and-forth movements, the last PLC band continues shifting about 15 mm following the UTS, before being damped after a short backward movement. Similar observations were reported in [Ait-Amokhtar and Fressengeas, 2010]. Figure 4.4c presents a series of DIC images corresponding to the propagation of the last two PLC bands and the onset of necking. Besides completing the representation provided in Fig. 4.4b, it also demonstrates the necking geometry most frequently observed in the present work. It rarely occurred along a well-defined plane determined by simple shear. More often, a competition between two conjugate bands took place during necking and resulted in a complex geometry of the fracture surface (see [Kang et al., 2006; Halim et al., 2007; Hadianfard et al., 2008; Cai et al., 2016]). The systematic analysis of the fracture geometry, however, goes beyond the scope of the present thesis.

Fig. 4.5 describes the opposite case when a decrease in  $\dot{\epsilon}_a$  below the reference strain rate gives rise to type *B* behavior. Each stress drop is produced by an individual deformation band whereas the following reloading corresponds to a roughly uniform plastic flow. The intensity of strain localization within the bands corresponds to  $\kappa \sim 50$ , which is considerably higher than for type *A* bands (see § 3.1.2). The subsequent bands form relay-race propagation series characteristic of type *B* dynamical regime. It can be seen in Fig. 4.5b that necking is associated with a restriction of the propagation length, leading to a damped wobbling movement. However, it does not change the basic pattern of either strain localizations or stress serrations, except for the disappearance of stress irregularities associated with the nucleation and exhaustion of relay-race sequences.

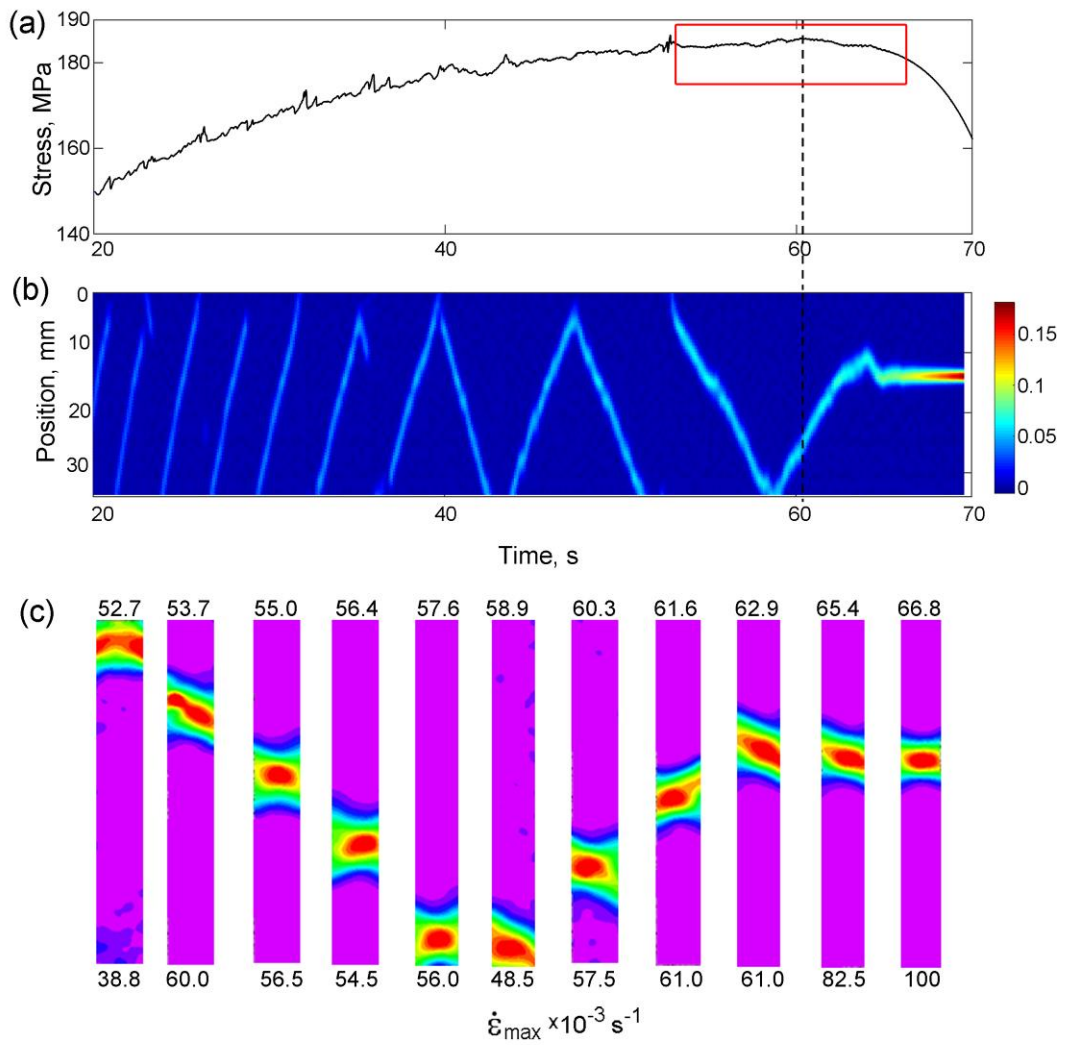


Figure 4.4: (a,b) Plots similar to Fig. 4.3, for a CG A1 sample tested at  $5 \times 10^{-3} \text{ s}^{-1}$ . The vertical dashed line indicates the maximum load; (c) DIC images of the specimen surface at the end of the test (see rectangle in the upper plot).

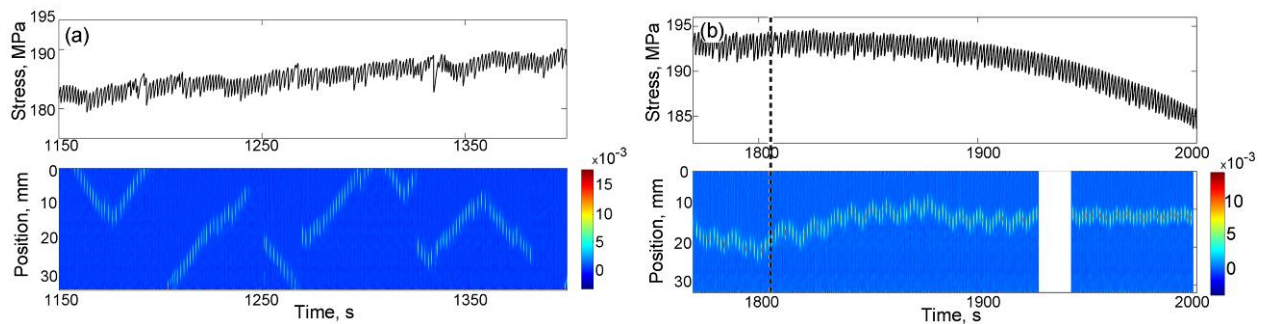


Figure 4.5: Plots similar to Fig. 4.3, for a CG A1 sample tested at  $1.43 \times 10^{-4} \text{ s}^{-1}$ . (a) Portion at the work-hardening stage; (b) Necking region. The vertical dashed line indicates the maximum load.

Fig. 4.6 presents a detailed view of such behavior at a later stage of neck development displaying the spatially stabilized strain localization. In addition to the overall strain-rate map (Fig. 4.6b), the evolution of  $\kappa$  in the corresponding cross-section is shown in Fig. 4.6c. Although the  $\dot{\epsilon}_{loc}$ -value on the specimen centerline does not necessarily correspond to the maximum  $\dot{\epsilon}_{loc}$  within the band, this plot allows for characterization of the intermittent character of strain localization. It can be seen that  $\dot{\epsilon}_{loc}$  jumps alternate with intervals of virtually uniform plastic flow with the strain rate approximately equal to  $\dot{\epsilon}_a$ . In other words, despite the stress concentration in the necked region, the intensity of strain localization does not constantly increase, as it would be observed in the absence of the PLC effect, but continues oscillating according to type *B* behavior of the PLC instability preceding the necking.

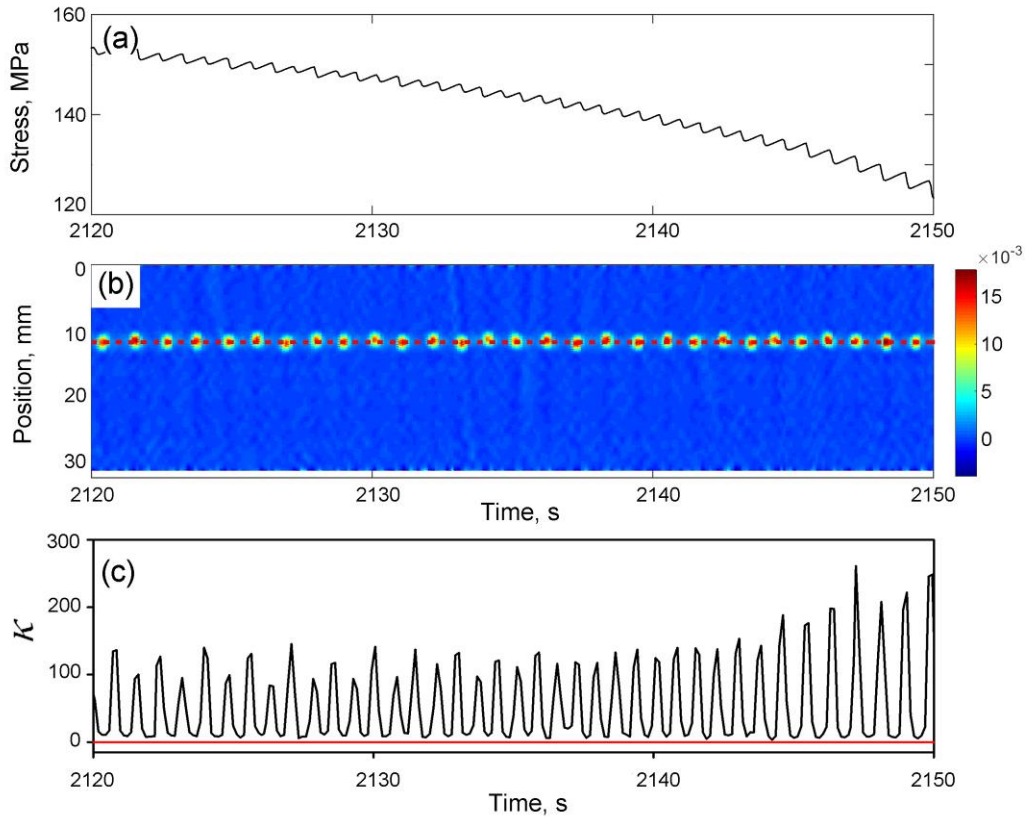


Figure 4.6: (a,b) Necking development for the sample of Fig. 4.5 and the corresponding evolution of the value of  $\kappa = \dot{\epsilon}_{loc} / \dot{\epsilon}_a$  in the cross-section shown by the dashed line in plot (b). The solid straight line in plot (c) presents the current value of the imposed strain rate corrected with respect to the actual specimen length.

The further decrease in the  $\dot{\epsilon}_a$  down to  $2.9 \times 10^{-5} \text{ s}^{-1}$  does not qualitatively change this behavior for CG A1 samples. Type *C* behavior becomes more pronounced with increasing strain, which is manifested as a loss of correlation between PLC bands, so that the relay-race

series become composed of only several PLC bands and start in visually random sites of the gage length. The visualization of the necking renders patterns similar to Figs. 4.5 and 4.6.

These descriptions fully apply to *C+A* behavior obtained in CG A2 material at  $1.4 \times 10^{-4} \text{ s}^{-1}$ . Despite the unusual mixture of types of PLC behavior in this case, so that weak propagating bands are found during smooth deformation between deep type *C* serrations (see § 3.1.4), this peculiarity does not change the necking onset and progressing. Indeed, as can be seen in Fig. 4.1a', the frequency of serrations increases and the smooth intervals vanish at larger strains. As a result, the strain localization pattern associated with the necking corresponds to the scenario presented in Figs. 4.5 and 4.6 for the CG A1 alloy tested at the same strain rate.

#### 4.3.2. *FG state*

As specified in § 3.2, the grain refinement does not give rise to any new type of serrations but results in a marked tendency to type *B* and type *C* behavior. This conclusion agrees with the respective changes in the strain localization patterns. Accordingly, the above examples of the PLC bands behavior and the development of necking in CG alloys cover practically all possible situations for the FG materials, too.

Two differences with the examples presented for the CG state were remarked in Chap. 3. First, the unusual propagation regime alternating with type *C* deformation bands at low strain rates is found in both A1 and A2 alloys in FG condition. Secondly, the propagation patterns in FG condition reveal a concurrency with the opposite trend to static strain localization, manifested as a beat in the band propagation pattern. Visualization of spatiotemporal maps beyond the UTS shows that the beat is sustained during necking, i.e., the degree of localization in the neck may not increase steadily, unlike the neck development in the absence of the PLC instability. An example of such behavior is presented in Fig. 4.7 for the A2 sample of Fig. 3.21. Plot (a) displays a strain interval before the UTS, similar to Fig. 3.21c. Plot (b) represents the beat during necking, in a more quantitative manner. It displays oscillations of the  $\kappa$ -ratio at a point chosen within the immobilized neck. Such a quantitative representation would be impossible for Fig. 4.7a because of the band motion. A similar beat was also observed during necking in some high strain-rate tests, e.g., for curve 5 in Fig. 4.1b'. It is also noteworthy that Fig. 4.7a illustrates a spring-back effect during type *C* stress drops (a decrease in the local strain rate outside the deformation band), which is caused by deformation bands nucleating close to the upper end of the sample.

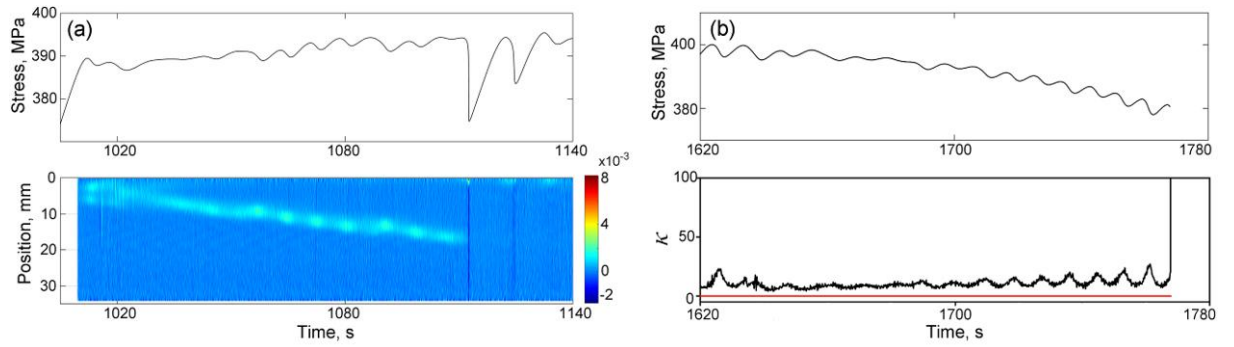


Figure 4.7: (a) Portion of stress-time curve in the work-hardening region and the corresponding strain-rate map showing a beat in the band propagation pattern for a FG A2 sample tested at  $1.43 \times 10^{-4} \text{ s}^{-1}$ . (b) Portion of stress-time curve corresponding to necking stabilized in some cross-section and the evolution of the  $\kappa$ -ratio in this section.

#### 4.3.3. FGH state

Although the deformation curves of FGH materials are quite smooth in the work-hardening region, the DIC analysis presented in § 3.2.2 showed that the smoothness is not due to a uniform plastic flow but to the propagation nature of the PLC instability at all strain rates. The A2 alloy demonstrates virtually the same behavior at all  $\dot{\epsilon}_a$  values, illustrated in Fig. 4.8 for the reference strain rate. The entire pattern demonstrates the same scenario as the propagation of the last type *A* bands in Fig. 4.4. Despite the already decreasing applied stress after the reflection of the band at the maximum load, it continues shifting over a long distance and is finally damped to give rise to the ultimate necking. It can be seen that at the reference strain rate, the neck development proceeds by a beat accompanied with small stress oscillations (cf. Fig. 4.7). Smooth deformation during necking and continuously increasing strain localization are found at high and low strain rates.

The FGH A1 alloy showed qualitatively similar behavior, except that, as described in § 3.2.2, the band propagation was less steady and usually occurred over shorter distances, thus indicating a competition with the trend to static strain localization consistent with the overall type *C* character of stress serrations. It is also noteworthy in this context that in one of the tests at  $1.43 \times 10^{-4} \text{ s}^{-1}$ , the oscillatory strain localization associated with the neck formation started away from the specimen cross-section where the propagation of the initial deformation band terminated (Fig. 4.9). Such an abrupt shift of the site of nucleation of PLC bands is characteristic of type *C* behavior.

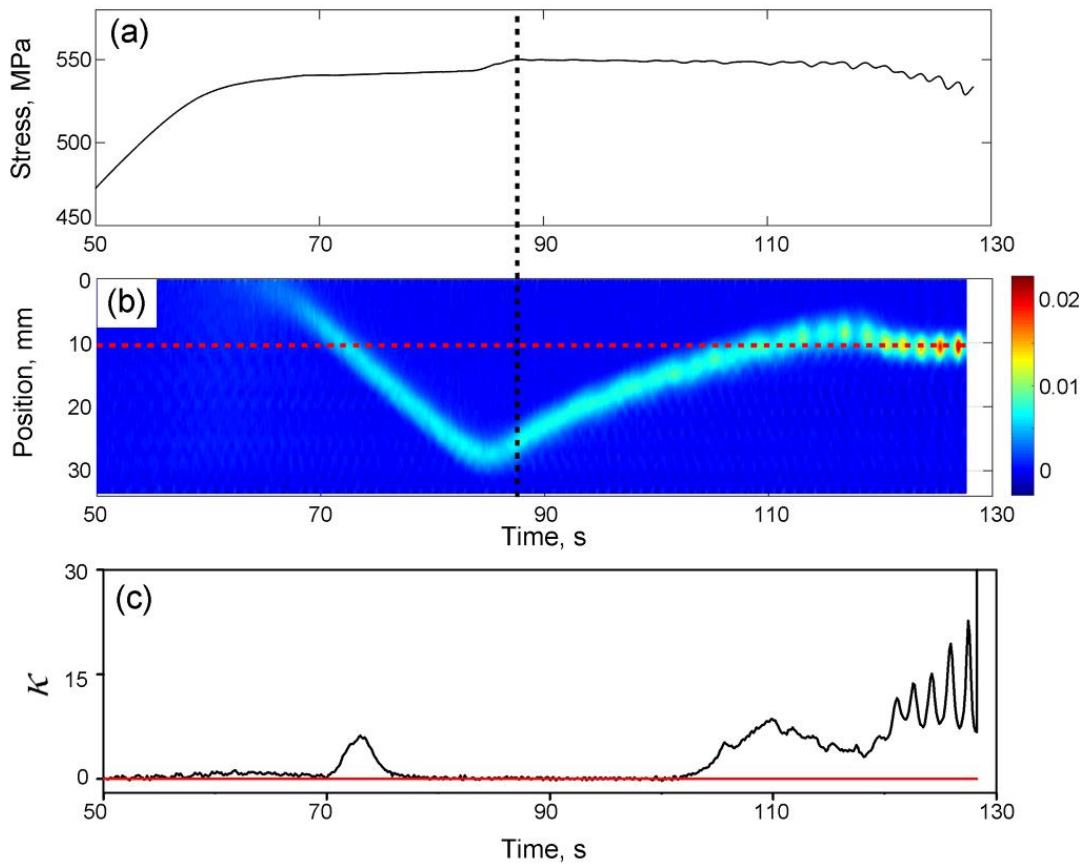


Figure 4.8: Plot similar to Fig. 4.6, for an FGH A2 sample tested at  $1 \times 10^{-3} \text{ s}^{-1}$ . The vertical dashed line indicates the maximum load. (cf. Fig. 3.25).

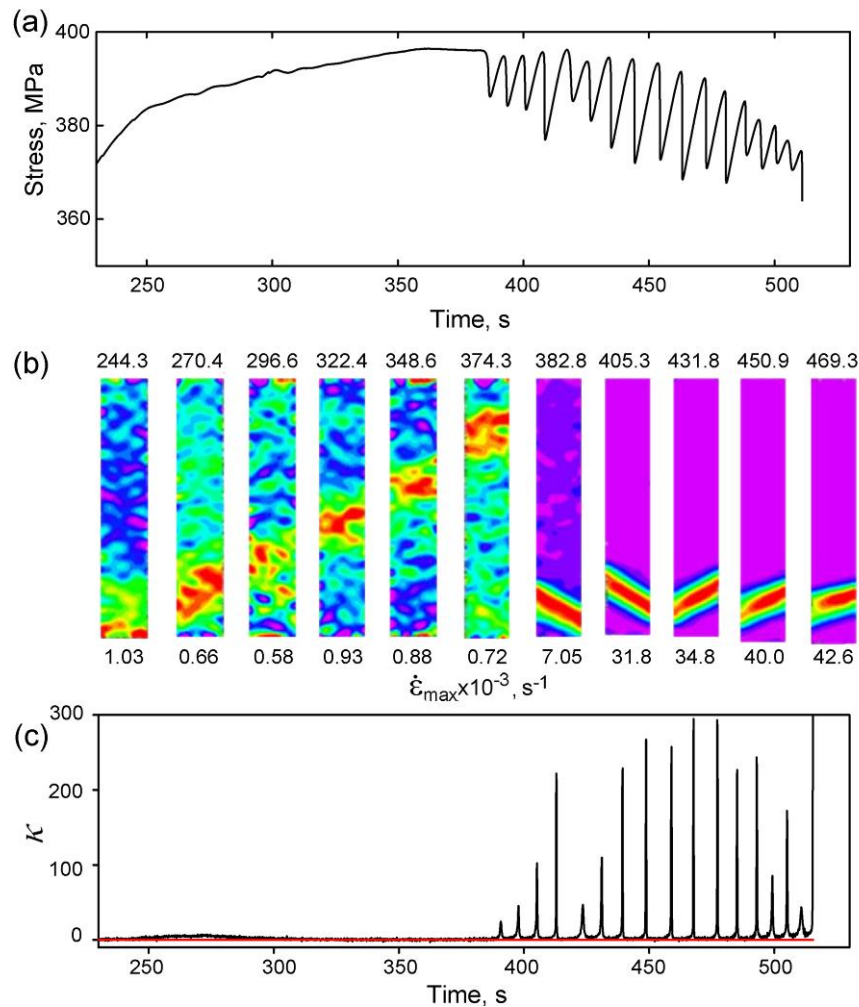


Figure 4.9: (a) Stress-time curve for an FGH A1 sample tested at  $1.43 \times 10^{-4} s^{-1}$ . (b) Series of corresponding DIC images of the specimen surface, taken within the interval indicated by the numbers above the images. (c) The corresponding evolution of the  $\kappa$  - value in the cross-section of the sample. The solid straight line in plot (c) presents the current value of the imposed strain rate corrected with respect to the actual specimen length.

## 4.4. Discussion

### 4.4.1. Fulfillment of the Considère criterion in the presence of jerky flow

Despite the diversity of spatiotemporal behaviors obtained through variation of the microstructure and deformation conditions for two alloys, the analysis of the deformation curves with smoothened-out serrations bears evidence that the onset of necking corresponds well to the Considère criterion stemming from the geometric instability of the uniform plastic flow. This observation does not agree with some literature data testifying to an early onset of necking in alloys exhibiting DSA [Chung et al., 1977; Jobba et al., 2015; Kang et al., 2005, 2006]. The general character of the present observations thus requires further

verification. It should, however, be noted that such a discrepancy may be due to an ambiguity in the definition of the maximum load on a serrated curve. Indeed, some local maximum corresponding to a stress rise associated with the nucleation of a PLC band may exceed the vertex of the smoothed curve and lead to a conclusion on a (apparent) premature necking. In any case, the good correspondence between the Considère criterion and the UTS determined on the smoothed curves in all experimental conditions testifies to a profound role of the geometric instability.

To interpret this uniqueness, it can be remarked that the work hardening plays the same stabilizing role in the case of finite strain localizations caused by the PLC bands, as in the case of small geometric non-uniformities in the Considère analysis. Indeed, the fast straining within the PLC band must lead to an excessive hardening of the material in the respective cross-sections and force the transfer of plastic activity to other sites. The validity of the Considère criterion can be due to the fact that although the work hardening occurs locally, i.e., within the deformation bands, their displacement along the specimen, be it through a quasi-continuous propagation, a relay race, or uncorrelated jumps, provides a uniform straining on the average. In addition to this general argument, two observations can be remarked in support of it. First, both FGH materials, possessing a low work hardening capacity, do not only have a low ductility but also display fluctuations of the stress level, leading to an ambiguity in the determination of the Considère strain. Secondly, the supposed “uniformization by propagation” is consistent with the tendency to a lower ductility of the FGH A1 alloy. Indeed, the entirety of experiments testifies that the deformation band propagation is strongly impeded in the FGH A1 samples, whereas the band propagates through the whole gage length in the FGH A2 samples. Although such mesoscopic-scale experiments do not allow for judging the relevant physical mechanism explaining this difference, a reasonable hypothesis stems from the fact that both materials have the dislocation density approaching the critical value for failure of AlMg alloys with similar Mg contents,  $\rho \sim 10^{15} \text{ m}^{-2}$  [Jobba et al., 2015; Park and Niewczas, 2008]. Thus, the dislocation hardening mechanism is close to exhaustion in both alloys. Therefore, the additional dispersion hardening in the A2 alloy may explain its advantageous ductility [Huskins et al., 2010]. This reasoning is also corroborated by the observation of a stronger tendency to the deformation band propagation at low strain rate in the A2 alloys.

#### 4.4.2. Interrelation between the PLC bands and necking

Although the onset of necking is well described by the Considère criterion, the results obtained bear strong evidence that the PLC bands prepare the ultimate strain localization. Indeed, regardless the material's initial microstructure, the strain rate, and the types of the characteristic spatiotemporal pattern, the same scenario of neck formation through bounding of the PLC band displacement was realized in all experiments (see strain-rate maps in Figs. 4.3-5, 4.9). No diffuse deformation band was observed prior to the ultimate strain localization in one or two intersecting shear bands. According to the progressive character of immobilization of the PLC bands, the selection of the necking site must have a dynamical character. On the one hand, the material hardening within the PLC band maintains its mobility. On the other hand, if the PLC band becomes being captured by a (random) geometrical constraint acquired in the course of plastic flow, the longer it passes in the constraint region, the more powerful becomes the constraint itself due to the resulting reduction in the cross-section area.

The evolution of the PLC band after the UTS is reached (and before its complete immobilization) testifies that the concurrency between the necking development and the attempts of the PLC band to leave the localization site may last quite a long time (Figs. 4.3-5, 4.9). As unexpected as it could have seemed, this observation agrees with the well-known property of the slow rate of neck development, which allows for a significant straining before fracture. A more surprising observation concerns its intermittent character. It is particularly evident in the case of type *B* or type *C* behavior characterized by series of (correlated or not) static bands. It occurs that when the banding is already arrested in one region, the further necking process does not become continuous but inherits the intermittent nature of the PLC effect (Figs. 4.5, 4.6, 4.9). Such intermittence can be explained by the abrupt unloading caused by the PLC bands, leading to a temporary interruption of the fast straining and its resuming upon reloading. In some cases, the unloading does not fully stop the localized straining, and the local strain-rate pattern is transformed into a beat (Figs. 4.7, 4.8). It can be concluded on the whole that the necking and the PLC instability coexist until fracture. In particular, this process gives rise to stress oscillations on the descending part of the (engineering) deformation curve. Such a persistence of the PLC instability and its coexistence with the necking instability did not receive a deserved attention from researchers so far. Nevertheless, the fact that undulatory deformation curves are systematically observed during necking (see Chap. 1) testifies to a common character of this behavior. It is noteworthy in this context that the PLC effect and deformation band propagation were also

reported for notched specimens where the strain non-uniformity was imposed by the initial specimen geometry [Graff et al., 2004].

Whereas the above discussion was mostly concentrated on the influence of the PLC instability on necking, the data also demonstrate the inverse influence. It is the most obvious in the tests on the FGH A1 samples deformed at intermediate strain rates. Indeed, in this case, the quasi-continuous propagation of a PLC band related to a smooth flow before necking is substituted with intermittent strain localization and oscillations on the deformation curve. In other words, the strain localization imposed by the necking instability forces a transition from the propagation to localization type of behavior of the PLC instability. The same tendency can be seen when a PLC band propagating in the FGH A2 sample or, in a range of high strain rates, in CG and FG materials, is transformed into a beat (Fig. 4.8).

#### **4.5. Concluding remarks**

In summary of the present Chapter, despite the ubiquitous presence of the strain-rate softening PLC instability and the diversity of behaviors of the PLC bands observed in two AlMg-based alloys with different initial microstructures, the necking was never observed to onset before the Considère strain determined for smoothed deformation curves. At the same time, the DIC analysis reveals a close relationship between the neck formation and the prior PLC bands. The entirety of various scenarios observed experimentally can be rationalized in a unique framework considering that the neck is formed through immobilization of the PLC bands. The process involves two concurrent trends. On the one hand, the strain produced by a PLC band must help to create conditions for the geometric instability. On the other hand, the concomitant local work hardening caused by fast straining within the PLC band maintains its propagation to the less hardened cross-sections.

It can be concluded that two physically different kinds of plastic instability, namely, the material-dependent strain-rate softening (the PLC effect), which leads to transient strain localizations propagating along the crystal, and the geometric instability (necking) bounding the strain localization to one site, may coexist during the neck development. Moreover, evidences are found that the two kinds of instability modify each other's behavior. In particular, the strain localization upon the onset of necking in the FGH samples forces the transition from mobile to static PLC bands giving rise to oscillatory deformation curves. More generally, the concurrency of the trends to the strain propagation and strain localization gives rise to a beat in the spatiotemporal maps.

# Chapter 5

## Effect of microstructure on the statistics of instabilities

As underlined in the literature review in Chap. 1, the PLC effect is associated with complex patterns of stress serrations related to nucleation and motion of deformation bands in the deforming material, and requires investigation of self-organization of dislocations responsible for their dynamics. Although self-organization in complex dissipative systems generally results in very sophisticated behaviors, it turns out that this complexity often allows for quantitative characterization due to specific scaling properties hidden in the evolution of dynamic variables. Various kinds of scaling analysis, reported in the literature, allowed for a better understanding of dynamical mechanisms giving rise to the transition between different types of behavior of the PLC effect.

Previous chapters revealed peculiarities in both the stress serration sequences and the kinematics of deformation bands in the investigated AlMg-based alloys containing precipitates and/or submicron grains. It was shown that these microstructural features can promote one or another type of spatiotemporal patterns of the PLC effect and, therefore, have an impact on the mechanisms of collective behavior of dislocations. These findings have motivated a statistical approach to stress serrations and the accompanying acoustic emission, so far applied to a multiscale study of collective effects in binary alloys (see Chap. 1). In the present chapter, this approach was used to investigate jerky flow in the A3 alloy in CG and FG states.

### 5. 1. Stress serrations

Details of mechanical behavior and kinematics of different PLC bands observed in CG and FG microstructure conditions of A3 alloy were reported in Chap. 3. A short outline of the above-described results, necessary for understanding the specific features of statistics of deformation processes, is repeated below.

Figure 5.1 compares examples of stress-strain curves for samples of A3 alloy in CG and FG states. In the CG case, the PLC effect is observed for  $\dot{\epsilon}_a$  above  $10^{-4} \text{ s}^{-1}$  (Fig. 5.1a, curves 1–3). It sets on after some critical strain depending on  $\dot{\epsilon}_a$  [Lebedkina and Lebyodkin, 2008]. The smooth character of curve 4 testifies that the corresponding strain-rate lies below

the strain-rate domain of plastic instability. In the FG state, jerky flow starts immediately after the onset of plastic flow and occurs in the whole range of strain rates (Fig. 5.1b).

The curves obtained in the CG state present signatures of the main types of behavior of the PLC effect (Fig. 5.1a): Curve 1 demonstrates type *A* serrations over a large portion of the curve, which become superimposed with type *B* oscillations at large strains; Well-developed type *B* behavior becomes preponderant at intermediate strain rates (curve 2); Yet deeper type *C* serrations occur close to  $10^{-4} \text{ s}^{-1}$  (curve 3). More specifically, the serration patterns are somewhat atypical at middle strain rates where a mixture of signatures of all three types can be recognized. Anyhow, the overall changes in the patterns produced by  $\dot{\epsilon}_a$  variations correspond to the habitual sequence of transitions between the common types.

For the FG material, type *B* serrations dominate at strain rates of  $10^{-3} - 1.4 \times 10^{-2} \text{ s}^{-1}$  (Fig. 5.1b, curves 1-2), while crude type *A* patterns superimposed with type *B* oscillations are only discernible at the highest strain rate of  $4.3 \times 10^{-2} \text{ s}^{-1}$  (curve 1). Type *C* stress drops occur at  $1.4 \times 10^{-4} \text{ s}^{-1}$  and  $3 \times 10^{-5} \text{ s}^{-1}$  (curves 3 and 4 in Fig. 5.1b). In contrast to the usual behavior of binary CG alloys, characterized by stress serrations intensifying with deformation, the end of the low-strain rate tests on the FG alloy displays a significant smoothing of the deformation curves, so that stress oscillations become weaker or almost disappear.

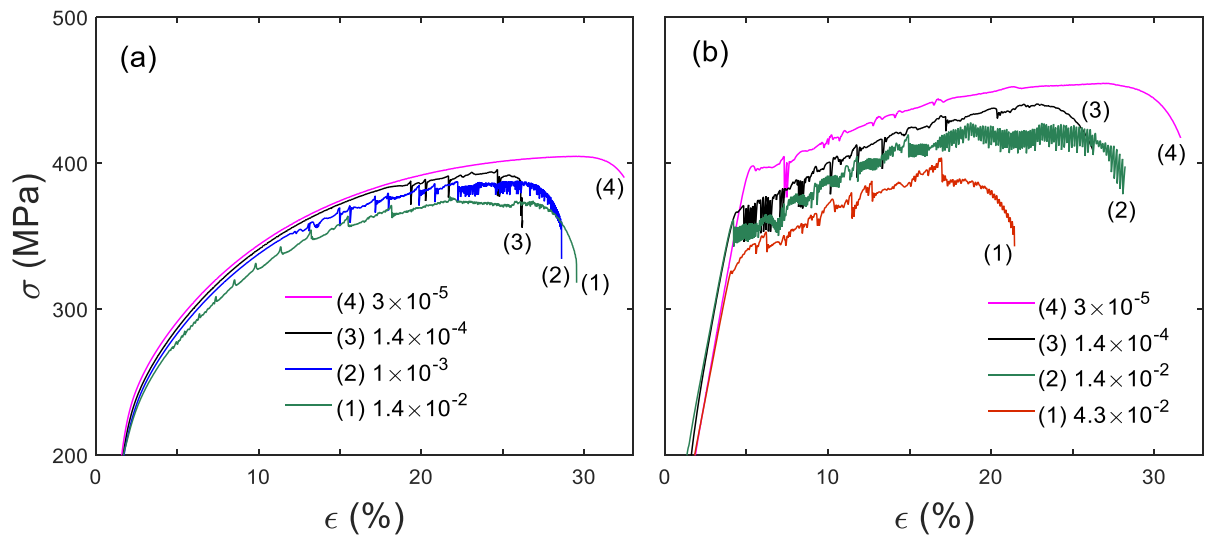


Figure 5.1: Examples of engineering stress-strain curves  $\sigma(\epsilon)$  of A3 alloy: (a) CG state, (b) FG state. The values of the imposed strain rate are given in  $\text{s}^{-1}$ . For clarity, curve 1 in the chart (b) is shifted by 20 MPa downwards.

The analysis of the corresponding strain-rate maps in §§ 3.3.1, 3.3.2 showed that overall behavior is characterized by an unusual proneness to the propagation mode both in

the CG and FG states. The regular propagation of deformation bands was found to be dominant even at the low strain rate, where deep stress drops expectedly correspond to static deformation bands and smooth intervals are related to the continuous band propagation.

The statistical distributions of amplitudes of stress serrations in the CG material qualitatively agree with those reported for binary alloys [Pink and Weinhandl, 1998; Lebedkina and Lebyodkin, 2008; Lebyodkin et al., 2012; Chinh et al., 2012]. Curve 1 in Fig. 5.2 demonstrates a power-law PDF,  $P(\Delta s) \propto \Delta s^{-\alpha}$ , at  $\dot{\epsilon}_a = 1.4 \times 10^{-2} \text{ s}^{-1}$ . This behavior agrees with the SOC hypothesis generally discussed in the case of type *A* serrations. Moreover, such scale invariance covers four orders of serrations magnitude, although it is usually observed over shorter intervals, about two orders of magnitude or less. The values of critical exponent  $\alpha$  found for different samples deformed at  $\dot{\epsilon}_a \geq 10^{-3} \text{ s}^{-1}$  lie within the interval between 1 and 1.8 commonly reported in the literature. Deep type *B* or type *C* serrations give rise to a characteristic scale (Fig. 5.3). At the same time, as described in Chap. 1.5 (see Fig. 1.23), the amplitude distributions obtained at slow deformation are often bimodal and contain a small-scale branch obeying a power law. It occurs that in comparison with binary AlMg alloys, this feature is much more pronounced in the studied material (see Legend of Fig. 5.3). Curve 2 in Fig. 5.2 represents such a  $P(\Delta s)$ -dependence in log-log coordinates for the lowest strain rate at which plastic instability was observed in CG material. The rare deep type *C* serrations correspond to two dots at the right edge of the PDF. The amplitudes of small serrations display a power law over more than one order of  $\Delta s$ , with saturation at low values which is likely due to the stress resolution limit. However, in contrast to the data for a binary AlMg alloy with similar Mg content, for which  $\alpha$  in the range of 1–1.5 was found at low strain rates [Lebyodkin et al., 2012], the investigated alloy is characterized by  $\alpha$  about 2.5 (see figure caption). Since the higher  $\alpha$  means higher probabilities of smaller events relative to larger ones, this difference can be interpreted as a tendency to less correlated deformation processes in the alloy containing precipitates, in agreement with the very fact of the enhanced role of the small-scale events in comparison with type *C* serrations.

The statistical analysis of stress serrations in the FG alloy corroborates the above-discussed observations of changes in their morphology. Indeed, convincing scale-free behavior was only detected at low strain rates corresponding to apparent type *C* behavior,  $\dot{\epsilon}_a = 1.4 \times 10^{-4} \text{ s}^{-1}$ , as illustrated by curve 3 in Fig. 5.2, whereas histograms with a maximum reflecting a characteristic scale were obtained at medium and even high rates. It is noteworthy that scale-invariant behavior represented by curve 3 covers almost the entire

range of the observed amplitudes, so that the probability of deep drops only slightly deviates upward from the extrapolated straight line. The scatter between various samples deformed with the same strain rate prevents making a reliable comparison between the power-law dependences found at low  $\dot{\epsilon}_a$  in the FG and CG materials. Nevertheless, some tendency to lesser  $\alpha$ -values in the FG state for the same  $\dot{\epsilon}_a$  can be noticed, as illustrated by curves 2 and 3.

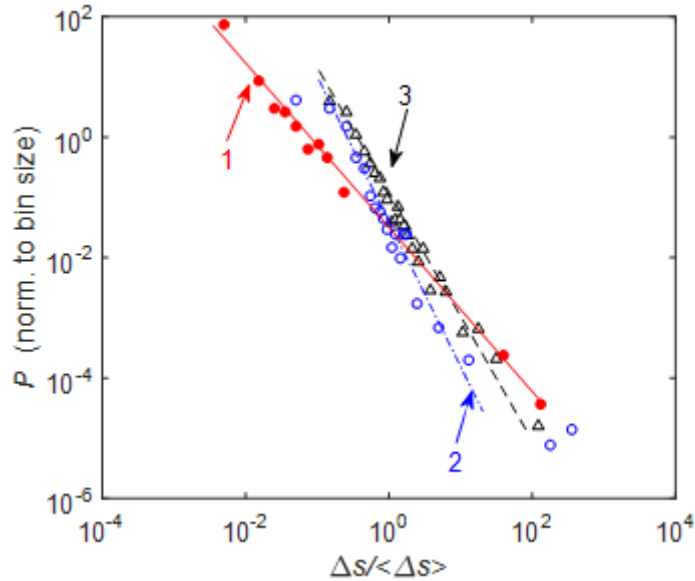


Figure 5.2: Examples of the probability density function  $P(\Delta s / \langle \Delta s \rangle)$  for amplitudes of serrations: 1 – CG alloy,  $\dot{\epsilon}_a = 1.4 \times 10^{-2} \text{ s}^{-1}$ ; the least-squares estimate of the slope and the corresponding root-mean-square error render  $\alpha \approx 1.4 \pm 0.1$ . 2 – CG alloy,  $\dot{\epsilon}_a = 1.4 \times 10^{-4} \text{ s}^{-1}$ ,  $\alpha \approx 2.5 \pm 0.2$ . 3 – FG alloy,  $\dot{\epsilon}_a = 1.4 \times 10^{-4} \text{ s}^{-1}$ ,  $\alpha \approx 1.9 \pm 0.1$ .

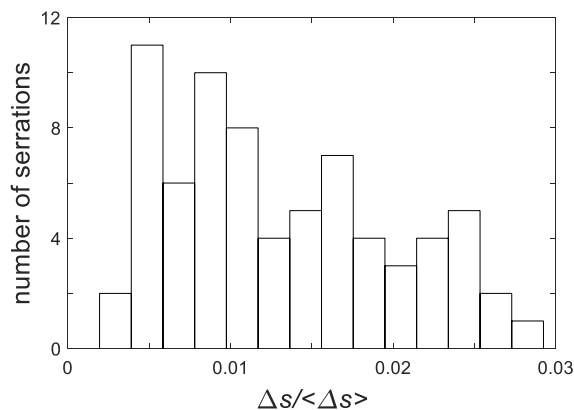


Figure 5.3: Example of a histogram of distribution of amplitudes of deep type *B* serrations for the CG alloy deformed at  $\dot{\epsilon}_a = 10^{-3} \text{ s}^{-1}$ . As the concomitant low-amplitude serrations are much more numerous and shade the histogram for deep serrations, a threshold was used to cut off small events.

Figure 5.4a presents an example of a peaked histogram, typical of type *B* serrations (cf. [Bharathi et al., 2001]), for one of the high strain-rate values,  $\dot{\epsilon}_a = 5 \times 10^{-3} \text{ s}^{-1}$ . More precisely, the histograms obtained in the fastest tests, at  $4.3 \times 10^{-2} \text{ s}^{-1}$ , reveal the common tendency to power-law distributions at fast deformation. Indeed, the example of Fig. 5.4b manifests a roughly monotonically descending dependence. However, even then, the seeming transition to scale-free behavior is far from being completed.

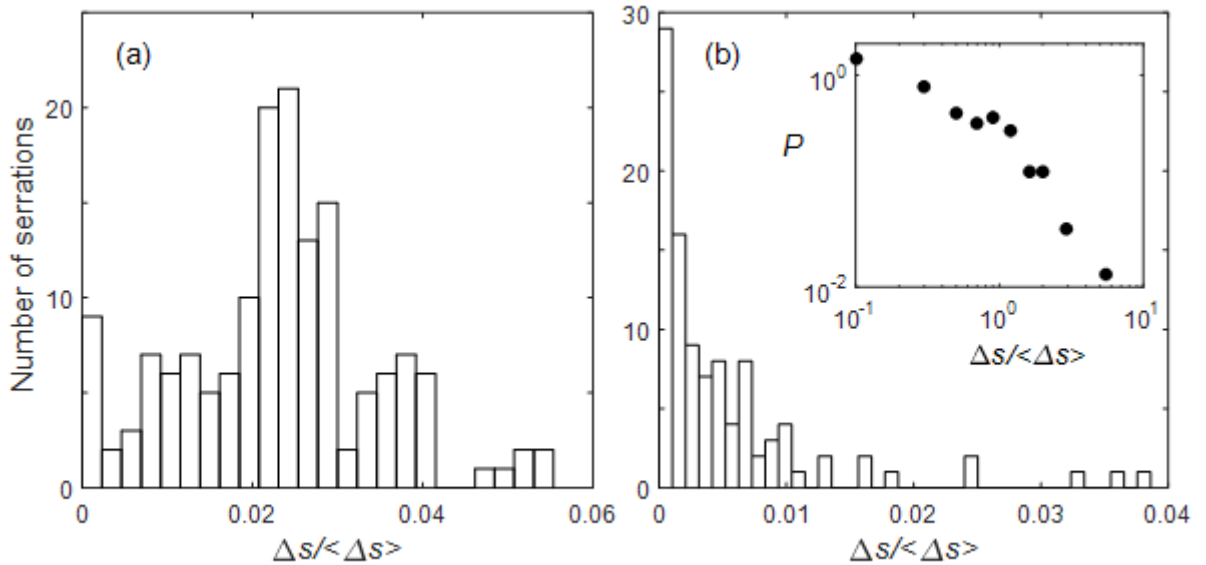


Figure 5.4: Examples of histograms of distribution of stress serration amplitudes for the FG alloy deformed at high strain rates: (a)  $\dot{\epsilon}_a = 5 \times 10^{-3} \text{ s}^{-1}$ , (b)  $\dot{\epsilon}_a = 4.3 \times 10^{-2} \text{ s}^{-1}$ .

Insert: the corresponding PDF dependence.

## 5.2. Acoustic emission

Figure 5.5 gives an example of evolution of AE during a mechanical test on a CG sample. The count rate traced in Fig. 5.5b represents the average AE activity that quantifies the frequency with which the acoustic signal crosses the threshold  $U_\theta$ . The overall evolution shown in the figure is typical of most materials [Mathis and Chmelik, 2012] and was observed in all experimental conditions in the present work. The AE occurs during elastic deformation, reaches maximum at the transition to macroscopic plasticity (yield limit), and further decreases in the course of deformation. The presence of AE during the elastic stage is usually explained by micro-plasticity [Maaß and Derlet, 2018]; the activity growth during the elastoplastic transition is explained by an intense multiplication of dislocations; and the further decrease is ascribed to the accumulation of obstacles to the motion of dislocations. The last factor can also justify the depression of the AE intensity at large strains, which can be recognized in Fig. 5.5c resolving series of amplitudes of individual hits.

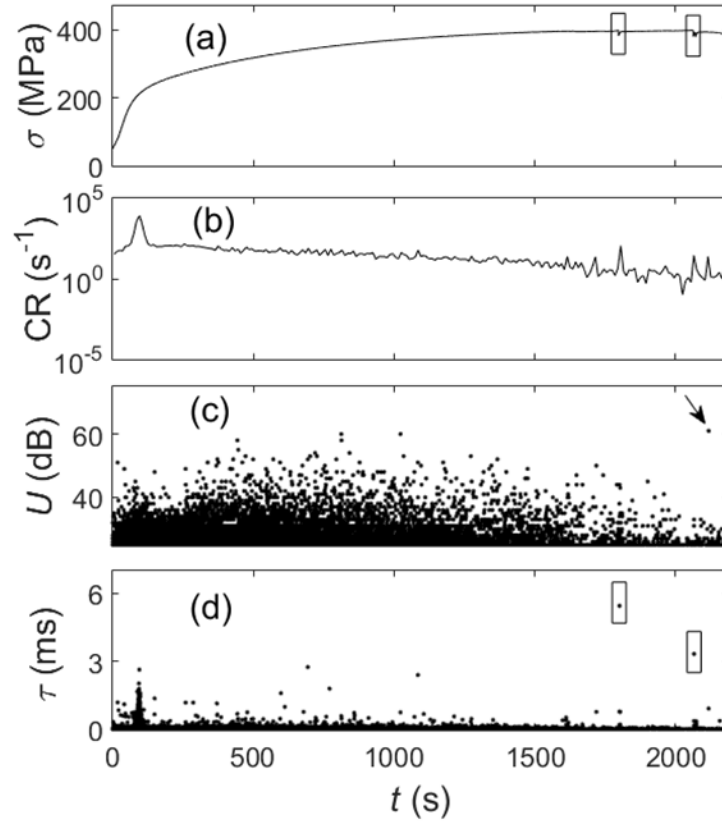


Figure 5.5: (a) Time-stress curve  $\sigma(t)$  and the evolution of various characteristics of the accompanying AE during testing a CG sample: (b) the average count rate (CR) calculated over 10 s time intervals, (c) logarithmic amplitudes  $U$  of AE events, and (d) the corresponding durations  $\tau$ .  $\dot{\varepsilon}_a = 1.4 \times 10^{-4} \text{ s}^{-1}$ . Rectangles in plots (a, d) show two macroscopic stress serrations and the respective bursts in  $\tau$ . The arrow in plot (c) indicates a high-amplitude event during macroscopically smooth plastic flow.

When the strain rate is varied, such series display diverse patterns similar to those described in detail for binary alloys [Lebedkina and Lebyodkin, 2008; Lebyodkin et al., 2012]. More specifically, Fig. 5.5 demonstrates that the conjecture of synchronization of dislocation avalanches as a mechanism of deep stress serrations (see. Chap. 1, Fig. 1.6) is also valid for the studied material. Indeed, the amplitudes of the hits occurring at the instants of stress drops do not stand out from those generated during smooth plastic flow. For example, the prominent event shown by an arrow in Fig. 5.5c does not correspond to a stress serration. On the other hand, the serrations are correlated with bursts in the event durations  $\tau$ , as marked by rectangles in Figs. 5.5a and 5.5d. As presented in Chap. 1, such bursts were explained in [15,16] in terms of synchronization of dislocation avalanches in the sense of the chaining of many acoustic events, each one reflecting the occurrence of a dislocation avalanche, so that they are recorded as a single event with a long duration. In comparison with this behavior, characteristic of type *C* serrations occurring downward from the general

stress level, bursts in both  $U$  and  $\tau$  are observed during stress rises accompanying type  $B$  and type  $A$  curves (Fig. 5.6). Such rises mark nucleation of a new deformation band after the material has been work-hardened by the passage of the previous band (type  $A$ ) or the previous sequence of bands (type  $B$ ) through the entire gage length.

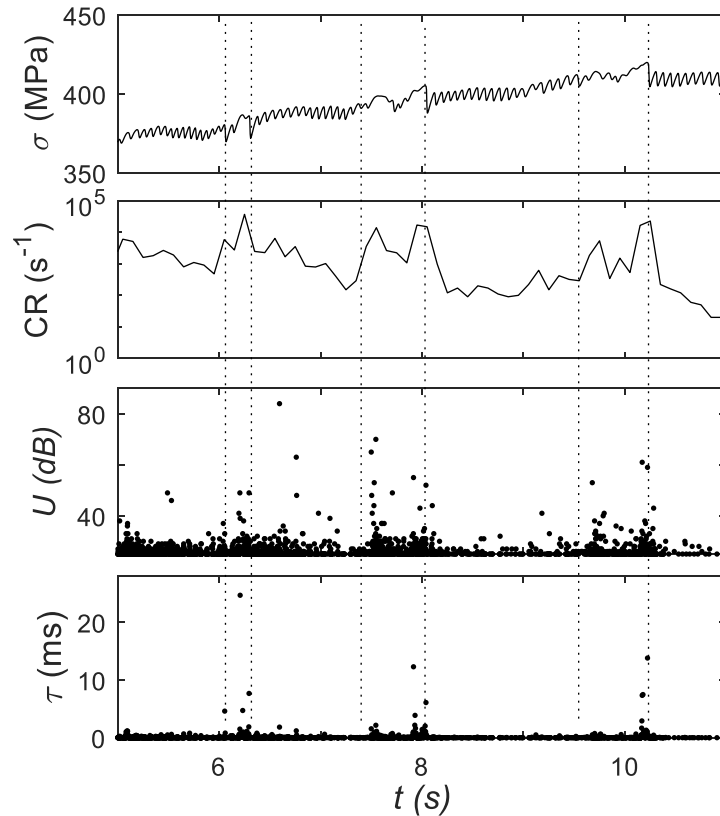


Figure 5.6: Plots similar to Fig. 5.5, for an FG sample deformed at  $\dot{\epsilon}_a = 1.4 \times 10^{-2} \text{ s}^{-1}$ . Pairs of vertical lines delineate the nucleation of new sequences of type  $B$  bands.

These observations apply to both CG and FG alloys. The major differences between these two cases are that for the same strain rate, the number of recorded events is usually lower, while their maximum amplitude can be much higher in the FG alloys. Typically,  $U$  reaches 60–70 dB in CG state and 60–90 (sometimes up to 100 dB) in the FG state (cf. Figs. 5.5 and 5.6).

As with the results for binary AlMg alloys (Chap. 1), the statistical analysis revealed power-law distributions of AE intensity,  $P(I) \propto I^{-\alpha_{AE}}$ , in all experimental conditions. Unexpectedly, investigated alloy demonstrated a qualitatively different effect of strain on the critical exponent  $\alpha_{AE}$ , as compared with that reported for binary alloys. Figure 5.7 presents examples of power-law dependences determined over two strain intervals for a CG alloy

deformed at  $\dot{\varepsilon}_a = 10^{-3} \text{ s}^{-1}$ . The respective slope is considerably lower at large strain, while an opposite trend was found in [Lebyodkin et al., 2012]. Such strain effect was observed in most tests. Figure 5.8 shows deformation curves with the evolution of  $\alpha_{AE}$  for one specimen of each kind and three strain rates. The strain dependences of  $\alpha_{AE}$  found for these and other samples are quite diverse, most likely because of the influence of the initial microstructure that may strongly vary between samples subjected to complex treatments. Nevertheless, several common features can be identified. The exponent usually takes on relatively low values during the initial quasi-elastic deformation. More exactly, it is close to the value of 2 which approaches typical exponents reported for various materials in the absence of dynamic strain aging and is similar to the exponent found in cyclic tension-compression of pure aluminum [Weiss et al., 2015]. Similar to results [Lebyodkin et al., 2012] for binary AlMg alloy, for convenience presented in Fig. 5.9,  $\alpha_{AE}$  strongly grows in the region of the elasto-plastic transition. However, whereas the  $\alpha_{AE}$ -values reported in [Lebyodkin et al., 2012] increase from 1.5-2 at the onset of plastic deformation to 2-3 during the unstable flow, the present results display a clear tendency to a decrease in  $\alpha_{AE}$  with further deformation. An exception to this rule is shown by solid lines in Fig. 5.8a. It corresponds to a CG specimen deformed at  $\dot{\varepsilon}_a = 1.4 \times 10^{-2} \text{ s}^{-1}$ , which demonstrates a pattern of macroscopic serrations very similar to that observed in binary alloys.

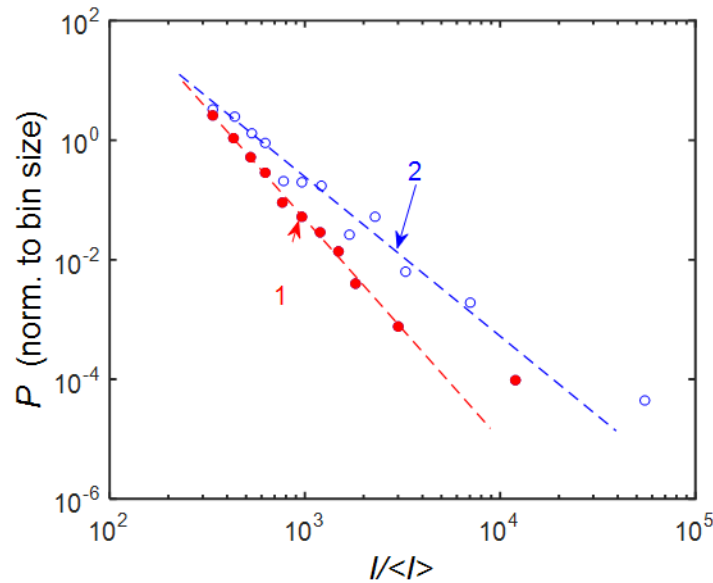


Figure 5.7: Examples of the probability density function  $P(I/\langle I \rangle)$  of the AE intensity for a CG sample deformed at  $\dot{\varepsilon}_a = 10^{-3} \text{ s}^{-1}$ . 1 – strain interval from 3% to 6 %,  $\alpha_{AE} \approx 3.6 \pm 0.1$ .

2 - strain interval from 15% to 20 %,  $\alpha_{AE} \approx 2.4 \pm 0.1$ .

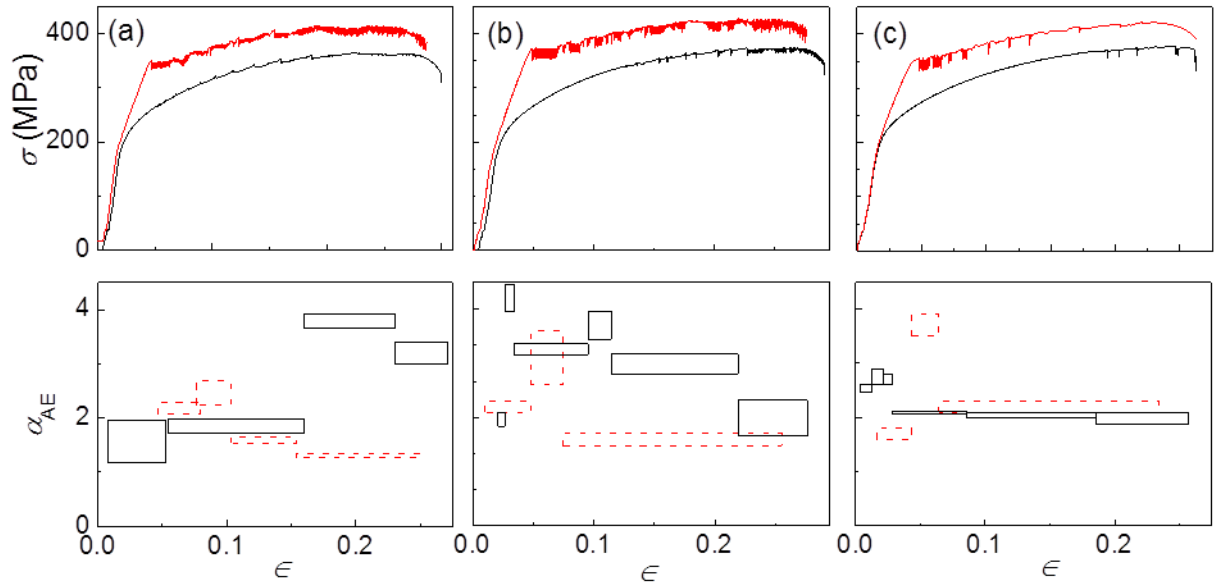


Figure 5.8: Examples of comparison of deformation curves with evolution of the critical exponent for the AE intensity statistics. (a)  $\dot{\epsilon}_a = 1.4 \times 10^{-2} \text{ s}^{-1}$ ; (b)  $\dot{\epsilon}_a = 10^{-3} \text{ s}^{-1}$ ; (c)  $\dot{\epsilon}_a = 1.4 \times 10^{-4} \text{ s}^{-1}$ . All deformation curves are traced using solid lines: The curves for the FG alloy pass above their counterparts for the CG alloy (cf. Fig. 1). Rectangles in the bottom plots show the length of the strain intervals over which  $\alpha_{AE}$ -values were estimated and the corresponding root-mean-square errors. Solid and dashed lines present results of calculation for the CG and UFG alloys, respectively.

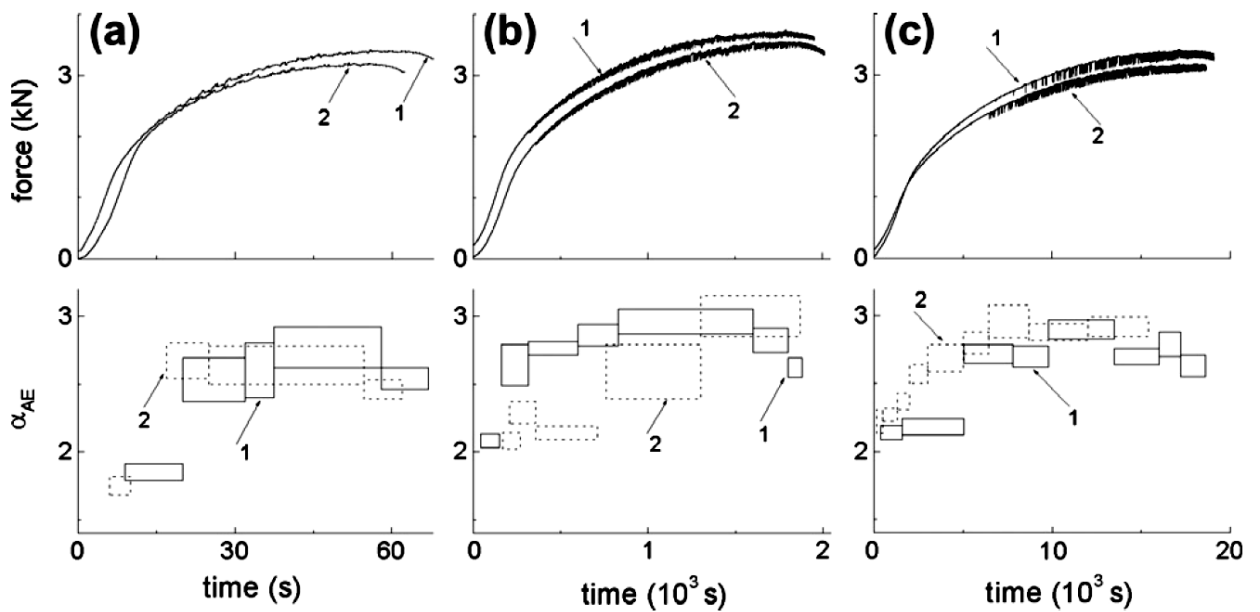


Figure 5.9: Force vs. time curves and variation of the power-law index  $\alpha_{AE}$  for the AE energy distribution for two samples of Al-3Mg alloy [Lebyodkin et al., 2012].

(a)  $\dot{\epsilon}_a = 6 \times 10^{-3} \text{ s}^{-1}$ ; (b)  $\dot{\epsilon}_a = 2 \times 10^{-4} \text{ s}^{-1}$ ; (c)  $\dot{\epsilon}_a = 2 \times 10^{-5} \text{ s}^{-1}$ .

The overlapping deformation curves are deliberately shifted along the ordinate axis.

Two more observations should be mentioned. First, for large enough strain,  $\alpha_{AE}$  is usually lower in the FG material than in the CG alloy, which agrees with the similar relationship for the statistics of stress serrations (see § 5.1). Finally, it is noteworthy that the maximum  $\alpha_{AE}$  observed for both investigated alloys is as high as 4, while it did not exceed 3 for binary alloys.

### 5.3. Discussion and concluding remarks

The results of the statistical analysis realized on the A3 alloy in CG and FG conditions corroborate the conclusions made in the previous Chapters, concerning peculiar behaviors of the PLC instability which occur in alloys with complex microstructures. The CG state displays an unusual proneness to power-law distributions over the entire  $\dot{\epsilon}_a$ -range (Fig. 5.2). This result agrees with the observation of the predominance of the PLC band propagation (type *A* behavior) for the same material (Chap. 3). The FG alloy displays even less common features, so that scale-free statistics are only observed at the lowest strain rate, in consistence with the unusual transition from type *C* to type *A* serrations after some deformation. Only a weak trend to power-law statistics can be recognized at high  $\dot{\epsilon}_a$ , in agreement with the incomplete *B* to *A* transition in the serration patterns. These distinct differences from behavior of binary alloys confirm the conjecture that the microstructure can strongly affect the self-organization of dislocations.

The analysis of the AE statistics corroborates the discussion in Chap. 3 and testifies that the peculiarities of both the PLC band kinematics and the statistics of instabilities at different scales are caused by the effect of microstructure on the relaxation and homogenization of internal stresses generated by strain localizations. As outlined in Chap. 1, the variation of the conditions for internal stress relaxation may explain the concurrence between SOC, leading to critical-type power-law statistics and associated with deformation band propagation, and synchronization phenomenon, giving rise to static deformation bands and histograms with a characteristic scale.

At a given strain rate, the effectiveness of relaxation processes depends on the material microstructure. In particular, observation of high  $\alpha_{AE}$ -values in binary AlMg alloys, as compared with various data for materials not showing the PLC effect, was attributed to a stronger randomization of dislocation processes in alloys because of the additional solute hardening and, therefore, an increase in the probability of small dislocations avalanches (Chap. 1). This framework directly applies to the present data displaying even higher upper

bounds of  $\alpha_{AE}$  during microplastic flow and elastoplastic transition in the material with complex initial microstructures than in the binary coarse-grained AlMg alloy. Indeed, it agrees with the suggestion made in Chap. 3 that the role of precipitates and grain boundaries as obstacles to the dislocation motion is important for explanation of the particular behavior of the PLC effect.

At the same time, the randomization of the dislocation motion cannot explain the strong decrease in  $\alpha_{AE}$  back to the value of 2 at larger strains (see Figs. 5.7 and 5.8). In addition, the tendency to lower  $\alpha_{AE}$ -values in the FG state than in the CG state also contradicts this model. To interpret the entirety of data, a competition of several factors should be considered. Indeed, while arresting mobile dislocations on obstacles breaks the correlation of deformation processes, the resulting concentration of internal stresses would act in the opposite sense and enhance the dislocation avalanches through nucleation and remobilization of dislocations in the same grain and initiation of dislocation glide in the neighboring grains. The latter assumption was applied to explain relatively low  $\alpha_{AE}$  in polycrystalline ice [Zaiser, 2007]. Again, grain boundaries may play even a more complex role, assisting either the local stress concentration because of the dislocation pinning, or its relaxation, e.g., by serving as sources of dislocations (see Chap. 1). For example, it may explain the globally weaker AE activity in FG alloy. The real behavior of complex alloys may thus result from a subtle balance between all these factors.

In summary, the results of AE investigations suggest a unique approach to interpretation of various serration patterns and, more generally, spatiotemporal behavior of the PLC effect. It should be underlined that the conjecture of a double role of precipitates and grain boundaries as obstacles and stress concentrators was engaged to explain both the decrease in  $\alpha_{AE}$  during deformation and the unusual PLC band propagation at low strain rates, in particular, the type  $C \rightarrow$  type  $A$  transition after some deformation (see Chap. 3). Although the fast and slow deformation regimes are known to correspond to qualitatively different dynamical modes of unstable flow, the formation of the macroscopic instability and the transitions between different regimes can be rationalized within a general framework considering dislocation avalanches as basic elements. Moreover, the validity of this approach does not only follow from the study of the PLC instability but is also corroborated by the avalanche-like character of smooth plastic flow on the AE scale.

# General conclusions and perspectives for future research

The Portevin-Le Chatelier effect is an outstanding example of self-organized behavior of dislocations manifesting itself on the macroscopic scale of deformation curves and strain localization bands. Investigations of jerky flow from this viewpoint have begun since more than twenty years. However, such studies were so far mostly carried out using model binary alloys. Even if commercial alloys were also considered, the objective of this work was similar to that on model materials and pursued the understanding of the basic dynamical mechanisms leading to well-known types of behavior, while the effect of the complex composition and microstructure on the mechanisms themselves remained virtually unexplored. These investigations were thus disconnected from the practical tasks of understanding the behavior of real alloys used in industry, the solution of which was mainly based on the traditional characterization of the microstructure and mechanical properties.

The present thesis was aimed at relating these two approaches. It was focused on comprehensive investigations of the effect of the microstructure on complex spatiotemporal behavior of the PLC instability in several materials including a model binary Al-3%Mg and three AlMg-based alloys with Zr and Sc additives and different initial microstructures. The study combined several experimental techniques making possible to access distinct scales of plastic flow processes, namely, mechanical testing in a wide strain-rate range, acoustic emission, high-frequency 1D local extensometry, and digital image correlation. In summary, the main results can be formulated as follows:

- An unusual mode of slow quasi-continuous propagation of deformation bands was found at low imposed strain rates in the alloys with precipitates (both coherent and incoherent) and in all FG alloys obtained by SPD. This dynamic is qualitatively different from the conventional pattern suggesting that the PLC bands propagate at high strain rates (type *A* behavior) but are static in the low strain-rate limit (type *C*). Moreover, the observed behavior is associated with an unusual proneness to quasi-continuous propagations at all strain rates, found for CG materials with precipitates. Besides, these samples demonstrate an atypical transition from type *C* to type *A* serration patterns taking place at a low constant strain rate after some deformation. At the same time, although FG materials also display the slow propagation mode, their overall behavior, strikingly similar for all alloys in the FG state, is different from the CG case in the range of intermediate and high strain rates, where it shows a strong tendency to relay-race propagation (type *B*). Finally, the plastic flow of the

FGH samples severely strained using the additional cold rolling after ECAP provided an interesting example of an apparently uniform deformation, if judged from the smooth deformation curves, which is nevertheless associated with the propagation of a PLC band.

An interpretation of these findings is proposed suggesting that the presence of additional obstacles to dislocation motion, precipitates and/or high density of grain boundaries, leads to local stress concentrations favoring the transfer of plastic flow to neighboring cross-sections, i.e., propagation of the strain localization. At the same time, the differences between coarse-grained and fine-grained cases implies that the role of grain boundaries is more complicated and must involve competing trends, both the pinning of dislocations, leading to stress concentrations, and the relaxation of internal stress, e.g., due to the escape of dislocations on the interfaces or dislocation multiplication.

- Visualization of the evolution of the local strain-rate field allowed to find evidence that two physically distinct mechanisms of plastic instability, namely the PLC effect related to the material-dependent strain-rate softening, and the necking stemming from geometric instability, are closely interrelated and modify each other's behavior. Despite the presence of the PLC effect, the Considère criterion for geometric instability occurs to describe well the onset of necking. Nevertheless, from the viewpoint of the specific mechanism of neck formation, it is prepared by the prior PLC bands, so that the neck is associated with a progressive immobilization of the PLC bands, ending by the ultimate strain localization. The subsequent neck development depends on the microstructural state, the strain rate, and the types of the PLC effect, and indicates the coexistence of two kinds of instability. Particularly, it displays unusual spatiotemporal patterns giving rise to regular stress oscillations and a beat in the local strain rate.

- The acoustic emission investigation of the PLC effect in a dispersion-hardened Al-Mg-Sc-Zr alloy in CG and FG conditions provided a different approach to the same problems, which corroborated the above hypothesis following from the study of the deformation band kinematics. The AE allows to reveal the avalanche-like nature of the dislocation dynamic on the time and energy scales much finer than those accessible to extensometry techniques. It is argued that the observed peculiarities of the AE statistics regarding the literature data for binary alloys, as well as the changes occurring after ECAP, can be interpreted in the same general framework considering the influence of the overstresses on the correlation of deformation processes. The observed effects of the strain and strain rate on the AE statistics bear evidence to a competition between the phenomena of synchronization and randomization of dislocation avalanches, which may be responsible for

the high variety of jerky flow patterns observed experimentally. It can thus be expected that the analysis of the factors controlling the strength of correlation between such avalanches may shed light on some peculiarities of behavior of applied alloys with complex composition and microstructure.

Two more results which were not studied in detail and require further investigation are noteworthy:

- Although the time resolution of the available DIC technique did not suffice for a minute survey of different phases of the development of deformation bands, a careful search of relevant time intervals allowed to observe weak diffuse bands prior and after the abrupt stress drops. The stress drop itself corresponds to a well-delineated PLC band characterized by a high intensity of strain-rate localization. This result does not corroborate the hypothesis of the PLC band formation via the phases of nucleation and growth of the nucleus but bears evidence to a simultaneous strain localization over the entire region of the forming band.
- The analysis of the power-law dependences of the PLC band velocity on the true stress and imposed strain rate testify that for a given material: (i) The velocity is likely to evolve with strain hardening according to the same law at different strain rates and (ii) It obeys a unique strain-rate dependence over the entire strain-rate range covering quasi-continuous (both type *A* and slow modes) and hopping propagation. At the same time, the obtained dependences depend on the material.

Besides these open questions, several issues that were not explored in this work should be mentioned:

- The hypothesis of the role of the local stress concentrations in the PLC band propagation implies a detailed investigation of the dislocation pinning by precipitates/grain boundaries and residual stresses with the aid of the electron microscopy and X-ray diffraction. First TEM data confirmed this hypothesis, as illustrated in Fig. I. It shows the microstructure of deformed CG and FG samples of the A4 alloy. Indeed, it can be seen that in both cases, the  $\text{Al}_3(\text{Sc,Zr})$  particles are mostly located in the vicinity or directly on the dislocations, while the areas free of dislocations contain few precipitates.

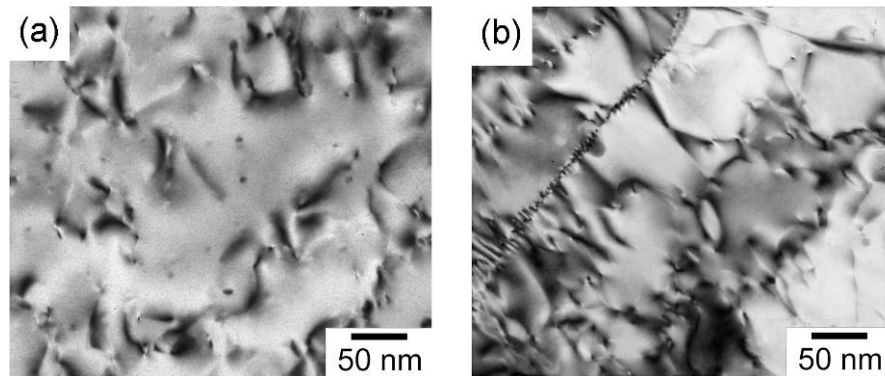


Figure I: Microstructure of the A4 alloy deformed till fracture at  $10^{-3} \text{ s}^{-1}$ : (a) CG state; (b) FG state. The TEM foils were cut approximately 10 mm from the fracture site.

- The present investigations were focused on two ranges of scales, namely, the coarse scale of the PLC bands and stress serrations, and the fine scale pertaining to the accompanying acoustic emission. It is known that optical methods of local extensometry, such as DIC, reveal a wavy or intermittent character of plastic flow on a mesoscopic scale intermediate with respect to these two scale ranges [Zuev, 2007; Mudrock et al., 2011; Fressengeas et al., 2009]. This phenomenon is usually studied in the conditions of a macroscopically smooth deformation. In the present work, rich patterns of small-scale heterogeneities were detected both before the onset of the PLC instability and during serrated flow, as can be remarked, e.g., in Figs. 3.2 and 3.15. Besides the general interest, this phenomenon also presents interest in relation with the PLC effect, e.g., from the viewpoint of nucleation and development of a macroscopic instability.

- In Chap. 4, the main accent was put on the relationship between the PLC instability and the onset of necking, while the ultimate fracture remained beyond the scope of this study. The real-time survey of the neck development in the region of the fracture, combined with the post-mortem investigations of the fracture surfaces, would provide important information on the fracture mode in dynamically strain-aging alloys.

- The investigation of the texture effect on the PLC instability also remained beyond the scope of this thesis. This was partly justified by the control measurements on the AlMg alloy, which showed that the Taylor factor  $M$  was very close in all material conditions. Namely, the EBSD figures provided estimates  $M = 3.1$  (CG, FG) and  $M = 3.22$  (FGH). It is also worth noting that very insignificant effects of texture on jerky flow were found up to now for Al-Mg [Eddahbi et al., 2012] or Al-Cu [Böhlke et al., 2009] alloys that showed relatively similar behaviors. Nevertheless, qualitative changes were reported for Al-Li alloys [Shen et al., 2004]. On the whole, although the texture evolution caused by SPD of Al-based alloys has been investigated in the literature, there exist very few data on the influence of texture on their jerky flow. It is thus of interest to extend the approaches used in the present thesis to alloys with controlled textures.

# Bibliography

[Abbadi et al., 2002] Abbadi M., Hähner P., Zeghloul A. On the characteristics of Portevin-Le Chatelier bands in aluminium alloy 5182 under stress-controlled and strain-controlled tensile testing, *Mater. Sci. Eng. A* 337 (2002) 194-201.

[Aboulfadl et al., 2015] Aboulfadl H., Deges J., Choi P., Raabe D. Dynamic strain aging studied at the atomic scale, *Acta Mater.* 86 (2015) 34-42.

[Ait-Amokhtar et al., 2006-1] Ait-Amokhtar H., Vacher P., Boudrahem S. Kinematics fields and spatial activity of Portevin-Le Chatelier bands using the digital image correlation method, *Acta Mater.* 54 (2006) 4365-4371.

[Ait-Amokhtar et al., 2006-2] Ait-Amokhtar H., Boudrahem S., Fressengeas C. Spatiotemporal aspects of jerky flow in Al–Mg alloys, in relation with the Mg content, *Scripta Mater.* 54(12) (2006) 2113-2118.

[Ait-Amokhtar and Fressengeas, 2010] Ait-Amokhtar H., Fressengeas C. Crossover from continuous to discontinuous propagation in the Portevin-Le Chatelier effect, *Acta Mater.* 58 (2010) 1342-1349.

[Ait-Amokhtar et al., 2015] Ait-Amokhtar H., Fressengeas C., Bouabdallah K. On the effects of the Mg content on the critical strain for the jerky flow of Al–Mg alloys, *Mater. Sci. Eng. A* 631 (2015) 209-213.

[Ananthakrishna and Bharathi, 2004] Ananthakrishna G., Bharathi M.S. Dynamical approach to the spatiotemporal aspects of the Portevin–Le Chatelier effect: Chaos, turbulence, and band propagation, *Phys. Rev. E* 70 (2004) 026111.

[Ananthakrishna, 2007] Ananthakrishna G. Current theoretical approaches to collective behavior of dislocations, *Physics Reports*, 440 (2007) 113-259.

[Ananthakrishna and Valsakumar, 1982] Ananthakrishna G., Valsakumar M. C. Repeated yield drop phenomenon: a temporal dissipative structure, *J. Phys. D: Appl. Phys.* 15 (1982) L171.

[Andreau et al., 2014] Andreau A., Gubicza J., Zhang N.X., Huang Y., Jenei P., Langdon T.G. Effect of short-term annealing on the microstructures and flow properties of an Al–1%Mg alloy processed by high-pressure torsion, *Mater. Sci. Eng. A* 615 (2014) 231–239.

- [Antolovich and Armstrong, 2014] Antolovich S.D., Armstrong R.W. Plastic strain localization in metals, *Prog. Mater. Sci.* 59 (2014) 1–160.
- [Bak et al., 1988] Bak P., Tang C., Wiesenfeld K. Self-organized criticality, *Phys. Rev. A* 38, (1988) 364-374.
- [Bakir, 1995] Bakir S., *Instabilité plastique propagative liée au phénomène Portevin-Le Chatelier dans les alliages aluminium-magnésium*, Doctoral Thesis, Université de Metz, 1995.
- [Bal k and Lukáč, 1993] Bal k J., Lukáč P. Portevin-Le Chatelier instabilities in Al-3Mg alloy conditioned by strain rate and strain, *Acta Metall. Mater.* 41 (1993) 1447–1454.
- [Bal k et al., 2000] Bal k ., Lukáč P., Kubin L. P. Inverse critical strains for jerky flow in Al-Mg alloys, *Scripta Mater.* 42(5) (2000) 465-471.
- [Bazarnik et al., 2012] Bazarnik P., Lewandowska M., Kurzydłowski K.J. Mechanical behavior of ultrafine grained Al-Mg alloys obtained by different processing routes, *Arch. Metall. Mater* 57 (2012) 869-876.
- [Bharathi et al., 2001] Bharathi M.S., Lebyodkin M., Ananthakrishna G., Fressengeas C., Kubin L.P. Multifractal Burst in the Spatiotemporal Dynamics of Jerky Flow, *Phys. Rev. Lett.* 87(16) (2001) 165508/1–165508/4.
- [Bharathi et al., 2002] Bharathi M. S., Lebyodkin M., Ananthakrishna G., Fressengeas C., Kubin L.P. The hidden order behind jerky flow, *Acta Mater.* 50 (2002) 2813–2824.
- [Bharathi and Ananthakrishna, 2002] Bharathi M.S., Ananthakrishna G. Chaotic and power law states in the Portevin-Le Chatelier effect, *Europhys. Lett.* 60 (2002) 234-240.
- [Böhlke et al., 2009] Böhlke T., Bondár G., Estrin Y., Lebyodkin M.A. Geometrically non-linear modeling of the Portevin–Le Chatelier effect, *Comput. Mater. Sci.* 44 (2009) 1076–1088.
- [Bird et al., 1987] Bird J.E., Newman K.E., Narasimhan K., Carlson J.M. Heterogeneous initiation and growth of sample-scale shear bands during necking of Al-Mg sheet, *Acta Metall* 35 (12) (1987) 2971-2982.

[Bougherira, 2011] Bougherira Y. Etude des phénomènes d'auto-organisation des ensembles de dislocations dans un alliage au vieillissement dynamique, Phd thesis, Université Paul Verlaine - Metz (2011).

[Bouaziz et al., 2011] Bouaziz O., Allain S., Scott C.P., Cugy P., Barbier D. High manganese austenitic twinning induced plasticity steels: A review of the microstructure properties relationships, *Current Opinion in Solid State and Materials Science* 15 (4) (2011) 141–168.

[Brechet and Estrin, 1994] Brechet Y., Estrin Y. On a pseudo-Portevin-Le Chatelier effect, *Scripta Metall. Mater.* 31 (2) (1994) 185-190.

[Brechet and Estrin, 1995] Brechet Y., Estrin Y. On the influence of precipitation on the Portevin-Le Chatelier effect, *Acta Metall. Mater.* 43 (3) (1995) 955–963.

[Brindley and Worthington, 1969] Brindley B.J., Worthington P.J. Serrated yielding in Aluminium-3% Magnesium, *Acta Metall.* 17 (1969) 1357-1361.

[Cai et al., 2016] Cai Y.L., Yang S.L., Wang Y.H., Fu S.H., Zhang Q.C. Characterization of the deformation behaviors associated with the serrated flow of a 5456 Al-based alloy using two orthogonal digital image correlation systems, *Mater. Sci. Eng. A* 664 (2016) 155–164.

[Casarotto et al., 2003] Casarotto L., Tutsch R., Ritter R., Weidenmuller J., Ziegenbein A., Klose F., Neuhäuser H. Propagation of deformation bands investigated by laser scanning extensometry, *Comput. Mater. Sci.* 26 (2003) 210-218.

[Casarotto et al., 2005] Casarotto L., Tutsch R., Ritter R., Dierke H., Klose F., Neuhäuser H. Investigation of PLC bands with optical techniques, *Comput. Mater. Sci.* 32 (2005) 316-322.

[Casarotto et al., 2009] Casarotto L., Dierke H., Tutsch R., Neuhäuser H. On nucleation and propagation of PLC bands in an Al–3Mg alloy, *Mater. Sci. Eng. A* 527 (2009) 132–140.

[Chihab et al., 1987] Chihab K., Estrin Y., Kubin L.P., Vergnol J. The kinetics of the Portevin-Le Chatelier bands in an Al-5at%Mg alloy, *Scr. Metall.* 21 (1987) 203–208.

[Chihab et al., 2002] Chihab K., Ait-Amokhtar H., Bouabdellan K. Serrated yielding due to Portevin-Le Chatelier effect in commercial Al-Mg alloys, *Ann. Chim. Sci. Mater.* 27 (2002) 69–75.

- [Chinh et al., 2012] Chinh N.Q., Gyori T., Gubicza J., Lendvai J., and Langdon T.G. Possible self-organized criticality in the Portevin–Le Chatelier effect during decomposition of solid solution alloys, *MRS Commun.* 2 (1) (2012) 1-4.
- [Chmelik et al., 1998] Chmelik F., Pink E., Krol J., Balak J., Pesicka J., Lukáč P. Mechanism of serrated flow in aluminium alloys with precipitates investigated by acoustic emission, *Acta Mater.* 46 (12) (1998) 4435-4442.
- [Chung et al., 1977] Chung N., Embury J.D., Evenson J.D., Hoagland R.G., Sargent C.M. Unstable shear failure in a 7075 aluminum alloy, *Acta Metall.* 25 (1977) 377–381.
- [Cottrell and Bilby, 1949] Cottrell A.H., Bilby B.A. Dislocation Theory of Yielding and Strain Ageing of Iron, *Proc. Phys. Soc. London A* 62 (1949) 49-62.
- [Cuddy and Leslie, 1972] Cuddy L.J., Leslie W.C. Some aspects of serrated yielding in substitutional solid solutions of iron, *Acta Metall.* 20(10) (1972) 1157-1167.
- [Curtin et al., 2006] Curtin W.A., Olmsted D.L., Hector L.G. A predictive mechanism for dynamic strain ageing in aluminium-magnesium alloys, *Nat. Mater.* 5 (2006) 875–880.
- [Davydov et al., 2000] Davydov V.G., Rostova T.D., Zakharov V.V., Filatov Yu.A., Yelagin V.I. Scientific principles of making an alloying addition of scandium to aluminium alloys, *Mater. Sci. Eng. A* 280 (2000) 30-36.
- [Davis, 1993] Davis J.R. Aluminum and aluminum alloys. Materials Park, OH: ASM International; 1993.
- [Darowicki et al., 2007] Darowicki K., Orlikowski J., Zieliński A., Jurczak W. Quadratic Cohen representations in spectral analysis of serration process in Al–Mg alloys, *Comp. Mater. Sci.* 39 (2007) 880-886.
- [Dierke et al., 2007] Dierke H., Krawehl F., Graff S., Forest S., Sachl J., Neuhäuser H. Portevin–LeChatelier effect in Al–Mg alloys: Influence of obstacles – experiments and modelling, *Computational Mater. Sci.* 39 (2007) 106-112.
- [Dorogovtsev et al., 2008] Dorogovtsev S.N., Goltsev A.V., Mendes J.F.F. Critical phenomena in complex networks, *Rev. Mod. Phys.* 80 (2008) 1275-1335.
- [Dritz et al., 1982] Dritz M.Ye., Toropova L.S., Bykov Yu.G., Yelagin V.I., Filatov Yu.A. Metallurgy and Metal Science of Non-ferrous Alloys, Nauka, Moscow, 1982, pp. 213–223.

- [Dimiduk et al., 2006] Dimiduk D.M., Woodward C., LeSar R., Uchic M.D. Scale-free intermittent flow in crystal plasticity, *Science* 312 (2006) 1188-1190.
- [Estrin and Kubin, 1990] Estrin Y., Kubin L.P. Collective dislocation behavior in dilute alloys and the Portevin-Le Chatelier effect, *J. Mech Behav. Mater.* 2 (1990) 255-292.
- [Estrin and Kubin, 1991] Estrin Y., Kubin L.P. Plastic instabilities: phenomenology and theory, *Mater. Sci. Eng. A* 137 (1991) 125-134.
- [Estrin and Kubin, 1995] Estrin Y., Kubin L.P., 1995. Spatial coupling and propagative plastic instabilities. In: Muhlhaus, H.-B. (Ed.), *Continuum Models for Materials with Microstructure*. John Wiley & Sons Ltd, pp. 395–450.
- [Eddahbi et al., 2012] Eddahbi M., Monge M.A., Muñoz A., Pareja R. Serrated flow in powder metallurgy Al-5%Mg-1.2%Cr alloy processed by equal channel angular pressing, *Mater. Charact.* 73 (2012) 16-30.
- [Estrin and Lebyodkin, 2004] Estrin Y., Lebyodkin M.A. The influence of dispersion particles on the Portevin–Le Chatelier effect: from average particle characteristics to particle arrangement, *Mater. Sci. Eng. A* 387–389 (2004) 195–198.
- [Estrin and Vinogradov, 2013] Estrin Y., Vinogradov A. Extreme grain refinement by severe plastic deformation: A wealth of challenging science, *Acta Mater.* 61 (2013) 782–817
- [Fazeli et al., 2008] Fazeli F., Poole W.J., Sinclair C.W. Modeling the effect of Al<sub>3</sub>Sc precipitates on the yield stress and work hardening of an Al–Mg–Sc alloy, *Acta Mater.* 56 (2008) 1909–1918.
- [Feng et al., 2012] Feng X., Fischer G., Zielke R., Svendsen B., Tillmann W. Investigation of PLC band nucleation in AA5754, *Mater. Sci. Eng. A* 539 (2012) 205-210.
- [Filatov et al., 2000] Filatov Yu.A, Yelagin V.I, Zakharov V.V. New Al-Mg-Sc alloys, *Mater. Sci. Eng. A* 280 (1) (2000) 97-101.
- [Fressengeas et al., 2009] Fressengeas C.; Beaudoin A.J., Entemeyer D., Lebedkina T., Lebyodkin M., Taupin V. Dislocation transport and intermittency in the plasticity of crystalline solids, *Phys. Rev. B* 79 (2009) 014108.

- [Gen Li et al., 2014] Gen Li, Naiqin Zhao, Tao Liu, Chunnian He, Chunsheng Shi, Enzuo Liu, Junwei Sha. Effect of Sc/Zr ratio on the microstructure and mechanical properties of new type of Al–Zn–Mg–Sc–Zr alloys, *Mater. Sci. Eng. A* 617 (2014) 219-227.
- [Girard et al., 2004] Girard S.X., Azari H., Wilkinson D.S. Effect of thermomechanical processing on grain structure development in a twin-belt strip cast automotive aluminum alloy, *Mater. Trans. A* 35 (2004) 949-952.
- [Graff et al., 2004] Graff S., Forest S., Strudel J.-L., Prioul C., Pilvin P., Béchade J.-L. Strain localization phenomena associated with static and dynamic strain ageing in notched specimens: experiments and finite element simulations, *Mater. Sci. Eng. A* 387–389 (2004) 181–185.
- [Greer and Hosson, 2011] Greer J. R., De Hosson J. Th. M. Plasticity in small-sized metallic systems: Intrinsic versus extrinsic size effect, *Prog. Mater. Sci.* 56 (2011) 654-724.
- [Hadianfard et al., 2008] Hadianfard M.J., Smerd R., Winkler S., Worswick M. Effects of strain rate on mechanical properties and failure mechanism of structural Al–Mg alloys, *Mater. Sci. Eng. A* 492 (2008) 283–292.
- [Hähner, 1996-1] Hähner P. On the physics of the Portevin–Le Chatelier effect part 1: The statistics of dynamic strain ageing, *Mater. Sci. Eng. A* 207 (1996) 208–215.
- [Hähner, 1996-2] Hähner P. On the physics of the Portevin–Le Chatelier effect part 2: From microscopic to macroscopic behavior, *Mater. Sci. Eng. A* 207 (1996) 216–23.
- [Haken, 1982] Haken H. *Synergetik - Eine Einführung*, Springer-Verlag, Berlin Heidelberg New York, 1982.
- [Halim et al., 2007] Halim H., Wilkinson D.S., Niewczas M. The Portevin-Le Chatelier (PLC) effect and shear band formation in an AA5754 alloy, *Acta Mater.* 55 (2007) 4151-4160.
- [Hallai and Kyriakides, 2013] Hallai J.F., Kyriakides S. Underlying material response for Lüders-like instabilities, *Int. J. Plast.* 47 (2013) 1-12.
- [Hill, 1952] Hill R. On discontinuous plastic states, with special reference to localized necking in thin sheets, *J. Mech. Phys. Solids*, 1 (1952) 19-30.

- [Hopperstad et al., 2007] Hopperstad O.S., Børvik T., Berstad T., Lademo O-G., Benallal A. A numerical study on the influence of the Portevin Le Chatelier effect on necking in an aluminium alloy, *Modelling Simul. Mater. Sci. Eng.* 15 (2007) 747–772.
- [Horvath et al., 2007] Horvath G., Chinh N.Q., Gubicza J., Lendvai J. Plastic instabilities and dislocation densities during plastic deformation in Al-Mg alloys, *Mater. Sci. Eng. A* 445–446 (2007) 186–192.
- [Huskins et al., 2010] Huskins E.L., Cao B., Ramesh K.T. Strengthening mechanisms in an Al–Mg alloy, *Mater. Sci. Eng. A527* (2010) 1292–1298.
- [Iliopoulos et al., 2015] Iliopoulos A.C., Nikolaidis N.S., Aifantis E.C. Portevin Le Chatelier effect and Tsallis nonextensive statistics, *Phys. A: Statist. Mech. and its Appl.* 438 (2015) 509-518.
- [Jiang et al., 2007] Jiang H., Zhang Q., Chen X., Chen Z., Jiang Z., Wu X., Fan J. Three types of Portevin-Le Chatelier effects: experiment and modeling, *Acta Mater.* 55 (2007) 2219-2228.
- [Jobba et al., 2015] Jobba M., Mishra R.K., Niewczas M. Flow stress and work-hardening behaviour of AlMg binary alloys, *Int. J. Plast.* 65 (2015) 43–60.
- [Jones and Humphreys, 2003] Jones M.J., Humphreys F.J. Interaction of recrystallization and precipitation: The effect of Al<sub>3</sub>Sc on the recrystallization behavior of deformed aluminium, *Acta Mater.* 51 (7) (2003) 2149–2159.
- [Junying Min et al., 2014] Junying Min, Jianping Lin, Bo Sun. Effect of strain rate on spatio-temporal behavior of Portevin–Le Châtelier bands in a twinning induced plasticity steel, *Mechanics of Materials* 68 (2014) 164–175.
- [Kang et al., 2005] Kang J., Wilkinson D.S., Embury J.D., Jain M., Beaudoin A.J. Effect of type-B Portevin–Le Chatelier bands on the onset of necking in uniaxial tension of strip cast AA5754 sheets, *Scripta Mater.* 53 (2005) 499–503.
- [Kang et al., 2006] Kang J., Wilkinson D.S., Jain M., Embury J.D., Beaudoin A.J., Kim S., Mishra R., Sachdev A.K. On the sequence of inhomogeneous deformation processes occurring during tensile deformation of strip cast AA5754, *Acta Mater.* 54 (2006) 209–218.

- [Kawamura et al., 2012] Kawamura H., Hatano T., Kato N., Biswas S., Chakrabarti B.K. Statistical physics of fracture, friction, and earthquakes, *Rev. Mod. Phys.* 84 (2012) 839-840.
- [Kendig and Miracle, 2002] Kendig K.L., Miracle D.B. Strengthening mechanisms of an Al-Mg-Sc-Zr alloy, *Acta Mater.* 50 (16) (2002) 4165–4175.
- [Kharakterova et al., 1994] Kharakterova M.L., Eskin D.G., Toropova L.S. Precipitation hardening in ternary alloys of the Al-Sc-Cu and Al-Sc-Si systems, *Acta Metall. Mater.* 42 (7) (1994) 2285-2290.
- [Klose et al., 2004] Klose F.B., Hagemann F., Hähner P., Neuhäuser H. Investigation of the Portevin-LeChâtelier effect in Al-3wt.%Mg alloys by strain-rate and stress-rate controlled tensile tests, *Mater. Sci. Eng. A* 387–389 (2004) 93–97.
- [Kobeleev et al., 2017]. Kobeleev N. P., Lebyodkin M.A., Lebedkina T.A. Role of Self-Organization of Dislocations in the Onset and Kinetics of Macroscopic Plastic Instability, *Metall. Mater. Trans A* 48(3) (2017) 965–974.
- [Kocks, 1981] Kocks U.F. In: *Progress in materials Science. Chalmers anniversary volume.* Oxford: Pergamon Press; 1981. p. 225
- [Kok et al., 2002] Kok S., Beaudoin A.J., Tortorelli D.A., Lebyodkin M.A. Finite Element Model for the Portevin–Le Chatelier Effect Based on Polycrystal Plasticity, *Modelling Simul. Mater. Sci. Eng.* 10 (2002) 745–763.
- [Kok et al., 2003] Kok S., Bharathi M.S., Beaudoin A.J., Fressengeas C., Ananthakrishna G., Kubin L.P., Lebyodkin M. Spatial coupling in jerky flow using polycrystal plasticity, *Acta Mater.* 51 (2003) 3651–3662.
- [Konstantinidis and Aifantis, 2002] Konstantinidis A.A., Aifantis E.C. Recent developments in gradient plasticity - Part II: Plastic heterogeneity and wavelets, *J. Eng. Mater. Technol.* 124 (2002) 358-364.
- [Komarasamy and Mishra, 2014] Komarasamy M., Mishra R.S. Serration behavior and shear band characteristics during tensile deformation of an ultrafine-grained 5024 Al alloy, *Mater. Scie. Eng. A* 616 (2014) 189–195.

- [Korbel et al., 1986] Korbel A., Embury J.D., Hatherly M., Martin P.L., Erbsloh H.W. Microstructural aspects of strain localization in Al-Mg alloys, *Acta Metall* 34 (10) (1986) 1999-2009.
- [Král and Lukáč, 1997] Král R., Lukáč P. Modelling of strain hardening and its relation to the onset of Portevin-Le Chatelier effect in Al-Mg alloys, *Mater. Scie. Eng. A* 234-236 (1997) 786-789.
- [Kubin, 1993] Kubin L.P. Dislocation patterning, *Treatise in Materials Science and Technology* (edited by H. Mughrabi), Wiley-VCH, Weinberg, Vol. 6 (1993).
- [Kubin et al., 2002] Kubin L.P., Fressengeas C., Ananthakrishna G. Collective behavior of dislocations in plasticity, *Dislocations in Solids* (edited by F.R.N. Nabarro and M.S. Duesbery) Elsevier Science BV, Amsterdam, Vol. 11 (2002) p. 101.
- [Kubin and Estrin, 1985] Kubin L.P., Estrin Y. The Portevin-Le Chatelier effect in deformation with constant stress rate, *Acta Metall.* 33 (3) (1985) 397–407.
- [Kubin and Estrin, 1990] Kubin L.P., Estrin Y. Evolution of dislocation densities and the critical conditions for the Portevin-Le Châtelier effect, *Acta Metall. Mater.* 38 (1990) 697–708.
- [Kubin and Estrin, 1991] Kubin L.P., Estrin Y. Dynamic strain ageing and the mechanical response of alloys, *J. Phys. III France* 1 (1991) 929-943.
- [Kugiumtzis et al., 2004] Kugiumtzis D., Kehagias A., Aifantis E.C., Neuhäuser H. Statistical analysis of the extreme values of stress time series from the Portevin–Le Châtelier effect, *Phys. Rev. E* 70 (2004) 036110.
- [Kumar and Ananthakrishna, 2011] Kumar J., Ananthakrishna G. Multiscale modeling approach to acoustic emission during plastic deformation, *Phys. Rev. Lett.* 106 (2011) 106001.
- [Kumar and Ananthakrishna, 2018] Kumar J., Ananthakrishna G. Modeling the complexity of acoustic emission during intermittent plastic deformation: Power laws and multifractal spectra, *Phys. Rev. E* 97 (2018) 012201.
- [Kumar and Pink, 1995] Kumar S., Pink E. Effect of  $\delta'$  precipitates on serrated flow, *Scripta Metall. Mater.* 32(5) (1995) 749-753.

[Le Chatelier, 1909] Le Chatelier A. Influence du temps et de la température sur les essais au choc, *Revue de Métallurgie* 6 (1909) 914-917.

[Lebyodkin and Estrin, 2005] Lebyodkin M.A., Estrin Y. Multifractal analysis of the Portevin–Le Chatelier effect: General approach and application to AlMg and AlMg/Al<sub>2</sub>O<sub>3</sub> alloys, *Acta Mater.* 53 (2005) 3403–3413.

[Lebedkina and Lebyodkin, 2008] Lebedkina T.A., Lebyodkin M.A. Effect of deformation geometry on the intermittent plastic flow associated with the Portevin–Le Chatelier effect, *Acta Mater.* 56 (2008) 5567–5574.

[Lebedkina and Lebyodkin, 2009] Lebedkina T.A., Lebyodkin M.A., Château J.-Ph., Jacques A., Allain S. On the mechanism of unstable plastic flow in an austenitic FeMnC TWIP steel, *Mater. Sci. Eng. A* 519 (2009) 147–154.

[Lebedkina et al., 2014] Lebedkina T.A., Lebyodkin M.A., Lamark T.T., Janecek M., Estrin Y. Effect of equal channel angular pressing on the Portevin–Le Chatelier effect in an Al<sub>3</sub>Mg alloy, *Mater. Sci. Eng. A* 615 (2014) 7–13.

[Lebedkina et al., 2018-1] Lebedkina T.A., Zhemchuzhnikova D.A., Lebyodkin M.A. Correlation versus randomization of jerky flow in an AlMgScZr alloy using acoustic emission, *Phys. Rev. E* 97 (2018) 013001.

[Lebedkina et al., 2018-2] Lebedkina T.A., Bougherira Y., Entemeyer D., Lebyodkin M.A., Shashkov I.V. Crossover in the scale-free statistics of acoustic emission associated with the Portevin-Le Chatelier instability, *Scripta Mater.* 148 (2018) 47-50.

[Lebyodkin et al., 1995] Lebyodkin M.A., Brechet Y., Estrin Y., Kubin L.P. Statistics of the catastrophic slip events in the Portevin-Le Chatelier effect, *Phys. Rev. Lett.* 74 (1995) 4758-4761.

[Lebyodkin et al., 2000] Lebyodkin M., Dunin-Barkowskii L., Brechet Y., Estrin Y., Kubin L.P. Spatio-temporal dynamics of the Portevin-Le Chatelier effect: Experiment and modelling, *Acta Mater.* 48 (2000) 2529–2541.

[Lebyodkin and Lebedkina, 2008] Lebyodkin M.A., Lebedkina T.A. Multifractality and randomness in the unstable plastic flow near the lower strain-rate boundary of instability, *Phys. Rev. E* 77 (2008) 026111.

[Lebyodkin et al., 2012] Lebyodkin M.A., Kobelev N.P., Bougherira Y., Entemeyer D., Fressengeas C., Gornakov V.S., Lebedkina T.A., Shashkov I.V. On the similarity of plastic flow processes during smooth and jerky flow: Statistical analysis, *Acta Mater.* 60 (2012) 3729–3740; On the similarity of plastic flow processes during smooth and jerky flow in dilute alloys. *Acta Mater.* 60 (2012) 844-850.

[Louche et al., 2005] Louche H., Vacher P., Arrieux R. Thermal observations associated with the Portevin–Le Châtelier effect in an Al–Mg alloy, *Mater. Sci. Eng. A* 404 (2005) 188–196.

[Maaß and Derlet, 2018] Maaß R., Derlet P.M. Micro-plasticity and recent insights from intermittent and small-scale plasticity, *Acta Mater.* 143 (2018) 338-363.

[Malopheyev and Kaibyshev, 2015] Malopheyev S., Kaibyshev R. Strengthening mechanisms in a Zr-modified 5083 alloy deformed to high strains, *Mater. Sci. Eng. A* 620 (2014) 246–252.

[Marquis and Seidman, 2005] Marquis E.A., Seidman D.N. Coarsening kinetics of nanoscale Al<sub>3</sub>Sc precipitates in an Al-Mg-Sc alloy, *Acta Mater.* 53 (15) (2005) 4259–4268.

[Marsha E. van Dalen et al., 2005] Marsha E. van Dalen, Dunand D.C., Seidman D.N. Effects of Ti additions on the nanostructure and creep properties of precipitation-strengthened Al-Sc alloys, *Acta Mater.* 53 (2005) 4225–4235.

[Markushev and Murashkin, 2013] Markushev M.V., Murashkin M.Yu. Structure and mechanical properties of commercial Al–Mg 1560 alloy after equal-channel angular extrusion and annealing, *Mater. Sci. Eng. A* 367 (2004) 234–242.

[Masson, 1841] Masson A.M. Sur l'élasticité des corps solides, *Ann. Chim. Phys.* 3 (1841) 451-462.

[Mathis and Chmel k, 2012] Mathis K., Chmel k F. *Acoustic Emission* (edited by W. Sikorsky), IntechOpen (2012), Rijeka, Croatia.

[Mazière et al., 2010] Mazière M., Besson ., Forest S., Tanguy B., Chalons H., Vogel F. Numerical aspects in the finite element simulation of the Portevin–Le Chatelier effect, *Comput. Methods Appl. Mech. Eng.* 199 (2010) 734–754.

- [Mazière and Dierke, 2012] Mazière M., Dierke H. Investigations on the Portevin Le Chatelier critical strain in an aluminum alloy, *Comput. Mater. Sci.* 52 (2012) 68–72.
- [McCormic, 1972] McCormick P.G. Serrated yielding and the occurrence of strain gradients in an Al-Cu alloy, *Scr. Metall.* 6 (1972) 165–170.
- [McCormic, 1988] McCormick P.G., Theory of flow localization due to dynamic strain ageing, *Acta Metall.* 36 (1988) 3061-3067.
- [McCormick et al., 1993] McCormick P.G., Venkadesan S., Ling C.P. Propagative instabilities: An experimental view, *Scripta Metall. Mater.* 29 (1993) 1159-1164.
- [McCormick and Ling, 1993] McCormick P.G., Ling C.P. Numerical modelling of the Portevin-Le Chatelier effect, *Acta Metal. Mater.* 43 (1995) 1969-1977.
- [McDonald, 2009] McDonald R.J. Characterization of delamination in 2099-T861 aluminum-lithium, PhD thesis, University of Illinois at Urbana-Champaign –USA (2009).
- [Meng et al., 2018] Meng X., Liu B., Luo L., Ding Y., Xi-Xin Rao, Hu B., Liu Y., Lu J. The Portevin-Le Châtelier effect of gradient nanostructured 5182 aluminum alloy by surface mechanical attrition treatment, *Journal of Mater. Sci. & Technology* 34 (2018) 2307-2315.
- [Mogucheva et al., 2013] Mogucheva A., Babich E., Ovsyannikov B., Kaibyshev R. Microstructural evolution in a 5024 aluminum alloy processed by ECAP with and without back pressure, *Mater. Sci. Eng. A* 560 (2013) 178–192.
- [Mogucheva et al., 2016] Mogucheva A., Yuzbekova D., Kaibyshev R., Lebedkina T., Lebyodkin M. Effect of grain refinement on jerky flow in an Al-Mg-Sc alloy, *Metall. Mater. Trans. A* 47 (2016) 2093-2106.
- [Mudrock et al., 2011] Mudrock R.N., Lebyodkin M.A., Kurath P., Beaudoin A.J., Lebedkina T.A. Strain-rate fluctuation during macroscopically uniform deformation of a solution-strengthened alloy, *Scr. Mater.* 65 (2011) 1093–1096.
- [Mulford, 1979] Mulford R.A. The effect of precipitation hardening on dynamic strain aging and jerky flow, *Metallurg. Trans A* 10 (1979) 1527- 1532.
- [Nicolis and Prigogone, 1977] Nicolis G., Prigogine I. Self-organization in nonequilibrium systems: from dissipative structures to order through fluctuations, Wiley (1977) New York.

- [Nikulin et al., 2012] Nikulin I., Kipelova A., Malopheyev S., Kaibyshev R. Effect of second phase particles on grain refinement during equal-channel angular pressing of an Al–Mg–Mn alloy, *Acta Mater.* 60 (2012) 487–497.
- [Nogueira et al., 2011] Nogueira de Codes R., Hopperstad O.S., Engler O., Lademo O.-G., Benallal A. Spatial and Temporal Characteristics of Propagating Deformation Bands in AA5182 Alloy at Room Temperature, *Metall. Mater. Trans. A* 42 (2011) 3358-3369.
- [Norman et al., 1998] Norman A.F., Pragnell B.P., McEwen R.S. The solidification behavior of dilute aluminium-scandium alloys, *Acta Mater.* 46 (1998) 5715-5732.
- [Noronha et al., 1997] Noronha S.J., Ananthakrishna G., Quaouire L., Fressengeas C., Kubin L.P. Chaos in the Portevin-Le Chatelier effect, *Int. J. Bifurcation Chaos*, 7 (1997) 2577-2586.
- [Pineau et al., 2016] Pineau A., Benzerga A.A., Pardoën T. Failure of metals I: Brittle and ductile fracture, *Acta Mater.* 107 (2016) 424-483.
- [Pink, 1989] Pink E. The effect of precipitates on characteristics of serrated flow in AlZn<sub>5</sub>Mg<sub>1</sub>, *Acta Metall.* 37 (7) (1989) 1773-1781.
- [Park and Niewczas, 2008] Park D.Y., Niewczas M. Plastic deformation of Al and AA5754 between 4.2 K and 295 K, *Mater. Sci. Eng. A* 491 (2008) 88–102.
- [Picu and Zhang, 2004] Picu R.C, Zhang D. Atomistic study of pipe diffusion in Al–Mg alloys, *Acta Mater.* 52 (2004) 161–171.
- [Pink and Krol, 1995] Pink E., Krol J. Precipitation and serrated flow in AlZn<sub>10</sub>, *Acta Metal. Mater.* 43(6) (1995) 2351-2357.
- [Pink et al., 2000] Pink E., Kumar S., Tian B. Serrated flow of aluminium alloys influenced by precipitates, *Mater. Sci. Eng. A* 280 (2000) 17–24.
- [Pink and Weinhandl, 1998] Pink E., Weinhandl H. The distribution of stress-drop sizes in serrated flow of an aluminium alloy and a mild steel, *Scr. Mater.* 39 (2008) 1309-1316.
- [Pérez et al., 1996] Pérez C. , Corral Á., Díaz-Guilera A., Christensen K., Arenas A. On self-organized criticality and synchronization in lattice models of coupled dynamic systems, *Int. J. Mod. Phys. B* 10 (1996) 1111.

- [Penning, 1972] Penning P. Mathematics of the Portevin-Le Chatelier effect, *Acta Metall.* 20 (1972) 1169-1175.
- [Polmear, 2006] Polmear I.J. *Light Alloys: From Traditional Alloys to Nanocrystals*, 4th ed.; Butterworth-Heinemann/Elsevier: Oxford (2006) UK, pp. 205–235.
- [Portevin and Le Chatelier, 1923] Portevin A., Le Chatelier F. Sur un Phénomène Observé lors de L'essai de Traction d'Alliages en Cours de Transformation, *C. R. Acad. Sci.* 176 (1923) 507-510.
- [Portevin and Le Chatelier, 1924] Portevin A., Le Chatelier F. Heat treatment of aluminum-copper alloys, *Trans of Amer Soc for Steels Treating*, 5 (1924) 457-478.
- [Pustovalov, 2008] Pustovalov V.V. Serrated deformation of metals and alloys at low temperatures, *Low Temp. Phys.* 34(9) (2008) 683-723.
- [Qiao et al., 2016] Qiao J., Jia H., Liaw P. K. Metallic glass matrix composites, *Mater. Sci. Eng. R* 100 (2016) 1-69.
- [Qi Hu et al., 2011] Qi Hu, Qingchuan Zhang, Shihua Fu, Pengtao Cao, Ming Gong. Influence of precipitation on the Portevin-Le Chatelier effect in Al-Mg alloys, *Theoretical & Applied Mechanics Letters* 1 (1) (2011) 011007.
- [Ranc and Wagner, 2005] Ranc N., Wagner D. Some aspects of Portevin–Le Chatelier plastic instabilities investigated by infrared pyrometry, *Mater. Sci. Eng. A* 394 (2005) 87–95.
- [Rizzi and Hähner, 2004] Rizzi E., Hähner P. On the Portevin–Le Chatelier effect: theoretical modeling and numerical results, *J. Int. Plast.* 20 (2004) 121–165.
- [Robinson, 1994] Robinson J.M. Serrated flow in aluminium base alloys, *Intern Mater Reviews* 39 (6) (1994) 216-227.
- [Robinson and Shaw, 1994] Robinson J.M., Shaw M.P. Microstructural and mechanical influences on dynamic strain ageing phenomena, *Intern. Mater. Reviews* 39 (3) (1994) 113-122.
- [Rodriguez, 1984] Rodriguez P. Serrated plastic flow, *Bull. Mater. Sci.* 6 (1984) 653–663.
- [Røyset and Ryum, 2005] Røyset ., Ryum N. Scandium in aluminium alloys, *Intern Mater Reviews* 50 (2005) 19-44.

- [Saad et al., 2010] Saad G., Fayek S.A., Fawzy A., Soliman H.N., Nassr E. Serrated flow and work hardening characteristics of Al-5356 alloy, *Jour. of Alloys and Compounds* 502 (2010) 139–146.
- [Sabirov et al., 2013] Sabirov I., Murashkin M.Yu., Valiev R.Z. Nanostructured aluminium alloys produced by severe plastic deformation: New horizons in development, *Mater. Sci. Eng. A* 560 (2013)1–24.
- [Saltykov, 1970] Saltykov S.A., *Stereometric Metallography*. Moscow: Metallurgiya (1970), 376 p (in Russian).
- [Sarkar et al., 2008] Sarkar A., Charles L., Webber Jr., Barat P., Mukherjee P. Recurrence analysis of the Portevin–Le Chatelier effect, *Physics Letters A* 372 (2008) 1101-1105.
- [Sarkar et al., 2013] Sarkar A., Barat P., Mukherjee P. Investigation of PortevinLe Chatelier effect in Al-2.5 pct Mg alloy with different microstructure, *Metall. Mater. Trans. A* 44 (2013) 2604-2612.
- [Savart, 1937] Savart F. Recherches sur les vibrations longitudinales, *Ann. Chim. Phys.* 65 (1937) 337.
- [Schwab and Ruff, 2013] Schwab R., Ruff V. On the nature of the yield point phenomenon, *Acta Mater.* 61 (2013) 1798–1808.
- [Shabadi et al., 2004] Shabadi R., Kumar S., Roven H.J., Dwarakadasa E.S. Characterisation of PLC band parameters using laser speckle technique, *Mater. Sci. Eng. A* 364 (2004) 140–150.
- [Sheikh, 2010] Sheikh H. Investigation into Characteristics of Portevin-Le Chatelier Effect of an Al-Mg Alloy, *J. Mater. Eng. and Performance*, 19(9) (2010) 1264–1267.
- [Shen et al., 2004] Shen Y.Z., Oh K.H., Lee D.N. The effect of texture on the Portevin-Le Chatelier effect in 2090 Al-Li alloy, *Scr. Mater* 51 (2004) 285-289.
- [Shashkov et al., 2012] Shashkov I.V., Lebyodkin M.A., Lebedkina. T.A. Multiscale study of acoustic emission during smooth and jerky flow in an AlMg alloy, *Acta Mater.* 60 (2012) 6842 -6850.
- [Sleeswijk, 1958] Sleeswijk A.W. Dynamic strain ageing of alloys, *Acta Metall.* 6 (1958) 548.

[Smallman and Bishop, 1999] Smallman R.E., Bishop R. J. Modern Physical Metallurgy and Materials Engineering, Butterworth-Heinemann, 6th edition (1999) Oxford.

[Spencer et al., 2002] Spencer K., Corbin S.F., Lloyd D.J. The influence of iron content on the plane strain fracture behaviour of AA5754 Al–Mg sheet alloys, *Mater. Sci. Eng. A* 325 (2002) 394-404.

[Taleff et al., 2001] Taleff E.M., Nevland P.J., Krajewski E. Tensile ductility of several commercial aluminum alloys at elevated temperatures, *Metall. Mater. Trans. A* 32 (2001) 1119–1130.

[Tamimi et al., 2015] Tamimi S., Andrade-Campos A., Pinho-da-Cruz J. Modelling of the Portevin-Le Chatelier effects in aluminium alloys: a review, *J. Mech. Behav. Mater.* 24 (2015) 67-78.

[Thevenet et al., 1999] Thevenet D., Mliha-Touati M., Zeghloul A. The effect of precipitation on the Portevin-Le Chatelier effect in an Al–Zn–Mg–Cu alloy, *Mater. Sci. Eng. A* 266 (1999) 175–182.

[Tong et al., 2005] Tong W., Tao H., Zhang N., Hector L.G.Jr. Time-resolved strain mapping measurements of individual Portevin–Le Chatelier deformation bands, *Scripta Mater.* 53 (2005) 87–92.

[Toropova et al., 1998] Toropova L.S., Eskin D.G., Kharakterova M.L., Dobatkina T.V. Advanced aluminium alloys containing scandium, Publishing: Gordon and Breach (1988) p.188.

[Turcotte, 1999] Turcotte D.L. Self-organized criticality, *Rep. Prog. Phys.* 62 (1999) 1377-1429.

[Valiev and Langdon, 2006] Valiev R.Z., Langdon T.G. Principles of equal-channel angular pressing as a processing tool for grain refinement, *Prog. Mater. Sci.* 51 (2006) 881–981.

[Valiev et al., 2014] Valiev R.Z., Zhilyaev A.P., Langdon T.G. Bulk Nanostructured Materials: Fundamentals and Applications, Hoboken, NJ: John Wiley & Sons Inc (2014) USA.

[Valdes-Tabernerero et al., 2017] Valdes-Tabernerero M.A., Sancho-Cadenas R., Sabirov I., Murashkin M.Yu., Ovidko I.A., Galve F. Effect of SPD processing on mechanical behavior

and dynamic strain aging of an Al-Mg alloy in various deformation modes and wide strain rate range, *Mater. Sci. Eng. A* 6 96 (2017) 348–359.

[Van den Beukel, 1975] Van den Beukel A. Theory of the effect of dynamic strain aging on mechanical properties, *Phys. Stat. Sol. A* 30 (1975) 197-206.

[Vic-2D system] Vic-2D system. <http://www.correlatedsolutions.com/vic-2d>.

[Vinogradov et al., 2016] Vinogradov A., Yasnikov I. S., Matsuyama H., Uchida M., Kaneko Y., Estrin Y. Controlling strength and ductility: Dislocation-based model of necking instability and its verification for ultrafine grain 316L steel, *Acta Mater.* 106 (2016) 295-303.

[Wagenhofer et al., 1999] Wagenhofer M., Erickson-Natishan M., Armstrong R.W., Zerilli F.J. Influences of strain rate and grain size on yield and serrated flow in commercial Al-Mg alloy, *Scr. Mater* 41 (1999) 1177-1184.

[Wei Wen and Morris, 2004] Wei Wen, Morris, J.G. The effect of cold rolling and annealing on the serrated yielding phenomenon of AA5182 aluminum alloy, *Mater. Sci. Eng. A* 373 (2004) 204–216.

[Wen et al., 2005] Wen Wei, Zhao Yumin, Morris J.G. The effect of Mg precipitation on the mechanical properties of 5xxx aluminum alloys, *Mater. Sci. Eng. A* 392 (2005) 136–144.

[Weiss et al., 2001] Weiss J., Grasso J.-R., Miguel M.-C., Vespignani A., Zapperi S. Complexity in dislocation dynamics: experiments, *Mater. Sci. Eng. A* 309 (2001) 360-364.

[Weiss et al., 2007] Weiss J., Richeton T., Louchet F., Chmel k F., Dobron P., Entemeyer D., Lebyodkin M., Lebedkina T., Fressengeas C., McDonald R.J. Evidence for universal intermittent crystal plasticity from acoustic emission and high-resolution extensometry experiments, *Phys. Rev. B* 76 (2007) 224110.

[Weiss et al., 2015] Weiss J., Rhouma W.B., Richeton T., Dechanel S., Louchet F., Truskinovsky L. From Mild to Wild Fluctuations in Crystal Plasticity, *Phys. Rev. Lett.* 114 (2015) 105504.

[Yasnikov et al., 2014] Yasnikov I.S., Vinogradov A., Estrin Y. Revisiting the Considère criterion from the viewpoint of dislocation theory fundamentals, *Scripta Mater.* 76 (2014) 37-40.

- [Yilmaz, 2011] Yilmaz A. The Portevin-Le Chatelier effect: a review of experimental findings, *Sci. Technol. Adv. Mater.* 12 (2011) 063001.
- [Yuzbekova et al., 2017] Yuzbekova D., Mogucheva A., Zhemchuzhnikova D., Lebedkina T., Lebyodkin M., Kaibyshev R. Effect of microstructure on continuous propagation of the Portevin–Le Chatelier deformation band, *Int. J. Plast.* 96 (2017) 210-226.
- [Zaiser, 2007] Zaiser M. Scale invariance in plastic flow of crystalline solids, *Adv. Phys.* 55 (2007) 185-245.
- [Zhang et al., 2012] Zhang F., Bower A.F., Curtin W.A. The influence of serrated flow on necking in tensile specimens *Acta Mater.* 60 (2012) 43–50.
- [Zbib and Aifantis, 1988] Zbib H.M., Aifantis E.C. A gradient dependent model for the Portevin – Le Chatelier effect, *Scripta Metall.* 22 (1988) 1331-1336.
- [Zhimin Yin et al., 2000] Zhimin Yin, Qinglin Pan, Yonghong Zhang, Feng Jiang. Effect of minor Sc and Zr on the microstructure and mechanical properties of Al-Mg based alloys, *Mater. Sci. Eng. A* 280 (2000) 151- 155.
- [Zhao et al., 2014] Zhao S., Meng C., Mao F., Hu W., Gottstein G. Influence of severe plastic deformation on dynamic strain aging of ultrafine grained Al-Mg alloys, *Acta Mater.* 76 (2014) 54-67.
- [Zhang et al., 2005] Zhang Q., Jiang Z., Jiang H., Chen Z., Wu X. On the propagation and pulsation of Portevin-Le Chatelier deformation bands: An experimental study with digital speckle pattern metrology, *Int. J. Plast.* 21 (2005) 2150–2173.
- [Zhemchuzhnikova et al., 2013] Zhemchuzhnikova D., Mogucheva A., Kaibyshev R. Mechanical properties and fracture behavior of an Al–Mg–Sc–Zr alloy at ambient and subzero temperatures, *Mater. Sci. Eng. A* 565 (2013) 132–141.
- [Zdunek et al., 2008] Zdunek J., Brynk T., Mizera J., Pakieła Z., Kurzydłowski K. J. Digital Image Correlation investigation of Portevin–Le Chatelier effect in an aluminium alloy, *Mater. Charact.* 59 (2008) 1429-1433.
- [Zuev, 2007] Zuev L.B. On the way of plastic flow localization in pure metals and alloys, *Ann. Phys.* 16 (4) (2007) 286-310.

**Résumé.** L'élaboration de nouveaux alliages maintient un fort intérêt pour le phénomène d'instabilité plastique, ou l'effet Portevin-Le Chatelier (PLC), provoqué par l'interaction des dislocations avec des atomes de soluté. Par ailleurs, l'effet PLC attire l'intérêt comme un exemple remarquable d'auto-organisation dans les systèmes dynamiques. Il est associé à des motifs complexes de séries de chutes de contrainte liées à la nucléation et au mouvement des bandes de déformation dans le matériau déformé, et nécessite une compréhension de l'auto-organisation des dislocations.

La déformation plastique des alliages Al-Mg est sujette à l'instabilité dans une large gamme de conditions expérimentales. Pour cette raison, les alliages Al-Mg binaires ont longtemps servi d'objets modèles pour l'étude de l'effet PLC. En même temps, l'utilisation pratique des alliages binaires Al-Mg est limitée en raison d'une faible résistance mécanique. Une amélioration significative de leurs propriétés peut être atteinte en ajoutant des solutés supplémentaires, conduisant en particulier à la formation de précipités. En outre, une forte réduction de la taille de grains du polycristal pourrait être une technique clé pour produire des matériaux à haute résistance et ténacité. Cependant, il existe très peu d'information, souvent contradictoire, sur l'instabilité PLC dans les alliages Al-Mg à grains fins et contenant des précipités. Le but de l'étude de cette thèse a été d'étudier les caractéristiques spécifiques de l'effet PLC dans les alliages à base AlMg, avec et sans nanoparticules, à gros grains et à grains fins, ces derniers obtenus par une méthode de déformation plastique sévère.

Grâce à l'application de méthodes d'extensométrie locale, notamment de la technique de corrélation d'images, ces études ont révélé une persistance non habituelle de la propagation des bandes de déformation dans les alliages comprenant des précipités et/ou des grains fins. Ce mode dynamique est observé dans un large intervalle de vitesses de déformation, tandis qu'il n'apparaît qu'à haute vitesse dans des alliages modèles AlMg. Par ailleurs, l'analyse des distributions statistiques des amplitudes des chutes de contrainte a révélé une tendance vers une statistique en loi puissance, caractéristique du mode de propagation. Ce phénomène est attribué à une modification du couplage spatial entre les dislocations, due à la concentration de contraintes internes. La combinaison de ces études avec l'analyse de l'émission acoustique a mis en évidence une influence de la microstructure sur la compétition entre un facteur aléatoire et la synchronisation des dislocations. Enfin, l'étude par corrélation d'images a permis d'observer une interrelation entre l'instabilité PLC et la formation de la striction.

**Mots clés :** Effet Portevin - Le Chatelier, Alliages d'aluminium, Matériaux nanocristallins, Bandes de déformation, Mécanisme de rupture, Auto-organisation des dislocations

**Abstract.** The elaboration of new alloys sustains a strong interest to the phenomenon of unstable plastic flow, or the Portevin–Le Chatelier (PLC) effect, caused by interaction of dislocations with solute atoms. Moreover, this effect attracts interest as a rich example of self-organization in dynamical systems. It is associated with complex patterns of stress serrations related to nucleation and motion of deformation bands in the deforming material, and requires understanding of self-organization of dislocations.

Plastic deformation of Al-Mg alloys is prone to instability in a wide range of experimental conditions. For this reason, binary Al-Mg alloys served for a long time as model objects for investigation of the PLC effect. At the same time, the practical use of binary Al-Mg alloys is limited because of their low strength. A significant improvement of their properties can be achieved by additional alloying, in particular, leading to precipitation. Further, extensive grain refinement could be a key technique used to produce tough and high-strength materials. However, there exists very limited and often contradictory information on the PLC instability in fine-grained Al-Mg alloys containing precipitates. The objective of the present thesis was to investigate specific features of the PLC effect in AlMg-based alloys with and without nanoscale particles, both in coarse-grained and fine-grained states, the latter obtained by severe plastic deformation.

Using local extensometry methods, particularly the image correlation technique, these studies revealed an unusual persistence of the propagation of deformation bands in alloys with precipitates and/or fine grains. This dynamic mode is observed in a wide range of strain rates, whereas it only appears at high strain rate in model Al-Mg alloys. Moreover, the analysis of statistical distributions of stress drop amplitudes revealed a tendency to power law statistics characteristic of the propagation mode. This phenomenon was attributed to a modification of the spatial coupling between dislocations due to the concentration of internal stresses. The combination of these studies with the acoustic emission analysis uncovered an influence of the microstructure on the competition between a random factor and the dislocation synchronization. Finally, the study by the image correlation made it possible to observe an interrelation between the PLC instability and the neck formation.

**Keywords :** Portevin-Le Chatelier effect, Aluminum alloys, Nanocrystalline materials, Deformation bands, Fracture mechanism, Self-organization of dislocations

## Résumé de thèse

La présente étude de thèse réunit deux domaines de recherche. Le premier concerne l'effet Portevin-Le Chatelier (PLC) [Portevin et Le Chatelier, 1923] - phénomène d'instabilité plastique dans les alliages, provoqué par l'interaction des dislocations avec les atomes de soluté, ou vieillissement dynamique. Il est lié à des motifs spatio-temporels complexes de localisation des déformations dans des bandes de déformation mobiles ou immobiles et aux variations concomitantes de la contrainte appliquée. Outre l'effet néfaste évident des bandes de déformation sur la qualité de surface des pièces fabriquées, l'instabilité affecte également diverses propriétés mécaniques du matériau, notamment l'écrouissage, la résistance à la traction, la ductilité et le mode d'endommagement et de rupture [Estrin et Kubin, 1995]. L'élaboration de nouveaux alliages révèle une grande diversité de comportements de matériaux de composition et/ou de microstructure différentes et maintient un intérêt constant pour l'instabilité PLC depuis sa découverte il y a plus d'un siècle. De plus, l'instabilité plastique suscite un intérêt croissant depuis le milieu des années 1990 comme exemple frappant d'auto-organisation des dislocations [Kubin et al., 2002]. En même temps, cela rend la tâche d'élaboration encore plus compliquée parce que la prédiction des comportements réels nécessite la compréhension de l'auto-organisation des dislocations.

Le deuxième thème concerne un domaine en plein développement des matériaux nanostructurés produits par déformation plastique sévère (SPD), dont la granulométrie est réduite à un micron ou moins et qui présentent des propriétés mécaniques et physiques exceptionnelles [Valiev et al., 2014]. Ces matériaux ont non seulement une structure à grains fins, mais aussi des propriétés spécifiques telles que les joints métastables des grains, le maclage et les particules à l'échelle nanométrique, la ségrégation aux joints de grains, et ainsi de suite. Ces caractéristiques se traduisent par une amélioration des propriétés fonctionnelles (mécanique, électrique, corrosion, etc.), notamment en termes de résistance mécanique élevée.

Il n'est pas surprenant que l'influence de l'instabilité plastique sur le comportement mécanique de ces matériaux attire l'attention. Cependant, des études récentes ont révélé un large éventail de comportements souvent contradictoires. La raison possible de ces ambiguïtés peut être une influence complexe de la microstructure sur l'écoulement plastique instable qui est intrinsèquement multi-échelle en raison de l'auto-organisation des dislocations. La présente thèse vise donc une étude multi-échelle combinant plusieurs techniques expérimentales, à savoir les essais mécaniques, l'émission acoustique (EA) et l'extensométrie locale, sur plusieurs alliages à base d'AlMg avec différentes microstructures contrôlées.

Le choix d'un système basé sur l'AlMg a été imposé par deux facteurs. Premièrement, en raison de leur faible poids et de leur résistance mécanique élevée, les alliages AlMg sont des matériaux technologiques importants pour diverses applications. Deuxièmement, les alliages binaires d'AlMg ont longtemps été utilisés comme matériaux modèles pour l'étude des mécanismes physiques associés à l'instabilité PLC. En même temps, leur utilisation pratique est limitée en raison de leur faible résistance mécanique et de leur forte susceptibilité à la fissuration par corrosion sous contrainte [Polmear, 2006]. De nombreux efforts pour améliorer les propriétés d'utilisation de ces alliages par durcissement par précipitation et/ou raffinement extrême des grains ont montré que la microstructure spécifique peut fortement affecter l'écoulement saccadé [Aboufadi et al., 2015; Halim et al., 2007; Mogucheva et al., 2016; Zhao et al., 2014; Sarkar et al., 2013; Lebedkina et al., 2014; Wagenhofer et al., 1999; Bazarnik et al., 2012]. L'influence de divers précipités sur l'instabilité PLC a été étudiée pendant longtemps. Cependant, ces recherches visaient principalement à caractériser les propriétés mécaniques globales, alors que les particularités du comportement spatio-temporel restaient largement négligées. Les recherches sur l'effet du raffinement des grains ont commencé récemment et ont conduit à des conclusions contradictoires [Sarkar et al. 2013 ; Lebedkina et al. 2014 ; Wagenhofer et al. 1999 ; Bazarnik et al. 2012 ; Mogucheva et al. 2016 ; Zhao et al. 2014]. De plus, l'application de nouvelles méthodes expérimentales a révélé une plus grande diversité de comportements même pour les alliages binaires conventionnels à gros grains [Ait-Amokhtar et al., 2006 ; Chihab et al., 1987].

Ces exemples prouvent la nécessité d'investigations systématiques et complètes de l'effet de la microstructure initiale sur le comportement spatio-temporel complexe de l'instabilité PLC. L'objectif de la thèse de doctorat était de réaliser de telles études dans une large gamme de vitesse de déformation couvrant différents types d'instabilité et de comparer les comportements d'un alliage binaire d'Al-3%Mg et de plusieurs alliages avec des additifs Zr et/ou Sc, qui ont un potentiel d'application élevé [Filatov et al., 2000]. Les alliages ont été étudiés à l'état initial à gros grains (CG) et à l'état à grains fins (FG) obtenu par Equal Channel Angular Pressing (ECAP). Deux alliages ont également été soumis à un laminage à froid supplémentaire à la suite de l'ECAP (cet état matériel est également appelé FGH). En conséquence, dix nuances de microstructure ont été comparées.

La thèse contient une introduction, cinq chapitres, un résumé général et la bibliographie. L'introduction décrit l'état de l'art dans le domaine de la recherche et formule les objectifs des recherches. Le premier chapitre présente une revue de littérature qui aborde divers aspects concernant l'effet PLC, la microstructure et les propriétés mécaniques des alliages AlMg renforcés par des additifs Zr et Sc, la technique ECAP de déformation plastique sévère, les bases de

l'approche statistique de l'analyse de la complexité de l'écoulement saccadé, dont l'EA qui accompagne la déformation plastique.

Le chapitre 2 présente les objets d'investigation et les approches expérimentales. Il décrit d'abord les matériaux étudiés, y compris leurs compositions chimiques et de phase, leur microstructure, ainsi que les techniques appliquées pour la caractérisation de la microstructure et de la phase dans diverses conditions. La principale différence entre les alliages à base d'AlMg étudiés provient de leur composition de phase. En plus de l'alliage binaire, trois autres matériaux contenaient respectivement des particules grossières, fines et un mélange de particules grossières et fines de seconde phase. La structure granulaire initiale à l'état CG était différente dans les différents alliages. La densité des dislocations de la maille cristalline était proche pour tous les matériaux et relativement faible ( $\leq 10^{13} \text{ m}^{-2}$ ). L'ECAP a donné lieu à la formation de microstructures à grains fins uniformes similaires et à une densité des dislocations de la maille proche de  $10^{14} \text{ m}^{-2}$  pour tous les alliages. La densité des dislocations la plus élevée de  $10^{15} \text{ m}^{-2}$  a été observée dans l'état FHG. Dans tous les alliages, la SPD n'a produit aucun effet visible sur la taille et la distribution des particules de la deuxième phase.

Ce chapitre décrit également des détails expérimentaux sur les essais mécaniques, la technique EA et deux méthodes complémentaires d'extensométrie locale appliquées pour quantifier la cinématique des bandes de déformation. L'extensométrie unidimensionnelle basée sur l'enregistrement des déplacements longitudinaux d'une séquence de marqueurs de surface à l'aide d'une caméra CCD (charge-coupled device) a permis une bonne combinaison de résolution spatiale ( $1.3 \mu\text{m}$ ) et temporelle ( $10^3 \text{ Hz}$ ). La deuxième technique, basée sur la corrélation d'images (DIC) en deux dimensions, avait une résolution inférieure mais fournissait des informations précieuses sur la géométrie de la bande de déformation.

Les résultats des enquêtes sont présentés aux chapitres 3 à 5.

Le chapitre 3 constitue la majeure partie de la thèse. Il rend compte des résultats d'une étude approfondie des motifs des courbes de déformation en dents de scie et des cartes des vitesses de déformation locales associées à l'effet PLC pour toutes les microstructures décrites ci-dessus et dans une large gamme de vitesses de déformation couvrant différents types de comportement spatiotemporel. L'étude la plus détaillée de la structure polycristalline et de son effet sur l'instabilité PLC, couvrant les conditions CG et deux états différents à grains fins obtenus soit par l'ECAP soit par l'ECAP suivi du laminage à froid, a été réalisée pour l'alliage binaire et l'alliage contenant les gros précipités non sécables. Le comportement global à la traction à l'état CG des deux alliages s'est avéré conforme aux types bien connus de courbes de déformation en dents de scie et de la cinématique des bandes PLC [Rodriguez, 1984]. En particulier, le comportement à vitesse de

déformation élevée est caractérisé par une propagation quasi-continue des bandes de déformation donnant lieu à des fluctuations irrégulières de contrainte (comportement de type *A*). Lorsque la vitesse de déformation appliquée est réduite, ce modèle se transforme progressivement en une propagation à saut (« propagation relais ») caractérisée par des séries spatialement corrélées de bandes localisées et par des oscillations de contrainte relativement régulières (type *B*), et enfin en bandes non corrélées entraînant des chutes de contrainte brusques (type *C*). Ces observations fournissent un lien avec les mécanismes connus de l'instabilité PLC et justifient l'étude de ses caractéristiques spécifiques dans les matériaux à microstructures complexes.

L'application des techniques d'extensométrie locale a permis d'obtenir de nouvelles informations sur la cinématique des bandes de déformation et a révélé plusieurs caractéristiques inconnues de l'effet PLC. L'un des résultats majeurs dans le cadre des travaux de thèse est l'observation d'une propagation persistante des bandes de déformation sur l'ensemble de la gamme des vitesses de déformation dans le cas de l'alliage renforcé par précipitation [Zhemchuzhnikova et al., 2018]. Ce comportement, inconnu jusqu'à présent, est lié à un mélange inhabituel de motifs de type *C+A* trouvés à la plus faible vitesse de déformation. Les résultats présentés au chapitre 3 ont permis de suggérer que le mécanisme de propagation inhabituelle des bandes de déformation à faible vitesse de déformation est dû à la concentration des contraintes internes sur les précipités, qui représentent de forts obstacles au mouvement de dislocation, de sorte que les surcharges résultantes favorisent le transfert de la déformation plastique aux sites voisins.

En prenant en compte le fait que les joints de grains sont également des obstacles efficaces au mouvement de dislocation, cette hypothèse a d'abord été vérifiée en utilisant les mêmes alliages soumis au SPD. L'ECAP a radicalement modifié les motifs spatio-temporels, donnant lieu à une forte tendance aux comportements de type *B* et de type *C*. En même temps, on a constaté que la propagation inhabituelle à faible vitesse de déformation, qui n'a été détectée que pour l'alliage renforcé par particules à l'état CG, s'est produite dans les deux matériaux après l'ECAP. Le motif respectif des bandes de déformation a également été associé à une transition peu fréquente entre les chutes de contrainte de type *C* et de type *A* pendant la déformation. Une telle persistance du mode de propagation à faible vitesse de déformation dans le matériau avec une densité élevée de joints de grains corrobore l'hypothèse ci-dessus. Un autre argument frappant en faveur du rôle important du champ de contraintes internes sur la dynamique de l'instabilité de PLC provient des résultats trouvés dans l'état FGH des deux alliages. Il arrive qu'un tel prétraitement sévère du matériau supprime complètement les chutes de contrainte, au moins pendant la phase d'érouissage, c'est-à-dire avant l'apparition de la striction (voir ci-dessous l'analyse de la striction). Néanmoins, l'analyse DIC montre que ces courbes lisses ne sont pas dues à une

déformation uniforme de l'éprouvette en traction, comme on pourrait le suggérer, mais sont associées à la propagation d'une ou deux bandes PLC.

La vérification plus poussée du mécanisme proposé a été fournie par une comparaison de ces résultats avec les données obtenues pour l'alliage avec des précipités fins et l'alliage contenant les deux types de précipités, dans des conditions CG et après l'ECAP. En effet, il a été constaté que malgré les différents types de particules, les changements qualitatifs dans la cinématique des bandes PLC, ainsi que leurs caractéristiques, sont similaires pour tous les alliages étudiés et peuvent être rationalisés en termes d'augmentation, d'une manière ou d'une autre, des contraintes locales favorisant la propagation des bandes de déformation.

Plusieurs autres observations présentées au chapitre 3 peuvent être évoquées :

- Un battement de la vitesse de déformation locale donnant lieu à des oscillations de contrainte a été observé au cours de la propagation de la bande PLC à de faibles vitesses de déformation. Aussi inhabituel qu'il puisse paraître, il est cependant cohérent avec le rôle commun de la vitesse de déformation imposée, c'est-à-dire une tendance à la localisation statique de la déformation à charge lente. Apparemment, un tel rythme révèle une concurrence entre deux tendances opposées, la tendance bien connue à la localisation de déformation et la tendance à la propagation des bandes dont il a été question plus haut ;

- La cartographie à résolution temporelle des bandes de déformation statiques de type *B* a montré que la formation et la terminaison de la bande se font progressivement, à travers la phase de faible localisation de déformation dans une bande de déformation diffuse. Cette bande couvre toute la section transversale de l'échantillon. La chute de contrainte elle-même correspond à une bande PLC bien délimitée caractérisée par une intensité beaucoup plus élevée de localisation de la vitesse de déformation. Ainsi, en plus des modèles existants de formation de la bande PLC via les phases de nucléation et de croissance d'un noyau, ce résultat démontre la possibilité d'un mécanisme alternatif par une localisation simultanée de la déformation sur toute la région de la bande en formation [Lebyodkin et al., 2019].

- L'analyse quantitative de la vitesse de propagation de la bande de déformation dans les états CG et FG a montré que son évolution en cours de déformation peut être décrite par une fonction de loi de puissance de contrainte réelle avec une coupure proche de la charge maximale, où les bandes sont progressivement immobilisées. Pour un matériau et une microstructure donnés, il obéit à une dépendance unique de la vitesse de déformation sur l'ensemble de la plage de vitesse de déformation couvrant la propagation quasi-continue (à la fois de type *A* et la propagation lente) et celle par sauts. En même temps, les dépendances trouvées pour différents matériaux correspondent à des exposants de loi de puissance distincts. Ces résultats suggèrent un mécanisme

dynamique sous-jacent pertinent aux différentes vitesses de déformation et influencé par la microstructure.

Le chapitre se termine par un résumé général et une discussion sur le mécanisme possible du régime de propagation lente. L'omniprésence de la propagation lente, en ce sens qu'elle a été observée pour différents types d'obstacles supplémentaires au mouvement de dislocation (précipités cohérents et non cohérents, joints de grains), suggère l'existence d'un mécanisme inhérent commun dans tous les cas. Comme indiqué plus haut, il a probablement été attribué à la concentration des contraintes sur les obstacles qui durcissent localement le matériau et peuvent favoriser la propagation de la bande de déformation. La discussion finale intègre cette hypothèse dans un cadre général proposé récemment [Bharathi et al., 2002 ; Lebyodkin et al., 2012], qui est basé sur les considérations des conditions de relaxation et d'homogénéisation des contraintes internes générées par les localisations de déformation dans les bandes PLC. Il est avancé que la propagation est favorisée lorsque la relaxation des contraintes d'incompatibilité est insuffisante, que ce soit en raison du rechargement rapide (comportement de type *A*) ou d'une densité élevée d'obstacles au mouvement des dislocations. Dans l'ensemble, les transitions entre des motifs spatio-temporels qualitativement différents sont causées par une compétition entre la synchronisation des dislocations, conduisant à la localisation des déformations lorsque le champ de déformation local est suffisamment uniforme, et la propagation de l'activité plastique dans des conditions hétérogènes. L'un des facteurs qui contrôlent cette contre action est l'efficacité de la relaxation des contraintes internes qui est affectée à la fois par les précipités et les joints de grains. Par conséquent, les manifestations précises de l'instabilité PLC dans les alliages à composition complexe peuvent être spécifiques au système et nécessiter une étude systématique de divers alliages.

Le chapitre 4 soulève la question d'une relation entre l'instabilité PLC et une instabilité (géométrique) aussi générale que la striction. Il présente une étude expérimentale de cette relation dans les alliages binaires et renforcés par les précipitations (grosses particules) dans les trois conditions de microstructure initiale différentes et dans la plage de vitesse de déformation couvrant trois ordres de grandeur. On constate qu'en dépit de la diversité des comportements spatio-temporels obtenus par variation de la microstructure et des conditions de déformation de deux alliages, l'apparition de striction dans les conditions de l'effet PLC correspond bien au critère géométrique Considère. En même temps, l'analyse DIC révèle une relation étroite entre la formation de striction et les bandes PLC antérieures : la striction se trouve dans la section transversale où la dernière bande PLC est localisée. En d'autres termes, l'apparition de striction est

associée à une immobilisation progressive des bandes PLC, qui se termine par la localisation de la contrainte ultime.

De plus, les deux types d'instabilité plastique physiquement différents, à savoir l'adoucissement par la vitesse de déformation dépendant du matériau (l'effet PLC), qui conduit à la propagation de localisations transitoires de déformation le long du cristal, et l'instabilité géométrique (de striction) qui limite la localisation de la déformation à un site, peuvent coexister pendant le développement de la striction et modifier leur comportement mutuel. En particulier, on a constaté que la localisation de la déformation au début de striction dans les échantillons FGH peut forcer la transition entre les bandes PLC mobiles et statiques et donner lieu à des courbes de déformation oscillatoires. Plus généralement, la concomitance des tendances à la propagation et à la localisation de la déformation peut produire un battement dans les cartes spatio-temporelles (voir ci-dessus).

Le chapitre 5 explore une approche différente de l'étude de l'instabilité plastique, empruntée à l'analyse des séries temporelles. Elle a non seulement apporté des arguments indépendants aux conclusions présentées au chapitre 3, mais a également révélé de nouveaux aspects du rôle de la microstructure [Lebedkina et al., 2018]. Plus précisément, cette dernière partie de la thèse est consacrée à l'analyse statistique des chutes de contrainte et de l'EA concomitante pour l'alliage aux précipités fins et à la comparaison de ces statistiques avec les données bibliographiques pour les alliages binaires. Tout d'abord, on sait que différents types de comportement de l'effet PLC correspondent à des types distincts de distributions d'amplitude des chutes de contrainte [Lebyodkin et al., 2000]. Des distributions de loi de puissance invariantes d'échelle sont couramment observées pour le comportement de type *A* à des vitesses de déformation élevées, tandis que des échelles caractéristiques apparaissent lorsque la vitesse de déformation est réduite aux valeurs correspondant au comportement de type *B* et de type *C*, comme le reflètent les histogrammes avec pics. Cette séquence est fortement modifiée dans le cas du matériau renforcé par les précipitations étudiées. En particulier, l'état CG montre une tendance inhabituelle à la distribution des lois de puissance des chutes de contrainte sur l'ensemble de la plage de vitesse de déformation, en accord avec l'observation de la prédominance de la propagation des bandes PLC pour le même matériau. L'alliage FG présente des caractéristiques encore moins communes, de sorte que les statistiques invariantes d'échelle ne sont observées qu'à la vitesse de déformation la plus faible, ce qui correspond à la transition inhabituelle entre les bandes statiques et les bandes PLC propagées après une certaine déformation. Ces résultats corroborent les hypothèses évoquées ci-dessus selon lesquelles les comportements particuliers de l'instabilité PLC dans les alliages à microstructures complexes sont dus à l'effet de microstructure sur la relaxation et l'homogénéisation des contraintes internes générées par les localisations de déformation. Plus

spécifiquement, les différences par rapport au comportement des alliages binaires confirment l'hypothèse que la microstructure peut fortement affecter l'auto-organisation des dislocations.

Deuxièmement, on a récemment découvert que l'EA qui accompagne la déformation plastique des alliages binaires d'AlMg obéit aux lois de puissance dans toutes les conditions de déformation [Lebyodkin et al., 2012]. De plus, de telles statistiques invariantes d'échelle caractérisent l'écoulement plastique de tous les matériaux étudiés jusqu'à présent, y compris le cas de la déformation macroscopique stable de cristaux purs [Weiss et al., 2007]. Ces résultats ont conduit à suggérer que l'EA révèle une nature avalancheuse inhérente de la dynamique des dislocations sur les échelles de temps et d'énergie beaucoup plus fines que celles accessibles dans les tests mécaniques conventionnels et les tests d'extensométrie locale. L'analyse effectuée au chapitre 5 a montré que les statistiques de l'EA en alliage avec précipités sont également invariantes d'échelle à toutes les vitesses de déformation. Cependant, la comparaison quantitative a révélé des différences essentielles avec les alliages binaires, pour lesquels on a observé que l'exposant de la loi de puissance de la fonction de densité de probabilité de l'intensité de l'EA augmente avec la déformation. Comme un exposant plus élevé reflète une probabilité plus élevée de petits événements, cette évolution s'explique par la randomisation des processus de déformation en cours d'écrouissage, car l'accumulation des dislocations crée des obstacles à leur mouvement [Lebyodkin et al., 2012]. Dans l'alliage étudié, en revanche, la valeur correspondante est élevée au début de l'essai et diminue pendant la déformation, en accord avec la tendance à la propagation de la bande de déformation et contre l'hypothèse de randomisation. Cette controverse donne à penser que les obstacles au mouvement des dislocations peuvent jouer un double rôle. Bien que l'arrêt des dislocations sur les obstacles briserait leur corrélation, la concentration des contraintes peut déclencher le glissement de dislocations à proximité, entraînant ainsi des avalanches plus fortes.

De plus, les effets des joints de grains et des précipités ne sont pas équivalents. En effet, bien que le raffinement de grains et la présence de précipités aient conduit à la propagation des bandes PLC à basse vitesse de déformation, l'ECAP a également entraîné une tendance à la localisation des déformations et aux chutes profondes à des vitesses de déformation élevées. Le rôle des joints de grains peut donc être plus complexe, p. ex. en raison de la nucléation ou de l'absorption des dislocations, ce qui permet la relaxation des contraintes. On peut donc s'attendre à ce que les comportements réels des alliages complexes résultent d'un équilibre subtil entre tous ces facteurs, ce qui peut donner lieu à une grande variété de motifs d'écoulement saccadé.

Enfin, un résumé général des résultats obtenus et une discussion sur les perspectives d'études futures complètent la thèse.

## Bibliographie

- [Aboulfadl et al., 2015] Aboulfadl H., Deges J., Choi P., Raabe D. Dynamic strain aging studied at the atomic scale, *Acta Mater.* 86 (2015) 34-42.
- [Ait-Amokhtar et al., 2006] Ait-Amokhtar H., Vacher P., Boudrahem S. Kinematics fields and spatial activity of Portevin-Le Chatelier bands using the digital image correlation method, *Acta Mater.* 54 (2006) 4365-4371.
- [Bazarnik et al., 2012] Bazarnik P., Lewandowska M., Kurzydowski K.J. Mechanical behavior of ultrafine grained Al-Mg alloys obtained by different processing routes, *Arch. Metall. Mater* 57 (2012) 869-876.
- [Bharathi et al., 2002] Bharathi M. S., Lebyodkin M., Ananthakrishna G., Fressengeas C., Kubin L.P. The hidden order behind jerky flow, *Acta Mater.* 50 (2002) 2813–2824.
- [Chihab et al., 1987] Chihab K., Estrin Y., Kubin L.P., Vergnol J. The kinetics of the Portevin-Le Chatelier bands in an Al-5at%Mg alloy, *Scr. Metall.* 21 (1987) 203–208.
- [Estrin and Kubin, 1995] Estrin Y., Kubin L.P., 1995. Spatial coupling and propagative plastic instabilities. In: Muhlhaus, H.-B. (Ed.), *Continuum Models for Materials with Microstructure*. John Wiley & Sons Ltd, pp. 395–450.
- [Filatov et al., 2000] Filatov Yu.A., Yelagin V.I., Zakharov V.V. New Al-Mg-Sc alloys, *Mater. Sci. Eng. A* 280 (1) (2000) 97-101.
- [Halim et al., 2007] Halim H., Wilkinson D.S., Niewczas M. The Portevin-Le Chatelier (PLC) effect and shear band formation in an AA5754 alloy, *Acta Mater.* 55 (2007) 4151-4160.
- [Kubin et al., 2002] Kubin L.P., Fressengeas C., Ananthakrishna G. Collective behavior of dislocations in plasticity, *Dislocations in Solids* (edited by F.R.N. Nabarro and M.S. Duesbery) Elsevier Science BV, Amsterdam, Vol. 11 (2002) p. 101.
- [Lebedkina et al., 2014] Lebedkina T.A., Lebyodkin M.A., Lamark T.T., Janecek M., Estrin Y. Effect of equal channel angular pressing on the Portevin–Le Chatelier effect in an Al3Mg alloy, *Mater. Sci. Eng. A* 615 (2014) 7–13.
- [Lebedkina et al., 2018] Lebedkina T.A., Zhemchuzhnikova D.A., Lebyodkin M.A. Correlation versus randomization of jerky flow in an AlMgScZr alloy using acoustic emission, *Phys. Rev. E* 97 (2018) 013001.
- [Lebyodkin et al., 2019] Lebyodkin M.A., Zhemchuzhnikova D.A., Lebedkina T.A., Aifantis E.C. Kinematics of formation and cessation of type B deformation bands during the Portevin-Le Chatelier effect in an AlMg alloy, *Results in Physics* 12 (2019) 867–869.
- [Lebyodkin et al., 2012] Lebyodkin M.A., Kobelev N.P., Bougherira Y., Entemeyer D., Fressengeas C., Gornakov V.S., Lebedkina T.A., Shashkov I.V. On the similarity of plastic flow processes during smooth and jerky flow: Statistical analysis, *Acta Mater.* 60 (2012) 3729–3740; On the similarity of plastic flow processes during smooth and jerky flow in dilute alloys. *Acta Mater.* 60 (2012) 844-850.

- [Lebyodkin et al., 2000] Lebyodkin M., Dunin-Barkowskii L., Brechet Y., Estrin Y., Kubin L.P. Spatio-temporal dynamics of the Portevin-Le Chatelier effect: Experiment and modelling, *Acta Mater.* 48 (2000) 2529–2541.
- [Mogucheva et al., 2016] Mogucheva A., Yuzbekova D., Kaibyshev R., Lebedkina T., Lebyodkin M. Effect of grain refinement on jerky flow in an Al-Mg-Sc alloy, *Metall. Mater. Trans. A* 47 (2016) 2093-2106.
- [Polmear, 2006] Polmear I.J. *Light Alloys: From Traditional Alloys to Nanocrystals*, 4th ed.; Butterworth-Heinemann/Elsevier: Oxford (2006) UK, pp. 205–235.
- [Portevin et Le Chatelier, 1924] Portevin A., Le Chatelier F. Heat treatment of aluminum-copper alloys, *Trans of Amer Soc for Steels Treating*, 5 (1924) 457-478.
- [Rodriguez, 1984] Rodriguez P. Serrated plastic flow, *Bull. Mater. Sci.* 6 (1984) 653–663.
- [Valiev et al., 2014] Valiev R.Z., Zhilyaev A.P., Langdon T.G. *Bulk Nanostructured Materials: Fundamentals and Applications*, Hoboken, NJ: John Wiley & Sons Inc (2014) USA.
- [Sarkar et al., 2013] Sarkar A., Barat P., Mukherjee P. Investigation of Portevin-Le Chatelier effect in Al-2.5 pct Mg alloy with different microstructure, *Metall. Mater. Trans. A* 44 (2013) 2604-2612.
- [Wagenhofer et al., 1999] Wagenhofer M., Erickson-Natishan M., Armstrong R.W., Zerilli F.J. Influences of strain rate and grain size on yield and serrated flow in commercial Al-Mg alloy, *Scr. Mater* 41 (1999) 1177-1184.
- [Weiss et al., 2007] Weiss J., Richeton T., Louchet F., Chmelík F., Dobron P., Entemeyer D., Lebyodkin M., Lebedkina T., Fressengeas C., McDonald R.J. Evidence for universal intermittent crystal plasticity from acoustic emission and high-resolution extensometry experiments, *Phys. Rev. B* 76 (2007) 224110.
- [Zhemchuzhnikova et al., 2018] Zhemchuzhnikova D., Lebyodkin M., Yuzbekova D., Lebedkina T., Mogucheva A., Kaibyshev R. Interrelation between the Portevin Le-Chatelier effect and necking in AlMg alloys, *Int. J. Plast.* 110 (2018) 95–109.
- [Zhao et al., 2014] Zhao S., Meng C., Mao F., Hu W., Gottstein G. Influence of severe plastic deformation on dynamic strain aging of ultrafine grained Al-Mg alloys, *Acta Mater.* 76 (2014) 54-67.